2010

Developing an efficient nanocatalyst system for enhanced photocatalytic degradation of toxic aqueous contaminants

Srimanta Ray
University of Windsor

DEVELOPING AN EFFICIENT NANOCATALYST SYSTEM FOR ENHANCED PHOTOCATALYTIC DEGRADATION OF TOXIC AQUEOUS CONTAMINANTS

by

Srimanta Ray

A Dissertation
Submitted to the Faculty of Graduate Studies and Research
through the Department of Civil & Environmental Engineering
in Partial Fulfillment of the Requirements for
the Degree of Doctor of Philosophy at the
University of Windsor

Windsor, Ontario, Canada

2010

Your file Votre référence
ISBN: 978-0-494-62762-4
Our file Notre référence
ISBN: 978-0-494-62762-4

DECLARATION OF PREVIOUS PUBLICATION

This thesis includes two original papers that have been published in a peer reviewed journal and in a conference proceeding. The papers appear in Chapter 3 and 4 are as follows:

Dissertation Chapter	Publication title	Publication status
Chapter 3	Using the Box-Benkhen technique to statistically model phenol photocatalytic degradation by titanium dioxide nanoparticles ***Chem. Eng. J.***, 2009, 150, 15-24	*Published*
Chapter 4	Statistical model for photocatalysis of *p*-cresol with titanium dioxide nanoparticles. ***Proc. World Cong. Chem. Eng.,*** 2009, Montreal, PQ	*Published*

I certify that I have obtained a written permission from the copyright owner(s) to include the above published material(s) in my thesis. I certify that the above material describes work completed during my registration as graduate student at the University of Windsor.

I declare that, to the best of my knowledge, my thesis does not infringe upon anyone's copyright nor violate any proprietary rights and that any ideas, techniques, quotations, or any other material from the work of other people included in my thesis, published or otherwise, are fully acknowledged in accordance with the standard referencing practices. Furthermore, to the extent that I have included copyrighted material that surpasses the bounds of fair dealing within the meaning of the Canada Copyright Act, I certify that I have obtained a written permission from the copyright owner(s) to include such material(s) in my thesis.

I declare that this is a true copy of my thesis, including any final revisions, as approved by my thesis committee and the Graduate Studies office, and that this thesis has not been submitted for a higher degree to any other university or institution.

ABSTRACT

Heterogeneous photocatalysis is an emerging treatment option for degrading phenolic contaminants. This dissertation focused on using Titanium dioxide (TiO_2) nanomaterials as a potential heterogeneous photocatalyst. The various factors affecting the TiO_2 nanoparticle catalyzed photo-degradation process were discussed and the photocatalysis of phenol using TiO_2 nanoparticles was evaluated. A statistical model was developed to consolidate the factors based on the Box-Benkhen statistical design (BBD) technique. The degradation rate constant was considered as the model response, and expressed as a function of the independent variables for the photocatalysis. The independent variables considered for developing the BBD based model were as follows: TiO_2 nanoparticle size and concentration, dissolved oxygen (DO) concentration, and substrate concentration. The model-predicted phenol photocatalytic rates were in agreement with the experimental rates for all four variables under consideration. The model developed for phenol degradation was later used to predict the photocatalytic degradation rate of *p*-cresol, a substituted phenol. Except at high DO concentration and low *p*-cresol concentration, the model-predicted rates were in close agreement with the experimental degradation rate for *p*-cresol. A comparison of quantum yield and activation energy for phenol and *p*-cresol revealed that the latter degraded faster than the former.

The practical limitations associated with the use of TiO_2 nanoparticle slurry in photocatalytic process, and the challenges in immobilizing TiO_2 nanoparticles onto a solid catalyst support were discussed. A study on fabrication of immobilized TiO_2 nanofiber using sol-gel electrospinning was presented in the later chapters of this dissertation. The characterization procedures followed to fabricate the immobilized TiO_2 nanofiber catalyst was presented. Literature suggested that stability of the immobilized nanofiber catalyst was an issue. A surface treated catalyst support

material was used to improve the stability of the immobilized nanofiber catalyst. The optimum process variable settings of sol-gel electrospinning for minimum nanofiber diameter were identified using the BBD procedure. The diameter of the TiO_2 nanofiber generated from the BBD optimization was significantly lower than that reported in the literature. Other than the electrospinning variables, the calcination condition and catalyst loading on the support affected the specific surface area (SSA) of the immobilized catalyst. The immobilized TiO_2 nanofiber catalyst fabricated by sol-gel electrospinning under optimum process conditions had high SSA and improved catalytic property. A comparison of phenol photocatalytic rates of TiO_2 nanoparticle slurries against the immobilized TiO_2 nanofiber demonstrated that the latter had higher (approximately twice) catalytic activity than that of the former at comparable SSA.

DISSERTATION ORGANIZATION

The heterogeneous photocatalytic process is introduced in Chapter 1 as an emerging treatment option in context to the challenges of conventional treatment processes such as, their effectiveness and limitations in removal of phenolic contaminants. An outline of existing constraints facing the development of heterogeneous photocatalytic degradation process is discussed in this section. The various research objectives are also discussed in Chapter 1. Chapter 2 elaborates on the outlines presented in Chapter 1. The literature review presented in Chapter 2 provides the necessary background to execute the research objectives discussed in Chapter 1. The literature reviews associated with the concept of Titanium dioxide (TiO_2) photocatalysis, factors affecting the process, and the advantages of the immobilized photocatalyst system are examined in Chapter 2. The limitations of the immobilization processes and the potential of the electrospinning technique in context to catalyst immobilization are also discussed. Earlier studies on electrospinning TiO_2 for photocatalytic applications are reviewed and the shortcomings of those reports are highlighted. The overall aim of this chapter is to disseminate sufficient information related to the scope of the research. The dissertation is presented in manuscript format with the results from five phases of the research presented in Chapter 3 to Chapter 7. Each chapter contained separate introduction, methodology, and discussion on results pertaining to a research phase. Due to the overlap in the objectives between the (five) research phases, there is some similarity in the introduction and methodology among the chapters. Chapter 3 detailed the study on developing and validating a statistical model for the photocatalytic degradation of phenol using TiO_2 nanoparticles. The optimum condition for the maximum photocatalytic degradation of phenol in batch reactors is reported in this chapter. A validation study to extend the use of the phenol model on other phenol derivatives such as *p*-

cresol, is presented in Chapter 4. Chapter 5 provides an outline on earlier attempts to generate TiO_2 nanofiber catalyst and identifies the limitations involved therein. The characterization results of immobilized TiO_2 nanofiber catalyst with improved stability are presented in Chapter 5. Chapter 6 focuses on optimizing the electrospinning process to generate TiO_2 nanofiber with enhanced surface area. A model for predicting the diameter of the nanofibers using a statistical experimental design method is also described in this chapter. The study presented in Chapter 7 examines the photocatalytic performance of the immobilized TiO_2 nanofibers. Chapter 8 summarizes the research presented in different chapters and draws general conclusions from the study. The engineering significance of the research described in Chapters 3 to 7 is described in Chapter 9.

DEDICATION

I dedicate my dissertation to my parents for their sacrifices, sharing equally my entire emotional burdens, offering me all their love and inspiring me to this goal.

My sincere gratitude to my loved one whose support and encouragement has provided me the strength and perseverance needed to complete this dissertation.

ACKNOWLEDGEMENTS

I owe thanks to many people who deserve credit and appreciation for their role in making this dissertation possible

I wish to thank my principal advisor, Dr. Jerald A. Lalman, for his continued technical advice, constructive appraisal and on-going feedback throughout the duration of this work. I express my deepest appreciation for his suggestions and guidance, which were invaluable for this work and essential for its completion.

I extend my sincere gratitude to my co-advisor, Dr. N. Biswas, who provided me with the opportunity to enter in a graduate program at the University of Windsor. His financial support during the initial stage of my research is gratefully acknowledged.

My sincere appreciation to Dr. S. H. Eichhorn for providing access to several analytical instruments and invaluable assistance with x-ray diffraction (XRD), differential scanning calorimetry (DSC) and thermogravimetric analysis (TGA). I thank Dr. R. Aroca for allowing me to use the atomic force microscope (AFM). I extend my gratitude to Dr. C. Weisener for introducing me with the Great Lakes Institute of Environmental Reserarch (GLIER) testing facilities and providing me with the access to the the Brunauer-Emmett-Teller (BET) and the field emission gun scanning electron microscope (FESEM). A special thank to Dr. A. A. Asfour and Dr. R. Carriveau, member of my dissertation committee and in the past members of my comprehensive examination committee, for their participation and for their perceptive comments and suggestions.

I extend my earnest appreciation to external examiner, Dr. Chuck (Charles) Mims from University of Toronto for agreeing to serve on the committee and for taking the time to review this dissertation. Your comments and suggestions are much appreciated.

This dissertation would not be possible without the support, camaraderie and assistance of Mr. Bill Middleton, Mrs. Sharon Lackie, Mr. Matt St. Louis and Mr. Pat Seguin. Thank you for offering your time and support on occasions when I needed it the most. Your dedication to the students' need in the lab and beyond were priceless. A special word of thank to Ms. Ann-Marie Bartlett and Mrs. Catherine Wilson for their continued help throughout my academic tenure. My thanks also go to my lab colleagues and office friends for their cooperation and company.

I would like to thank the Department of Civil and Environmental Engineering at the University of Windsor and Natural Science Engineering Research Council of Canada (NSERC) for providing me with the financial assistance to make this work possible.

I must thank those closest to me whose tremendous support has never left my side and motivated throughout my academic pursuit. Your encouragement has driven me to stay focused and your word has provided the solace at the most stressful of times.

Lastly, I thank all others who have not been named directly, but whose friendship remains important to me; you deserve my gratitude for supporting me through this portion of my life.

TABLE OF CONTENTS

LIST OF TABLES

LIST OF FIGURES

CHAPTER 2

CHAPTER 3

CHAPTER 5

CHAPTER 6

LIST OF ACRONYMS

AFM	Atomic force microscope
ANOVA	Analysis of variance
AOP	Advanced Oxidation Process
ASTM	ASTM International (formerly American Society for Testing of Materials)
BAT	Best available treatment method
BBD	Box-Benkhen experimental design
BET	Brunauer-Emmett-Teller
CO_2	Chemical formulae of carbon dioxide
CCD	Central Composite design
CB	Conduction band
DMF	Dimethylformamide
DO	Dissolve oxygen
DSC	Differential scanning calorimeter
EDS	Energy dispersive spectroscopy
EHC	Environmental Health Criteria
FESEM	Field emission Scanning Electron Microscope
FFD	Full factorial design
FTIR	Fourier transform infrared
FWHM	Full-width at half of maximum
GAC	Granular activated carbon
GC	Gas chromatograph
HPLC	High performance liquid chromatograph
JCPDS	Joint Committee on Powder Diffraction Standards

NSERC	Natural Sciences and Engineering Research Council of Canada
$^{\bullet}OH$	Chemical formulae of hydroxyl radical
OFAT	One-factor-at-a-time
O_2	Chemical formulae of oxygen
O_3	Chemical formulae of Ozone
PVAc	Polyvinyl acetate
RSM	Response surface methodology
SSA	Specific surface area
THF	Tetrahydrofuran
TGA	Thermogravimetric analyzer
TIP	Titanium tetraisopropoxide
TiO_2	Titanium dioxide
UNESCO	United Nations Educational, Scientific and Cultural Organization
USEPA	United States Environmental Protection Agency
UV	Ultraviolet
VB	Valence band
XRD	X-ray diffraction

CHAPTER 1: INTRODUCTION

1.1. Context

"In an age when man has forgotten his origins and is blind even to his most essential needs for survival, water along with other resources has become the victim of his indifference"

~ Rachel Carson (*Silent Spring*; 1962).

Many environmental and health issues facing our planet are related to the discharge of chemicals via anthropogenic and industrial activities. Large numbers of organic pollutants are relentlessly released into the environment through industrial discharges from many manufacturing facilities (McFarlane and Nilsen, 2003; Bibeault and Hudon, 2006; Schindler, 2001). The effectiveness of conventional water treatment processes in removing these pollutants from the influent water is a major problem in many occasions (Smith et. al., 1991; United States Environmental Protection Agency (USEPA), 2001; Westerhoff, 2003; Li et al., 2005). According to Canadian and United States (U.S.) regulatory agencies, the release of these contaminants are a major threat to our environment (Environment Canada and USEPA, 2005). Humans exposed to these contaminants through ingestion suffer from severe health effects (USEPA, 2001; Meknassi et al., 2004). Health problems related to development and growth retardation, reproduction problems, endocrine disruptions, and numerous other ailments have been widely reported (Meknassi et al., 2004; Safe, 2004; Ying et al., 2004). According to Environment Canada, a startling 80% of diseases in developing countries are water-born (Environment Canada and USEPA, 2005). Many Canadian communities have faced several water quality issues in the recent past (Bibeault and Hudon, 2006). An ongoing effort is already in place to ensure the safeguarding of water bodies through improved treatment approaches,

source water protection and increasing the understanding of the fate-transport mechanism of contaminants in the water bodies (Smith et. al., 1991; USEPA, 2001; Schindler, 2001; Bibeault and Hudon, 2006).

A water treatment plant uses a variety of treatment processes to remove the contaminants from influent raw water. The choice of a treatment sequence depends mainly on the influent flow rate, its composition, end-use requirements, and cost (Ekenfelder, 2000; Tchobanoglous et al., 2003). Generally, in a conventional water treatment facility the biological treatment process receives 80% of the influent organic load. As a result, the efficiency of removal of a pollutant mainly depends on the quantity and biodegradability of the polluting compound (Tchobanoglous et al., 2003; Westerhoff, 2003). On occasions the removal is strongly affected by the toxicity of the pollutant on the microbial consortium effecting the removal in the biological treatment process (Autenrieth et al., 1991; Martinez et al., 2006). Thus, an imperative research focus is directed towards advanced water treatment techniques capable of removing recalcitrant aqueous contaminants, when incorporated in the treatment sequence.

In recent years, heterogeneous photocatalysis using titanium dioxide (TiO_2) has been identified as a potential treatment route for a variety of organic aqueous contaminants (Ollis et al., 1991; Matthews, 1992). TiO_2 photocatalysis offers a unique advantage over other alternatives because it degrades toxic organic pollutants into carbon dioxide (CO_2) and water in presence of light and provides a green treatment approach (Bhatkhande et al., 2001; Herrmann, 2005). The ability of TiO_2 to degrade organic compounds originates from the semiconductor band gap. The photocatalysis is actuated by means of photo-generated electron-hole pairs (Linsebigler et al., 1995; Bhatkhande et al., 2001). The literature suggests that the photocatalytic process with TiO_2 is dependent on a number of factors (Lee and Mills, 2004; Herrmann, 2005). Several reports

have examined the impact of individual factor on TiO_2 photocatalytic performance (Bhatkhande et al., 2001; Gogate and Pandit, 2004). However, the factor effects are not studied collectively in an integrated approach. Additionally, the photocatalytic rates reported in the literature are often difficult to compare due to the different reporting units and experimental conditions and factor effects are not studied collectively in an integrated approach (Davydov, 2001; Carp et al., 2004). Hence, an existing research gap is identified to study the effect of various factors affecting TiO_2 photocatalysis in a systematic manner and develop a predictive model.

Augmented photocatalytic performance is often reported in studies using TiO_2 nanoparticles when compared to micron size particles (Bhatkhande et al., 2001; Carp et al., 2004). However, the applicability of TiO_2 nanoparticles in photocatalytic processes in the form of slurries have several practical constraints (Ibañez et al., 1999; Houari et al., 2005). Immobilizing TiO_2 nanoparticles onto a solid support material could become a viable route for resolving these constraints. However, the immobilization technique has its own disadvantages. The illuminated surface area of the immobilized TiO_2 nanocatalyst systems is reported to be smaller than that of discrete nanoparticles by several orders of magnitude (Ibañez et al., 1999). Consequently, the photocatalytic efficiency is drastically hindered. Immobilization of TiO_2 in nanofabricated form, without hindering the surface area, can potentially eliminate these problems and assist in enhancing the photocatalytic efficiency.

Electrospinning is a technique used for fabricating nanostructures. The method utilizes a high static voltage to produce fibers with diameters in nanometer range (Doshi and Renker, 1995). Recently, the electrospinning technique has been extended to fabricate TiO_2 nanofibers (Li and Xia, 2003). Due to the complexity of the electrospinning process none of the earlier reports has been successful in fabricating nanofibers bearing diameters less than 50 nanometers (nm)

(Madhugiri et al., 2004; Doh et al., 2008; Alves et al., 2009). Moreover, two major constrains related to immobilizing TiO_2 nanofibers catalyst are as follows: 1. Limited stability (adhesion) of the nanofiber on solid support after catalytic immobilization (Madhugiri et al., 2004; Doh et al., 2005); 2. Reduced specific surface area (SSA) of the immobilized nanocatalyst compared to particles in the nanometer range (Madhugiri et al., 2004; Alves et al., 2009). The work presented in this dissertation evolves from these current research issues and possible solutions are described in Chapters 3 to 7.

1.2. Research objectives

The purpose of this study is to improve the understanding and resolve the practical constraints related to the use of TiO_2 photocatalysis for the degradation of aqueous contaminants. Phenol and a phenol derivative such as p-cresol, were selected as model compounds. The choice of phenolic model pollutants for the photocatalytic studies is justified by their widespread use in industrial and commercial applications, serious health impacts, severe microbial toxicity, considerable environmental discharges, and lack of proper treatment options for removing them from contaminated water sources (EHC 161, 1994; EHC 168, 1995; USEPA, 2001; Bukowska and Kowalska, 2003; Auriol, et al., 2006).

1.3. Research phases

The following phases of the dissertation are described with their associated objectives:

***Phase 1*: (Chapter 3 Objectives)**

(A) Assess the effect of TiO_2 size, TiO_2 concentration, dissolve oxygen (DO) concentration and phenol concentration on the photocatalytic degradation rate of phenol using TiO_2 nanoparticles.

(B) Optimize the photocatalytic degradation of phenol using a Box-Benkhen experimental design (BBD) and develop a statistical model to predict the phenol degradation rate

***Phase 2*: (Chapter 4 Objectives)**

(A) Use the statistical model developed for phenol to predict the photocatalytic degradation rate of a para-substituted phenol derivative, *p*-cresol.

(B) Verify the model by using the predicted values to establish optimum process conditions for maximum photocatalytic degradation of *p*-cresol.

***Phase 3*: (Chapter 5 Objectives)**

(A) Fabricate a TiO_2 nanocatalyst system with enhanced stability by immobilizing the electrospun nanofibers on an improved support surface.

(B) Characterize the nanocatalyst by determining its crystal structure, fiber morphology, and stochiometric composition.

***Phase 4*: (Chapter 6 Objectives)**

(A) Evaluate the effect of potential difference, infusion rate and separation distance on the diameter of electrospun TiO_2 nanofibers.

(B) Optimize the electrospinning variables to minimize the diameter of TiO_2 fibers using a Box-Benkhen experimental design (BBD), and develop a statistical model to predict the TiO_2 nanofiber diameter.

***Phase 5*: (Chapter 7 Objectives)**

(A) Assess the effect of catalyst composition and immobilization parameters on the specific surface area (SSA) and bandgap energy of the TiO_2 nanofiber catalyst.

(B) Determine the photocatalytic performance (degradation rate of phenol and quantum yield) of immobilized TiO_2 nanocatalyst and assess its performance after repeated use.

The summary of outcomes of each research phases are summarized in Chapter 8. The engineering significance of the research outcomes are discussed in Chapter 9 of this dissertation.

1.4. References

1. Alves, A.K.; Berutti, F.A.; Clemens, F.J.; Graule, T.; Bergmann, C.P. (2009). Photocatalytic activity of titania fibers obtained by electrospinning. *Mater. Res. Bull.* 44, 312–317.
2. Auriol, M.; Meknassi, Y.F.; Tyagi, R.D.; Adams, C.D.; Surampalli, R.Y. (2006). Endocrine disrupting compounds removal from wastewater, a new challenge. *Process Biochem.* 41, 525–539.
3. Autenrieth, R.L.; Bonner, J.S.; Akgerman, A.; Okaygun, M. (1991). Biodegradation of phenolic wastes. *J. Hazard. Mat.*, 28, 29 - 53.
4. Bhatkhande, D.S.; Pangarkar, V.G.; Beenackers, A.A.C.M. (2001). Photocatalytic degradation for environmental applications - a review. *J. Chem. Technol. Biotechnol.*, 77 102-116.
5. Bibeault, J-F.; Hudon, C. (2006). Water availability in the St. Lawrence: Institutional context and major issues. Talbot, A. (Eds), *Water availability for the St. Lawrence river: An Environmental Synthesis.* Ministry of Environment Canada Publication, Montreal, PQ, pp. 1-5.
6. Bukowska, B.; Kowalska, S. (2003). The presence and toxicity of phenol derivatives – Their effect on human erythrocytes. *Curr. Top. Biophys.*, 27, 47-51.
7. Carp, O.; Huisman, C.L.; Reller, A. (2004). Photoinduced reactivity of titanium dioxide. Prog. *Solid State Chem.* 32, 33-177.
8. Davydov, L. (2001). Photocatalytic degradation of organic contaminants: Novel catalysts and processes, *Ph. D. Dissertation*, University of Cincinnati, 10-20.
9. Doh, S.J.; Kim, C.; Lee, S.G.; Lee, S.J.; Kim, H. (2008). Development of photocatalytic TiO_2 nanofibers by electrospinning and its application to degradation of dye pollutants. *J. Haz. Mat.*, 154, 118–127.
10. Doshi, J.; Renker, R.H. (1995). Electrospinning process and application of electrospun fibers. *J. Electrostat.*, 35, 151 - 160.
11. Ekenfelder, Jr. W.W. (2000). *Industrial Water Pollution Control.* McGraw-Hill Publishing. Co. Ltd., Toronto, ON, 3rd edition. pp. 64 –109. (ISBN 0-0703-9364-8).

12. Environment Canada and United States Environmental Protection Agency (USEPA) (2005). *Our Great Lakes Report*. Great Lakes and Corporate Affairs Branch, Environment Canada Publication, Toronto, ON. pp. 3- 6. (ISBN 0-662-36264-0).

13. Environmental Health Criteria (EHC) No. 161 (1994). *Phenol*. World Health Organization. Geneva, Switzerland. (ISBN 92-4-157161-6).

14. Environmental Health Criteria (EHC) No. 168 (1995). *Cresol*. World Health Organization. Geneva, Switzerland. (ISBN 92-4-157168-1).

15. Gogate, P.R.; Pandit, A.B. (2004). A review of imperative technologies for wastewater treatment I: oxidation technologies at ambient conditions. *Adv. Environ. Res.* 8, 501–551.

16. Herrmann, J.M. (2005). Heterogeneous photocatalysis: state of the art and present applications. *Top. Catal.* 34, 49-65.

17. Houari, M.; Saidi, M.; Tabet, D.; Pichat, P.; Khalaf, H. (2005). The Removal of 4-chlorophenol and Dichloroacetic Acid in Water Using Ti-, Zr- and Ti/Zr-Pillared Bentonites as Photocatalyst. *Am. J. Appl. Sci.*, 2, 1136-1140.

18. Lee, S.K.; Mills, A. (2004). Detoxification of water by semiconductor photocatalysis, *J. Ind. Eng. Chem., 10,* 173-187.

19. Li, D.; Xia, Y. (2003). Fabrication of titania nanofibers by electrospinning. *Nano Lett.*, 3, 555 -560.

20. Li, L.; Zhang, P.; Zhu, W.; Han, W.; Zhang, Z. (2005). Comparison of O_3-BAC, UV/O_3-BAC and TiO_2/UV/O_3-BAC processes for removing organic pollutants in secondary effluents. *J. Photochem. Photobiol. A.*, 171, 145-151.

21. Linsebigler, L.; G. Lu, Yates Jr., J.T. (1995) Photocatalysis on TiO_2 surfaces: Principles, mechanisms and selected results. *Chem. Rev.* 95 735-758.

22. Martinez, A.B.; Barbot, E.; Marrot, B.; Moulin, P.; Roche, N. (2006). Degradation of synthetic phenol containing wastewater by MBR, *J. Membrane. Sci.*, 281, 288-296.

23. Matthews, R.W. (1992). Photocatalytic oxidation of organic contaminants in water: An aid to environmental preservation, *Pure Appl. Chem.* 64, 1285-1290.

24. McFarlane, S.; Nilsen, E. (2003). On Tap: Urban Water Issues in Canada. *Canada West Foundation (CWF) Report -2003-10*. CWF Publication, Calgary, AB. pp.1 – 14 (ISBN 1-894825-20-9).

25. Meknassi, Y.F.; Tyagi, R.D.; Surampalli, R.Y.; Barata, C.; Riva, M.C. (2004). Endocrine-Disrupting Compounds in Wastewater, Sludge-Treatment Processes, and Receiving Waters: Overview. *Prac. Period. Hazard. Toxic. Radioactive Waste Manag.* 8, 39-56.

26. Ollis, D.F.; Pelezzetti, E.; Serpone, N. (1991). Photocatalyzed destruction of water contaminants, *Environ. Sci. Technol.* 25, 1522-1529.

27. Ibañez, P.F.; Malato, S.; Enea, O. (1999). Photoelectrochemical reactors for the solar decontamination of water. *Catal. Today*, 54, 329–339.

28. Madhugiri, S.; Sun, B.; Smirniotis, P.G.; Ferraris, J.P.; Balkus (Jr), K.J. (2004). Electrospun mesoporous titanium dioxide fibers. *Microporous Mesoporous Mater.*, 69, 77–83.

29. Safe, S. (2004). Endocrine disruptors and human health: is there a problem. *Toxicology*, 205, 3 – 10.

30. Schindler, D.W. (2001). The cumulative effects of climate warming and other human stresses on Canadian freshwaters in the new millennium. *Can. J. Fish. Aquat. Sci.*, 58, 18–29.

31. Smith, J.E.; Renner, R.C.; Hegg, B.A.; Bender, J.H. (1991). Technologies for Upgrading Existing or Designing New Drinking Water Treatment Facilities. Noyes Data Corp. Park Ridge, NJ. pp. 3 - 158. (ISBN 0-8155-1262-7).

32. Tchobanoglous, G.; Burton, F.L.; Stensel, H.D. (2003). *Wastewater Engineering: Treatment and Reuse*. Metcalfe & Eddy Inc. McGraw-Hill Publishing. Co. Ltd., Toronto, ON, 4th edition. pp. 311 – 315, 1196 (ISBN 0-0704-1878-0)

33. United States Environmental Protection Agency (USEPA) (2001). *Removal of Endocrine Disruptor Chemicals Using Drinking Water Treatment Processes*. EPA/625/R-00/015. USEPA Office of Research and Development Publication, Cincinnati, OH. pp.1-27.

34. Westerhoff, P. (2003). Removal of endocrine disruptors, pharmaceuticals and personal care products during water treatment. *Southwest Hydrol.* 2, 18-19.

35. Ying, G-G.; Kookana, R.; Waite, T.D. (2004). Endocrine disruptors (EDCs), pharmaceuticals and personal care products (PPCPs) in reclaimed water in Australia. *Report of Australian Water Conservation and Reuse Research Program.* Australian Commonwealth Scientific and Research Organization (*CSIRO*) and Australian Water Association (AWA), Sydney, NSW. pp. 21- 25 (ISBN 0-643-09180-7).

CHAPTER 2: LITERATURE REVIEW

2.1. Overview

"Water, water, everywhere, nor any drop to drink"

~ Samuel Taylor Coleridge (*The Rhyme of the Ancient Mariner*; 1817).

Water is an indispensable resource for all forms of life. Fresh water accounts for approximately 2.5% of the total water reserve on this planet (Gleick, 1996; United Nations Educational, Scientific and Cultural Organization (UNESCO), 2006). Exponential rise in world's population, growing industrial and commercial activities, extensive urbanization, increased agricultural activities have brought about a tremendous crisis regarding global freshwater reserves (UNESCO, 2006). Water consumption has been disproportionately rising over the past few decades ensuing severe water shortages across the globe (World Bank Institute, 2000). On the other hand, the quality of water in surface water bodies and subsurface aquifers has drastically deteriorated under the influence of intense anthropogenic and industrial activities (Bibeault, et al., 2006; UNESCO, 2006). A large number of toxic compounds are released into the environment from industrial discharges, urban wastes, and agricultural run-offs (Environment Canada, 2007). The accumulation of these pollutants in every phase of the environment, such as water bodies in particular, have caused permanent damage to many ecosystems and brought about serious human health problems (World Bank Institute, 2000; Environment Canada and United States Environment Protection Agency (USEPA), 2005; UNESCO, 2006).

In 2005 alone, over 100,000 tonnes of waste and contaminants were discharged into Canadian surface water bodies (Environment Canada, 2007). Pesticides and herbicides, pharmaceutical and personal care products, industrial chemicals and oils are major classes of contaminants routinely released through industrial, institutional, and municipal discharges

(Bibeault, et al., 2006; Environment Canada, 2007). Over 360 chemicals, many of which are known to be recalcitrant ecotoxins, have been identified in the Great Lakes (Environment Canada and USEPA, 2005). Phenol and phenol derivatives with a global production of approximately 3 million tonnes are examples of such pollutants (Environmental Health Criteria (EHC) 161, 1994). Humans exposed to these contaminants through ingestion and inhalation suffer from growth retardation, endocrine disruption, development as well as reproduction problem, foetal immaturity, and genetic disruption (EHC 161, 1994; Bukowska and Kowalska, 2003).

2.2. Phenolic contaminants

Phenol and cresol (*p*-cresol in particular) are crystalline solids with a distinctive odour (EHC 161, 1994; EHC 168, 1995). Additional physical and chemical properties of these chemicals are listed in Table 2.1. *p*-Cresol is less volatile and less water soluble than phenol, and therefore, it tends to be more bioaccumulative. The normal range for pH in surface water is 6.5 to 8.5, and for groundwater is 6.0 to 8.5 (McNeely et al., 1979). Under these pH ranges both phenol and *p*-cresol remain mostly undissociated.

Phenol and substituted phenol derivatives are collectively known as phenolics. Phenolics are the key constituents used in the manufacture of a variety of chemicals, pharmaceuticals and hormonal compounds, structured polymers and resins products (Bukowska and Kowalska, 2003). These manufactured products have widespread industrial and commercial applications such as in insulation panels, insecticides, paints and lubricants. Phenolics are normal constituent of human and animal wastes. Phenolics are also produced from microbiological decomposition of organic matter and natural coal tar formation (EHC 161, 1994; EHC 168, 1995, Martinez et al., 2006). From product manufacturing facilities or land fills phenolic contaminants migrate through

atmospheric transport processes and make their way into the surface water bodies and groundwater aquifers.

For more than two decades phenolic compounds have been classified with carcinogenic, teratogenic, and mutagenic properties (Bukowska and Kowalska, 2003). Lately, phenolic contaminants have received a large amount of attention because of their endocrine disrupting abilities (Meknassi et al., 2004). Growth retardation, development, as well as reproduction problems and genetic disruptions are some ensuing health effects from exposure to these phenolic contaminants (Ying et al., 2004; Martinez et al., 2006). These toxicological health effects coupled with the widespread use of phenolic compounds as chemical intermediates and largescale discharge of phenolic wastes in the environment suggest the need for developing effective treatment options.

Table 2.1: Select properties of phenol and p-cresol (EHC 161, 1994; EHC 168, 1995).

Property	**Phenol**	***p*-Cresol**
Structure	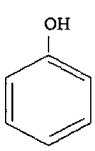	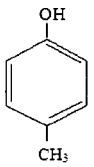
CAS no.	108-95-2	106-44-5
Relative molecular mass	94.11	108.13
Air odour threshold(mg m^{-3})	0.021	0.004
Melting Point (°C)	40.9	34.74
Boiling point (°C)	181.75	201.94
Vapour pressure at 20°C (mmHg)	0.357	0.13
Relative density at 25°C	1.071	1.154
Vapour density (air = 1 at 20°C)	3.24	3.72
Solubility in water at 25°C ($g \cdot l^{-1}$)	67	21.52
pK_a at 25°C	9.99	10.26

2.3. Conventional treatment and phenolic contaminants

A wastewater treatment plant uses a complex array of treatment processes to remove selected contaminants from municipal and industrial influents. Individual treatment processes are arranged in a sequence to form a treatment train based on the wastewater flow and composition, as well as regulatory guidelines for effluent quality. Conventional wastewater treatment processes are classified into primary, secondary, and tertiary treatments. Primary treatment usually refers to removal of suspended solids by settling or floatation. In secondary treatment, the microbial degradation of organic matter proceeds via a series of biochemical oxidation reactions. A specific tertiary treatment process, such as chlorination, is added to remove the pathogens. However, other processes might be added to remove specific groups of chemical contaminants (Tchobanoglous et al., 2003; Ekenfelder, 2000).

The removal of phenolic compounds from raw water supplies during primary treatment is mostly effected by coagulation and flocculation. No more than 20% removals of phenolic compounds is expected through primary treatment (Smith et al., 1991; Westerhoff, 2003). In municipal influents, removing phenols during primary treatment is attributed mostly to adsorption onto settling solids (Westerhoff, 2003; Auriol et al., 2006). In a wastewater treatment plant, the biological treatment process is responsible for removal of approximately 80% of the organic load present in the influent waste stream (Tchobanoglous et al., 2003). However, the efficiency of the biological process strictly depends on the prevalent concentration and the toxicity of the compound on the microbial population. Studies have shown that biological treatments of phenolic contaminants are often impaired beyond a threshold concentration (Autenrieth et al., 1991; Martinez et al., 2006). Moreover, biological treatment of phenolic compounds requires longer solids residence time (Pera-Titus et al., 2004; Kavitha and

Palanivelu, 2005). Because of these limitations associated with conventional treatment methods, tertiary treatment processes are often recommended for removing phenolic compounds from wastewater effluents (Li et al., 2005a).

Activated carbon adsorption and membrane filtration are the two tertiary treatments reported to be successful in removing phenolic contaminants (USEPA, 2001; Auriol et al., 2006). The applications of membrane based processes, namely nanofiltration and reverse osmosis (RO), have several practical constraints. The membrane based processes are very susceptible to fouling due to the presence of particulates and the requirement of high-pressures making these processes significantly expensive for wastewater treatment applications (Ying et al., 2004). The USEPA has identified granular activated carbon (GAC) adsorption as the best available treatment method (BAT) for removing phenolic contamination (Smith et al., 1991; USEPA, 2001). The removal efficiency of the activated carbon adsorption process is drastically reduced when the adsorption sites are completely occupied. Regenerating the bed is energy intensive and complicated (Westerhoff, 2003; Ying et al., 2004). Tertiary physical treatment processes like membrane filtration and activated carbon adsorption, rely on phase transfer rather than degradation of the contaminants. Hence, the pollutant is not removed and instead a transfer takes place from one phase to another.

A chemical treatment method which has been reported to be successful in removing phenolic contaminants is enzymatic treatment. Enzymatic treatment using laccase and horseradish peroxidase enzymes have been reported to accomplish approximately 95% removal of phenol from industrial wastewater effluents (Wu et al., 1993; Cooper and Nicell, 1996; Kurniawati and Nicell, 2005). Enzymatic treatment is reported to be more advantageous over physical processes because of the process selectivity towards phenolic compounds (Wu et al., 1993). However, the

enzymatic treatment process is limited by the high enzyme cost and its short shelf-life (Cooper and Nicell, 1996; Caza et al., 1999). Moreover, the enzymatic treatment relies on partial polymerization and phase transfer of contaminants rather than complete degradation. An alternative tertiary treatment method for wastewater is a hydroxyl radical ($^{\bullet}OH$) based advanced oxidative route, which ensures complete degradation of the phenolic contaminants (Ollis et al., 1991).

2.4. Advanced oxidative process

The Advanced Oxidative Process (AOP) is a collective name for processes that involve generation of hydroxyl radicals ($^{\bullet}OH$) to degrade organic pollutants (Glaze et al., 1997). The advantages of AOP for water treatment applications include the following: non-specificity towards most reduced carbon compounds and degradation of organic pollutants into carbon dioxide (mineralization) (Munter et al., 2001). The $^{\bullet}OH$ radical is the second strongest known oxidizing agent after fluorine (Table 2.2), and the former radical is successful in oxidizing recalcitrant organic compounds (Pera-Titus et al., 2004).

Table 2.2: Oxidization potentials of various oxidizing agents (Hunsberger, 1977).

Oxidizing agent	Oxidation potential (V)
Fluorine	3.06
Hydroxyl radical	2.80
Oxygen (atomic)	2.42
Ozone	2.08
Hydrogen peroxide	1.78
Hypochlorite	1.49
Chlorine	1.36
Chlorine dioxide	1.27
Oxygen (molecular)	1.23

NB: Oxidation potential is a measure of the tendency of these chemical species to gain electrons and thereby, effect oxidation (Munter et al., 2001).

Several possible routes for generation of $^{\bullet}OH$ radicals include ozone (O_3) decomposition, catalytic decomposition of hydrogen peroxide (H_2O_2), electrochemical oxidation-reduction, photolytic (ultraviolet) oxidation-reduction, and photocatalytic oxidation-reduction (Pera-Titus et al., 2004; Gogate and Pandit, 2004a). In some cases more than one $^{\bullet}OH$ radical based processes are combined to enhance the process efficiency (Gogate and Pandit, 2004b).

2.4.1. Ozonation

Ozone (O_3) is a strong oxidant and is commercially used as disinfectant in water treatment. In aqueous solutions, molecular ozone either can remain as O_3 or it can decompose to a $^{\bullet}OH$ radical, a stronger oxidizing agent than O_3 (Glaze et al., 1997). The reaction of molecular O_3 with organic contaminants is slow and selective, limited to unsaturated organic compounds with electron-rich double bond (Gogate and Pandit, 2004a; Rice, 1997). In comparison, the oxidation of organic contaminants by O_3 via $^{\bullet}OH$ radical is fast and non-selective (Rice, 1997, Wang et al., 2003). However, in either process the decomposition of O_3 is the rate limiting step and the limited solubility of O_3 in water (8 – 20 $mg \cdot l^{-1}$) often impede the efficiency of the ozonation process (Wang et al., 2003). Accordingly, in many of the earlier studies it was concluded that the efficiency of the ozonation process increases by a few fold when conjugated with another treatment technique such as photolysis with ultraviolet (UV) radiation (Gogate and Pandit, 2004b; Li et al., 2005a).

2.4.2. Electrochemical oxidation

The electrochemical oxidation technique utilizes electron generated from an external power source to degrade water contaminants (Bejankiwar et al., 2005). Accounts of electrochemical degradation of phenolic compounds have been reported in the literature (Torres et al., 2003; Li et

al., 2005b) The electrically driven oxidation-reduction reactions between the contaminants and a pair of oppositely charged electrodes (anode and cathode) are responsible for the degradation of the contaminants to carbon dioxide (CO_2). Hence, choosing a proper electrode material is an important factor if the electrochemical oxidation process is to be effective. TiO_2 electrodes doped with nobel-metals have been reported to be particularly effective (Gogate and Pandit, 2004a; Li et al., 2005b). However, the exorbitant cost of the doped electrodes and the complexity of the doping processes are major practical drawbacks of this electrochemical oxidation process.

2.4.3. Homogeneous catalytic oxidation

Fenton oxidation is a typical homogeneous catalytic process involving $^{\bullet}OH$ radicals (Munter et al., 2001). •OH radical based, iron-salt mediated decomposition of H_2O_2 is collectively known as Fenton oxidation process (Gogate and Pandit, 2004a). The Fenton oxidation reaction proceeds through the combination of H_2O_2 and iron (II) salt with subsequent formation of $^{\bullet}OH$ radicals (Kavitha and Palanivelu, 2005). The $^{\bullet}OH$ radicals then mediate the oxidation of organic contaminants. This homogeneous catalysis is established by existence of iron-hydroxyl complexes. The substrate nature and the iron-peroxide ratio are two process variables controlling efficiency of the Fenton oxidation (Gogate and Pandit, 2004a). Two variations to the Fenton oxidation process include the electro-Fenton (Oturan et al., 2001) and photo-Fenton processes (Ikehata and Gamal El-Din 2006). In the electro-Fenton process, $^{\bullet}OH$ radicals are generated from H_2O_2 by application of electrical current through an iron electrode (Oturan et al., 2001). In comparison, the $^{\bullet}OH$ radical formation in the photo-Fenton reaction proceeds by reaction of iron (II) salt with H_2O_2 in presence of ultraviolet (UV) radiation. Light with a wavelength less than 580 nanometer (nm) is used in the photo-Fenton process for simultaneous photo-reduction of the iron (III) to iron (II) radical, and thereby, aids the catalytic oxidation process (Ikehata and Gamal

El-Din 2006). The main disadvantage of the Fenton oxidation is that the process requires constant pH monitoring. The optimum pH for Fenton oxidation is between pH 3 and 4, and at pH < 3, the reaction of iron salts are inhibited and $^{\bullet}OH$ radicals are quickly scavenged by hydrogen ions (protons). At pH > 4, availability of free iron species are limited due to the formation of stable iron complexes (Gogate and Pandit, 2004a). Additional monitoring is also required for maintaining an optimum iron-peroxide ratio (1.5% (w/w)) (Gogate and Pandit, 2004a; Kavitha and Palanivelu, 2005). Higher process cost and a narrow range of operating variables are major factors limiting the practical application of Fenton oxidation as an advanced oxidative treatment option.

2.4.4. Photochemical oxidation

In photosynthesis, the electromagnetic radiation is used to initiate chemical reactions between water and CO_2. In general, electromagnetic radiation with a wavelength between 100 to 1000 nm is utilized to initiate chemical reactions; however, the energy of radiation with wavelengths higher than 1000 nm is too low to initiate these chemical reactions, while at wavelengths less than 100 nm ionization is a major problem (Zhang, 2004). Except some bacterial photochemical reactions, which are initiated with light at wavelengths of 700–1000 nm (near infrared region), all photochemical reactions occur in the visible range (400–700 nm) (Zhang, 2004). For the purpose of photochemical degradation of organic contaminants, the region of interest lies with ultraviolet (UV) radiation having a wavelength between 200 to 400 nm (Legrini et al., 1993). The quantum yield of UV radiation was reported to decrease significantly with increasing wavelength; therefore, the efficiency of this photochemical process strongly depends on the incident radiation wavelength (Zhang, 2004). The degradation of pollutants by a photochemical process proceeds simultaneously through direct photolysis, as well as the $^{\bullet}OH$ radical initiated

pathway. This leads to complete mineralization of the organic pollutant into CO_2 and water (Legrini et al., 1993). $^{\bullet}OH$ mediated reactions are favored by the presence of strong oxidizing agents like H_2O_2 or O_3. Photochemical oxidation based on the generation of $^{\bullet}OH$ radicals, produced from the decomposition of H_2O_2 or O_3 by UV radiation, is a typical form of photolysis which is categorized as homogeneous photocatalysis (Pera-Titus et al., 2004). Homogeneous photocatalysis or photolysis has been studied with a wide variety of organic contaminants; however, the major limitation observed with this process is the low quantum yield (Zhang, 2004). The limitation of low quantum yield associated with homogeneous photocatalysis (photolysis) can be significantly reduced by the efficient capture of incident photons through use of a heterogeneous photocatalyst.

2.5. Heterogeneous photocatalysis

Heterogeneous photocatalysis is a generic name for the processes which rely on the generation of $^{\bullet}OH$ radicals on the surface of heterogeneous catalyst particles when they are irradiated with electromagnetic radiation having suitable wavelength to initiate the formation of an electron-hole pair (Bhatkhande et al., 2001; Lee and Mills, 2004). Like other advanced oxidative process (AOP), heterogeneous photocatalysis presents another green approach. In this approach toxic organic pollutants are converted into CO_2 and water using $^{\bullet}OH$ radicals (Herrmann, 2005). Metal oxides, particularly semiconductor metal oxides, have been extensively studied as heterogeneous photocatalysts for the efficient conversion of photonic energy into chemical energy with the ability to degrade various organic contaminants (Bhatkhande et al., 2001; Herrmann, 2005).

2.5.1. Choice of photocatalyst

Photocatalysts are solid materials which on exposure to a specific wavelength of light generate electron-hole pairs (Mills et al., 1993). For most solid catalyst materials, the photocatalysis is initiated by radiation with a wavelength between 200–400nm (UV region); however, some have photocatalysis initiated at wavelengths between 400–700nm (Sato et al., 2005). Most of the solid materials initiating photocatalysis in UV or visible light region are oxides of transition metal or their derivatives, commonly classified as semiconductors. Semiconductors have electrons in the ground (unexcited) state confined in the valence band, while those in the excited state enter into the conduction band. The electrons leaving the valence band have a high reduction potential, while the holes formed in the valence band have a high oxidation potential. Together the electron-hole pair induces photocatalytic reactions on the solid catalyst surface.

The valence band is separated from the conduction band (energy level when the electrons are excited) by an energy barrier denoted as the bandgap or bandgap energy (E_g). E_g of the semiconductor photocatalyst dictates the required energy level of the incident photons for exciting an electron from valence band (VB) to conduction band (CB). The energy of a photon is inversely related to the wavelength of the incident radiation. Accordingly, different photocatalytic materials having different E_g values are excited in the different incident radiation wavelengths (Linsebigler et al., 1995; Herrmann 2005). The E_g of various semiconductor materials used in photocatalysis are tabulated in Table 2.3.

The photocatalyst with E_g higher than the oxidation potential of $^{\bullet}OH$ radicals mediate the formation of $^{\bullet}OH$ radicals when they are photoexcited. Thus, the E_g value is the single most important parameter controlling the photocatalytic ability of semiconductor materials. Other desirable factors for an efficient photocatalyst include the stability and toxicity of the catalytic

material. Among the photocatalyst listed in Table 2.3, the photocatalysts with E_g values > 2.8 eV can effectively promote $^{\bullet}OH$ radical oxidation. Additionally, the use of zinc oxide (ZnO) as a photocatalyst is limited by its stability in an aqueous medium (Rajeshwar, 1995; Bhatkhande et al., 2001). The cost and availability are some other factors considered in selecting a photocatalyst. Considering all of the above factors, titanium dioxide (TiO_2) is widely chosen and extensively studied as a heterogeneous photocatalyst for degradating organic contaminants (Rajeshwar, 1995; Herrmann, 2005).

Table 2.3. Bandgap energy (E_g) of various photocatalysts (Rajeshwar, 1995).

Photocatalyst	Bandgap Energy (eV)
Si	1.1
WSe_2	1.2
Fe_2O_3	2.2
CdS	2.4
WO_3	2.7
TiO_2 - Rutile	3.0
TiO_2 - Anatase	3.2
ZnO	3.2
$SrTiO_3$	3.4
ZnS	3.7

2.5.2. Titanium dioxide (TiO_2) as photocatalyst

Titanium is the ninth most abundant element in the world, constituting about 0.63% of the earth's crust and is primarily found in minerals such as rutile, ilmenite, leucoxene and brookite. In naturally occurring minerals TiO_2 exists in either the photocatalytically active anatase crystal form or thermodynamically stable rutile crystal form. The relative abundance of TiO_2 makes sourcing of this photocatalyst easier for commercial applications. Additionally, by virtue of the chemical configuration, TiO_2 is chemically stable and biologically inert in nature (Carp et al.,

2004). Thus, TiO_2 is routinely preferred over other semiconductor materials for photocatalytic applications (Herrmann, 2005). TiO_2 also has a long historical background of over 80 years as a photocatalytically active material. The unique photocatalytic property of TiO_2 was first recognized as a nuisance known by the "chalking" phenomena of paints. In 1972, the phenomenon was clarified by Fujishima and Honda as photocatalytic effect of TiO_2 through their work (Fujishima and Honda, 1972). Fujishima and Honda (1972) discovered that TiO_2 can photocatalytically split water into hydrogen and oxygen. Later, Ollis and his coworkers demonstrated the use of TiO_2 for oxidative mineralization of organic pollutants in water (Ollis et al., 1991). Since then, heterogeneous photocatalysis with TiO_2 has been considered as a promising treatment option for degrading eco-toxic and bio-persistent chemicals (Matthews 1992; Blake, 2001; Herrmann, 2005).

2.6. TiO_2 photocatalysis

2.6.1. Mechanism of TiO_2 photocatalysis

The photocatalytic activity of TiO_2 originates from the semiconductor band gap. TiO_2 on illumination with light (wavelength < 380nm) having energy higher than the band gap (E_g), produces an electron (e^-) in the conduction band (CB) and a hole (h^+) in the valence band (VB) (Linsebigler et al., 1995; Lee and Mills, 2004). The charge carriers (electron-hole pairs) either recombine with the bulk of the material or migrate to the particle surface (Figure 2.1) (Herrmann, 2005).

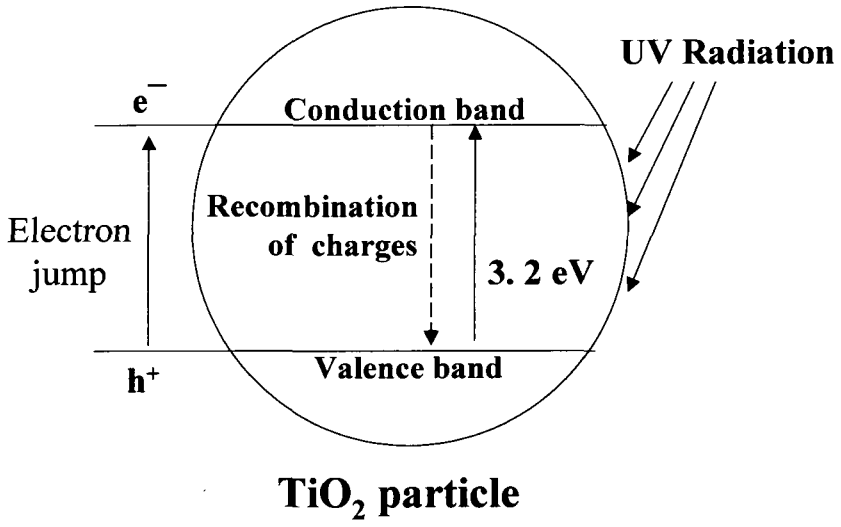

Figure 2.1. Principles of photocatalytic activity of Titanium dioxide (adapted from Bhatkande et al., 2001)

Upon reaching the catalyst surface the pairs initiate oxidation – reduction reactions by reacting with the surface hydroxyl (OH^-) groups (Rajeshwar, 1995). In the aqueous phase the holes are scavenged by surface OH^- groups to generate hydroxyl radicals ($^{\bullet}OH$) (Table 2.4). These $^{\bullet}OH$ radicals, whether free or surface bound, are the active oxidizing species in the heterogeneous photocatalytic process. The migration of electrons onto a catalyst surface, in the aqueous phase with dissolved oxygen (DO), results in the formation of $^{\bullet}O_2^-$ (superoxide) anions (Matthews, 1992), which thereafter react with H^+ ions (protons) to produce H_2O_2 (Table 2.4). The decomposition (disproportionation) of H_2O_2 in turn produces more hydroxyl radicals. The $^{\bullet}OH$ radicals produced by photo-excitation of TiO_2 mediate the degradation of organic molecules (Table 2.4) (Matthews, 1992; Bhatkhande et al., 2001).

Table 2.4. Photocatalytic reactions mediated by TiO_2 (adapted from Matthews 1992)

Reactions	
$TiO_2 + h\nu \rightarrow TiO_2(e^-) + TiO_2(h^+)$	(2.1)
$TiO_2(h^+) + H_2O \rightarrow TiO_2 + H^+ + {}^{\bullet}OH$	(2.2)
$TiO_2(h^+) + OH^- \rightarrow TiO_2 + {}^{\bullet}OH$	(2.3)
$TiO_2(h^+) + R \rightarrow TiO_2 + R_{oxid}$	(2.4)
$TiO_2(e^-) + O_2 \rightarrow TiO_2 + {}^{\bullet}O_2^-$	(2.5)
$\frac{1}{2}\,{}^{\bullet}O_2^- + \frac{1}{2}\,H^+ \rightarrow H_2O_2 + O_2$	(2.6)
${}^{\bullet}O_2^- + 2\,H^+ \rightarrow 2\,HO^{\bullet}$	(2.7)
${}^{\bullet}O_2^- + H_2O \rightarrow O_2 + H_2O_2 + 2\,OH^-$	(2.8)
$TiO_2(e^-) + H_2O_2 \rightarrow TiO_2 + OH^- + {}^{\bullet}OH$	(2.9)
${}^{\bullet}OH + R \rightarrow R_{oxid} (+ H_2O)$	(2.10)

Note: R denotes reduced form and R_{oxid} is the oxidized form of the organic compound

2.6.2. Factors affecting TiO_2 photocatalysis

The ability of a heterogeneous catalyst to photocatalytically degrade organic compounds depends upon the catalytic material properties (crystal structure and surface area), catalyst loading, radiation intensity, radiation wavelength, substrate concentration, DO concentration, pH levels, and temperature. The impact of these factors on the reaction rates of TiO_2 catalyzed photodegradation of phenolic compounds have been reported in several studies (Blake, 2001; Bhatkhande et al., 2001; Herrmann, 2005).

2.6.2.1. Characteristics of incident radiation

The energy of photons impinging on the catalyst surface is an important factor for the generation of photo-induced electron-hole pairs. The energy of the impinging photons is inversely proportional to the wavelength of the incident radiation. The energy of incident radiation with a wavelength < 380nm is sufficient to excite an electron in TiO_2 from the VB to the CB across an energy barrier of 3.2eV (Bhatkande et al., 2001; Lee and Mills, 2004; Sato et al., 2005). Based on the skin sensitivity of humans the UV region is subdivided into three distinct zones, namely UVA (400–315 nm), UVB (280–315 nm) and UVC (200–280 nm). TiO_2 has been reported to be photocatalytically active in all three UV zones, with the highest photocatalytic activity associated with UVC radiation (Zhang, 2004). However, considering the health hazard associated with UVC radiation, UVB radiation with an average wavelength of 300nm is preferred for photocatalytic applications (Tsai and Cheng, 1997). Another factor affecting the photocatalytic reaction rates is the number of photons impinging on the TiO_2 surface and this number depends on the irradiance of the UV source. UV light irradiance is reported to vary from 4–10 $mW \cdot cm^{-2}$ (Lee and Mills, 2004). A choice of 10 $mW \cdot cm^{-2}$ UV source is expected to generate the most number of photons.

2.6.2.2. Characteristics of the catalytic (TiO_2) material

The crystal structure (Rajeshwar, 1995) and catalytic surface area (Carp et al., 2004) are factors known to affect the photo-oxidative properties of TiO_2. The crystal structure dictates the bandgap energy (E_g) and the oxidative potential (Gogate and Pandit, 2004a). The different crystalline forms of TiO_2 includes anatase (kinetically stable), rutile (thermodynamically stable), brookite and monoclinic. In comparison to the other crystal forms, the anatase form (distorted orthogonal structure) has the highest E_g (3.2 eV) value and greater photocatalytic activity (Carp

et al., 2004). Consequently, the anatase form is selectively utilized in many studies because it is more photocatalytically active (Tsai and Cheng, 1997; Blake 2001; Bhatkhande et al., 2001; Gogate and Pandit, 2004a).

The specific surface area (SSA) is a function of the particle size for any heterogeneous catalyst. Hence, smaller diameter TiO_2 photocatalysts are associated with larger SSA. An increase in the total number of free charge carriers (electron (e^-) and hole (h^+)) on the TiO_2 surface with increasing SSA is expected to increase the efficiency of the catalyst. The number of free charge carriers are affected by the number and the lifetime of free e^- and h^+, and the latter depends upon the particle size. In the case of large particles, the volume recombination of e^- and h^+ dominates and the result is a reduction of free charges on the surface. Ultimately, the photocatalytic activity is reduced and the efficiency decreases (Shah et al., 2002).

TiO_2 particle size within the micrometer range is normally used in the manufacture of a variety of industrial and consumer products. However, TiO_2 particles within this range are not utilized in photocatalysis because they are not effectively photoactive (Allen et al., 2004; Hurum et al., 2006). In addition, the light scattering phenomena for micrometric TiO_2 particles lead to a loss of photon energy (Allen et al., 2004). Because of these problems associated with using micrometer size particles, a growing research interest has recently developed for utilizing nanoparticles. Increasing innovations in manufacturing processes have resulted in production of different nanometer size TiO_2 particles. Several nanometer size TiO_2 particles have been tested over past years for their photocatalytic potential to degrade organic compounds (Blake 2001; Bhatkande et al., 2001; Gogate and Pandit, 2004a).

2.6.2.3. Effect of photocatalytic process variables

The number of catalyst particles in the reaction zone has been reported to affect the photocatalytic degradation rates (Herrmann, 2005). The number of catalyst particles is directly related to the concentration of TiO_2 or the TiO_2 mass loading. Typically, an increase in the photocatalytic rate is associated with an increase in the TiO_2 loading (Mills et al., 1993). However, a threshold is often observed in studies with suspended TiO_2 particles. The threshold level in photocatalytic rates is related to an increase in the turbidity of the suspension at higher TiO_2 concentrations and the limited penetration depth of the incident UV radiation (Gogate and Pandit, 2004a).

Another major factor affecting the photocatalytic activity is the availability of oxygen, or the DO concentration (Herrmann, 2005). The availability of oxygen facilitates the generation of $^{\bullet}OH$ radicals and minimizes the loss of charge carriers (electron-hole pairs) (Table 2.4) (Fox and Dulay, 1993). Accordingly, enhanced photocatalytic rates are reported at elevated DO levels (Matthews and McEvoy, 1992).

Photocatalysis is strongly influenced by the number of substrate molecules adsorbed onto the catalytically active sites on the TiO_2 surface (Lee and Mills, 2004; Herrmann, 2005). Thus, the dissociation form (dissociated or undissociated) and initial concentration of substrate are reported to alter the photocatalytic rates (Dalrymple et al., 2007). In the millimolar concentration range, the substrate adsorption is reported to be monolayer, and according to Lee and Mills (2004), monolayer adsorption is preferred for maximum reaction rates. Additionally at elevated substrate levels, the availability of photons at the catalyst surface decreases due to the direct absorption of photons by organic (substrate) molecules. For phenolic compounds, the adsorption of substrates on the catalyst surface is strongly correlated with the type of functional groups and

substitution patterns. Hence, different photocatalytic rates are reported for phenols with different substitution (mono-, di- or tri-) patterns and varied substituted functional groups (cresol to chlorophenol to nitrophenol) (Tsai and Cheng, 1997; Bhatkhande et al., 2001; Gogate and Pandit, 2004a; Pera-Titus et al., 2004; Kusvuran et al., 2005).

2.6.2.4. Effect of environmental variables

TiO_2 catalytic particles have an iso-electric point or point of zero surface charge. The iso-electric point of TiO_2 in solution is reported to be at near neutral pH (~ pH 7.0) (Bhatkhande et al., 2001; Guzman et al., 2006). The surface charge controls the aggregation tendency of TiO_2 nanoparticles and adsorption of the substrate onto the TiO_2 surface (Guzman et al., 2006). Thus, monitoring and control of pH is crucial for photocatalytic reactions, particularly in an aqueous medium. However, pH is often not considered a factor in photocatalysis of phenols with TiO_2 due to their high dissociation pH (pK_a) and tendency for strong adsorption onto TiO_2 surfaces in the undissociated form (Bhatkhande et al., 2001).

Temperature is another variable whose effect is not clearly reported in literature. Some earlier studies have reported that photocatalytic reaction rates are temperature dependent and follow an Arrhenius-type behavior (Kartal et al., 2001). However, some studies have suggested that photocatalytic reactions are not sensitive to temperature changes particularly within the region from 20° to 80°C (Fox and Dulay, 1993; Hermann, 1999).

Variation in reporting units and a lack of systematic examination of the various factors affecting the TiO_2 photocatalytic rates have developed a knowledge gap in the literature (Davydov, 2001). This research gap created a need for a systematic investigation of the factor effects in TiO_2 photocatalysis. It is also conclusive that the practical limitations associated with TiO_2 photocatalysis can be resolved with a critical evaluation of the various factors.

2.6.3. Mode of application of TiO_2 in the photocatalytic process

In recent years nanometric TiO_2 particles have gained significant commercial interest for enhanced photocatalytic performance. The nanoparticles of TiO_2 can be synthesized by various techniques such as precipitation, e-beam evaporation, magnetron sputtering technique, chemical vapor deposition, hydrothermal, and glyco-thermal method (Carp et al., 2004; Sankapal et al., 2006; Centi and Perathoner, 2009). However, the most popular method for preparing TiO_2 nanoparticles is the sol-gel conversion based synthesis method (Hamid and Rahman, 2003). In the sol-gel technique, a titanium alkoxide (sol-precursor) is hydrolyzed to produce nano-sized TiO_2 particles bearing high SSA. Aqueous dispersion or slurry composed of nanoparticles are thereafter used to catalyze photochemical reactions. However, the use of TiO_2 nanoparticles for catalytic activity in the form of suspension or slurry is associated with several serious limitations in terms of their practical applications (Ibañez et al., 1999; Houari et al., 2005; Baan et al., 2006). These limitations include slow settling velocities of the nanoparticles, the ineffectiveness of using conventional gravity separators in solid-liquid separation for nanoparticle slurry, and the presence of remnant catalyst particles having toxicological implications in the process stream (Baan et al., 2006). Hence, the use of nanoparticles in the form of slurry requires an additional solid/liquid separation process to recycle the catalyst and prevent catalyst wash-out (Rajeshwar, 1995, Houari et al., 2005). Another limitation of using the particle suspension is associated with limiting depth of UV penetration with increasing TiO_2 concentration due to incremental suspension turbidity (Houari et al., 2005). The aggregation of nanoparticles in aqueous medium and resultant surface area losses is also a limitation of the slurry process (Ibañez et al., 1999). Human exposures from fugitive emissions of nanoparticles, during the process stream handling and during the slurry preparation processes, result in serious health problems linked to the use of

nanoparticle slurries (Baan et al., 2006). The immobilization of TiO_2 nanoparticles onto a support medium could potentially resolve many of these practical limitations.

2.6.4. Immobilized TiO_2 nanocatalyst for heterogeneous photocatalysis

Several innovative techniques have been reported to immobilize TiO_2 nanoparticles. In most of these techniques, TiO_2 nanoparticles were formed by the sol-gel conversion based synthesis technique and the nanoparticles were then deposited onto a solid support through dipping or coating processes. Glass plates (Hamid and Rahman, 2003; Ling et al., 2004), glass fibres (Pozzo et al., 1997), polymeric fibres (Ding et al., 2004), and textile materials (Bozzi et al., 2005) were some of the materials which have been examined as fixed support materials for TiO_2 photocatalysts. Activated charcoal (Carpio et al., 2005), TiO_2/SiO_2 nanocomposite particles (Hwang et al., 2005), zeolite ZSM-5 (Chang, 2004), and bentonites (Houari et al., 2005) were some other materials which have been investigated as support for fluidized applications. However, a major constraint of many supported catalysts is related to the lower surface area compared to discrete nanoparticles. Loss of surface area is caused by the sintering or aggregation of the nanocatalyst onto the support surface during the stabilization or immobilization step (Ibañez et al., 1999). Particle sintering results in the formation of a film or sheet on the surface, and this lowers the catalytic surface area when compared to discrete nanoparticles (Carp et al., 2004). Hence, laying a mat of nanofibers onto a support surface might resolve many of the problems associated with using non-supported particles and limitations of supported catalysts. An established method of fabricating nanostructure with a high aspect ratio (fibers/wires) is electrospinning. In this method, nanofibers can be layered onto a support surface.

2.7. Electrospinning and generation of nanofibers

Electrospinning is a process of producing nanostructures with a high aspect ratio (fibers/wires) by applying a high voltage through a capillary filled with a conductive solution (Reneker and Chun, 1996). The first report of electrospinning dates back to 1934. However, the technique was solely limited to polymer melts and did not gain much attention (Fomhals 1934). In 1995, Doshi and Reneker demonstrated that a wide variety of polymers in solution can be electrospun into very small diameter fibers (Doshi and Reneker, 1995). Since the initial work by Doshi and Reneker, the technique has been widely exploited to generate ultra thin fibers from a variety of polymers, including engineering plastics, biopolymers, conducting polymers, block copolymers, and polymer blends (Frenot and Chronakis, 2003; Subbiah et al., 2005).

2.7.1. Principle of electrospinning

The process of electrospinning can be considered as a variation of the process of electro-spraying. The electrospraying principle has been used in various applications such as fuel atomization, aerosol production and paint spraying. Electrospraying is associated with low molecular weight liquids, where the fluid stream is broken into small charged droplets on application of an electrostatic field (Deitzel et al., 2001a). The electrospraying method, when applied on high viscosity polymer solutions or melts, result in production of fibers that have diameters in the submicron range (Reneker and Chun, 1996).

In a typical electrospinning apparatus, a DC power supply is connected to a metallic capillary. A viscous solution of high-molecular weight polymer or polymer blend in a low boiling solvent is delivered at a constant flow rate to the metal capillary. The counter charged terminal from the power supply is connected to the targeted collector material for the nanofibers/wires (Figures 2.2). The orientation of the apparatus can be positioned in the

horizontal, vertical or inclined direction based on the type of solution feed system selected. For gravity feed system, a horizontal set up is preferred (Subbiah et al., 2005).

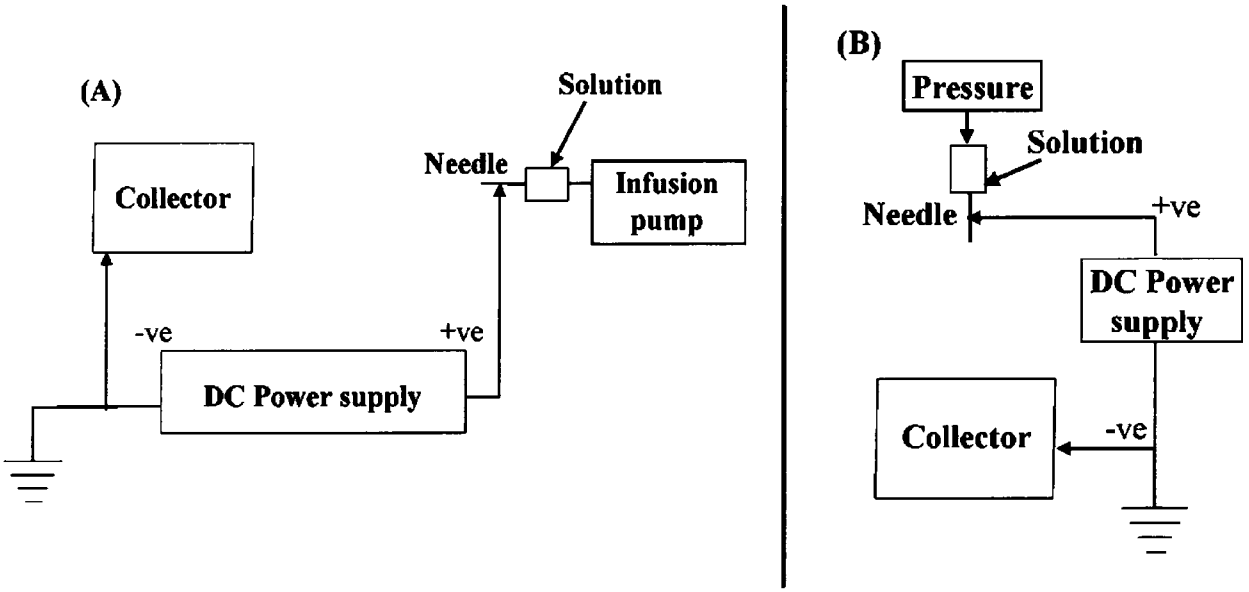

Figure 2.2 Schematic of the electrospinning apparatus – (A) Horizontal (B) Vertical

When an external electric field is applied to a solution of high-molecular weight polymer or polymer blends, the ions in the solution aggregate around the electrode of opposite polarity. Thus, a volume of solution near an electrode has an excess of ions of opposite polarity. A drop of solution, suspended in equilibrium at the end of a capillary, under an applied voltage has the ions of like-polarity expelled to the surface of the droplet. As the electrostatic repulsive forces overcome the surface tension forces the distortion of the drop initiate. The electric field generated by an accumulation of surface charges cause the surface of the hemispherical liquid drop to distort into a conical shape (Taylor Cone). Once the electrical potential of the surface charge exceeds a critical value, the electrostatic forces overcome the solution surface tension and a thin jet of solution is ejected from the surface of the cone and travels towards the electrode bearing an opposite polarity. This solution jet can be thought of as a string of charged elements connected by a viscoelastic material, with one end fixed at the point of its origin and the other

end remaining free. The free end of the electrospinning jet follows a chaotic path as it travels towards the oppositely charged electrode. Electrostatic forces associated with mutual columbic interactions of different sections of the jet make it unstable to bending perturbations. This chaotic motion, or instability, rearranges the jet in a sequence of connected loops. These loops again become unstable and form secondary and tertiary loops. As the jet of polymer solution travels in air, the solvent evaporates, leaving behind a charged polymeric fiber on the counter electrode (Deitzel et al., 2001a, 2001b; Hohman, 2001a, 2001b)

2.7.2. Factors affecting electrospinning

The applied electrical field strength and the flow rate of the solution are the most important variables controlling the electrospinning process, other than the fluid property of the electrospinning solution. The applied electrical field strength is defined as the ratio of applied electrical potential and separation distance between the charged and counter charged electrodes. A variation of either of the two parameters, the applied electrical potential or the separation distance, alters the electrical field strength in the electrospinning process. Increasing the applied potential is limited by an electrical breakdown of the resistance in the air surrounding the gap between the electrodes, and decreasing the separation distance is limited by the collection of wet fibers on the target electrode. As the fibers migrate they loose their shape due to the presence of solvent. An increase in the applied electrical field strength translates directly into higher electrostatic stresses. However, higher applied field strength also affects the spinning rate by withdrawing more solution out of the capillary, particularly in cases where the feed rate of the solution is not positively controlled (Deitzel et al., 2001a; Shim et al., 2001; Subbiah et al., 2005). In order to avoid this complexity, positive control of the flow of the electrospinning solution is desirable. The electrical potential for a particular solution flow rate in the

electrospinning process is associated with different transitions of the fluid jet, namely, the dripping of fluid and stabilization of the fluid jet. The electrical potential for these transitions are redefined upon a change in the solution flow rate. Also, a higher flow rate increases the charge transport rate between the electrodes and this ensues a higher jet current resulting in more instability in the fiber formation (Deitzel et al., 2001a; Shim et al., 2001).

The viscosity, surface tension, and electrical conductivity are the three parameters of the solution which affect the electrospinning process. The viscosity and surface tension of the spinning solution are the direct function of the polymer concentration and molecular weight of the polymer. There exists a critical range of the solution viscosity and surface tension for fiber formation in the electrospinning process, and the critical range varies with the polymer, the chain length of the polymer, and the solvent used in the solution preparation (Deitzel et al., 2001a; Frenot and Chronakis, 2003; Subbiah et al., 2005). Beyond either extremes of the critical viscosity range the fiber formation process is unstable and electrospinning process is discontinuous. Thus, a thorough evaluation of the effect of variables on the electrospinning process for a particular polymer-solvent system and optimization of the parameters is mandatory in order to manipulate the process such that smaller diameter nanofibers can be generated.

2.8. TiO_2 nanofibers immobilization

2.8.1. Electrospinning of TiO_2 nanofibers

In 2003, the formation of TiO_2 nanofibers by electrospinning was first reported by Li and Xia (2003). According to these authors, TiO_2 fibers with nanometric dimensions were fabricated by coupling the sol gel conversion based method of TiO_2 nanoparticle synthesis with the

electrospinning technique (Li and Xia, 2003). Few studies have thereafter employed the sol-gel electrospinning method for fabricating TiO_2 nanofibers (Sigmund et al., 2006; Chronakis, 2005; Ramaseshan, 2007). Typically in sol-gel electrospinning method, a blended solution of a high-molecular weight polymer with a sol-precursor of TiO_2 is electrospun to produce an organo-metallic composite nanofiber. Hydrolysis of the sol-precursor leads to the formation of TiO_2 in composite nanofiber. The polymer constituent of the composite nanofibers is later eliminated by thermal treatment to obtain pure TiO_2 nanofibers (Li and Xia, 2003). Many studies have suggested that in addition to the variables discussed earlier (Section 2.7.2), the proportion of sol-precursor in the electrospinning solution has a strong influence on the fiber formation process in the sol-gel electrospinning technique (Watthanaarun et al., 2005). The challenge of generating TiO_2 nanofibers for catalytic application by the electrospinning process is to control these variables in a fashion that the diameters of the nanofibers are minimized.

2.8.2. Challenges of TiO_2 nanofibers immobilization

The first effort to produce TiO_2 nanofibers for heterogeneous photocatalysis of organic contaminants was reported by Madhugiri et al. in 2004. According to these authors, TiO_2 nanofibers for photocatalysis were produced in two steps. Initially, the TiO_2 nanofibers were fabricated by the sol-gel electrospinning technique and collected on aluminum support. The nanofibers deposited on the support material were later subjected to a thermal treatment to immobilize the pure TiO_2 nanofibers on an aluminum support. Similar attempts towards developing an immobilized TiO_2 nanofiber catalyst for photocatalytic application have been reported by Doh et al. (2008) and Alves et al. (2009). However, none of the earlier efforts have been very successful in developing a high surface area immobilized TiO_2 nanofiber catalyst for photocatalytic application. Madhugiri *et al.* (2004) reported using electrospun TiO_2 nanofibers

for photocatalytic application after grounding the TiO_2 nanofibers into powder form. TiO_2 nanofibers reported in the study had low specific surface area (SSA) (32 $m^2 \cdot g^{-1}$) and the average diameter was greater than 100nm. In the account of Alves and his coworkers the electrospun TiO_2 nanofibers were utilized in the form of an unsupported mat (SSA: 53 $m^2 \cdot g^{-1}$) for photocatalytic application (Alves et al., 2009). Two limitations associated with immobilized TiO_2 nanofiber catalysts were documented by the earlier researchers. One of the limitations was inferior photocatalytic performance compared to nanoparticles (Madhugiri et al., 2004; Alves et al., 2009). The lower photocatalytic rates of the electrospun TiO_2 nanofibers, compared to nanoparticles, were probably linked to lower specific surface area of the nanofibers fabricated in earlier studies. The other practical constraint was inadequate stability of the immobilized catalyst due to poor adhesion of the TiO_2 nanofiber mat to the solid catalyst support (Fujihara et al., 2007).

2.9. Summary of research objectives

The motivation for this dissertation emerges from the background details described in the foregoing sections of this chapter. The research objectives were arranged in phases (Chapter 1, Section 1.3) to thoroughly assess the present constraints and propose the most viable path for resolving these problems. Phase 1 is concerned with evaluating the impact of the factors affecting the heterogeneous photocatalysis using TiO_2 nanoparticles. Then, an integrated approach was used to link the factors affecting photocatalytic rates using a statistical model. The work in phase 2 is concerned with validating the photocatalytic rate model and assessing the accuracy of the model developed for phenol on *p*-cresol. Process conditions were optimized such that the maximum photocatalytic degradation of phenol and *p*-cresol were observed.

Phases 3, 4 and 5 evolved from the need for developing a nanocatalyst system with better performance in comparison to the free unsupported TiO_2 catalyst. In phase 3, the problem of catalyst stability was addressed. In phase 4, the electrospinning process was optimized for generation of smaller diameter nanofibers, and in phase 5 the issue of surface area for immobilized catalyst was resolved. A comparative study of photocatalytic performance of the immobilized catalyst against nanoparticle slurry was conducted in phase 5. Each of the 5 phases are presented in manuscript format as chapters 3, 4, 5, 6 and 7. The summary of the research is presented in chapter 8, and the engineering significance of the research outcomes are discussed in chapter 9.

2.10. References

1. Allen, N.S.; Edge, M.; Ortega, A.; Sandoval, G.; Liauw, C.M.; Verran, J.; Stratton, J.; McIntyre, R.B. (2004). Degradation and stabilisation of polymers and coatings: nano versus pigmentary titania particles. *Polym. Degrad. Stab.*, 85, 927-946.
2. Alves, A.K.; Berutti, F.A.; Clemens, F.J.; Graule, T.; Bergmann, C.P. (2009). Photocatalytic activity of titania fibers obtained by electrospinning. *Mater. Res. Bull.*, 44, 312–317.
3. Auriol, M.; Meknassi, Y. F.; Tyagi, R.D.; Adams, C.D.; Surampalli, R.Y. (2006). Endocrine disrupting compounds removal from wastewater, a new challenge. *Process Biochem.*, 41, 525–539.
4. Autenrieth, R.L.; Bonner, J.S.; Akgerman, A.; Okaygun, M. (1991). Biodegradation of phenolic wastes. *J. Hazard. Mat.*, 28, 29 - 53.
5. Baan, R.; Straif, K.; Grosse, Y.; Secretan, B.; El Ghissassi, F.; Cogliano, V. (2006). Carcinogenicity of carbon black, titanium dioxide, and talc. *The Lancet Oncol.*, 7, 295-296.
6. Bejankiwar, R.; Lalman, J.A.; Seth, R.; Biswas, N. (2005). Electrochemical degradation of 1,2-dichloroethane (DCA) in a synthetic groundwater medium using stainless-steel electrodes. *Water Res.*, 39, 4715 – 4724.
7. Bhatkhande, D.S.; Pangarkar, V.G.; Beenackers, A.A.C.M. (2001). Photocatalytic degradation for environmental applications - a review. *J. Chem. Technol. Biotechnol.*, 77, 102-116.

8. Bibeault, J-F.; Hudon, C. (2006). Water availability in the St. Lawrence: Institutional context and major issues. Talbot, A. (Eds), *Water availability for the St. Lawrence river: An Environmental Synthesis*. Ministry of Environment Canada Publication, Montreal, PQ, pp. 1-5.

9. Blake, D.M. (2001). *Bibliography of work on the heterogeneous photocatalytic removal of hazardous compounds from water and air*. NREL/TP-510-3131. National Renewable Energy Laboratory, Golden, CO. Technical Report, 4, 3 – 16.

10. Bozzi, A.; Yuranova, T.; Guasaquillo, I.; Laub, D.; Kiwi, J. (2005). Self-cleaning of modified cotton textiles by TiO_2 at low temperatures under daylight irradiation. *J. Photochem. Photobiol. A: Chem.*, 174, 156–164.

11. Bukowska, B.; Kowalska, S. (2003). The presence and toxicity of phenol derivatives – Their effect on human erythrocytes, *Curr. Top. Biophys.*, 27, 47-51.

12. Carp, O.; Huisman, C.L.; Reller, A. (2004). Photoinduced reactivity of titanium dioxide. Prog. *Solid State Chem,* 32, 33-177.

13. Carpio, E.; Zuniga, P.; Ponce, S.; Solis, J.; Rodriguez, J.; Estrada, W. (2005). Photocatalytic degradation of phenol using TiO_2 nanocrystals supported on activated carbon. *J. Mol. Catal. A: Chem.*, 228, 293–298.

14. Caza, N.; Bewtra, J.K.; Biswas, N.; Taylor, K.E. (1999). Removal of phenolic compounds from synthetic wastewater using soybean peroxidase. *Water Res.*, 33, 3012-3018.

15. Centi, G.; Perathoner, S. (2009). The Role of nanostructure in improving the performance of electrodes for energy storage and conversion. Eur. J. Inorg. Chem., 2009, 3851–3878.

16. Chang, Y. (2004). Supported TiO2 photocatalyst synthesis and some application to water purification. M. Sc. Thesis. Department of Chemistry. University of Calgary. pp. 2 – 72.

17. Chronakis, I.S. (2005). Novel nanocomposites and nanoceramics based on polymer nanofibers using electrospinning process—A review. J. Mat. Process. Technol., 167, 283–293

18. Cooper, V.A.; Nicell, J.A. (1996). Removal of phenols from a foundry wastewater using horseradish peroxidase. *Water Res.*, 30, 954-964.

19. Dalrymple, O.K.; Yeh, D.H.; Trotz, M.A. (2007). Review: Removing pharmaceuticals and endocrine-disrupting compounds from wastewater by photocatlysis. *J. Chem. Technol. Biotechnol.,* 82, 121-134.

20. Davydov, L. (2001). Photocatalytic degradation of organic contaminants: Novel catalysts and processes, *Ph. D. Dissertation*, University of Cincinnati, pp. 10-20.

21. Deitzel, J.M.; Kleinmeyer, J.; Harris, D.; BeckTan, N.C. (2001a). The effect of processing variables on the morphology of electrospinning nanofibers and textiles. *Polymer,* 42 (2001a) 261-272.

22. Deitzel, J.M.; Kleinmeyer, J.; Harris, D.; BeckTan, N.C. (2001b). Controlled deposition of electrospun poly(ethylene oxide) fibers. *Polymer*, 42 (2001b) 8163–8170.

23. Ding, B.; Kim, J.; Kimura, E.; Shiratori, S.(2004). Layer-by-layer structured films of TiO_2 nanoparticles and poly(acrylic acid) on electrospun nanofibers. *Nanotechnology*, 15, 913–917.

24. Doh, S.J.; Kim, C.; Lee, S.G.; Lee, S.J.; Kim, H. (2008). Development of photocatalytic TiO_2 nanofibers by electrospinning and its application to degradation of dye pollutants. *J. Haz. Mat.*, 154, 118–127.

25. Doshi, J.; Renker, D.H. (1995). Electro spinning process and application of electrospun fibers. *J. Electrostat.*, 35, 151 - 160.

26. Ekenfelder, Jr. W.W. (2000). *Industrial Water Pollution Control.* McGraw-Hill Publishing. Co. Ltd., Toronto, ON, 3rd edition. pp. 64 –109. (ISBN 0-0703-9364-8).

27. Environmental Health Criteria (EHC) No. 161 (1994). Phenol. World Health Organization. Geneva, Switzerland. (ISBN 92-4-157161-6).

28. Environmental Health Criteria (EHC) No. 168 (1995). Cresol. World Health Organization. Geneva, Switzerland. (ISBN 92-4-157168-1).

29. Environment Canada and United States Environmental Protection Agency (USEPA) (2005). *Our Great Lakes Report.* Great Lakes and Corporate Affairs Branch, Environment Canada Publication, Toronto, ON. pp. 3- 6. (ISBN 0-662-36264-0).

30. Environment Canada (2007). Canadian Environmental Sustainability Indicators 2007 - Highlights. Catalogue No. EN81-5/1-2007-1E. Environment Canada Publications, Gatineau, QC. pp. 4 (ISBN 978-0-662-46932-2)

31. Formhals, A. (1934). Process and apparatus for preparing of artificial threads; *US Patent* 1,975,504.

32. Fox, M.A.; Dulay, M.T. (1993). Heterogeneous photocatalysis. *Chem. Rev.*, 93, 341-357.

33. Frenot, A.; Chronakis, I. (2003). Polymer nanofibers assembled by electrospinning. *Curr. Opin. Colloid Interface Sci.*, 8, 64–75.

34. Fujihara, K.; Kumar, A.; Jose, R.; Ramakrishna, S.; Uchida, S. (2007). Spray deposition of electrospun TiO_2 nanorods for dye-sensitized solar cell. *Nanotechnology*, 18, 1 – 5.

35. Fujishima, A.; Honda, K. (1972). Electrochemical Photolysis of Water at a Semiconductor Electrode. *Nature*, 238, 37-38.

36. Glaze, W.H.; Kang, J.W.; Chapin, D.H. (1997). The Chemistry of Water Treatment Process Involving Ozone, Hydrogen Peroxide and Ultraviolet Radiation. *Ozone Sci. Eng.*, 9, 335 - 352.

37. Gleick, P.H. (1996) Water resources, in *Encyclopedia of Climate and Weather*, ed. by S. H. Schneider, Oxford University Press, New York, NY. 2, pp.817-823.

38. Gogate, P.R.; Pandit, A.B. (2004a). A review of imperative technologies for wastewater treatment I: oxidation technologies at ambient conditions. *Adv. Environ. Res.*, 8, 501–551.

39. Gogate, P.R.; Pandit, A.B. (2004b). A review of imperative technologies for Waste water treatment II: Hybrid methods. *Adv. Environ. Res.*, 8, 2004, 553- 597.

40. Guzman, K.A.D.; Finnegan, M.P.; Banfield, J.F. (2006).Influence of surface potential on aggregation and transport of titania nanoparticles. *Environ. Sci. Technol.*, 40, 7688-7693.

41. Hamid, M.A.; Rahman, I.A. (2003). Preparation of titanium dioxide (TiO_2) thin films by sol gel dip coating method. *Malay. J. Chem.*, 5, 86 – 91.

42. Herrmann, J.M. (1999). Heterogeneous photocatalysis: fundamentals and applications to the removal of various types of aqueous pollutants. *Catal. Today.*, 53, 115-129.

43. Herrmann, J.M. (2005). Heterogeneous photocatalysis: state of the art and present applications, *Top. Catal.*, 34, 49 – 65.

44. Hohman; M.M.; Shin; M.; Rutledge, G.; Brenner, M.P. (2001a). Electro spinning and electrically forced jets-1. Stability theory. *Phys. Fluids.*, 13, 2201-2220.

45. Hohman; M.M.; Shin; M.; Rutledge, G.; Brenner, M.P. (2001b). Electro spinning and electrically force jets-II. Applications; *Phys. Fluids.*, 13, 2221-2236.

46. Houari, M.; Saidi, M.; Tabet, D.; Pichat, P.; Khalaf, H. (2005). The removal of 4-chlorophenol and dichloroacetic acid in water Using Ti-, Zr- and Ti/Zr-Pillared Bentonites as Photocatalyst. *Am. J. Appl. Sci.*, 2, 1136-1140.

47. Hunsberger, J.F. (1977). Standard reduction potentials. *Handbook of Chemistry and Physics*. R.C. Weast (Ed.). 58th ed., CRC Press, Cleveland, OH. pp. D141-144.

48. Hurum, D.C.; Agrios, A.G.; Crist, S.E.; Gray, K.A.; Rajh, T.; Thurnauer, M.C. (2006). Probing reaction mechanisms in mixed phase TiO_2 by EPR. *J. Electron. Spectrosc. Relat. Phenom., 150*, 155–163.

49. Hwang, S.T.; Hahn, Y.B.; Nahm, K.S.; Lee, Y.S. (2005). Preparation and characterization of poly(MSMA-co-MMA)-TiO_2/SiO_2 nanocomposites using the colloidal TiO_2/SiO_2 particles via blending method. *Colloid. Surfaces A.*, 259, 63–69.

50. Ibañez, P.F.; Malato, S.; Enea, O. (1999). Photoelectrochemical reactors for the solar decontamination of water. *Catal. Today*, 54, 329–339.

51. Ikehata, K.; Gamal El-Din, M. (2006). Aqueous pesticide degradation by hydrogen peroxide/ ultraviolet irradiation and Fenton-type advanced oxidation processes: a review. *J. Environ. Eng. Sci.*, 5, 81–135.

52. Kartal, O.E.; Erol, M.; Oguz, H. (2001). Photocatalytic destruction of phenol by TiO_2 powders, *Chem. Eng. Technol.* 24, 645-649.

53. Kavitha, V.; Palanivelu, K. (2005). Destruction of cresols by Fenton oxidation process. *Water Res.*, 39, 3062-3072.

54. Kurniawati, S.; Nicell, J.A. (2005). Kinetic model of laccase-catalyzed oxidation of aqueous phenol. *Biotechnol. Bioeng.*, 91, 114-123.

55. Kusvuran, E.; Samil, A.; Atanur, O. M.; Erbatur, O. (2005). Photocatalytic degradation kinetics of di- and tri-substituted phenolic compounds in aqueous solution by TiO_2/UV. *Appl. Catal. B.*, 58, 211–216.

56. Lee, S.K.; Mills, A. (2004). Detoxification of water by semiconductor photocatalysis, J. *Ind. Eng. Chem.*, 10, 173-187.

57. Legrini, O.; Oliveros, E.; Braun, A.M. (1993). Photochemical processes for water-treatment. *Chem. Rev.* 93, 2, 671–698.

58. Li, D.; Xia, Y. (2003). Fabrication of titania nanofibers by electrospinning. *Nano Lett.*, 3, 555 -560.

59. Li, L.; Zhang, P.; Zhu, W.; Han, W.; Zhang, Z. (2005a). Comparison of O_3-BAC, UV/O_3-BAC and TiO_2/UV/O_3-BAC processes for removing organic pollutants in secondary effluents. *J. Photochem. Photobiol. A.*, 171, 145-151.

60. Li, X.; Cui, Y.; Feng, Y.; Xie, Z.; Gu, J.D. (2005b). Reaction pathways and mechanisms of the electrochemical degradation of phenol on different electrodes. *Water Res.*, 39, 1972–1981.

61. Ling, C.M.; Mohamed, A.R.; Bhatia, S. (2004). Performance of photocatalytic reactors using immobilized TiO_2 film for the degradation of phenol and methylene blue dye present in water stream. *Chemosphere*, 57, 547–554.

62. Linsebigler, L.; Lu, G.; Yates Jr., J.T. (1995). Photocatalysis on TiO_2 surfaces: Principles, mechanisms and selected results. *Chem. Rev.*, 95, 735-758.

63. Madhugiri, S.; Sun, B.; Smirniotis, P.G.; Ferraris, J.P.; Balkus (Jr), K.J. (2004). Electrospun mesoporous titanium dioxide fibers. *Microporous Mesoporous Mater.*, 69, 77–83.

64. Martinez, A.B.; Barbot, E.; Marrot, B.; Moulin, P.; Roche, N. (2006). Degradation of synthetic phenol containing wastewater by MBR, *J. Membrane. Sci.*, 281, 288-296.

65. Matthews, R.W. (1992). Photocatalytic oxidation of organic contaminants in water: An aid to environmental preservation, *Pure Appl. Chem.*, 64, 1285-1290.

66. Matthews, R.W.; McEvoy, S.R. (1992). A comparison of 254nm and 350 nm of TiO_2 in simple photocatalytic reactors. *J. Photochem. Photobiol. A.*, 66, 355-366.

67. McNeely, R.N.; Neimanis, V.P.; Dwyer, L. (1979). *Water Quality Sourcebook*: *A Guide to Water Quality Parameters*. Inland Waters Directorate, Water Quality Branch, Environment Canada, Ottawa, ON. pp. 32 – 70. (ISBN 0-6621-0520-6)

68. Meknassi, Y.F.; Tyagi, R.D.; Surampalli, R.Y.; Barata, C.; Riva, M.C. (2004). Endocrine-disrupting compounds in wastewater, sludge-treatment processes and receiving waters: overview. *Prac. Period. Hazard. Toxic. Radioactive Waste Manag.*, 8, 39-56.

69. Mills, A., Davies, R.H., Worsley, D. (1993). Water purification by semiconductor photocatalysis. *Chem. Soc. Rev.*, 22, 417-425.

70. Munter, R.; Preis, S.; Kallas, J.; Trapido, M.; Veressinina, Y. (2001). Advanced oxidation processes (AOPs): Water treatment technology for the twenty-first century. *Kemia-Kemi.*, 28, 354-362.

71. Ollis, D.F.; Pelizzetti, E.; Serpone, N. (1991). Photocatalyzed destruction of water contaminants. *Environ. Sci.Technol.* 25, 1522-1529.

72. Oturan, M.A.; Oturan, N.; Lahitte, C.; Trevin, S. (2001). Production of hydroxyl radicals by electrochemically assisted Fenton's reagent: application to the mineralization of an organic micropollutant, pentachlorophenol. *J. Electroanal. Chem.* 507, 96–102.

73. Pera-Titus, M.; Garc´ıa-Molina, V.; Baños, M.A.; Giméneza, J.; Esplugas, S (2004). Degradation of chlorophenols by means of advanced oxidation processes: a general review. *Appl. Catal. B.* 47, 219-256.

74. Pozzo, R.L.; Baltanfis, M.A.; Cassano, A.E. (1997). Supported titanium oxide as photocatalyst in water decontamination: State of the art. *Catal. Today*, 39, 219-231.

75. Rajeshwar, K. (1995). Photoelectrochemistry and the environment. *J. Appl. Electrochem.* 25, 1067-1082.

76. Ramaseshan, R.; Sundarrajan, S.; Jose, R.; Ramakrishna, S. (2007). Nanostructured ceramics by electrospinning. *J. App. Phys.*, 102, 1-17.

77. Reneker, D.H.; Chun, I. (1996). Nanometer diameter fibers of polymer, produced by electrospinning. *Nanotechnology*, 7, 216 – 223

78. Rice, R.G. (1997). Application of Ozone for Industrial Wastewater Treatment. *Ozone Sci. Eng.* 18, 477 – 515.

79. Sankapal, B.R. ; Sartale, S.D. ; Lux-Steiner, M.C. ; Ennaoui, A. (2006). Chemical and electrochemical synthesis of nanosized TiO_2 anatase for large-area photon conversion. *C. R. Chimie*, 9, 702–707.

80. Sato, S.; Nakamura, R.; Abe, S. (2005). Visible-light sensitization of TiO_2 photocatalysts by wet-method N doping. Appl. Catal. A. 284, 131–137.

81. Schindler, D.W. (2001). The cumulative effects of climate warming and other human stresses on Canadian freshwaters in the new millennium. *Can. J. Fish. Aquat. Sci.*, 58, 18–29.

82. Shah, S.I.; Li, W.; Huang, C.P.; Jung, O. Ni, C. (2002). Study of Nd^{3+}, Pd^{2+}, Pt^{4+} and Fe^{3+} dopant effect on photoreactivity of TiO_2 nanoparticles. *Proc. Natl. Acad. Sci. USA.* 99 (Suppl. 2), 6482 - 6486.

83. Shim, Y.M.; Hohman, M.M.; Brenner, M.P.; Rutledge, G.C. (2001). Experimental characterization of electro spinning: The electrically forced jet and in stabilities. *Polymer*, 42, 9955-9967.

84. Sigmund, W.; Yuh, J.; Park, H.; Maneeratana, V.; Pyrgiotakis, G.; Daga, A.; Taylor, J.; Nino, J. C. (2006). Processing and Structure Relationships in Electrospinning of Ceramic Fiber Systems, *J. Am. Ceram. Soc.*, 89, 395–407.

85. Smith, J.E.; Renner, R.C.; Hegg, B.A.; Bender, J.H. (1991). Technologies for Upgrading Existing or Designing New Drinking Water Treatment Facilities. Noyes Data Corp. Park Ridge, NJ. pp. 3 - 158. (ISBN 0-8155-1262-7).

86. Subbiah, T.; Bhat, G.S.; Tock, R.W.; Parameswaran, S.; Ramkumar, S.S. (2005). Electrospinning of nanofibers. *J. Appl. Polym. Sci.*, 96, 557–569.

87. Torres, R.A.; Torres, W.; Peringer, P.; Pulgarin, C. (2003). Electrochemical degradation of p-substituted phenols of industrial interest on Pt electrodes. Attempts of a structure-reactivity relationship. *Chemosphere*, 50, 97 – 104.

88. Tsai, S.-J.; Cheng, S. (1997). Effect of TiO_2 crystalline structure in photocatalytic degradation of phenolic contaminants. *Catal. Today*. 33, 227-237.

89. Tchobanoglous, G.; Burton, F.L.; Stensel, H.D. (2003). *Wastewater Engineering: Treatment and Reuse*. Metcalfe & Eddy Inc. McGraw-Hill Publishing. Co. Ltd., Toronto, ON, 4th edition. pp. 311 – 315, 1196 (ISBN 0-0704-1878-0).

90. United Nations Educational, Scientific and Cultural Organization (UNESCO) (2006). The 2nd UN World Water Development Report: Water, a shared responsibility. Berghahn Books, New York, NY. pp. 6 – 40. (ISBN 92-3-104006-5).

91. United States Environmental Protection Agency (USEPA) (2001). *Removal of Endocrine Disruptor Chemicals Using Drinking Water Treatment Processes*. EPA/625/R-00/015. USEPA Office of Research and Development Publication, Cincinnati, OH. pp.1-27.

92. Wang, F.; Smith, D.W.; El-Din, M. G. (2003). Application of advanced oxidation methods for landfill leachate treatment — A review. *J. Environ. Eng. Sci.* 2, 413 – 427.

93. Watthanaarun, J.; Pavarajarn, V.; Supaphol, P. (2005). Titanium (IV) oxide nanofibers by combined sol–gel and electrospinning techniques: preliminary report on effects of preparation conditions and secondary metal dopant, *Sci. Technol. Adv. Mat.*, 6, 240-245.

94. Westerhoff, P. (2003). Removal of endocrine disruptors, pharmaceuticals and personal care products during water treatment. *Southwest Hydrol.* 2, 18-19.

95. World Bank Institute (2000). Integrated Water Resources Management. *Global Water Partnership Technical Advisory Committee Background Paper*. Global Water Partnership, Stockholm, Sweden. 4. pp. 1 – 26 (ISBN: 91-630-9229-8).

96. Wu, J.; Taylor, K.E. Bewtra, J.K.; Biswas, N. (1993). Optimization of the reaction conditions for enzymatic removal of phenol from wastewater in the presence of polyethylene glycol, *Water Res.* 27 1701-1706.

97. Ying, G-G.; Kookana, R.; Waite, T.D. (2004). Endocrine disruptors (EDCs), pharmaceuticals and personal care products (PPCPs) in reclaimed water in Australia. *Report of Australian Water Conservation and Reuse Research Program.* Australian Commonwealth Scientific and Research Organization (*CSIRO*) and Australian Water Association (AWA), Sydney, NSW. pp. 21- 25 (ISBN 0-643-09180-7).

98. Zhang, Y. (2004). Investigation of MTBE degradation using advanced oxidation technologies: UV/H_2O_2, UV/TiO_2, $UV/H_2O_2/TiO_2$. *M. A. Sc. Thesis*. Department of Chemical Engineering and Applied Chemistry. University of Toronto. pp. 5 – 29.

CHAPTER 3:

USING THE BOX-BENKHEN TECHNIQUE TO STATISTICALLY MODEL PHENOL PHOTOCATALYTIC DEGRADATION BY TITANIUM DIOXIDE NANOPARTICLES

3.1. Introduction

Over the past several decades growing industrial activities have caused increasing discharge of toxic organic pollutants into the environment. In particular, phenol with an annual global production of approximately 3 million tonnes is one such pollutant (Environmental Health Criteria (EHC) 161, 1994). According to Environment Canada approximately 500 tonnes of phenol are discharged annually into the Canadian environment from industries, such as petroleum refinery, pulp and paper, metal casting, coal gasification, and steel manufacturing (EHC 161, 1994; Environment Canada, 2000).

Phenol is an endocrine disrupting chemical with carcinogenic, teratogenic, and mutagenic properties (EHC 161, 1994; Environment Canada, 2000; Bukowska and Kowalska, 2003; Meknassi et al., 2004). It is used in the manufacture of numerous products for widespread industrial and commercial applications (Meknassi et al., 2004). Phenol and phenol derivatives are present in resins, insulation panels, herbicides, pesticides, paints, and lubricants (EHC 161, 1994; Environment Canada, 2000; Sobecka et al., 2005). During product manufacturing and waste land filling, many phenol based chemicals migrate into the atmosphere, surface water bodies, groundwater, soils, and rocks.

Phenolic based compounds can be removed from industrial effluents using conventional physical, chemical, and biological treatment techniques at varying degree of effectiveness (Sobecka et al., 2005; Westerhoff, 2003; Martinez et al., 2006). However, biological treatment

systems are severely impaired beyond threshold levels due to the toxicity imposed by these chemicals on microorganisms (Martinez et al., 2006; Autenrieth et al., 1991). Granular activated carbon (GAC) adsorption has been identified by the United States Environmental Protection Agency (USEPA) as the best available technology (BAT) for treating air and liquid emissions containing phenolic chemicals (USEPA, 2001). Enzymatic treatment methods using tyrosinase, laccase and horseradish peroxidase enzymes have been reported to remove phenols from industrial wastewater (Wu et al., 1993; Bevilaqua et al., 2002; Kurniawati and Nicell, 2005). However, because activated carbon absorption or enzymatic process relies on phase transfer or partial polymerization, phenols and phenol derivatives are not completely removed from the environment.

In recent years, the oxidative degradation of organic pollutants in aqueous phase using a photo-illuminated catalyst surface has emerged as a potential technology for treating industrial effluents (Ollis et al., 1991; Matthews, 1992). Heterogeneous photocatalysis offers a unique advantage over other alternative treatment methods because it presents a 'green' treatment approach; since, toxic organic pollutants are converted into carbon dioxide (CO_2) and water using photonic energy (Ollis et al., 1991; Matthews, 1992; Herrmann, 2005). Among the reported photocatalysts which have been used, Titanium dioxide (TiO_2) has received the most attention due to its high oxidative potential (Herrmann, 2005; Bhatkhande et al., 2001). The oxidative potential of TiO_2 originates from its semiconductor band gap. A photo-illuminated TiO_2 surface generates electron-hole pairs which migrate to the surface of the photocatalyst and initiate the formation of hydroxyl radicals ($^{\bullet}OH$). The $^{\bullet}OH$ radicals subsequently mediate the degradation of organic molecules (Herrmann, 2005; Bhatkhande et al., 2001; Linsebigler et al., 1995).

TiO_2 photocatalysis is affected by many factors, such as the number of photons impinging upon the surface, TiO_2 properties, the quantity of catalytic sites, and availability of oxygen (O_2). The number of photons impinging on the reaction surface is a direct function of the intensity of the incident radiation (irradiance). Due to a bandgap energy of approximately 3.2eV, photoexcitation of electrons from the valence band (VB) to the conduction band (CB) in TiO_2 is achieved by incident radiation with wavelengths below 380 nanometer (nm) (Matthews, 1992; Herrmann, 2005). In several batch studies, the photocatalytic process is mediated using ultraviolet (UV) light with an irradiance of 4–10 $mW \cdot cm^{-2}$ (Herrmann, 2005; Bhatkhande et al., 2001; Lee and Mills, 2004; Gogate and Pandit, 2004). Many photocatalytic studies with TiO_2 have reported using different wavelength and irradiance of the incident radiation, and this is a major issue preventing the comparison of the photocatalytic degradation rates. However, the rates can be compared using an alternative approach, which is known as the quantum yield (Bhatkhande et al., 2001; Davydov, 2001; Lee and Mills, 2004). Deriving the quantum yields using data from many studies require the use of monochromatic light. However, in several studies polychromatic light is used and calculating the quantum yield is not feasible.

Another factor affecting the photocatalytic reaction rate is the surface area per TiO_2 particle. Enhancing the TiO_2 photocatalytic efficiency is expected with increasing the specific surface area (SSA) or reducing the diffusion path of the charge carriers (Carp et al., 2004). TiO_2 particle sizes within the micrometer range lack photocatalytic activity because of recombination of charge carriers en-route to the catalyst surface (Carp et al., 2004; Allen et al., 2004; Herrmann, 2005; Hurum et al., 2006). Recent innovations have permitted manufacturers to produce TiO_2 particle sizes in nanometer range. Several nanometer size TiO_2 formulations have evolved and tested for their photocatalytic potential on selected organic compounds such as phenol. Degussa

P25 is an exemplary commercially available TiO_2 nanomaterial which has been used to degrade phenol and numerous organic pollutants (Bhatkhande et al., 2001; Gogate and Pandit, 2004). Although a few photocatalytic studies have reported using nanometer size TiO_2 catalysts, particle size is not the only parameter which differ between these catalysts (Bhatkhande et al., 2001; Davydov, 2001).

Crystal structure is another important catalytic property affecting the degree of photocatalysis. The crystal structure of TiO_2 dictates the semiconductor bandgap, and thereby, affects the photocatalytic activity of a particular TiO_2 crystal form. TiO_2 exists in four crystalline forms, which include anatase (kinetically stable), rutile (thermodynamically stable), brookite and monoclinic. In terms of photocatalytic activity, the anatase crystal form has the greatest catalytic activity among the other crystal forms. The crystal structure with next lower catalytic activity is the rutile form (Carp et al., 2004; Herrmann, 2005). Many photocatalysts, including the Degussa P25, which have been utilized for their excellent photocatalytic activity have the anatase crystal structure (Bhatkhande et al., 2001; Gogate and Pandit, 2004; Carp et al., 2004). Several studies have simultaneously varied physical properties such as crystal structure and particle size, as means to increase the degradation rates (Chen and Ray, 1998; Salinaro et al., 1999; Davydov, 2001). However, the data reported in these studies does not allow the reaction rates to be compared in a unified manner.

The TiO_2 photocatalytic rates are also affected by the availability of O_2 in the aqueous phase (dissolved oxygen (DO)), since DO is a precursor for generating the $^{\bullet}OH$ radicals (Lee and Mills, 2004; Carp et al., 2004). Photocatalysis occurs primarily at the surface. Hence, the adsorption properties of the substrate and the quantity of catalytic sites are known to affect the reaction rates (Linsebigler et al., 1995; Herrmann, 2005). Evidence from earlier studies have shown that

adsorption onto the photocatalyst at very low concentrations (less than the 1 mM) follows the Langmuir adsorption isotherm and can be modeled using first order kinetics (Lee and Mills, 2004; Herrmann, 2005).

Evidence from several reports have described the impact of individual factors on phenolic degradation; however, the photocatalytic rates reported are not comparable due to the difference in reporting units and/or experimental conditions (Bhatkhande et al., 2001; Davydov, 2001; Carp et al., 2004). Hence, further research is required to consolidate all the factors in a unified model. Accordingly, the effects of TiO_2 particle size (dry), TiO_2 concentration, DO concentration, and phenol concentration on the photodegradation rate of phenol are chosen to be evaluated using a statistical model.

Using a one-factor-at-a-time (OFAT) optimization approach is a complex method to evaluate the effects of different variables on an experimental outcome. Assessesing one factor at a time is time-consuming and expensive. Moreover, this approach often leads to misinterpretation of results when interactions between different factors are present. Another approach to accurately evaluate the impact of the variables on the degradation rate is to vary all the factors simultaneously in a systematic manner. This approach is referred to as response surface methodology (RSM). RSM is a statistical technique which can address the present scenario under consideration (Myer and Montogomery, 2002; Ray, 2006; Box and Draper, 1987), and it can be used to establish relationships between several independent variables and one or more dependent variables. Developing a first-degree polynomial model can be performed using statistical experimental design and RSM.

RSM optimizes multiple variables by systematic variation of all the variables with minimum number of experiments. The RSM optimization procedure involves the following steps: 1.

performing the statistically designed experiments; 2. estimating the coefficients of a mathematical model using regression analysis technique; and 3. predicting the response (experimental outcome) and then assessing the adequacy of the model (Myer and Montogomery, 2002; Ray, 2006). Among the available statistical designs, a full factorial design (FFD) is often considered unpractical due to its requirement of large number of experiments for accurately predicting the response (Box et al., 1978; Myer et al., 1989; Myer and Montogomery, 2002; Ray, 2006). Fractional factorial design (FFD) lacks the ability to accurately predict all the positions of the factor space that are equi-distant from the centre (rotatability). Based upon the desirable feature of othogonality and rotatability, Central-Composite design (CCD) and Box-Benkhen design (BBD) are commonly chosen for the purpose of response optimization (Bae and Shoda, 2005; Ray, 2006).

The BBD technique is a three-level design based upon the combination of two-level factorial design and incomplete block design. BBD is a spherical design with excellent predictability within the spherical design space and require fewer experiments than FFD or CCD procedures with the same number of factors. Compared to the CCD method, the BBD technique is considered the most suitable for evaluating quadratic response surfaces, particularly in cases when prediction of response at the extreme level is not the goal of the model. In addition, the BBD technique is rotatable or nearly rotatable regardless of the number of factors under consideration (Myer and Montogomery, 2002; Bae and Shoda, 2005; Ray, 2006).

The present study is focused on implementing the BBD technique. Hence, the objective of this study is to optimize the photocatalytic degradation of phenol using a Box-Benkhen experimental design and to develop a predictive model for the phenol degradation rate involving

four independent factors. The parameters under investigation are TiO_2 size, TiO_2 concentration, DO concentration, and phenol concentration.

3.2. Materials and Methods

3.2.1. Materials

TiO_2 anatase nanoparticles (5, 10, and 32nm) used in this study were procured from Alfa Aesar (Ward Hill, MA). X-ray diffraction was employed to confirm the anatase crystal structure and the variable under consideration was the particle size (dry). Phenol (Reagent grade (>99% purity)) was purchased from Sigma Aldrich (Oakville, ON) and ultrapure water (18M-ohm resistivity) was generated using a NANOpure Diamond water unit (Thermo Fisher Scientific Inc, Waltham, MA).

3.2.2. Photocatalysis of phenol

The photocatalytic experiments were performed in custom-built reaction tubes (25mm ID x 250mm length) fabricated from GE-214 clear fused quartz silica (Technical Glass Products Inc., Painesville, OH). Teflon® lined 20mm septa and aluminum crimp caps (Cobert Associates, St Louis, MO) were used to seal the reaction tubes. The sealed photocatalytic reaction tubes were placed in a modified Rayonet RPR-100 UV photocatalytic chamber (Southern New England Ultraviolet Co., Branford, CT). The chamber was equipped with sixteen phosphor-coated low-pressure mercury lamps (Southern New England Ultraviolet Co., Branford, CT) on the outer perimeter with a centrally located rotating inner carousel. In all experiments, the inner carousel was set at a constant rotational speed to minimize variation in irradiance between the reaction tubes. Three fused quartz reaction tubes (for triplicate study) were placed on the inner rotating carousel and the contents were magnetically stirred to maintain the catalyst in suspension,

minimize particle agglomeration, and minimize any mass transfer limitation (Figure 3.1). The average irradiance emitted from the lamps (300nm monochromatic UV light) was 9 mW/cm^2. An average irradiance of $10mW \cdot cm^{-2}$ was not achieved in the UV chamber with the available supply of lamps. The radiation intensity was measured using a calibrated UV-X radiometer equipped with a 300nm UV sensor (UV Process Supply, Chicago, IL). The reactor temperature was maintained constant by placing the UV photocatalytic chamber inside a temperature controlled chamber. All the photocatalytic experiments, except those evaluating the impact of temperature, were performed at 37±2°C. The adsorption of phenol onto TiO_2 is not limited near neutral pH, and hence, all the experiments were conducted with ultrapure (Milli-Q) water without further pH adjustments (Bhatkhande et al., 2001).

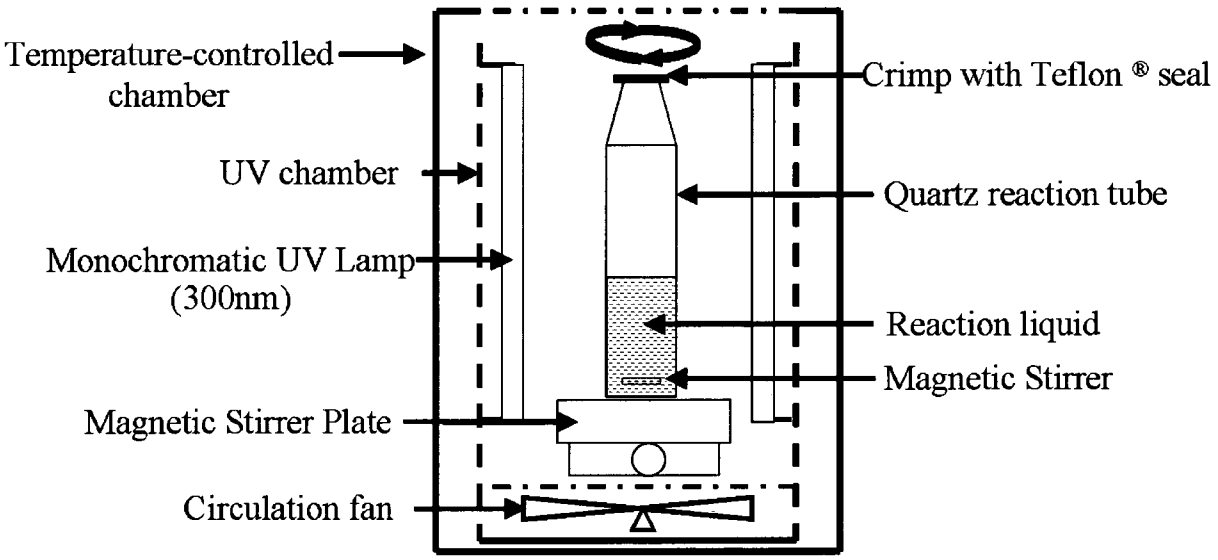

Figure 3.1 Schematic diagram of photocatalytic reactor (and experimental setup).

The effects of no O_2 and adding saturated levels of O_2 (BOC Canada, Windsor, ON) on phenol degradation in the presence of TiO_2 was achieved by purging the reaction tube suspension with nitrogen (N_2) and O_2 respectively for 10 minutes (BOC Canada, Windsor, ON). In the former case, N_2 was added to the headspace and in the latter, oxygen was added. The tubes were

subsequently sealed with 20mm Teflon® lined silicon rubber septa and aluminum crimp caps. In experiments conducted with O_2 less than at the saturated level, the headspace was purged and subsequently filled with air (BOC Canada, Windsor, ON). Over the duration of each experiment, a fixed amount of the reaction liquid (1ml) was withdrawn at specific time intervals and stored in capped tubes wrapped with aluminum foil. After centrifuging the samples, the centrates were analyzed by high performance liquid chromatograph (HPLC). To estimate the quantity of CO_2 produced, a fixed amount of headspace gas (50µl) was withdrawn and analyzed using a gas chromatograph (GC).

3.2.3. Analytical measurements and surface area measurements

The phenol concentration was monitored using HPLC (Dionex Ultimate 3000, Sunnyvale, CA). The instrument was equipped with a UV-visible photodiode array detector set at 215nm and configured with an Acclaim C18-3 µm-2.1mm (ID) x 100mm (length) column (Dionex, Sunnyvale, CA). The analysis was conducted isothermally with the oven temperature set at 45°C and with an eluent (acetonitrile-water mixture (1:4)) (Fisher Scientific, Ottawa, ON) flow rate set at 0.4ml/min. The HPLC detection limit for phenol was 5µg/l.

Headspace CO_2 was analyzed using a Varian CP 3800 GC (Varian, Palo Alto, CA). The GC was configured with a Shin Carbon ST 1mm (ID) x 2m (length) column (Restek, Bellefonte, PA) and the hydrogen carrier gas (BOC, Windsor, ON) flow rate was set at 20ml/min. The analysis was conducted using the following oven temperature program: 80°C for 0.5 min, ramp to 120°C at 30°C/min and hold for 1.0 min then ramp to 150°C at 40°C/min. The injection and detector temperatures were set at 100°C and 180°C, respectively. The GC detection limit was 0.2kPa for CO_2.

A DO probe (YSI 57 DO meter equipped with YSI 5905 DO probe (YSI, Yellow Springs, OH)) was calibrated using known levels of DO. In control studies, the DO levels were monitored for each experimental condition under consideration.

SSA (m^2/g) of the TiO_2 nanoparticles was determined using the Brunauer-Emmett-Teller (BET) gas adsorption technique (Quantachrome NOVA 1200e surface area analyzer, Quantachrome Instruments, Boynton Beach, FL). The instrument temperature was set at 77K and N_2 (BOC, Windsor, ON) was the adsorbate.

3.2.4. Experimental design and statistical analysis

A four factor three level Box-Benkhen design (BBD) having three central points with three replicates was used to determine the operating conditions for maximizing the phenol degradation rate. The method consisted of defining a minimum or low level (denoted as 1), a central or medium level (denoted as 2) and a high or maximum level (denoted as 3) for each experimental factor (Table 3.1).

Table 3.1: Selected factors and their levels for the Box-Benkhen design

Factors / Levels	TiO_2 Nanoparticle Size (nm) [Specific surface area of TiO_2 particles (m^2/g)]	TiO_2 catalyst Conc. (g/l)	DO Conc. (mg/l)	Initial Phenol Conc. (mg/l)
1	5[a] [275±15][b]	0.1	0.04	40
2	10[a] [131±12][b]	0.5	7.80	70
3	32[a] [47±2][b]	1.0	31.0	100

Notes:
[a] Particle size
[b] BET surface area; Average and standard deviation for triplicate samples.

The experiments were conducted under the conditions defined in Table 3.2. A full quadratic model was evaluated for the response function and the experimental data (apparent degradation rate constant (min^{-1})) were analyzed statistically using Minitab statistical software (Version 15,

Minitab Inc., State College, PA). Nine experiments (three batches with three replicates) were conducted at the central points to estimate the magnitude of error or "noise" in the experimental analysis. The experiments were performed in a random manner in order to avoid any systematic bias in the outcomes. The responses from process factors other than those selected for the experimental design were considered as error for the experimental design under examination. The coefficients of the quadratic model, which describes the degradation rate (response) as a function of the reaction conditions (independent variables), were calculated by a multiple regression analysis on the experimental data. The coefficients were analyzed using an analysis of variance (ANOVA) to evaluate if a given term had a significant effect ($p \leq 0.05$). The adequacy of the final model was verified by graphical and numerical analysis using the Minitab (version 15) statistical software (Box et al., 1978).

The factors and the experimental levels for each factor were selected based on literature values, available resources, and results from preliminary experiments. The levels of TiO_2 particle size (dry) were chosen based on the commercial availability of the photocatalyst with the same crystal structure. The maximum and minimum levels of TiO_2 concentrations were determined by preliminary experimental study. Below the lowest TiO_2 concentration, the photocatalytic effect was overwhelmed by photolysis; and any further increase in TiO_2 concentration above the highest level was counter-productive due to photo-hindrance caused by the turbidity of the suspension. The maximum and minimum boundaries of the DO concentration were selected so as to expand the capabilities of the model over a reasonable operating range. The phenol concentration was limited by the applicability of the apparent first order kinetics over the range reported for an industrial effluent (Lee and Mills, 2004; Herrmann, 2005).

Table 3.2: Design matrix for experimental factors and response at different factor levels

Expt. Order	Factors				Response		
	TiO_2 Size (nm)	TiO_2 Conc. (g/l)	DO Conc. (mg/l)	Phenol Conc. (mg/l)	Apparent degradation rate constant (min^{-1})		
					Replicate 1	Replicate 2	Replicate 3
1	10	0.1	0.04	70	0.001	0.0009	0.001
2	10	0.5	7.80	70	0.0127	0.0121	0.0105
3	32	0.5	7.80	40	0.0093	0.0087	0.0093
4	10	0.1	31.0	70	0.0161	0.0165	0.0168
5	10	1.0	0.04	70	0.0009	0.001	0.001
6	10	0.5	31.0	100	0.0258	0.0235	0.0265
7	10	0.5	7.80	70	0.0068	0.0073	0.0075
8	10	0.5	0.04	100	0.001	0.0007	0.0007
9	32	0.5	7.80	100	0.0036	0.0037	0.0037
10	10	0.5	31.0	40	0.0935	0.0853	0.1053
11	10	0.5	0.04	40	0.0012	0.0013	0.0013
12	5	0.1	7.80	70	0.0069	0.0072	0.0066
13	10	0.1	7.80	100	0.0027	0.0027	0.003
14	5	0.5	31.0	70	0.0231	0.0238	0.0269
15	10	1.0	7.80	100	0.0036	0.0036	0.0033
16	5	0.5	7.80	40	0.0053	0.0058	0.005
17	32	0.5	0.04	70	0.0002	0.0006	0.0012
18	32	0.5	31.0	70	0.0069	0.0067	0.0075
19	5	0.5	0.04	70	0.0007	0.0008	0.001
20	32	1.0	7.80	70	0.005	0.0053	0.0059
21	5	0.5	7.80	100	0.0039	0.003	0.0033
22	5	1.0	7.80	70	0.0041	0.0041	0.004
23	32	0.1	7.80	70	0.0051	0.0049	0.005
24	10	1.0	7.80	40	0.0074	0.0075	0.0077
25	10	0.5	7.80	70	0.0085	0.0076	0.01
26	10	1.0	31.0	70	0.0313	0.0402	0.0443
27	10	0.1	7.80	40	0.0056	0.0054	0.0063

The factors and the experimental levels for each factor were selected based on literature

3.3. Results and Discussions

3.3.1. Phenol photocatalysis

The residual phenol concentration was monitored over a one hour interval (Figure 3.2 (A)) and the disappearance rate (removal) was modeled using Equation 3.1.

$$-(dC/dt) = kC \tag{3.1}$$

In equation (1), k is the reaction rate constant, referred hereafter as apparent degradation rate constant (min^{-1}), C is the phenol concentration (mg/l) and $(-dC/dt)$ is the first order degradation disappearance (removal) rate. $-\ln(C/C_O)$ was plotted against the reaction time to determine the apparent degradation rate constant (Figure 3.2 (B)). Control experiments were performed without the TiO_2 catalyst. The quantum yield (ε) was determined using Equation 3.2 (Salinaro et al., 1999; Lee and Mills, 2004).

$$\varepsilon = \frac{\text{(number of phenol molecules degraded per unit time)}}{\text{(number of incident photon per unit time)}} \tag{3.2}$$

The calculated photolysis (no TiO_2) quantum yield of approximately 1.5% was significantly lower than the photocatalytic (with TiO_2) yield of 35%. The higher values observed for the photocatalytic degradation rate and quantum yield were likely due to the higher conversion of photo-generated electrons to $^{\bullet}OH$ radicals on the TiO_2 catalyst surface (Bhatkhande et al., 2001; Herrmann, 2005).

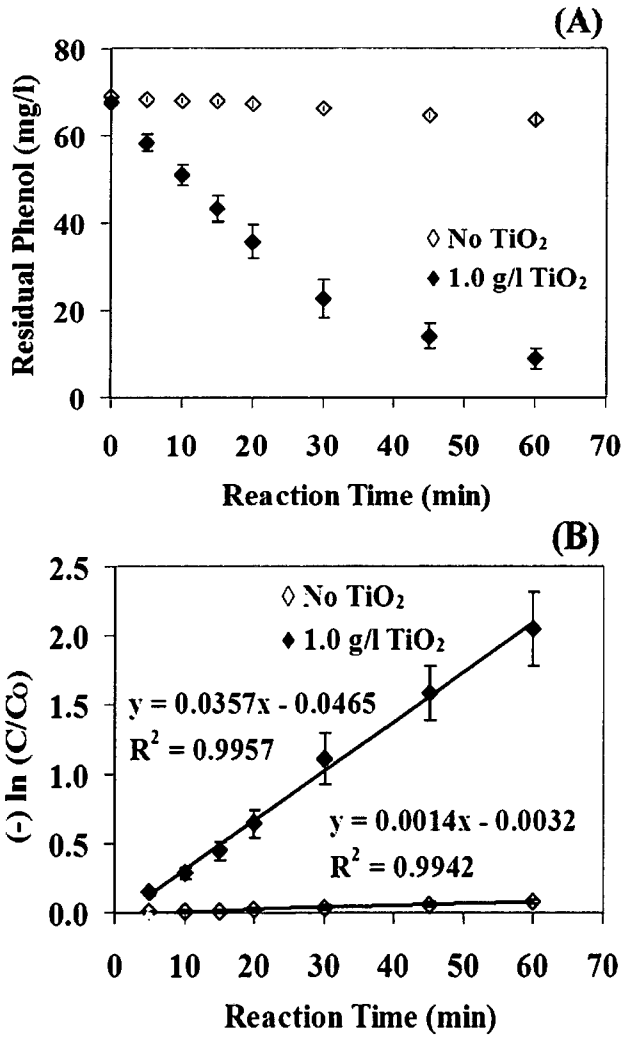

Figure 3.2 Phenol degradation profiles for photocatalysis and photolysis
(A) Residual concentration (B) Disappearance (removal) rate
[TiO_2 size: 10 nm; DO: 31.0 mg/l; Phenol concentration: 70 mg/l
Average with standard deviation (SD) for triplicate samples are shown]

3.3.2. Experimental design analysis

For the response surface optimization study, the photocatalytic degradation of phenol was performed at each design point of the four factors (TiO_2 size, TiO_2 concentration, DO concentration and phenol concentration) three levels Box-Benkhen design shown in Table 3.1.

Considering this design, three sets (replicates) of 27 experiments were performed. The residual phenol concentration was determined at regular intervals over the duration of each experiment and the data was used to compute the apparent degradation rate constant (min^{-1}). The apparent degradation rate constant (k) was considered as the response variable and the computed values at different factor-level combinations were treated statistically to develop the response surface model. The experimental response for the design with the natural level of the experimental factors in the form of a matrix is presented in Table 3.2. A quadratic model described by Equation 3.3 was evaluated for the experimental response. The terms a_0 to a_{14} in Equation 3.3 are the regression coefficients of the respective model factors.

$$\begin{aligned} k = {} & a_0 + a_1 * TiO_2\ size + a_2 * TiO_2\ Conc + a_3 * DO + a_4 * Phenol\ Conc \\ & + a_5 * (TiO_2\ size)^2 + a_6 * (TiO_2\ Conc)^2 + a_7 * (DO)^2 + a_8 * (Phenol\ Conc)^2 \\ & + a_9 * (TiO_2\ size) * (TiO_2\ Conc) + a_{10} * (TiO_2\ size) * (DO) \\ & + a_{11} * (TiO_2\ size) * (Phenol Conc) + a_{12} * (TiO_2\ Conc) * (DO) \\ & + a_{13} * (TiO_2\ size) * (Phenol\ Conc) + a_{14} * (DO) * (Phenol\ Conc) \end{aligned} \quad (3.3)$$

3.3.3. Effects of factors on response variable

The effect of the four factors on the response variable is shown in Figure 3.3(A). A larger apparent degradation rate was observed with TiO_2 particle size set at 10nm (the middle setting) and TiO_2 concentration of 0.5g/l. Notice the greater degradation rates were correlated with higher DO levels. At low phenol levels, the degradation was faster than at higher concentrations. One possible explanation is that at high phenol concentrations competition for active sites of the catalyst is greater than that at the lower concentration. In addition, loss of photons due to the absorption by the substrate molecules could also contribute to the lower photocatalytic rates at

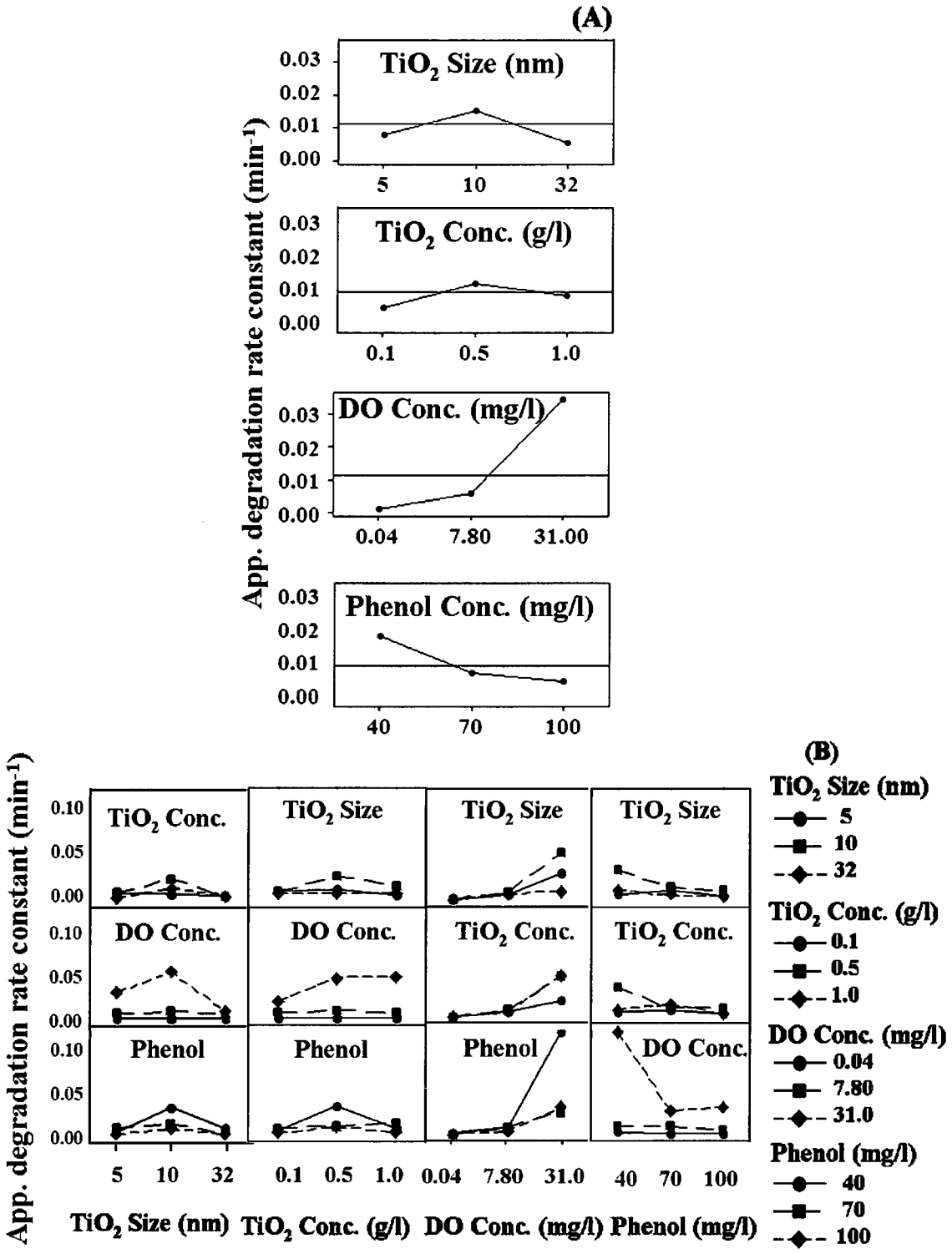

Figure 3.3 Matrix of plots of experimental factors for apparent degradation rate constant in a four factors, three levels Box-Benkhen design.

(A) Main effects plot (B) Two-factor interaction plots

higher phenol concentrations. At the lowest DO level (0.04mg/l), small response values were observed under all the factor-level combinations (Table 3.2). The largest degradation rate was recorded at 40mg/l phenol with 0.5g/l of the 10nm TiO_2 catalyst and at a DO level of 31mg/l. The higher availability of DO likely enhanced the formation of oxidative radicals and increased the photocatalytic rates. A plot of the two-factor interaction matrix (Figure 3.3(B)) showed evidence of interaction at all factor-level combinations.

Contour plots of the response variable (the apparent degradation rate constant (min^{-1})) for different experimental factors (two-factor-at-a-time) are presented in Figure 3.4 (A to E). Contour lines connect the points of equal response (equal apparent degradation rate constant). Strong evidence of interaction between the TiO_2 size and DO concentration was noticed in Figure 3.4(A). Also notice the contour line trend indicates that high apparent degradation rates were associated with elevated DO levels and lower TiO_2 nanoparticles size. Similarly, larger increases were observed for elevated TiO_2 concentrations as the DO concentration increased (Figure 3.4(B)). Unlike in Figure 3.3(A), interaction between the TiO_2 concentration and DO concentration is well evident in Figure 3.4(B). The reaction rate constant increased as the TiO_2 particle size decrease and as the DO levels increased. The contour plot for TiO_2 particle size and phenol concentration (Figures 3.4(C)) revealed that the middle level of the TiO_2 particle size is the most effective in degrading high phenol concentrations. From the contour plot for phenol concentration and DO concentration (Figure 3.4(D)), a strong interaction between the two factors was observed. Notice the apparent degradation rate constant was augmented with decreasing phenol levels and increasing DO concentrations. The optimum factor levels at which the apparent degradation rate constant attain a maximum is expected beyond the factor range under consideration. However, increasing the oxygen concentration beyond the saturation level is not

used in many treatment systems, hence, additional experiments were not conducted beyond the upper level of DO under examination. The contour plot of the apparent degradation rate constant for TiO_2 size and TiO_2 concentration predicted a polynomial relation with the response variable (Figure 3.4(E)). A maximum response was expected near the mid-region of the factor space. Further optimization analysis was performed to locate the region of maximum response. The numerical optimization function in the Minitab software, based on the D-optimality criterion, was used to locate the maximum response within the factor-space under evaluation. The D-optimality criterion varied between zero (worst case) and one (ideal case) for all the factors. The software searches for all possible factor settings and compute the largest D-optimality value. The optimality plot for the apparent degradation rate, beginning from the low setting for all four factors under consideration, is presented in Figure 3.4(F). A D-optimality of 1.00, with a maximum response (apparent degradation rate) value of $0.083min^{-1}$, was recorded at 40mg/l phenol using a TiO_2 particle size of 9.091nm together with 1.0g/l TiO_2 and 31mg/l DO. In comparison, the degradation rate computed using experimental data at 10nm TiO_2 particle size, 1.0g/l TiO_2 concentration, 31mg/l DO concentration, and 40mg/l phenol concentration was 0.072 min^{-1} (with standard deviation of 0.0017 min^{-1}). The experimental response was 13% less than the predicted maximum response. The predicted factor setting of the TiO_2 particle size for a maximum response corresponded with the experimental particle size of 10nm which was used to develop the model.

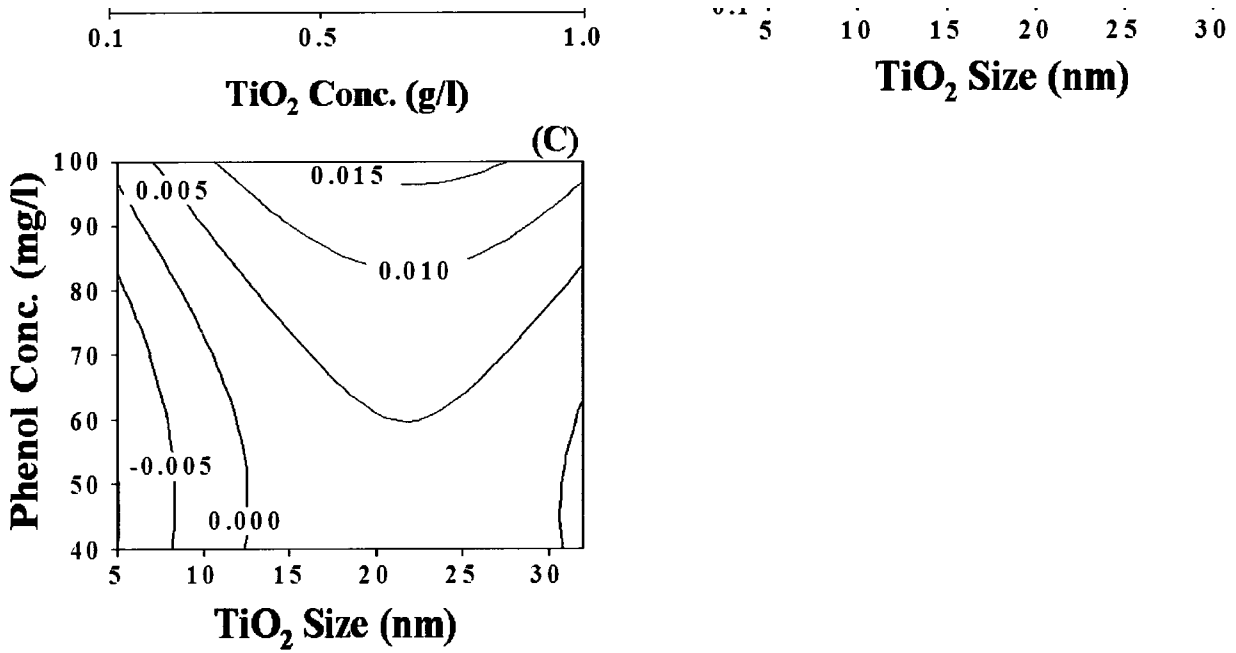
0.1
0.5
1.0
TiO2 Conc. (g/l)
5
10
15
20
25
30
TiO2 Size (nm)
(C)
Phenol Conc. (mg/l)
100
90
80
70
60
50
40
0.005
0.015
0.010
-0.005
0.000
5
10
15
20
25
30
TiO2 Size (nm)

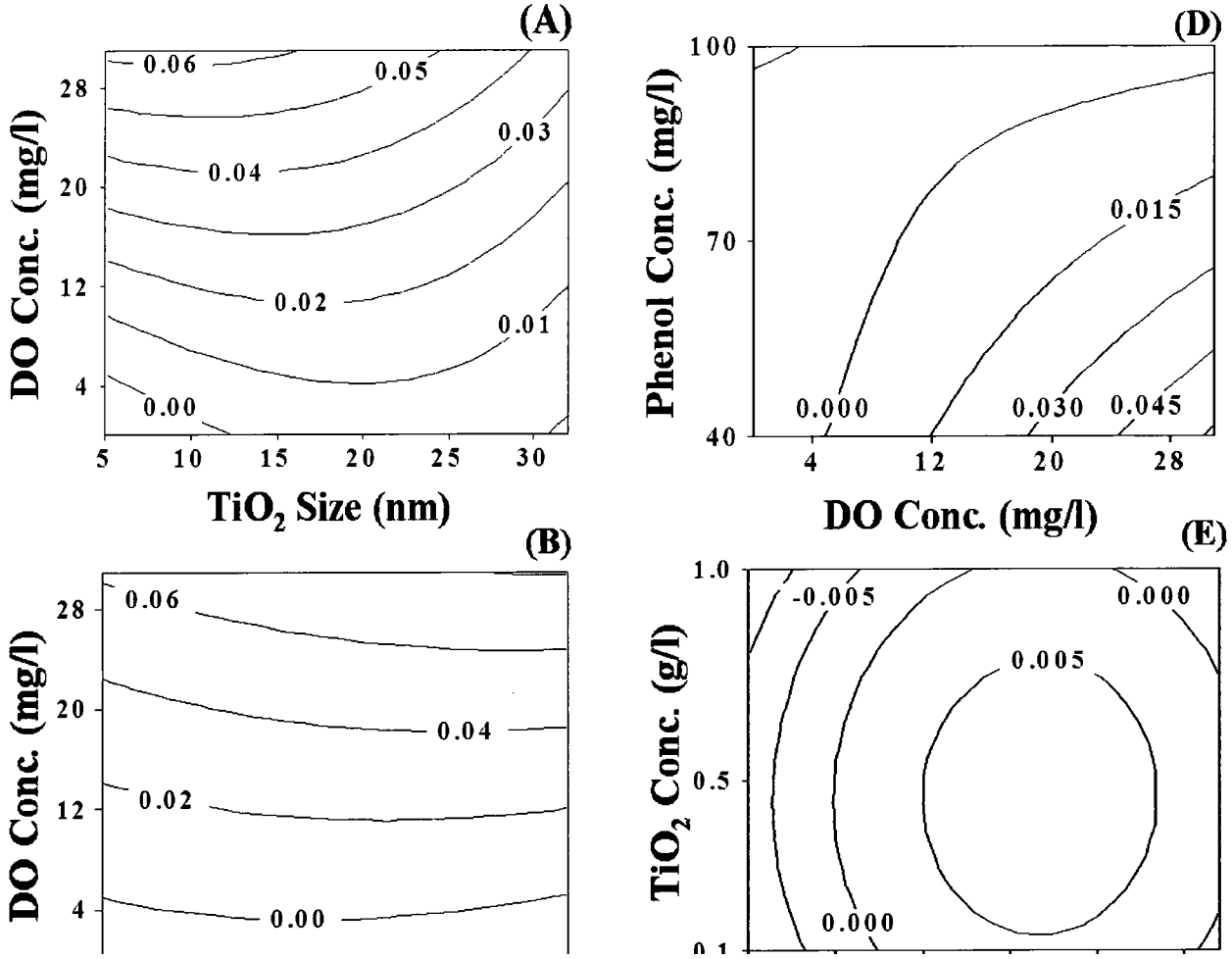
(A)
DO Conc. (mg/l)
28
20
12
4
0.06
0.05
0.04
0.03
0.02
0.01
0.00
5
10
15
20
25
30
TiO2 Size (nm)
(B)
DO Conc. (mg/l)
28
20
12
4
0.06
0.04
0.02
0.00
(D)
Phenol Conc. (mg/l)
100
70
40
0.015
0.000
0.030
0.045
4
12
20
28
DO Conc. (mg/l)
(E)
TiO2 Conc. (g/l)
1.0
0.5
0.1
-0.005
0.000
0.005
0.000

(F)

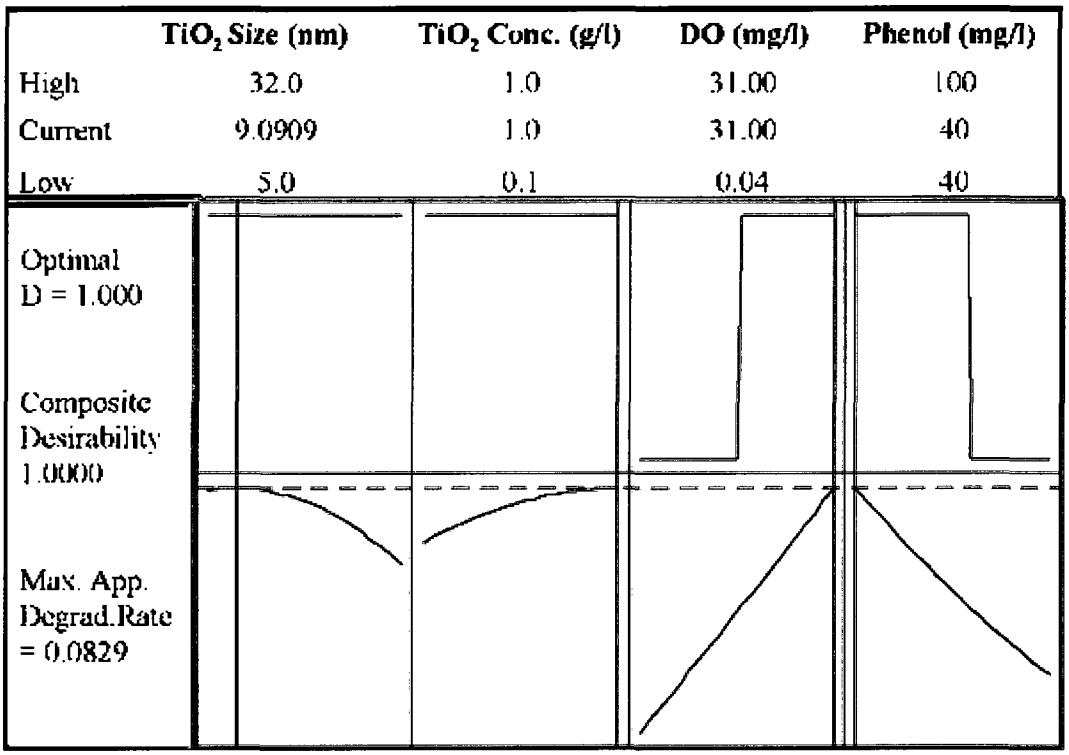

Figure 3.4 Effect of design factors on the response variable (apparent degradation rate constant).

(A) Contour plot of response for DO concentration and TiO_2 size

(B) Contour plot of response for DO concentration and TiO_2 concentration

(C) Contour plot of response for Phenol concentration and TiO_2 size

(D) Contour plot of response for Phenol concentration and DO concentration

(E) Contour plot of response for TiO_2 concentration and TiO_2 size

(F) Optimality plot to locate optimum factor levels for maximized response

[Lines in the contour plots connect the points of equal response (equal apparent degradation rate constant, min^{-1}) for a pair of experimental factors studied]

3.3.4. Development of the response surface model

An analysis of variance (ANOVA) was performed to evaluate a full quadratic response surface model presented in Equation 3.3. The ANOVA results (Table 3.3) of the experimental data revealed that the model was statistically significant with linear, quadratic, and interaction terms. Note the differences between replicates were statistically insignificant ($p = 0.816$). A multiple regression analysis was performed on the experimental data to estimate the regression coefficients for the model. The computed regression coefficients for the model along with their respective p-values are presented in Table 3.4. A backward elimination method was applied and statistically insignificant terms ($p > 0.05$) were deleted from the full quadratic model to obtain a final response surface model (Equation 3.4).

$$\begin{aligned} k = {} & 0.0022244 * (TiO_2\ size) + 0.0037492 * (DO) - 0.0000523 * (TiO_2\ size)^2 \\ & - 0.0224267 * (TiO_2\ Conc)^2 - 0.0000430 * (TiO_2\ size) * (DO) \\ & + 0.0008159 * (TiO_2\ Conc) * (DO) - 0.0000414 * (DO) * (Phenol\ Conc) \end{aligned} \quad (3.4)$$

Table 3.3: ANOVA results of the experimental response at different factor levels.

Source		DF[1]	Seq SS[2]	F	P
Blocks		2	0.000028	0.20	0.816
Regression	Linear	4	0.014907	14.63	0.000
	Square	4	0.001541	5.47	0.001
	2-Factor Interaction	6	0.007095	17.01	0.000
Residual Error	Lack-of-Fit	64	0.004589		
Total		80	0.028132		

Notes
1. DF = degrees of freedom
2. Seq SS = sequential sum of square

Table 3.4: Response surface model regression coefficients for the apparent degradation rate constant

Term	Coefficient	Regression Coefficient	P
Constant	a_0	-0.0117166	0.514
TiO_2 Size	a_1	0.0022244	0.017
TiO_2 Conc.	a_2	0.0200750	0.278
DO Conc.	a_3	0.0037492	0.000
Phenol Conc.	a_4	-0.0004234	0.234
TiO_2 Size*TiO_2 Size	a_5	-0.0000523	0.013
TiO_2 Conc*TiO_2 Conc.	a_6	-0.0224267	0.036
DO Conc.* DO Conc.	a_7	0.0000117	0.341
Phenol Conc*Phenol Conc.	a_8	0.0000044	0.065
TiO_2 Size*TiO_2 Conc.	a_9	0.0000300	0.933
TiO_2 Size* DO Conc.	a_{10}	-0.0000430	0.000
TiO_2 Size*Phenol Conc.	a_{11}	0.0000007	0.890
TiO_2 Conc.* DO Conc.	a_{12}	0.0008159	0.013
TiO_2 Conc.*Phenol Conc.	a_{13}	-0.0000021	0.991
DO Conc.*Phenol Conc.	a_{14}	-0.0000414	0.000

Note: Shaded values are statistically significant at 5% level of significance

3.3.5. Verification of the response surface model

A scatter plot of the experimental data against values predicted by the model (Figure 3.5(A)) revealed a reasonable correlation for all levels (experimental orders). The residuals (difference between the predicted and experimentally observed apparent degradation rate) are important indicators which are useful in judging the adequacy-of-fit of the model to the experimental data. An adequate fit of the model residuals to the normal distribution was verfied to ensure the model accuracy. The Anderson-Darling (AD) statistic was used to verify the normal distribution of the residuals (Figure 3.5(B)) (Stephens, 1974). The calculated AD statistic (0.736) was less than the critical value of the statistic (0.752) for a sample size of 81 and at a 5% level of significance (Stephens, 1974; Montogomery, 2005). Comparative AD statistic confirmed normal distribution of residuals and suggested that the model prediction correlated reasonably well with the

experimental results over the factor-space analyzed in this study. The results of a two sample t-test suggested that the difference between the experimental mean and the model predicted mean response (apparent degradation rate) is statistically insignificant at a 95% level of confidence. For the two sets of data under consideration, the difference between the mean values was considered statistically insignificant when $t_{computed}$ (1.45) was less than $t_{tabulated}$ (1.66) (Montogomery, 2005).

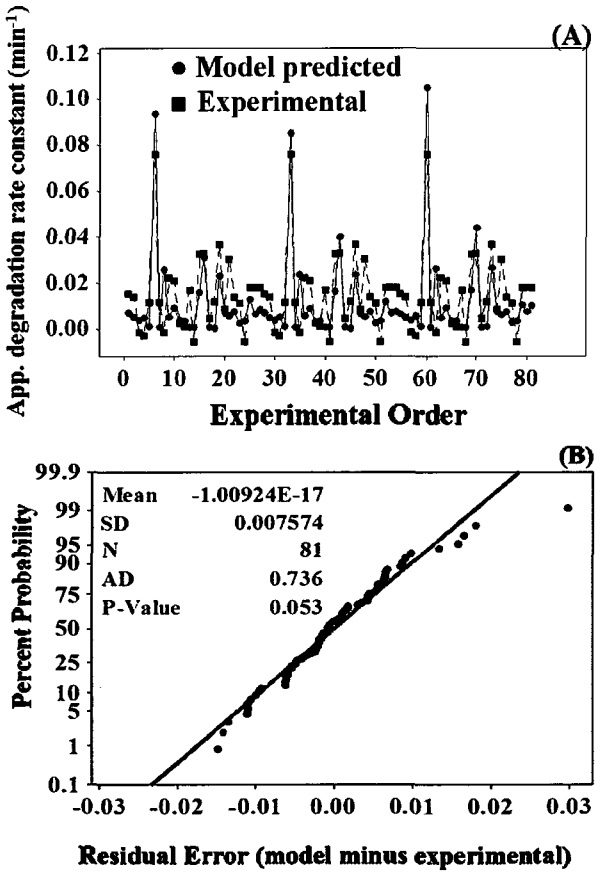

Figure 3.5 Assessing the accuracy of the response surface model.

(A) Scatter plot of the apparent degradation rate constant against experimental order (81 experiments);

(B) Anderson-Darling normality plot of residuals

[AD: Anderson Darling statistic; N: sample size; P: level of confidence; Mean: Mean value of residual for the apparent degradation rate constant (difference between model prediction and experimental result); SD: Standard deviation of the residuals for 81 experiments (N)]

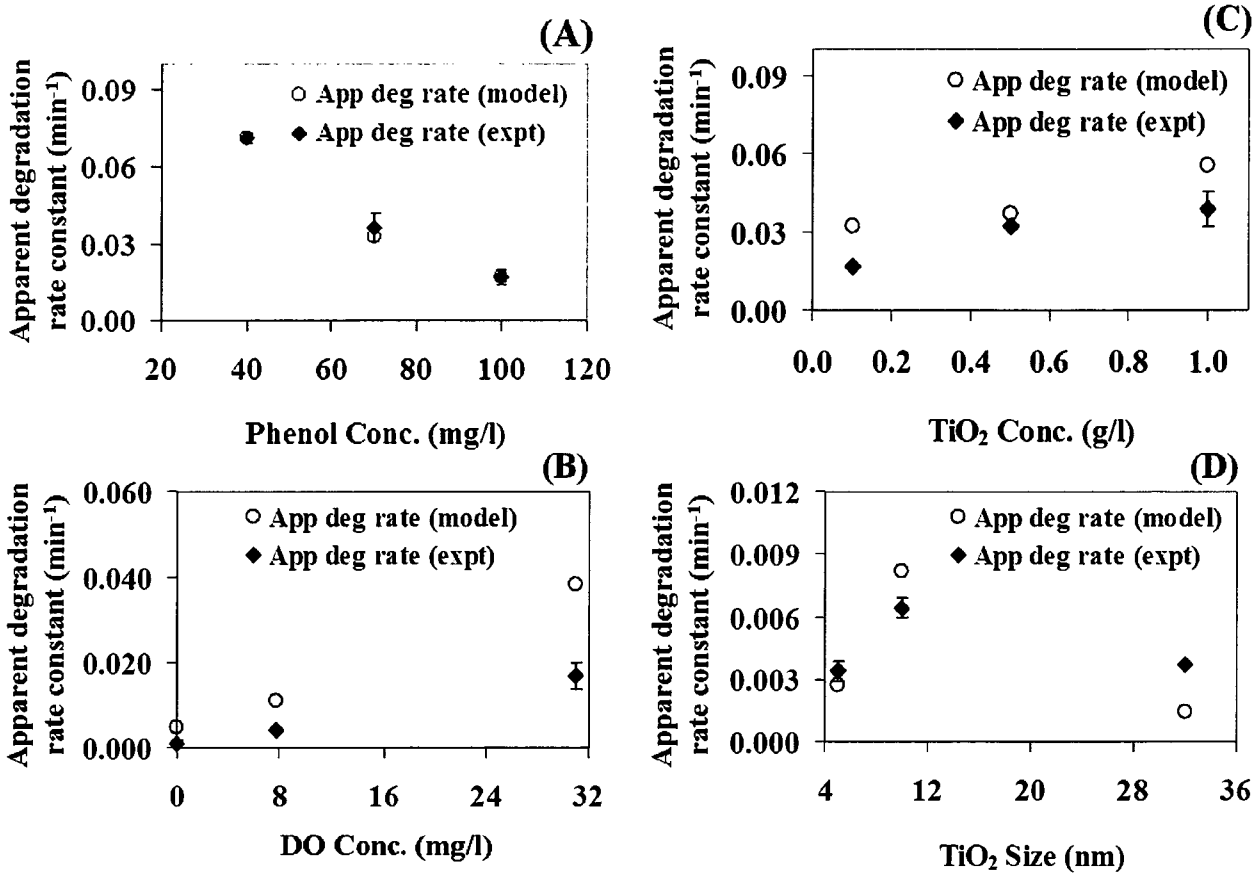

Figure 3.6 Validation of the response surface model for the design factors under consideration.

(A) Apparent degradation rate constant versus Phenol concentration.
[TiO_2 size: 10 nm; TiO_2 concentration: 1.0 g/l; DO: 31.0 mg/l]

(B) Apparent degradation rate constant versus DO concentration.
[TiO_2 size: 10 nm; TiO_2 concentration:1.0 g/l; Phenol concentration:100 mg/l]

(C) Apparent degradation rate constant versus TiO_2 concentration.
[TiO_2 size: 10 nm; DO: 31.0 mg/l; Phenol concentration: 100 mg/l]

(D) Apparent degradation rate constant versus TiO_2 size
[TiO_2 concentration: 0.5 g/l; DO: 7.8 mg/l; Phenol concentration: 100 mg/l]

[Average with standard deviation (SD) for triplicate samples are shown]

Additional experiments were conducted to confirm the validity and accuracy of the response surface model within the range of design variables under consideration. A separate validation study was performed for each of the four factors under evaluation. Model predictions were in agreement with the observed results for phenol levels ranging from 40 to 100mg/l (Figure 3.6(A)). For the DO concentration, the predicted results were consistent with the values observed. However, at high DO levels the model over estimated the apparent degradation rate (Figure 3.6(B)). Notice the trends for varying TiO_2 concentrations (Figure 3.6(C)) and TiO_2 sizes (Figure 3.6(D)) agreed with the experimental observations. The predicted value was slightly over-estimated compared to the actual observations for low and high TiO_2 concentrations and for the mid and high TiO_2 nanoparticle sizes.

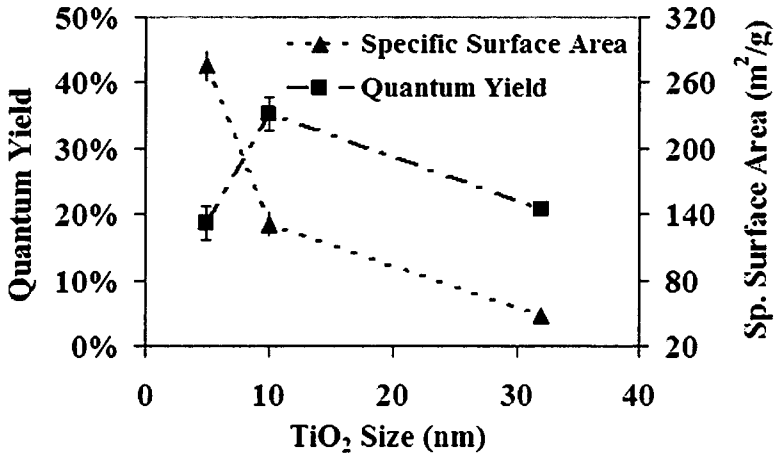

Figure 3.7 Quantum yield and specific surface area versus TiO_2 size
[TiO_2 Conc.: 0.5 g/l; DO: 7.8 mg/l; Phenol concentration: 100 mg/l
Average with standard deviation (SD) for triplicate samples are shown]

3.3.6. Quantum yield, mineralization rate and temperature dependency

Quantum yields (%) were computed for each of the three TiO_2 particle size. A plot of the quantum yield and specific surface area against particle size suggested that an increase in the

SSA augmented the quantum yield during the photocatalytic degradation process within the high and mid TiO_2 particle sizes under consideration. As the TiO_2 catalyst particle size was reduced from 10nm to 5nm with a corresponding increase in the SSA, the quantum yield did not show any improvement (Figure 3.7).

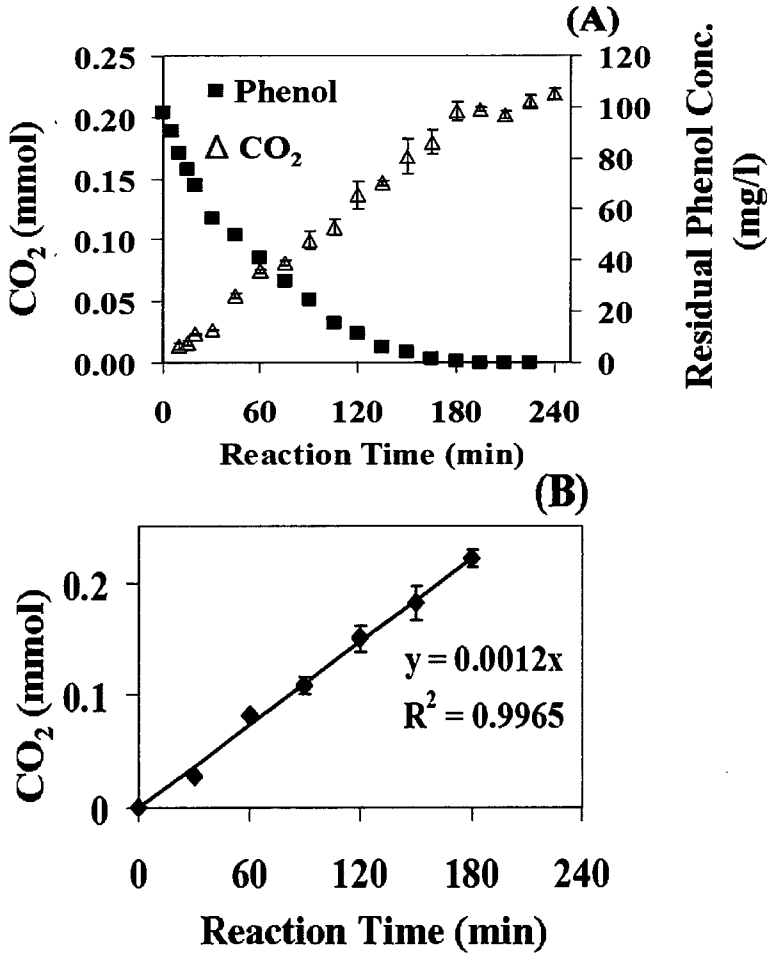

Figure 3.8 Mineralization profile for phenol during photocatalysis
(A) Residual phenol concentration and carbon dioxide formation profile
(B) Mineralization rate profile
[TiO_2 size: 10 nm; TiO_2 conc.: 1.0 g/l; DO: 31 mg/l; Phenol conc.: 100 mg/l
Average with standard deviation (SD) for triplicate samples are shown]

A correlation between the quantum yield and the SSA confirmed that the optimum TiO_2 particle size for maximum photocatalytic activity is approximately 10nm. Literature suggested

that an increase in bandgap energy (0.15eV) occur for TiO_2 nanoparticles as the particle size approach the quantum size barrier. This effect relates to the confinement of charge carriers (electron or hole) as the particle size approaches the order of de-Broglie wavelength (Linsebigler et al., 1995; Carp et al., 2004). Hence, the lower quantum yield observed below the optimum TiO_2 size (10nm) could be attributed to the quantum size effect. However, discrepancies exist in the literature sources with respect to the TiO_2 particle size where the quantum size effect is observable (Kormann et al., 1988; Beydoun et al., 1999). The present study can be considered useful in accounting the TiO_2 nanoparticle size (10nm) for maximum photocatalytic activity.

Experiments were performed at the optimum experimental factor settings for the highest phenol level under consideration. The degradation (or mineralization) rate was estimated by measuring the quantity of CO_2 formed in the headspace of the reaction tubes. Complete degradation of phenol was evident after 4 hours of reaction (Figure 3.8(A)) and the mineralization rate followed zero-order kinetics (Figure 3.8(B)) with a rate constant of 0.0012 mmol CO_2/minute.

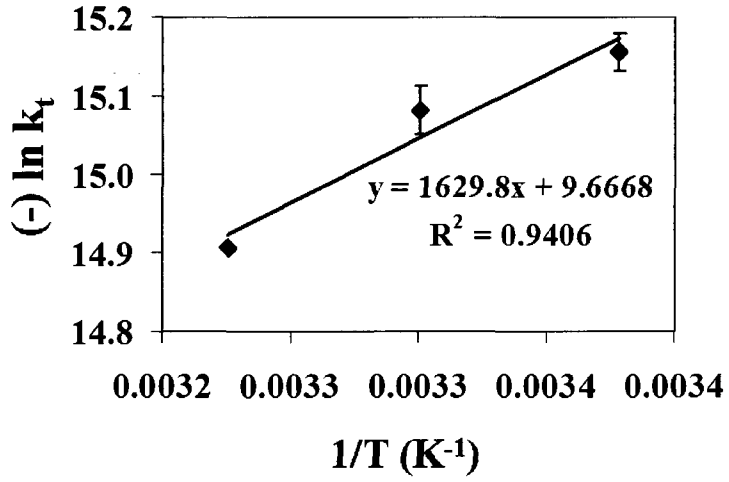

Figure 3.9 Arrhenius plot of photocatalytic degradation rate constant for phenol [TiO_2 size: 10 nm; TiO_2 conc.: 1.0 g/l; DO: 31 mg/l; Phenol conc.: 100 mg/l Average with standard deviation (SD) for triplicate samples are shown]

Photocatalytic degradation experiments conducted with 100mg/l phenol was performed under three temperature conditions (23°C (300K), 30°C (303K), and 37°C (310K)) in the presence of a 10nm TiO_2 catalyst at a concentration of 1.0g/l and with a DO level set at 31mg/l. The photocatalytic degradation rate, k_t, ($mol.s^{-1}$) was computed and a plot (Figure 3.9) of - ln k_t vesus 1/T showed evidence of Arrhenius dependency of the degradation rate. For the 10nm particle size TiO_2 photocatalyst, the calculated activation energy of 13.55 kJ/mol·K was within the range of values reported for the Degussa P25 TiO_2 photocatalyst (Kartal et al., 2001).

3.4. Conclusion

A response surface model, based on the Box-Benkhen technique, was developed to describe the photocatalytic degradation of phenol in an aqueous medium. A maximum degradation rate constant of $0.083min^{-1}$ was predicted with 40mg/l phenol concentration, 31mg/l DO, a TiO_2 particle size of 9.091nm and 1.0g/l TiO_2. The photocatalytic degradation rate constant was computed by conducting experiments at the optimum factor levels predicted by the model. The result ($0.072\ min^{-1}$) was approximately 13% less than the optimum response value predicted by the model.

Increasing the specific surface area by reducing the particle size within the nanometer range enhanced the phenol photocatalytic degradation rate. The degradation rate constant reached a maximum ($0.072 \pm 0.0017\ min^{-1}$) with a catalyst particle size of 10nm. The highest quantum yield ($35 \pm 2.5\%$) was observed for TiO_2 particle size in the range of approximately 10nm. Other than the catalyst size, the catalyst concentration and DO concentration had a significant impact on the apparent degradation rate constant. At low phenol levels, the degradation rate constant was greater when compared to elevated phenol concentrations. The photocatalytic

degradation rate constant followed an Arrhenius relationship with activation energy of 13.55 kJ/mol·K for 10 nm TiO_2 nanoparticle size.

3.5. References

1. Allen, N.S.; Edge, M.; Ortega, A.; Sandoval, G.; Liauw, C.M.; Verran, J.; Stratton, J.; McIntyre, R.B. (2004). Degradation and stabilisation of polymers and coatings: nano versus pigmentary titania particles. Polym. Degrad. Stab., 85, 927-946.
2. Autenrieth, R.L.; Bonner, J.S.; Akgerman, A.; Okaygun, M. (1991). Biodegradation of phenolic wastes. J. Hazard. Mater., 28, 29-53.
3. Bae, S.; Shoda, M. (2005). Statistical optimization of culture conditions for bacterial cellulose production using Box-Behnken design, Biotechnol. Bioeng., 90 (2005) 20-28.
4. Bevilaqua, J.V.; Cammarota, M.C.; Freire, D.M.G.; Sant'Anna, G.L. (2002). Phenol removal through combined biological and enzymatic treatments. Braz. J. Chem. Eng., 19, 151-158.
5. Beydoun, D.; Amal, R.; Low, G.; McEvoy, S. (1999). Role of nanoparticles in photocatalysis. *J. Nanoparticle Res.*, 1, 439–458.
6. Bhatkhande, D.S.; Pangarkar, V.G.; Beenackers, A.A.C.M. (2001). Photocatalytic degradation for environmental applications - a review, J. Chem. Technol. Biotechnol., 77, 102-116.
7. Box, G.E.P.; Hunter, W.G.; Hunter, W.S. (1978). Statistics for Experimenters: An Introduction to Design, Data Analysis, and Model Building, John Wiley and Sons, New York, NY, pp. 510 - 536. (ISBN 0-471-09315-7).
8. Box, G.E.P; Draper, N.R. (1987). Empirical Model Building and Response Surfaces, John Wiley & Sons, New York, NY, pp. 205 – 477 (ISBN 0-471-81033-9).
9. Bukowska, B.; Kowalska, S. (2003). The presence and toxicity of phenol derivatives – Their effect on human erythrocytes. Curr. Top. Biophys., 27, 47-51
10. Carp, O.; Huisman, C.L.; Reller, A. (2004). Photoinduced reactivity of titanium dioxide. Prog. *Solid State Chem.*, 32, 33-177.
11. Chen, D.; Ray, A.K. (1998). Photodegradation kinetics of 4-nitrophenol in TiO_2 suspension. *Wat. Res.* 32, 3223-3234.
12. Davydov, L. (2001). Photocatalytic degradation of organic contaminants: Novel catalysts and processes, *Ph. D. Dissertation*, University of Cincinnati. pp. 10-20.
13. Environmental Health Criteria (EHC) No. 161 (1994). *Phenol.* World Health Organization. Geneva, Switzerland. (ISBN 92-4-157161-6).

14. Environment Canada (2000). Priority substance list (PSL) 1 - Assessment report: Phenol. *Canadian Environmental Protection Act*. Minister of Public Works and Government Services, Gatineau, QC. pp. 7 – 46 (ISBN 0-662-28401-1).

15. Gogate, P.R.; Pandit, A.B. (2004). A review of imperative technologies for wastewater treatment I: oxidation technologies at ambient conditions. *Adv. Environ. Res.*, 8, 501–551.

16. Herrmann, J.M. (2005). Heterogeneous photocatalysis: state of the art and present applications, *Top. Catal.*, 34, 49 – 65.

17. Hurum, D.C.; Agrios, A.G.; Crist, S.E.; Gray, K.A.; Rajh, T.; Thurnauer, M.C. (2006). Probing reaction mechanisms in mixed phase TiO_2 by EPR. *J. Electron. Spectrosc. Relat. Phenom.*, 150, 155–163.

18. Kartal, O.E.; Erol, M.; Oguz, H. (2001). Photocatalytic destruction of phenol by TiO_2 powders, *Chem. Eng. Technol.*, 24, 645-649.

19. Kormann, C.; Bahnemann, D.W.; Hoffmann, M. (1988). Preparation and characterisation of quantum-size titanium dioxide. *J. Phys. Chem.*, 92, 5196–5201.

20. Kurniawati, S.; Nicell, J.A. (2005). Kinetic model of laccase-catalyzed oxidation of aqueous phenol. *Biotechnol. Bioeng.*, 91, 114-123.

21. Lee, S.K.; Mills, A. (2004). Detoxification of water by semiconductor photocatalysis. *J. Ind. Eng. Chem.*, 10, 173-187.

22. Linsebigler, L.; Lu, G.; Yates Jr., J.T. (1995). Photocatalysis on TiO_2 surfaces: Principles, mechanisms and selected results. *Chem. Rev.*, 95, 735-758.

23. Martinez, A.B.; Barbot, E.; Marrot, B.; Moulin, P.; Roche, N. (2006). Degradation of synthetic phenol containing wastewater by MBR. *J. Membrane. Sci.*, 281, 288-296.

24. Matthews, R.W. (1992). Photocatalytic oxidation of organic contaminants in water: An aid to environmental preservation. *Pure Appl. Chem.*, 64, 1285-1290.

25. Meknassi, Y.F.; Tyagi, R.D.; Surampalli, R.Y.; Barata, C.; Riva, M.C. (2004). Endocrine-disrupting compounds in wastewater, sludge-treatment processes, and receiving waters: Overview. *Pract. Periodical Haz. Toxic Radioactive Waste Mgmt.*, 8, 39-56.

26. Montogomery, D.C. (2005). *Design and analysis of experiments*, sixth ed., John Wiley and Sons, New York, NY. pp. 373-606 (ISBN 0-471-66159-7)

27. Myer, R.H.; Khuri, A.I.; Carter, W.H. (1989). Response surface methodology: 1966-1988. *Technometrics* 31, 137-157.

28. Myer, R.H.; Montogomery, D.C. (2002). *Response surface methodology: Process and product optimization using designed experiment*, second ed., John Wiley and Sons, New York, NY. pp. 343-350 (ISBN 0-471-41255-4).

29. Ollis, D. F.; Pelezzetti, E.; Serpone, N. (1991). Photocatalyzed destruction of water contaminants. *Environ. Sci. Technol.*, 25, 1522-1529.

30. Ray, S. (2006). RSM: A statistical tool for process optimization. *Ind. Tex. Jour.*, 117, 24-30.

31. Salinaro, A.; Emeline, A.V.; Zhao, J.; Hidaka, H.; Ryabchuk, V.K.; Serpone, N. (1999). Terminology, relative photonic efficiencies and quantum yields in heterogeneous photocatalysis. Part II: Experimental determination of quantum yields. *Pure & Appl. Chem.*, 71, 321-325.

32. Sobecka, B.S.; Tomaszewska, M.; Morawski, A.W. (2005). Removal of micropollutants from water by ozonation/biofiltration process. *Desalination*, 182, 151-157.

33. Stephens, M.A. (1974). EDF Statistics for Goodness of Fit and Some Comparisons. *J. Am. Stat. Soc.*, 69, 730-737.

34. United States Environmental Protection Agency (USEPA) (2001). *Removal of Endocrine Disruptor Chemicals Using Drinking Water Treatment Processes*. EPA/625/R-00/015. USEPA Office of Research and Development Publication, Cincinnati, OH. pp.1-27.

35. Westerhoff, P. (2003). Removal of endocrine disruptors, pharmaceuticals and personal care products during water treatment. *Southwest Hydrol.*, 2, 18-19.

36. Wu, J.; Taylor, K.E.; Bewtra, J.K.; Biswas, N. (1993). Optimization of the reaction conditions for enzymatic removal of phenol from wastewater in the presence of polyethylene glycol. *Water Res.*, 27, 1701-1706.

CHAPTER 4:

STATISTICAL MODEL FOR PHOTOCATALYSIS OF *p*-CRESOL WITH TITANIUM DIOXIDE NANO-PARTICLES

4.1. Introduction

Phenols and phenol derivatives such as cresols, have widespread industrial and commercial applications in the formulation of paints, lubricants, pesticides, and resins (Budkowska and Kowalska, 2003). Cresols are also produced as by-product from fractional distillation of crude oil, coal tars, and gasification of coal (EHC 168, 1995). Phenol and cresols (mono-substituted phenols) are toxic contaminants with carcinogenic, teratogenic, and mutagenic properties and are also known to have endocrine disrupting abilities (EHC 161, 1994; EHC 168, 1995; Budkowska and Kowalska, 2003). Conventional physical and chemical treatment processes are not designed to effectively remove or degrade phenolic compounds (United States Environmental Protection Agency (USEPA), 2001; Westerhoff, 2003; Auriol et al., 2006). The biological treatment methods are relatively ineffective beyond threshold concentration cresols because of the toxicity imposed on microorganisms (Autenrieth et al., 1991). Thus, conventional treatment facilities comprising of physical, chemical and biological treatment processes have varied level of effectiveness in removing cresols from industrial effluents (Westerhoff, 2003). The USEPA has suggested carbon adsorption as a preferred technique for treating effluents containing phenolic compounds, including cresols (USEPA, 2001). However, adsorption is essentially a phase transfer process rather than a degradative process and thus, these chemicals still persist in the environment.

In recent years, heterogeneous photocatalysis using Titanium dioxide (TiO_2) have been identified as a potential alternative to existing treatment technologies. TiO_2-photocatalysis offer a

unique advantage over other alternatives because in this treatment technique toxic organic pollutants are photo-oxidized to carbon dioxide (CO_2) and water (Ollis et al., 1991). The TiO_2 catalyst surface on photo-illumination generates electron-hole pairs which initiate the formation of hydroxyl radicals ($^{\bullet}OH$) (Linsebigler et al., 1995; Lee and Mills, 2004). These $^{\bullet}OH$ radicals subsequently mediate the degradation of organic molecules (Herrmann, 2005). The oxidative potential of TiO_2 originates from its semiconductor band gap and the process is initiated by radiation with wavelengths less than 380 nanometer (nm) (Matthews, 1992; Lee and Mills, 2004).

Many factors are known to affect the TiO_2 photocatalytic degradation rates of phenolic compounds (phenols and mono-substituted phenols). Increasing reaction rates are associated with higher photon energy and increase in the number of incident photons. The number of incident photons is directly related to the intensity of the incident radiation and lower wavelengths of radiation have higher energy photons (Lee and Mills, 2004; Herrmann, 2005). Another factor is the bandgap energy, which is controlled by the crystal structure of TiO_2 (Rajeshwar, 1995). Among all four crystal forms of TiO_2, anatase-TiO_2 has the highest bandgap energy (3.2eV), and therefore, photocatalytically it is the most active crystal form (Bhatkhande et al., 2001). The surface area of the catalysts also affects TiO_2 photocatalytic rates. The surface area is directly related to the particle size of the photocatalysts (Shah et al, 2002). Hence, nano-sized TiO_2 photocatalysts (e.g. Degussa P25, Hombikat) have higher photocatalytic efficiencies compared to the pigmentary grade (particle size in the micron range) (Bhatkhande et al.; 2001; Gogate and Pandit, 2004). The photocatalytic rates are strongly influenced by the number of catalyst particles, which in practice is synonymous with the catalyst concentration or catalyst loading (Mills et al.; 1993). At low TiO_2 catalyst concentrations, the rate of photolytic (no TiO_2)

degradation is greater than photocatalysis (with TiO_2). While at higher concentrations of the catalyst particles, the photocatalytic rates are impeded by the limited penetration depth of the incident light. This limited penetration of light is due to the incremental solution turbidity (Gogate and Pandit, 2004). The photocatalytic process is enhanced in the presence of oxygen (O_2) in the reaction medium as O_2 serves as a precursor for generating $^{\bullet}OH$ radicals (Fox and Dulay, 1993). The quantity and type of adsorption of reactant molecules onto the catalyst surface also affect the rate of photocatalytic degradation. According to Lee and Mills (2004), monolayer adsorption is preferred for maximum reaction rates. The phenolic compounds in the millimolar concentration range are reported to result in monolayer adsorption (Lee and Mills, 2004; Herrmann, 2005). The reaction rates at high substrate (phenolic) concentrations are hindered due to direct adsorption of photons by the organic (substrate) molecules. The adsorption of substrate on the catalyst surface is also correlated with the substitution pattern and the substituted functional group for phenolic compounds. Hence, different photocatalytic rates are reported for phenolic compounds with different substitution patterns and varied substituted functional groups on the benzene ring (Tsai and Cheng, 1997; Bhatkhande et al., 2001; Gogate and Pandit, 2004; Pera-Titus et al., 2004; Kusvuran et al., 2005).

Although some reports are available, evidence describing the effects of different process variables on the photocatalytic rate is limited (Bhatkhande et al., 2001; Kartal et al., 2001; Sakkas et al., 2010). In a recent study by Ray et al. (2009), the Box-Benkhen design (BBD) procedure was used to statistically model the photocatalytic degradation rate of phenol. These researchers developed a second-order (quadratic) model which included the following factors: TiO_2 particle size, TiO_2 concentration, dissolved oxygen (DO) concentration, and substrate (phenol) concentration. Ray et al. (2009) observed first (pseudo) order kinetics for the

photocatalytic degradation of phenol in presence of TiO_2 nanoparticles. The model equation for an apparent first order rate constant (k) is shown as Equation 4.1 (phenol model).

$$k = 0.0022244*(TiO_2\ size) + 0.0037492*(DO) - 0.0000523*(TiO_2\ size) - 0.0224267*(TiO_2\ Conc)^2$$
$$- 0.0000430*(TiO_2\ size)*(DO) + 0.0008159*(TiO_2\ Conc)*(DO) - 0.0000414*(DO)*(Substrate\ Conc) \quad (4.1)$$

A possible extension to the work reported by Ray et al. (2009) is to examine the validity of the phenol model (Equation 4.1) for other phenolic chemicals, such as substituted phenols. Among the various substituted phenols *p*-cresol is one, which is widely used in industrial applications and its presence in the environment has been documented in earlier studies (EHC 168, 1995; Clarke et al., 1997; Bhatkhande et al., 2001; Kusvuran et al., 2005; Sakkas et al., 2010). Hence, the objective of this work is to confirm the validity of the statistical phenol photocatalytic model for p-cresol degradation by TiO_2 nanoparticles. The phenol model (Equation 4.1) was validated for all the four experimental factors, namely, TiO_2 particle size, TiO_2 concentration, DO concentration, and *p*-cresol (substrate) concentration by conducting experiments at selected levels of the experimental factors.

4.2. Materials and methods

4.2.1. Photocatalysis of *p*-Cresol

Photocatalytic experiments were conducted in a custom-built ultraviolet (UV) photocatalytic reaction chamber (modified RPR-100, Southern New England Ultraviolet Co., Branford, CT) which was equipped with sixteen 300nm, monochromatic, low pressure, phosphor coated mercury vapor lamps (Southern New England Ultraviolet Co., Branford, CT) on the outer perimeter (Figure 3.1). An average radiation intensity of 9 $mW \cdot cm^{-2}$ was maintained throughout the experiment (calibrated by radiometer (UV-X with 300nm sensor, UV Process Supply,

Chicago, IL). The experimental apparatus was identical with that reported for developing the phenol model (Ray et al., 2009). Photocatalysis of *p*-cresol was conducted in a custom-built reaction tubes (25 mm ID x 250 mm length) constructed from 100% UV transmitant glass (GE-214 clear fused quartz silica, Technical Glass Products Inc., Painesville, OH). Photocatalytic experiments, except for those performed to evaluate the temperature effect, were conducted at 37±2°C (Ray et al., 2009). The temperature of the UV reaction chamber was maintained constant throughout the reaction by placing the reaction chamber into a temperature controlled chamber (MaxQ, Thermo Fisher Scientific Inc, Waltham, MA). The photocatalytic reaction rates are least affected by solution pH at the isoelectric point (point of zero surface charge (zpc)) of TiO_2. The isoelectric point of TiO_2 is reported to be at near neutral pH condition (Bhatkhande et al., 2001). Hence, all the experiments were conducted in ultra-pure water with pH 7.0 ± 0.5 without any further pH adjustment. The ultrapure water (18M-ohm resistivity) was generated using a NANOpure Diamond Lab water system (Thermo Fisher Scientific Inc, Waltham, MA).

4.2.2. Analytical methods

Liquid samples were removed at regular intervals and analyzed for residual *p*-cresol using a high performance liquid chromatograph (HPLC) configured with an Acclaim C18-3μm-2.1mm (ID) x 100mm (length) column (Dionex, Sunnyvale, CA). The eluent (acetonitrile-water mixture (2:5)) flow rate was set at 0.4ml·min^{-1} and the column temperature was maintained at 45°C. The headspace gas was analyzed for CO_2 using a gas chromatograph (GC) (Varian CP 3800, Varian, Palo Alto, CA). The GC was configured with a Shin Carbon ST 1mm (ID) x 2m (length) column (Restek, Bellefonte, PA) and the hydrogen carrier gas (BOC, Windsor, ON) flow rate was set at 20ml·min^{-1}. The analysis was conducted using the following oven temperature program: 80°C for 0.5min, ramp to 120°C at 30°C/min and hold for 1min then ramp to 150°C at 40°C/min. The

thermal conductivity detector (TCD) and the injector were set at 180°C and 100°C respectively. The GC analytical methods were adopted from Ray et al. (2009). The detection limit for *p*-cresol (HPLC) and CO_2 (GC) were 0.01mg·l^{-1} and 0.2kPa, respectively. All experimental conditions were evaluated in triplicates.

4.2.3. Experimental factor levels

The photocatalysis of *p*-cresol was conducted using TiO_2 nanoparticles with 5 nm, 10 nm, and 32 nm diameters (> 99% Purity, Alfa-Aesar, Ward Hill, MA). The crystal structure for each TiO_2 nanoparticle size was identical (anatase) and was confirmed by X-ray diffraction (D8 Discover, Bruker Corporation, Milton, ON). The levels of TiO_2 nanoparticle size were selected based on the commercial availability of the photocatalyst with the same crystal structure. The only difference in the catalyst particles was the size (dry powder) and the specific surface area (SSA). The SSA was determined by physisorption of nitrogen (N_2) between relative pressure of 0.0 – 0.3 at 77K using the Brunner Emmett Teller (BET) method (Nova 1200e, Quantachrome Instruments, Boynton Beach, FL). The TiO_2 concentration was varied between 0.1 to 1.0 g·l^{-1}. Preliminary experiments showed that at TiO_2 concentration < 0.1 g·l^{-1}, the effect of the TiO_2 nanoparticles was negligible and at concentration > 1.0 g·l^{-1}, the photocatalytic degradation rate was affected by the limited penetration depth of light due to high suspension turbidity. To validate the model over the entire range of DO concentration, the maximum and minimum boundaries of the DO concentration were set at 0.04mg·l^{-1} and 31.0mg·l^{-1}, respectively. The levels of the *p*-cresol concentration were determined by assuming monolayer (Langmuir type) adsorption on the photocatalyst surface (Lee and Mills, 2004; Herrmann, 2005). The experimental factors and their respective levels are summarized in Table 4.1.

Table 4.1: Factors and levels selected for *p*-cresol degradation

Factors / Levels	Size of TiO_2 nano-particles (nm) (Specific surface area (m^2/g))[a]	TiO_2 catalyst concentration (g/l)	DO concentration (mg/l)	Initial *p*-cresol concentration (mg/l)
1	5 (275±15)[b]	0.1	0.04	40
2	10 (131±12)[b]	0.5	7.80	70
3	32 (47±2)[b]	1.0	31.0	100

[a] The values in bracket is the specific surface area (m^2/g) of TiO_2 particles (dry)
[b] Average and standard deviation for triplicate samples.

4.2.4. Validation procedure

Photocatalytic experiments were conducted at the selected levels of each experimental factor. The experimental factors evaluated were TiO_2 particle size (dry), TiO_2 concentration, DO concentration and *p*-cresol (substrate) concentration. The reaction rates were computed from the photocatalytic experiments. The reaction rate order for *p*-cresol was determined to confirm the assumption of apparent first order reaction rate in the phenol model (Equation 4.1). The experimental photocatalytic rates were compared against the model predicted rates to confirm the validity of the model. Finally, the photocatalytic behavior of *p*-cresol was compared against phenol with respect to activation energy and quantum yield.

4.3. Results and discussion

4.3.1. Kinetic study of *p*-cresol photocatalysis

The residual *p*-cresol concentration was monitored over a duration of 1 hour in presence of TiO_2 (photocatalysis) and in absence of TiO_2 (photolysis) (Figure 4.1(A)). In both cases, the removal rate of *p*-cresol followed first-order kinetics (Equation 4.2).

$$-(dC/dt) = kC \tag{4.2}$$

where, k is the apparent first order reaction rate constant, referred herein as apparent degradation rate constant (min^{-1}), C is the *p*-cresol concentration (mg/l) and $(-dC/dt)$ is the first order disappearance (removal) rate. $[-\ln(C/C_o)]$ was plotted against the reaction time to determine the apparent degradation rate constant (Figure 4.1(B)).

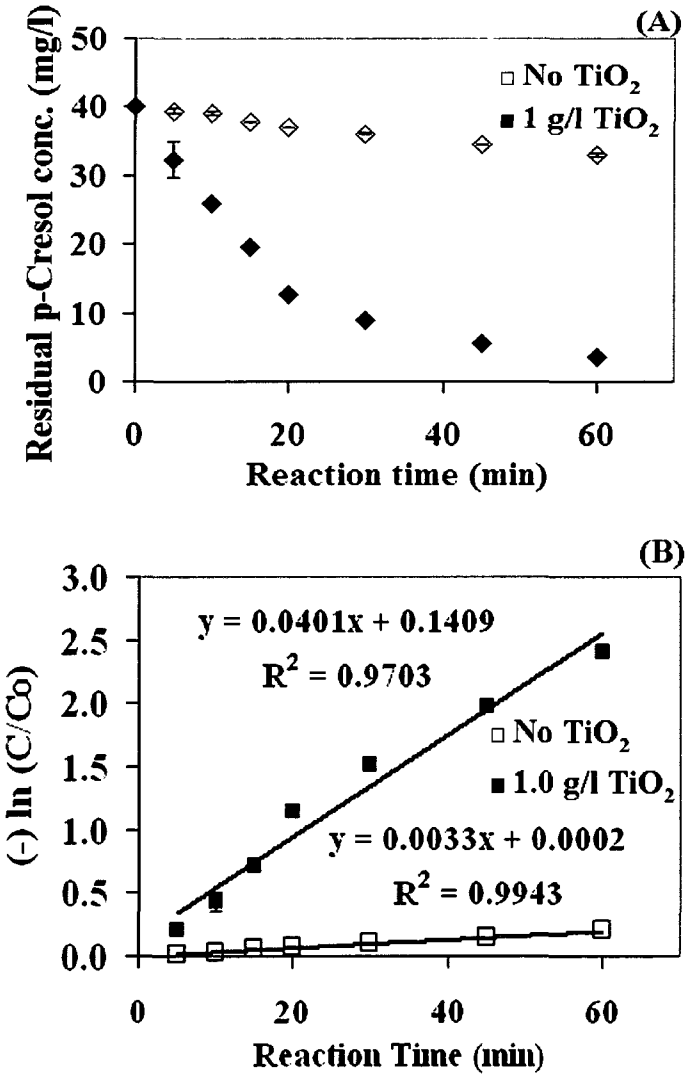

Figure 4.1 *p*-Cresol degradation profiles for photocatalysis and photolysis
(A) Residual concentration (B) Removal rate
[Averages with standard deviation (SD) for triplicate samples are shown]

Based on the conditions as those reported by Ray et al. (2009), the photolysis rate (UV without TiO_2) contributed 10% to the degradation rate of *p*-cresol, while the remaining 90% was attributed to photocatalysis (due to the presence of TiO_2). Recall the output of the phenol model is apparent first order rate constant for photocatalytic degradation with TiO_2 nanoparticles. Figure 4.1(B) confirms the validity of the apparent first order rate kinetics for *p*-cresol photocatalysis.

4.3.2. Validation of the statistical model for *p*-cresol photocatalysis

The phenol model (Equation 4.1) predicted the apparent degradation rate constant (k, min^{-1}) for *p*-cresol photocatalysis using four independent factors (TiO_2 size, TiO_2 concentration, DO concentration, and *p*-cresol (reactant) concentration) which were varied at three different levels (Table 4.1). The apparent degradation rate constant was determined using Equation 4.1 and the computed k value from the model was compared with the corresponding experimental value for each factor level. The model prediction was in close agreement with the experimental results for 0.4mg/l DO and 7.8mg/l DO; however, at 31mg/l DO, the model over estimated the apparent degradation rate constant by 33.4% (Figure 4.2 (A)). Notice large variations in the degradation rate were observed at high DO concentrations. Maintaining high DO levels in the reactor was difficult and this caused a large fluctuation in the degradation rate. The predicted value for the degradation rate constants correlated closely well with the experimental value for all the TiO_2 levels under examination (Figure 4.2(B)). Higher degradation rates constants were associated with higher TiO_2 concentrations. At low *p*-cresol concentration, degradation rate was faster than at high p-cresol concentrations. The experimental rate constant was lower than the value predicted by the model at lower *p*-cresol concentrations (Figure 4.2(C)). At 70mg/l and 100mg/l *p*-cresol, the predicted value for the degradation rate constant correlated closely with the

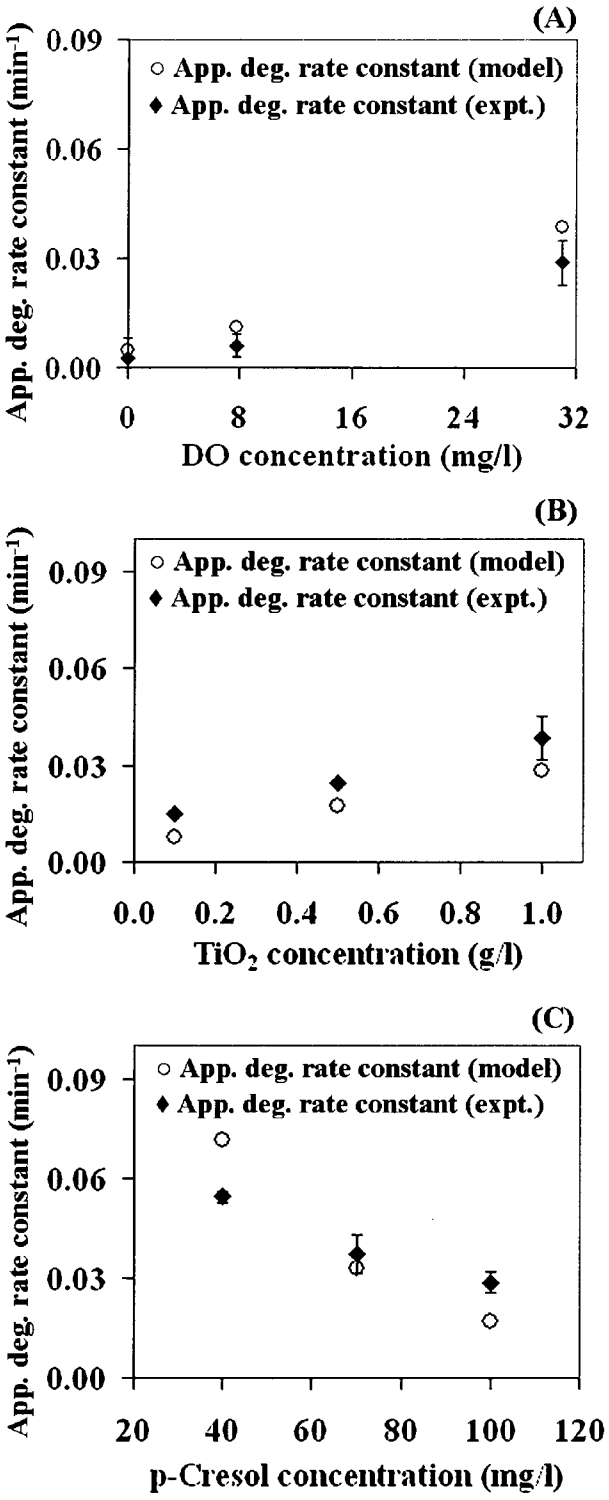

Figure 4.2 Comparison of the apparent degradation rate for the model with experimental values for different

(A) DO concentration, (B) TiO_2 concentration, (C) *p*-cresol concentration

[Averages with standard deviation (SD) for triplicate samples are shown]

experimental value. Photocatalysis is a surface phenomenon and competition for the active sites on the catalyst surface is expected to increase at high *p*-cresol concentrations compared to low levels. Hence, high photocatalytic degradation rates are expected at low *p*-cresol concentrations.

4.3.3. Verification of optimal condition from the statistical model

Optimizing the TiO_2 nanoparticle size for maximum photocatalytic degradation was reported by Ray et al. (2009). The D-optimality criterion, computed from the phenol model using numerical algorithm was used to identify the TiO_2 nanoparticle size associated with the greatest photocatalytic degradation rate constant (k). The maximum photocatalytic rate was predicted for a TiO_2 particle size of approximately 10nm (9.091nm) (Ray et al., 2009). The experimental degradation rate data for *p*-cresol verified the predicted TiO_2 particle size of approximately 10nm, when a maximum degradation rate was observed. A plot of the experimental apparent degradation rate constant and SSA against the particle size shows a maximum rate constant for the 10nm TiO_2 particles (Figure 4.3). In spite of an increase in the SSA, a lower apparent degradation rate was observed below 10nm. This lower photocatalytic degradation rate below the optimum TiO_2 size of 10 nm is likely attributed to a phenomenon known as quantum size effect (Linsebigler et al., 1995; Carp et al., 2004).

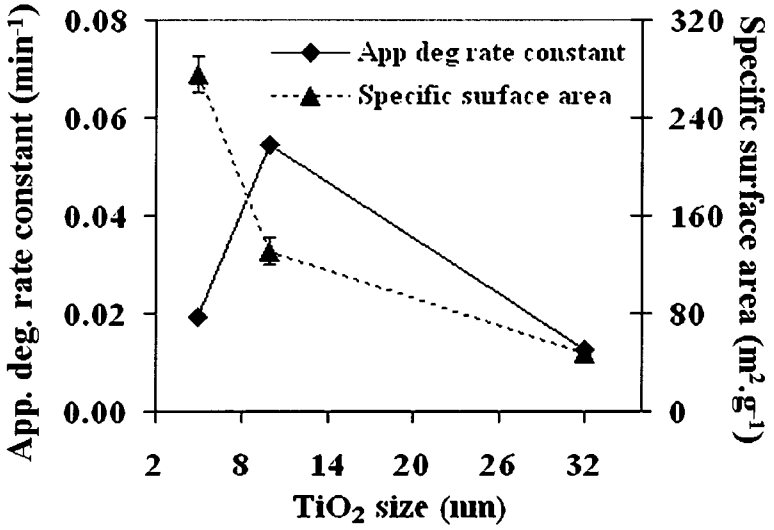

Figure 4.3 Apparent degradation rate constant and specific surface area versus TiO_2 particle size (dry).
[Averages with standard deviation (SD) for triplicate samples are shown)]

4.3.4. Comparison of activation energy, quantum yield and mineralization rate

The photocatalytic degradation of *p*-cresol with 10nm TiO_2 nanoparticle catalyst was conducted at 23°C (300K), 30°C (303K) and 37°C (310K). The degradation rate in mol/s (k_t) was computed and a plot of [- ln k_t] vesus [1/T] showed an Arrhenius dependency of the degradation rate (Figure 4.4). An activation energy of 10.77 kJ/mol·K for *p*-cresol degradation was computed using 10nm TiO_2 nanoparticles. The observed activation energy for *p*-cresol is comparable to the value reported for phenol (13.55 kJ/mol·K) (Ray et al., 2009). Photocatalysis being a surface phenomenon, the activation energy of the reaction is influenced by the affinity of the reactant (substrate) for the catalyst surface. The proximity of pk_a values for phenol (9.99) and *p*-cresol (10.09) could be a major reason for similar affinities of phenol and *p*-cresol for the catalyst surface (EHC 161, 1994; EHC 168, 1995).

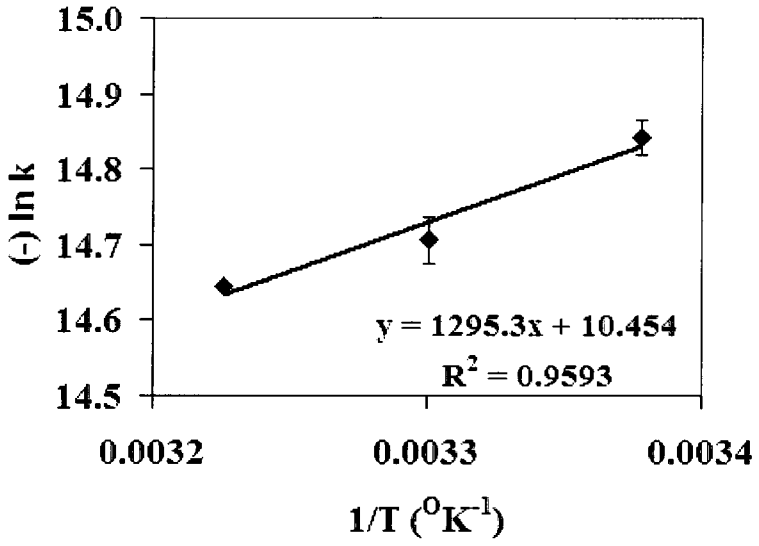

Figure 4.4 Arrhenius plot of photocatalytic degradation rate constant for *p*-cresol [Averages with standard deviation (SD) for triplicate samples are shown]

The quantum yield for the 10nm TiO_2 nanoparticles was computed for phenol and *p*-cresol to confirm the difference in activation energy. The quantum yield is defined as the ratio of the number of substrate molecules (phenol or *p*-cresol) degraded to the number of photons irradiated (Lee and Mills, 2004). The yield for *p*-cresol degradation (41 ± 1.8%) was statistically greater than the reported value of 35 ± 2.5 % for phenol (Ray et al., 2009). The result of two-sample t-test indicates that the quantum yields for the two substrates (p-cresol and phenol) are statistically different (Note $t_{computed}$ (3.4) is greater than $t_{tabulated}$ (3.2) (Montogomery, 1997)). The higher quantum yield of *p*-cresol suggests a lower activation energy. A slightly greater quantum yield for *p*-cresol when compared to phenol is a suitable indicator that the degradation rate for *p*-cresol is larger than for phenol.

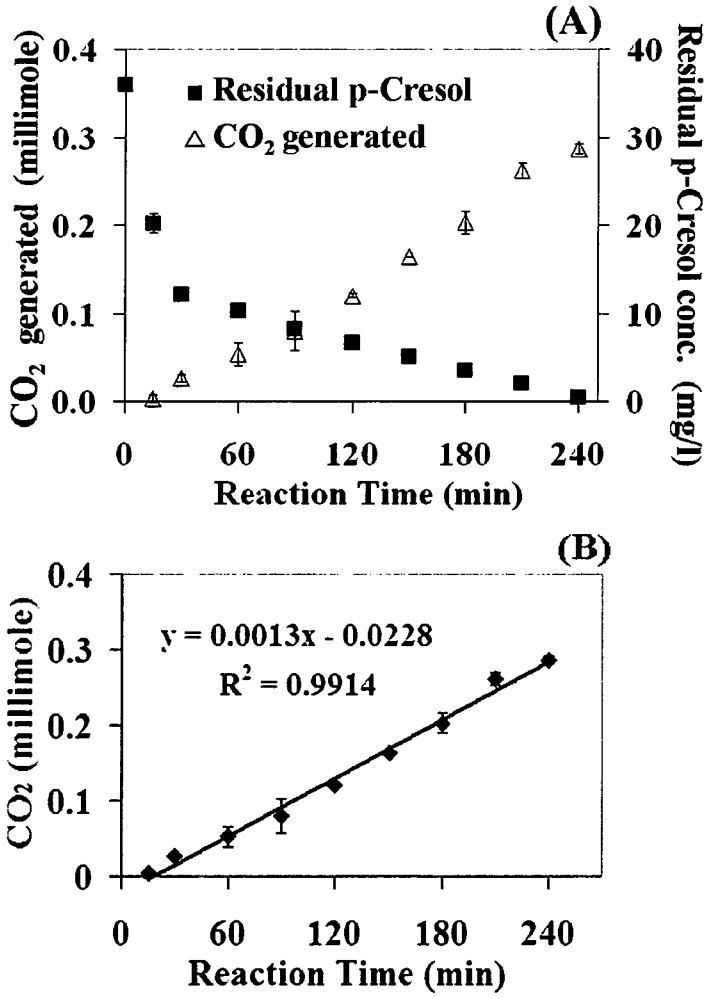

Figure 4.5 Photocatalytic profile - (A) Residual *p*-cresol concentration and CO_2 formation (B) Mineralization rate
[Averages with standard deviation (SD) for triplicate samples are shown]

The complete degradation (or mineralization) rate was estimated by measuring the quantity of CO_2 in the reactor headspace. Complete degradation of *p*-cresol was evident 4 hours after the reaction was initiated (Figure 4.5(A)). The mineralization rate followed zero-order kinetics (Figure 4.5(B)) with a rate constant of 0.0013 mmol CO_2/minute. The mineralization rate is in agreement with values reported for phenol (0.0012 mmol CO_2/minute) (Ray et al., 2009).

Based on calculated values for the quantum yield and activation energy, faster photocatalytic degradation of *p*-cresol with TiO_2 nanoparticles is expected in comparison to phenol. However,

the phenol model can be used to examine the degradation of *p*-cresol for the range of the four factors under consideration.

4.4. Conclusion

The photocatalytic degradation of phenolic contaminants with TiO_2 is a promising treatment option when compared to other techniques. The photocatalytic process is affected by factors which include catalytic material properties, incident radiation characteristics, catalyst loading, DO concentration, and temperature. Statistical experimental design is a very effective technique for understanding the interaction between these factors and to consolidate the factors into a statistical model. A recent study by Ray et al. (2009) reported the development of a statistical model to predict the degradation rate constant of phenol photocatalysis using TiO_2 nanoparticles (phenol model). In this study, the validity of the phenol model for photocatalytic degradation of *p*-cresol using TiO_2 nanoparticles was assessed. Deviation between predicted values with experimental values was observed when the DO concentration was high and *p*-cresol concentration was low. A maximum *p*-cresol degradation rate constant was recorded for 10nm TiO_2 particles. The activation energy and mineralization rate for photocatalysis of *p*-cresol were in agreement with that reported in the literature for phenol. The computed quantum yield for *p*-cresol photocatalysis concluded that *p*-cresol degrades slightly faster than phenol. However, the phenol model can be concluded to be valid for photocatalysis of *p*-cresol using TiO_2 nanoparticles over the range of values for the various factors under consideration.

4.5. References

1. Auriol, M.; Meknassi, Y.F.; Tyagi, R.D.; Adams, C.D.; Surampalli, R.Y. (2006). Endocrine disrupting compounds removal from wastewater, a new challenge. *Process Biochem.*, 41, 525–539.
2. Autenrieth, R.L.; Bonner, J.S.; Akgerman, A.; Okaygun, M. (1991). Biodegradation of phenolic wastes. *J. Hazard. Mater.*, 28, 29-53.
3. Bhatkhande, D.S.; Pangarkar, V.G.; Beenackers, A.A.C.M. (2001). Photocatalytic degradation for environmental applications - a review. *J. Chem. Technol. Biotechnol.*, 77, 102-116.
4. Bukowska, B.; Kowalska, S. (2003). The presence and toxicity of phenol derivatives – Their effect on human erythrocytes. *Curr. Top. Biophys.*, 27, 47-51
5. Clarke, J.; Hill, R.R.; Roberts, D.R. (1997). Primary processes in the catalytic photooxidation of p-cresol. *J. Chem. Tech. Biotechnol.*, 68, 397-404.
6. Environmental Health Criteria (EHC) No. 161 (1994). *Phenol.* World Health Organization. Geneva, Switzerland. (ISBN 92-4-157161-6).
7. Environmental Health Criteria (EHC) No. 168 (1995). *Cresol.* World Health Organization. Geneva, Switzerland. (ISBN 92-4-157168-1).
8. Fox, M.A.; Dulay, M.T. (1993). Heterogeneous photocatalysis. *Chem. Rev.*, 93, 341-357.
9. Gogate, P.R.; Pandit, A.B. (2004). A review of imperative technologies for wastewater treatment I: oxidation technologies at ambient conditions. *Adv. Environ. Res.*, 8, 501–551.
10. Herrmann, J.M. (2005). Heterogeneous photocatalysis: state of the art and present applications, *Top. Catal.*, 34, 49 – 65.
11. Kartal, O.E.; Erol, M.; Oguz, H. (2001). Photocatalytic destruction of phenol by TiO_2 powders, *Chem. Eng. Technol.*, 24, 645-649.
12. Kusvuran, E.; Samil, A.; Atanur, O.M.; Erbatur, O. (2005). Photocatalytic degradation kinetics of di- and tri-substituted phenolic compounds in aqueous solution by TiO_2/UV. *Appl. Catal. B.*, 58, 211–216.
13. Lee, S.K.; Mills, A. (2004). Detoxification of water by semiconductor photocatalysis, J. *Ind. Eng. Chem.*, 10, 173-187.
14. Linsebigler, L.; Lu, G.; Yates Jr., J.T. (1995). Photocatalysis on TiO_2 surfaces: Principles, mechanisms and selected results. *Chem. Rev.*, 95, 735-758.
15. Matthews, R.W. (1992). Photocatalytic oxidation of organic contaminants in water: An aid to environmental preservation, *Pure Appl. Chem.*, 64, 1285-1290.
16. Mills, A.; Davies, R.H.; Worsley, D. (1993). Water purification by semiconductor photocatalysis. *Chem. Soc. Rev.*, 22, 417-425.

17. Montogomery, D.C. (1997). *Design and analysis of experiments*, fourth ed., John Wiley and Sons, New York, NY. pp. 660 (ISBN 0-471-15746-5).

18. Ollis, D.F.; Pelezzetti, E.; Serpone, N. (1991). Photocatalyzed destruction of water contaminants. *Environ. Sci. Technol.*, 25, 1522-1529.

19. Pera-Titus, M.; Garc´ıa-Molina, V.; Baños, M.A.; Giméneza, J.; Esplugas, S. (2004). Degradation of chlorophenols by means of advanced oxidation processes: a general review. *Appl. Catal. B.*, 47, 219-256.

20. Rajeshwar, K. (1995). Photoelectrochemistry and the environment. *J. Appl. Electrochem.*, 25, 1067-1082.

21. Ray, S.; Lalman, J.A.; Biswas, N. (2009). Using the Box-Benkhen technique to statistically model phenol photocatalytic degradation by titanium dioxide nanoparticles. *Chem. Eng. J.*, 150, 1, 15-24.

22. Sakkas, V. A.; Islam, M. A.; Stalikas, C.; Albanis, T. A. (2010). Photocatalytic degradation using design of experiments: A review and example of the Congo Red degradation. *J. Haz. Mat.*, 175, 33 – 44.

23. Shah, S.I.; Li, W.; Huang, C.P.; Jung, O.; Ni, C. (2002). Study of Nd^{3+}, Pd^{2+}, Pt^{4+} and Fe^{3+} dopant effect on photoreactivity of TiO_2 nanoparticles. *Proc. Natl. Acad. Sci. USA*, 99 (Suppl. 2): 6482 - 6486.

24. Tsai, S.-J.; Cheng, S. (1997). Effect of TiO_2 crystalline structure in photocatalytic degradation of phenolic contaminants. *Catal. Today.*, 33, 227-237.

25. United States Environmental Protection Agency (USEPA) (2001). *Removal of Endocrine Disruptor Chemicals Using Drinking Water Treatment Processes*. EPA/625/R-00/015. USEPA Office of Research and Development Publication, Cincinnati, OH. pp.1-27.

26. Westerhoff, P. (2003). Removal of endocrine disruptors, pharmaceuticals and personal care products during water treatment. *Southwest Hydrol.*, 2, 18-19.

CHAPTER 5: FABRICATION AND CHARACTERIZATION OF AN IMMOBILIZED TITANIUM DIOXIDE NANOFIBER CATALYST

5.1. Introduction

In the 1970s the photo-induced catalytic ability of Titanium dioxide (TiO_2) was recognized by Fujishima and Honda (1972). Since this initial work, many reports have emerged examining the photocatalytic ability of TiO_2 (Blake, 1999). TiO_2 is utilized primarily as a catalyst to oxidize organic pollutants (Ollis et al., 1991). However, TiO_2 is also used as electrode materials in solar cells (Bach et al., 1998), photo-electrochemical cells (Barbe′ et al., 1997), solid oxide electrochemical cells (Guo, et al., 2007) proton exchange membrane fuel cells (Johannes et al., 2007), and very recently, in microbial fuel cells (Qiao et al., 2008). The demand for high catalytic efficiency in most of these applications has advanced research initiatives toward the development of a TiO_2 catalyst with a large surface-to-volume ratio (Centi and Perathoner, 2009; Chandrasekar et al., 2009). The charge carrier mobility, electron transfer efficiency, and the rate of recombination of charge carriers are the performance related size-dependent attributes of TiO_2 based materials (Centi and Perathoner, 2009). Naturally, decreasing the size to nanometric dimensions demonstrate an improvement of the performance with respect to micrometric-sized materials as a result of the increased specific surface area and surface reactivity (He et al., 2007).

TiO_2 nanoparticles have been widely studied for their enhanced catalytic activity (Sankapal et al., 2006). Nano-sized TiO_2 particles are synthesized by solvent routes, such as alkaline-hydrothermal, solvo-thermal, micro-emulsion, and anodic oxidation methods. TiO_2 nanoparicles are also generated by gas phase methods such as chemical vapor deposition, e-beam evaporation, magnetron sputtering, and spray pyrolytic deposition (Carp et al., 2004; Sankapal et al., 2006;

Centi and Perathoner, 2009). Many of these processes are associated with practical limitations in relation to intensive process control and high energy consumption, and are often considered uneconomical (Carp et al., 2004). Recently, sol-gel based synthesis methods are applied to prepare very large surface area TiO_2 nanomaterials (Carp et al., 2004). However, the properties of these TiO_2 nanomaterials are highly dependent on particle aggregation, nano-architecture, specific surface area, crystal structure, and presence of impurities (Centi and Perathoner, 2009). Among the different methods used to produce TiO_2 nanoparticles, the sol-gel based synthesis process has received the most research focus due to its easy coupling potential with different catalyst immobilization and thin film formation techniques such as dip-coating and spray application (Hamid and Rahman, 2003).

TiO_2 nanoparticles have been studied for their catalytic performance, either in free suspension or as immobilized on a fixed or fluidized support (Pozzo et al., 1997). The improved performance and larger catalytic surfaces have been reported for well mixed, pseudo-homogeneous nanoparticle slurries in comparison to supported nanocatalyst systems (Matthews and McEvoy, 1992; Dijkstra et al., 2001). Using TiO_2 nanoparticles in the form of suspended particles has been reported in many studies (Matthews and McEvoy, 1992; Blake, 1999; Bhatkhande et al., 2001; Ray et al., 2009). However, in solar cells and other photovoltaic or electrochemical applications, the demand for immobilizing TiO_2 onto solid support is increasing (Bach et al., 1998; Barbe´ et al., 1997). For engineering applications, there is an intrinsic drawback in using slurries of nanoparticles because of poor settling tendency, uneconomical solid/liquid separation process, and human health hazards associated with the fugitive emission of nanoparticles during slurry preparation (Ibañez et al., 1999; Houari et al., 2005; Baan et al., 2006). The limitations of the slurry process are not associated with the immobilized TiO_2

nanocatalyst systems; however, a major drawback for immobilizing TiO_2 nanoparticles is related to the loss of surface area. Particle sintering or aggregation on the support surface during the thermal treatment caused loss of surface area in supported TiO_2 nanocatalysts (Carp et al., 2004; Houari et al., 2005). Hence, developing an immobilized TiO_2 nanocatalyst system with a surface area comparable to that of discrete nanoparticles is a research priority for enhanced catalytic performance.

A method which has gained recognition as an effective alternative for fabricating immobilized nanostructures with high surface-to-volume ratio on a fixed support is electrospinning. The electrical forces are exploited in the electrospinning method to produce fibers with nanometric diameters (Doshi and Reneker, 1995). Electrospinning of nanofibers is initiated when the electrical forces at the surface of a viscous solution overcome the surface tension barrier and cause ejection of an electrically charged jet of fluid. As the solvent evaporates, the jet becomes solid. During the evaporative process electrically charged fibers are accelerated by electrical forces and stretched by several orders of magnitude (Reneker and Chun, 1996). In principle, the process of electrospinning can be considered as a variation of the process of electro-spraying. Electro-spraying is associated with low viscosity fluids, where the application of electrostatic field causes a fluid stream to disintegrate into small charged droplets or aerosols. The electrospinning process applies to highly viscous solution or melt, wherein application of electrical forces results in production of nanofibers (Deitzel et al., 2001).

The first reference to the electrospinning process dates back to 1934, when Formhals patented a process and an apparatus for the production of the polymer filament using electrostatic forces (Fomhals, 1934). In 1969 Taylor reported the shape distortion of the fluid droplet under an applied electrical field and introduced the concept of the "Taylor cone", related to the onset of

the fiber forming process (Subbiah, et al., 2005). Almost three decades later the electrospinning of nanofibers received a major impetus through the research of Reneker and his co-workers (Doshi and Reneker, 1995; Frenot and Chronakis, 2003). Later, other researchers reported using electrospinning to fabricate ultra thin fibers from a broad range of polymers (Subbiah, et al., 2005). Recently, electrospinning has been extended to fabricate nanofibers of TiO_2 through coupling with the sol-gel technique. Formation of the TiO_2 nanofibers by sol-gel electrospinning from an organo-titanium salt precursor was reported by Li and Xia (2003). TiO_2 nanofibers are produced in two stages. Initially nanofibers are generated by electrospinning a solution of a polymer mixed with a sol-gel precursor of TiO_2. Then, the composite nanofibers of polymer and TiO_2 are subjected to thermal treatment to obtain pure TiO_2 fiber (Viswanathamurthi et al., 2004).

Since the process of polymer assisted TiO_2 nanofiber production was reported by Li and Xia (2003), a considerable amount of research effort has been directed towards utilizing this technique for producing immobilized TiO_2 nanocatalysts (Sigmund et al., 2006; Chronakis, 2005). Madhugiri and her coworkers (2004) first reported producing immobilized TiO_2 nanofibers with diameter greater than 100 nanometer (nm). However, Madhugiri et al. (2004) reported using a powder form of the nanofiber catalyst in photocatalytic studies. Kokubo et al. (2007) also reported using a similar approach of disintegrating the fibrous structure through mechanical compression. In a recent study, Alves and his coworkers reported using electrospun TiO_2 in the form of an unsupported mat (Alves et al., 2009). The drawbacks associated with nanoparticles, such as solid/liquid separation, and health hazards due to remnant particles equally persist when the structure of the immobilized nanofibers are disintegrated by mechanical compression. The practical constraints associated with application of nanofiber catalysts in an

immobilized form was pointed out by Fujihara et al. (2007). According to Fujihara et al. (2007), TiO_2 nanofiber mesh has a tendency to peel off or dislodge from the catalyst support surface. The practical constraint due to limited stability of the immobilized TiO_2 nanofibers was also reported by Jo et al. (2005) and Ramaseshan et al. (2007). Improved adhesion of the TiO_2 nanocatalyst on the support is particularly important for effective electron transfer and maximum photon adsorption in photocatalytic applications (Ramaseshan et al., 2007). Several techniques have been reported in earlier studies which improve the adhesion of the nanocatalyst, in particular for solar cell applications. Song et al. (2004, 2005) reported implementing a post spinning treatment process with tetrahydrofuran (THF) while, others (Kokubo et al., 2007; Jo et al., 2009) used mechanical compression for improving the adhesion of the nanofibers. However, in both cases the TiO_2 catalyst lost its fibrous structures (Fujihara et al., 2007). So far no study has successfully fabricated an immobilized TiO_2 nanofiber catalyst with good stability and fiber structure integrity during application. Hence, the object of the present study is to fabricate a supported TiO_2 nanofiber catalyst with improved stability for photocatalytic applications.

5.2. Materials and methods

5.2.1. Electrospinning apparatus

The electrospinning apparatus used in this study (Figure 5.1) was custom built and fabricated in-house. The viscous electrospinning solution was delivered at a specific flow rate using a programmable syringe pump (PHD 22/2000, Havard Apparatus Canada, St. Laurent, QC) equipped with a 10ml luer-lock plastic syringe (Becton Dickinson, Oakville, ON). The syringe was fitted with a 22 gauge (0.7mm outer diameter (OD), 0.4mm inner diameter (ID)), 38mm long stainless steel hypodermic needle with a polypropylene hub (Becton Dickinson, Oakville,

ON). The delivery system had a low flow capability of 0.03 ± 0.001 µl/min. The delivery rate of the electrospinning solution is hereafter referred to as the infusion rate. The positive (anode) terminal of a variable high voltage DC power supply (ES 50P – 10W/DAM, Gamma High Voltage Research Inc. Ormond Beach, FL) capable of producing a potential difference of the order of 0 - 50 kV, was connected to the stainless steel needle using an alligator clip. The ground terminal (negative) of the power supply was attached to the conducting solid support material (cathode). The distance of separation between the two electrodes (needle tip to the surface of the support) in the electrospinning apparatus was denoted as the separation distance. The electrospinning section of the apparatus (needle to collector) was enclosed in a sealed chamber to eliminate the effect of air currents on the deposition process and to maintain a stable environment.

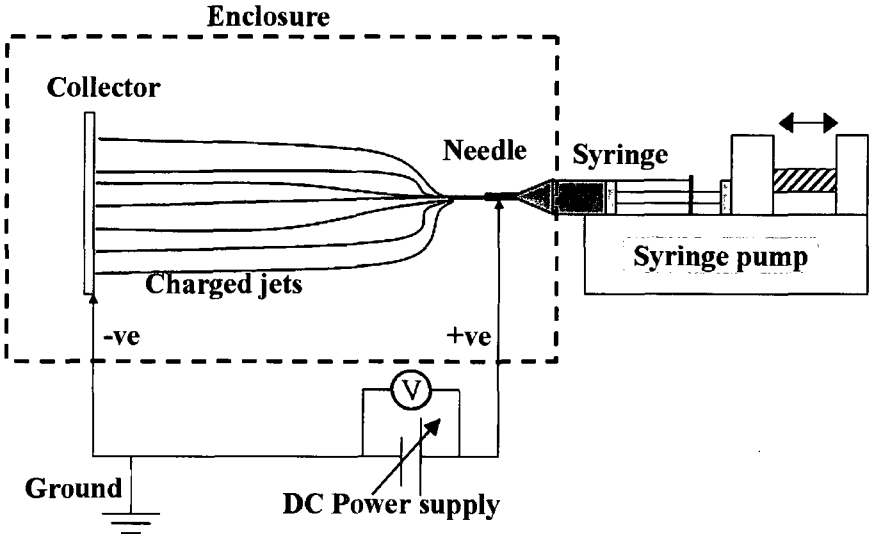

Figure 5.1 Schematic of the electrospinning process

5.2.2. Preparation of electrospinning solution

Titanium tetraisopropoxide (TIP), an organo-titanium sol-gel precursor to titanium dioxide (> 99.95% purity), and polyvinyl acetate (PVAc (average molecular weight (M_w) 50,000 Daltons)),

a carrier for the TIP, were purchased from Alfa Aesar (Ward Hill, MA). Acetic acid (>99% purity), a stabilizer for sol-gel conversion of TIP, was procured from EMD (Gibbstown, NJ). Dimethylformamide (DMF) and tetrahydrofuran (THF) solvents were supplied by Fischer Scientific (Ottawa, ON).

TIP was used as a sol-gel precursor for fabricating the TiO_2 fibers. Earlier studies reported that stochiometric stabilization of TIP with acetic acid could control hydrolysis of TIP. The control of hydrolysis of TIP results in the formation of a finer TiO_2 aggregate with a fibrillar structure (Santana-Aranda et al., 2005; Ayres et al., 2007). Accordingly, TIP was stabilized by adding glacial acetic acid in a molar ratio of 1: 4 (mol TIP per mol acetic acid) under slow stirring conditions (Solution A). The Solution A (TIP/acetic acid solution) was mixed with a polymer solution to maintain a viscosity between 130-160 centipoise (cps) at 21°C (Cui et al., 2008). According to Jo et al. (2005), PVAc possess better miscibility with TIP and maintain better homogeneity of the phases during electrospinning. Hence, PVAc was selected for the study. A PVAc solution was prepared by dissolving polymer beads in 3:2 volumetric mixtures of DMF and THF (Solution B). A 45% (weight per unit volume (w/v)) solution of PVAc (M_w 50,000 Dalton) in 3:2 (v/v) DMF/THF was measured (using cone and plate viscometer (Brookfield CAP 1000 viscometer, Brookfield, Middleboro, MA) to have a viscosity of 147.8 ± 0.6 cps (at shear rate $\geq 10{,}000 s^{-1}$).

Jo et al. (2005) had shown that the TIP/PVAc ratio affects the morphology of the nanofibers. Lowest TIP/PVAc ratio studied by Jo et al. (2005) was 1.0, which resulted in 100nm TiO_2 fibers. Hence, in order to produce TiO_2 nanofibers with smaller diameters (lower than 100nm), a TIP/PVAc ratio of 0.4 was selected. The electrospinning solution (Solution C) was prepared by

mixing a required amount of the TIP solution (Solution A) with a 45% PVAc (w/v) solution (Solution B).

5.2.3. Electrospinning and catalyst immobilization

A pump was used to deliver the electrospinning solution (Solution C) to the infusing needle. The infusion rate of the pump was adjusted to a selected value (between 0.6-3.0 $ml \cdot h^{-1}$). The upper and lower bounds of the infusion rate were established by the wastage of electrospinning solution due to excess flow (above $3.0ml \cdot h^{-1}$) and discontinuous fiber production due to limited flow (below $0.6ml \cdot h^{-1}$). The solution was delivered at a constant flow rate to the stainless steel needle connected to the positive terminal of the high voltage DC power supply. The ground terminal was attached to the solid support (collector) and positioned at 22.5cm from the needle tip. A potential gradient within a range of 1.11-1.78 $kV \cdot cm^{-1}$ was applied to initiate the electrospinning of nanofibers (Table 5.1). Below the lowest value of potential gradient (< 1.11 $kV \cdot cm^{-1}$), the fiber formation was discontinuous and beyond the highest value (>1.78$kV \cdot cm^{-1}$), electrical arcs were produced between the electrodes.

Table 5.1: Electrospinning variables and their levels examined.

Electrospinning variables		**Experimental levels of the variables**		
		Level 1	**Level 2**	**Level 3**
1	Potential gradient ($kV \cdot cm^{-1}$)	1.11	1.44	1.78
2	Infusion rate ($ml \cdot h^{-1}$)	0.6	1.8	3.0

Upon applying the potential gradient (1.11-1.78 $kV \cdot cm^{-1}$), a fluid jet was ejected from the capillary (needle) tip. After an initial instability period of a few seconds, a steady fluid jet was directed towards the grounded support. As the jet accelerated towards the cathode, the solvent evaporated and charged TiO_2/PVAc composite fibers were deposited on the solid support. The

presence of residual solvent allowed relaxation of the polymer chain and this resulted in a loss of stability in the structure of the deposited nanofiber. Hence, the TiO_2/PVAc nanofibers were dried under a vacuum of 600mm Hg at 105°C for 2 hours to remove the residual solvent, and allow further condensation of the structure (Ding et al., 2004; Madhugiri et al., 2004; Sheikh et al., 2009). The vacuum-dried TiO_2/PVAc nano-composite fibers were characterized for the thermal transitions and examined for structural features. The TiO_2/PVAc nano-composite fibers were thereafter subjected to thermal treatment to remove the polymer back bone (PVAc) and obtain an immobilized TiO_2 nanofiber catalyst. The thermal treatment procedure was developed as a pre-characterization process, and details of the procedure is provided in section 5.3.1 of this chapter (Chapter 5). Characterization entailed determining the crystal structure, stoichiometric composition, surface morphology, and dimension of the nanofibers.

5.2.4. Analytical measurements used to characterize the TiO_2 nanocatalyst

The thermal transition temperature of the TiO_2/PVAc composite nanofiber samples were determined by a differential scanning calorimeter (DSC) (Mettler DSC822E, Mettler-Toledo Inc., Columbus, OH). The temperature scan was conducted from 50° to 500°C at a linear heating rate of 20°C/min. Thermal degradation, in terms of weight loss, was determined by a thermogravimetric analyzer (TGA) (Mettler TGA/SDTA 851E, Mettler-Toledo Inc., Columbus, OH). The samples were heated in air from temperature between 30° to 500°C at 2°C/min. The TGA instrument was equipped with a mass spectroscopic (MS) detector which was capable of detecting mass from 1 to 300 a.m.u. The MS detector was used to identify degradation products from the thermal oxidation of the composite nanocatalyst samples.

The crystalline phase of the immobilized TiO_2 nanofibers were quantified using a X-ray diffractometer (D8 Discover, Bruker Corporation, Milton, ON) configured with a Cu K_α (α =

1.54 Å) source and outfitted with a general area detector diffraction system (GADDS). The specimen was scanned from 2θ-angle 17° to 55° in steps of 0.05°. The interplanar spacing (d-spacing) of the crystalline phase were computed using Bragg's law (Equation 5.1), where, n is an integer, d is interplanar spacing between subsequent crystalline plane of atoms, θ is the scattering angle, and λ is the wavelength of the x-ray.

$$2dSin\theta = n\lambda \tag{5.1}$$

The d-spacing and the diffraction peaks from the crystalline phases were identified by comparing against JCPDS cards (Joint Committee on Powder Diffraction Standards (JCPDS), powder diffraction file, Card No. 21-1272 (anatase) and 21-1276 (rutile), Swarthmore, PA). The crystal size was computed using the Debye-Scherrer formula (Equation 5.2), where K is a dimensionless constant having a value 0.89 (for lattice structures), α is the wavelength of the x-ray, B is a measure of peak width (full-width at half of maximum (FWHM)), and θ_B is the Bragg's angle for the diffraction peak.

$$Crytal\ size = \frac{K\alpha}{BCos\theta_B} \tag{5.2}$$

TiO_2 nanofibers were examined for the presence of organic functional groups using Fourier transform infrared (FTIR) spectroscopy. TiO_2 nanofibers were compressed and pelletized with potassium bromide (KBr) (Sigma Aldrich, Oakville, ON) under a compressive load of 4.5 metric ton, and thereafter scanned between wavenumber of 400 – 4000 cm^{-1} in the FTIR instrument (Vector-22, Bruker Optics Inc, Billerica, MA). The scans were analyzed using OPUS NET software (Bruker Optics Inc, Billerica, MA). For comparison, TiO_2/PVAc nanocomposite fibers were also examined in FTIR under the identical setting after pelletizing with KBr.

Images of the nanofibers were obtained using a field emission scanning electron microscope (FESEM) (Quanta 200, FEI Company, Hillsboro, OR) using Everhart-Thornley secondary

electron detector under high vacuum mode. The maximum resolution capacity of the microscope was 0.8nm. The energy dispersive spectroscopy (EDS) and GENESIS material characterization software (EDAX Inc., Mahwah, NJ) were used to analyze the stoichiometric composition of the nanofibers. The diameter of the nanofiber was determined from the FESEM image using an image processing software (SCANDIUM, Olympus Soft Imaging Solutions Corp, Lakewood, CO).

5.3. Results and discussions

5.3.1. Thermal characterization of the nanofibers

The DSC study was conducted with TiO_2/PVAc nanofibers to determine the thermal transition temperatures of the nanofibers (Figure 5.2(A)). No significant thermal transition was observed for the nanocomposite fibers between 50°C to 270°C, at a heating rate of $20^{\circ}C \cdot min^{-1}$. The absence of thermal transition peaks below 270°C confirmed the elimination of residual solvent in the composite nanofibers after vacuum drying. According to Chien et al. (2008), the glass-transition temperature of PVAc is well below 50°C (approximately 35°C) and hence, temperature less than 50°C were not examined in this study. Due to the thermoset nature of PVAc, degradation of the material is expected instead of melting (Holland and Hay, 2002; Chien et al., 2008). Hence, a there is no exothermic peak to mark the melting of PVAc. A small exothermic peak (data not shown) was observed at 270°C indicating the onset of the thermal degradation through the elimination of the functional group (Holland and Hay, 2002). Two noticeable exothermic peaks at approximately 340°C and 435°C were observed in the DSC profile for TiO_2/PVAc nanocomposite. The peaks at approximately 340°C was due to thermal degradation of the polyenic structure (backbone) of PVAc polymer (Holland and Hay, 2002),

and the subsequent exothermic peak (around 435°C) was likely due to further crystallization and crystal phase transformation of TiO_2 in the nanofibers (Nuansing et al., 2006; Alves et al., 2009).

The temperature at which organic material decomposes in the TiO_2/PVAc composite nanofibers was established using TGA. In the TGA analysis, the measured weight loss of a sample was associated with the thermal transition for a particular temperature. Differential thermal analysis (DTA) was also employed to determine transitions in the composite, relative to a reference material. The TGA and DTA profiles of the composite nanofibers are presented in Figure 5.2(B).

The TGA/DTA observations were in agreement with the findings of the DSC study (Figure 5.2(A)). Note the composite nanofibers underwent a cumulative weight loss of approximately 76% when heated from 30° - 500°C at 2°C/min during the TGA analysis. The degradative weight loss of the PVAc was initiated from a temperature above 240°C and continued until 330°C. Within this temperature range the nanocomposite underwent 50% weight loss with a differential weight loss peak at 285°C. The degradation of PVAc was confirmed by identifying gaseous degradation products (CH_3CO (m/z = 43), CO_2 (m/z = 44) and CH_3COOH (m/z = 60)) in mass-spectroscopic analysis. The differential weight loss peak between 400 - 435°C was attributed to the removal of residual carbon, transformation of TiO_2 crystal phase and sintering of the crystal with loss of moisture (Carpio et al., 2005, Zhan et al., 2006). The mass spectroscopic analysis confirmed the formation of products with m/z = 16, 18 and 44, between 400° - 435°C.

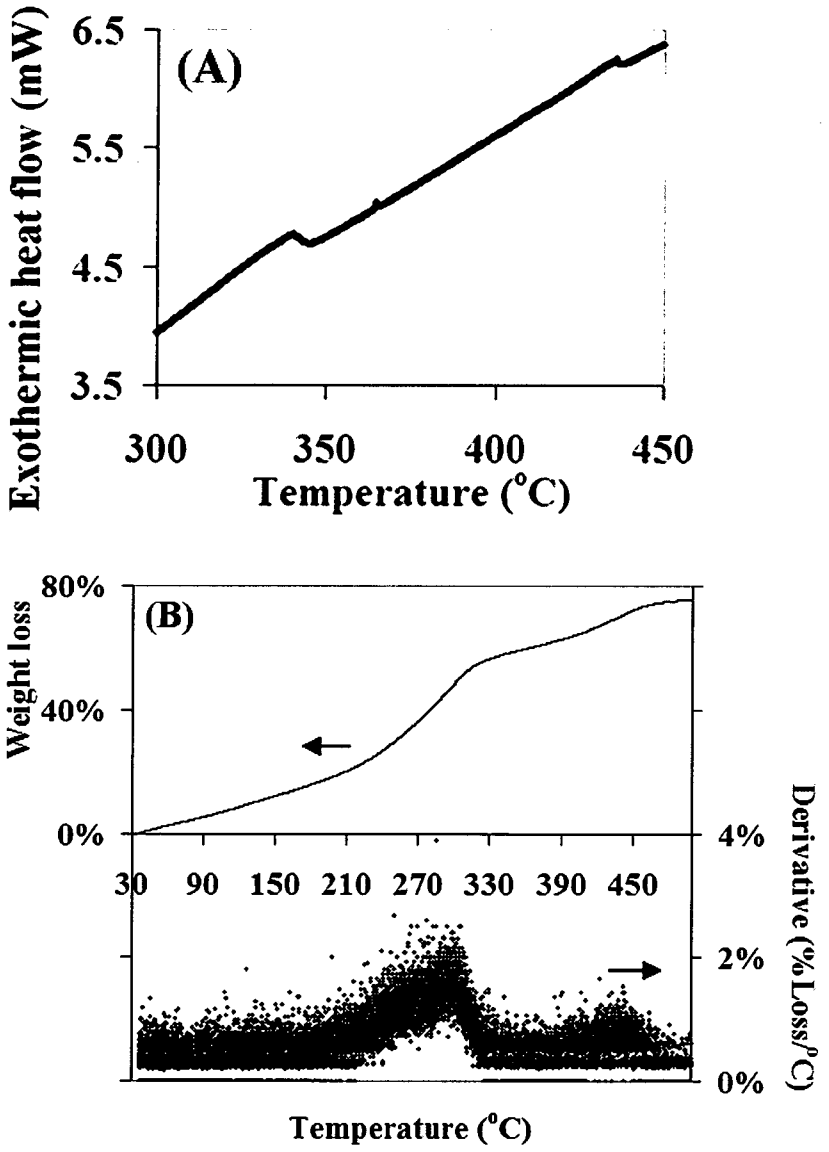

Figure 5.2 Thermal characterization profile of the TiO_2-Polyvinyl acetate nano-composite fibers. (A) DSC (B) TGA and DTA

Similar observations from the TGA study were reported in the literature (Zhan *et al.*, 2006; Nuansing et al., 2006; Chen et al., 2008). However, neither study provided supporting evidence of the formation of gaseous byproducts by a mass-spectroscopic analysis. Based on the findings of DSC and TGA studies, and the final calcination conditions reported in the literature for producing anatase TiO_2 (Zhan et al., 2006), a temperature program for calcination was developed

to obtain pure TiO_2 immobilized nanofibers from TiO_2/PVAc composite nanofibers. Slow stepwise heating was applied on the nanocomposite to maintain the nanofiber morphology of sintering TiO_2 particles (Reneker et al., 2008).

The vacuum dried TiO_2/PVAc composite nanofibers were heated at rate of 1.5°C/min in a temperature programmable oven (HP 5890, Hewlett-Packard, Avondale, PA) to 300°C and thereafter it was calcined in air in a muffle furnace (Thermolyne 1300, Thermo Fisher Scientific Inc., Newington, NH) at a calcination temperature of 400 ± 5°C for an additional 2 hours to obtain immobilized TiO_2 nanofibers. The immobilized nanofibers were then cooled to ambient temperature, cleaned with a gentle stream of clean dry air (to strip-off the loose particles attached on the surface of the catalyst), rinsed in ultrapure water to remove any remaining polymer ash, and finally, dried at 105°C to remove any moisture. Fibers calcined at 450°C and 500°C were also examined using x-ray diffraction (XRD) to establish the minimum temperature required for calcination.

5.3.2. X-ray diffraction (XRD) of the TiO_2 nanofibers

X-ray diffraction (XRD) studies were conducted on TiO_2 fibers calcined at 400°C, 450°C and 500°C. The interplanar distances (d-spacing) were computed using Equation 5.1 and the crystal planes were identified by comparing the d-spacing values and the 2θ degree angles. The results for these parameters are tabulated in Table 5.2. The reported d-spacing values for the crystalline phases (Table 5.2) from the experimentally obtained fibers were in close agreement with the d-spacing values reported for pure crystalline phases. Note the d-spacing value for pure anatase (101) is 3.51Å and that for pure rutile (110) is 3.24Å (JCPDS, PDF, Card No. 21-1272 (anatase) and 21-1276 (rutile)). The crystal size was computed using Equation 5.2 and the mass fraction of the rutile phase (X_R) was determined using Spurr equation, Equation 5.3 (Scotti et al., 2009). The

term I_A and I_R in Equation 5.3 are the integrated intensities of the (101) anatase and (110) rutile crystal plane respectively.

$$\frac{1}{X_R} = 1 + 0.8\left(\frac{I_A}{I_R}\right) \tag{5.3}$$

The values tabulated in Table 5.2 showed that increasing the calcination temperature above 400°C causes transformation of the TiO_2 crystalline phase in nanofibers. An increase in the rutile mass fraction was observed as the calcination temperature increased from 400°C to 500°C. Higher aggregation and sintering of the TiO_2 crystals were correlated with increasing crystal size at higher calcination temperatures. The study also examined the effect of increasing the calcination time on the size of TiO_2 crystals. The crystal size computed for TiO_2 nanofibers calcined for 2, 3, 4 and 6 hours were 9.7, 10.9, 13.0 and 17.3 nm respectively. Anatase TiO_2 is the most preferred crystal form for photocatalytic application due to its higher bandgap energy (Bhatkhande et al., 2001). A crystal size of 10 - 12 nm had been reported in the literature as a favorable size for efficient charge transfer in photocatalytic applications (Pozzo et al., 1997; Carpio et al., 2005). Accordingly, a calcination temperature of 400°C and calcination time of 2 hours was used for fabricating anatase TiO_2 nanofiber catalysts from TiO_2/PVAc composite nanofibers for the remaining study.

Table 5.2: X-Ray diffraction results of the TiO_2 nanofibers.

Calcination temperature (°C)	**Mass fraction (%)**		**d-spacing (Å)**		**Crystal size (nm)**
	Anatase	**Rutile**	**Anatase (101)**	**Rutile (110)**	
400	100	0	3.50	--	9.7
450	96	4	3.54	3.23	15.9
500	73	27	3.46	3.21	20.7

5.3.3. Fourier transform infrared (FTIR) spectroscopy study of the nanofibers

The FTIR spectra of the TiO_2/PVAc nanocomposite (Figure 5.3) showed a characteristic IR band for the presence of an ester carbonyl linkage (O=C-O-) of the acetate side-group at 1010 cm^{-1} and 1240cm^{-1}. The IR band at 600cm^{-1} and 650cm^{-1} could be attributed to deformational vibration of the O-C-O linkages in the ester functional group of the aliphatic vinyl acetate unit of the polymer. Peaks due to absorbance of C-C stretching and vibration of the polymer backbone were observed at 740cm^{-1} and 945cm^{-1} respectively (Holland and Hay, 2002). Disappearance of the IR bands associated with PVAc in the TiO_2 nanofibers, confirmed the removal of the polymer under the calcination condition (400°C for 2 hours). A band observed at 1115 cm^{-1} in TiO_2 nanofibers was attributed to Ti-OH stretching (Figure 5.3). The intense broad absorbance (transmittance minimum) band at 665cm^{-1} was due to Ti-O stretching and it confirmed the formation of the anatase crystalline phase in TiO_2 nanofibers (Ding et al., 2004, Zhan et al., 2006; Sathyamoorthy et al., 2007).

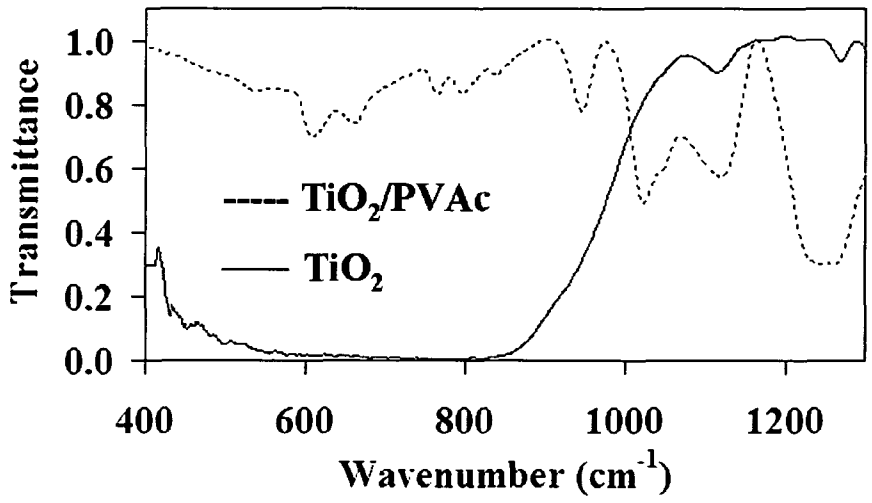

Figure 5.3 Fourier transform infrared (FTIR) spectra of the nanofibers.

5.3.4. Morphological studies of the TiO_2 nanofibers

The effect of electrospinning parameters on the morphology of TiO_2 nanofibers was studied using a one-factor-at-a-time (OFAT) approach. The experimental conditions used to generate the TiO_2 nanofibers are tabulated in Table 5.1. The potential gradient ($kV \cdot cm^{-1}$) across the electrodes was varied by increasing the applied potential across electrodes (22.5 cm apart). TiO_2 nanofibers were generated under potential gradients of 1.11, 1.44 and 1.78 $kV \cdot cm^{-1}$ with the infusion rate invariant at $1.8ml.h^{-1}$. No nanofiber formation was recorded below 1.11 $kV \cdot cm^{-1}$ and the formation of electrical arcs above 1.78 $kV \cdot cm^{-1}$ resulted in the discontinuity of the electrospinning process. Histograms of the nanofibers produced under different applied potential gradients are shown in Figure 5.4. The diameters of the nanofibers were computed. The applied potential gradient controlled the mass of solution drawn out of the needle and the extent of stretching of the fluid jet. A balance between the two opposing effects due to electrostatic stretch and viscoelastic drag determines the final diameter of the TiO_2 nanofibers (Tan et al., 2005). Contradictory observations of the applied potential on the fiber diameter have been reported in the literature. An increase in fiber diameter with increasing applied potential was reported by Li and Xia (2003), whereas a reverse trend was observed by Doh et al. (2008). Within the regime of applied potential gradient examined in this study, an increase in the potential gradient led to the formation of nanofibers with smaller diameters (Figure 5.4). The mean fiber diameters at three different potential gradients were 78±10.5nm (1.11 $kV \cdot cm^{-1}$), 63±14.2nm (1.44 $kV \cdot cm^{-1}$) and 60±8.7nm (1.78 $kV \cdot cm^{-1}$).

At the invariant applied potential gradient of 1.78$kV \cdot cm^{-1}$, the infusion rate was varied as follows: 0.6, 1.8 to 3.0 $ml.h^{-1}$. Similar to the applied potential, an increase in the infusion rate caused the production of larger diameter fibers (Figure 5.5). Increasing the infusion rate ($ml \cdot h^{-1}$)

directly translated into higher mass throughput and lower electrostatic charge per unit volume of the spinning solution at the needle tip. These changes resulted in an increase in fiber diameter (Doh et al., 2008). The mean fiber diameters recorded under these conditions were 54 ± 11.5nm (0.6 $ml.h^{-1}$), 60 ± 8.7nm (1.8 $ml.h^{-1}$) and 64 ± 9.6nm (3.0 $ml.h^{-1}$).

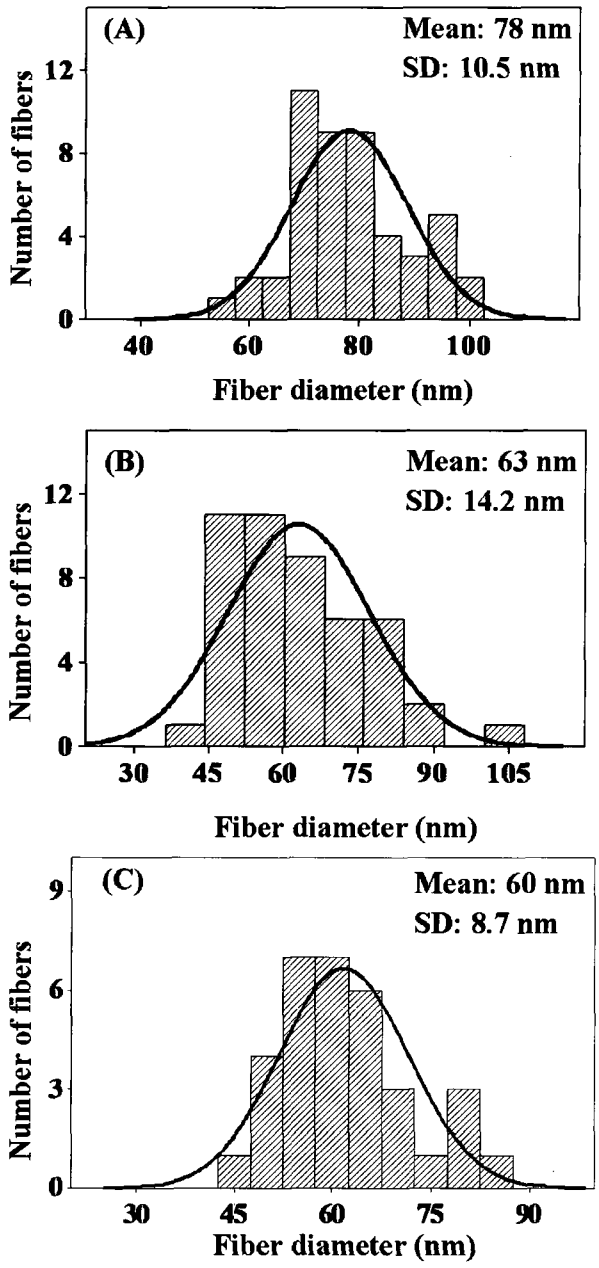

Figure 5.4 Histograms of the nano fibers – Effect of applied potential gradient (A) 1.11 $kV \cdot cm^{-1}$ (B) 1.44 $kV \cdot cm^{-1}$ (C) 1.78 $kV \cdot cm^{-1}$.

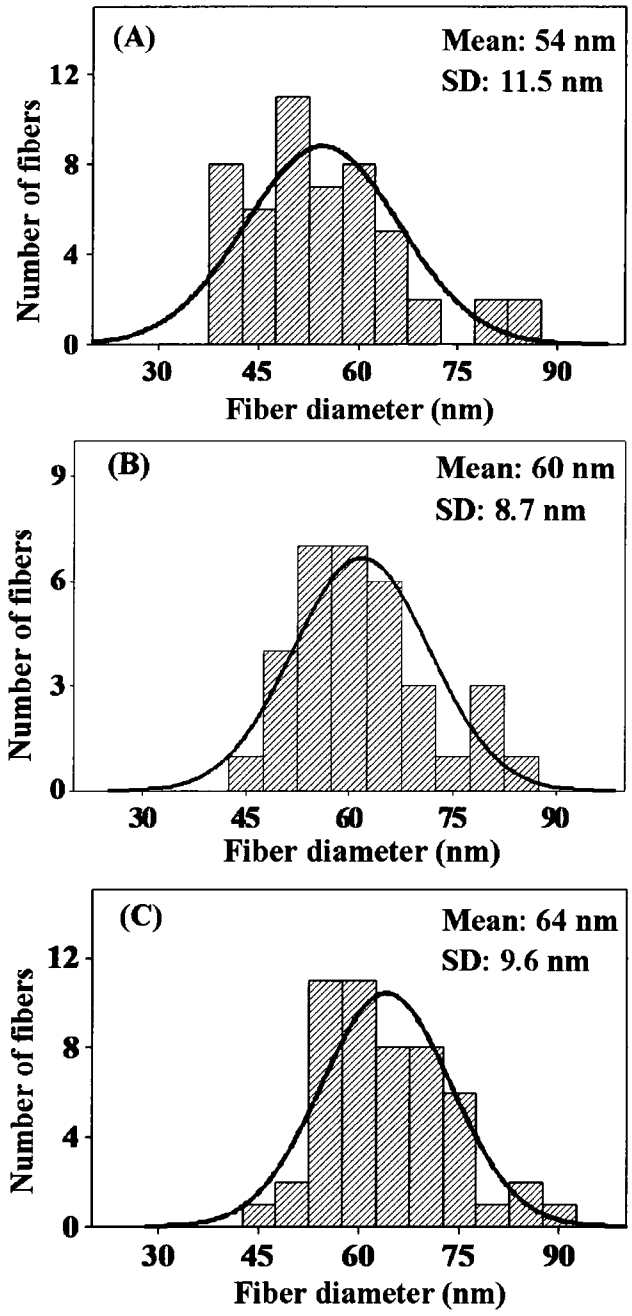

Figure 5.5 Histograms of the nano fibers – Effect of infusion rate
(A) 0.6 ml·h^{-1} (B) 1.8 ml·h^{-1} (C) 3.0 ml·h^{-1}

Restricted mass throughput and instability due to surface tension forces below the lowest infusion rate (< 0.6ml.h^{-1}) resulted a discontinuity in fiber formation. Above the infusion rate of 3.0ml.h^{-1}, instability was observed from fluctuation in droplet size at the needle tip due to

dripping of excess flow of the spinning solution. The most stable electrospinning infusion rate of 1.8ml.h^{-1} was established by the lowest standard deviation of the nanofiber diameters and comparatively higher stability in nanofiber production than at infusion rates of 0.6 and 3.0 ml.h^{-1}.

The effect of three different calcination temperatures (400°, 450°, and 500°C) on the morphology of TiO_2 nanofibers were examined and compared with the TiO_2/PVAc nanocomposite fibers. Figure 5.6(A) showed the FESEM image of the smooth surface of TiO_2/PVAc nanofibers, without any evidence of phase separation. No surface cracks were observed in TiO_2 nanofibers which were calcined at 400°C (Figure 5.6(B)). However, the images of TiO_2 nanofibers calcined at 450°C (Figure 5.6(C)) and 500°C (Figure 5.6(D)) showed visible signs of surface fissures and well developed surface cracks respectively. The structure and surface features of the nanofibers are controlled by the growth of the nanocrystals (Ramaseshan et al., 2007). The development of surface fissures observed in the FESEM images of the TiO_2 nanofibers are well correlated with the growth and sintering of nanocrystals with increasing calcination temperatures (Table 5.2). The surface fissures and aggregation at higher calcination temperature caused the TiO_2 nanofibers to become brittle and difficult to immobilize on the support surface.

The diameters of the TiO_2 nanofibers calcined at 400°, 450°, and 500°C were (a) 54±11.5nm, (b) 50±14.3nm, and (c) 49±15.1nm respectively. The mean fiber diameters recorded for the three calcination temperatures were compared statistically and the results from the t-statistic test showed that differences between the means of the fiber diameter (from three calcination temperatures) were not statistically significant. For the nanofibers calcined at three different temperatures under consideration, the $t_{calculated}$ (1.6 (a-b), 0.3 (b-c) and 1.9 (a-c)) values were

smaller than $t_{tabulated}$ (2.1) for 20 degrees of freedom and 95% level of confidence (Montogomery, 1997).

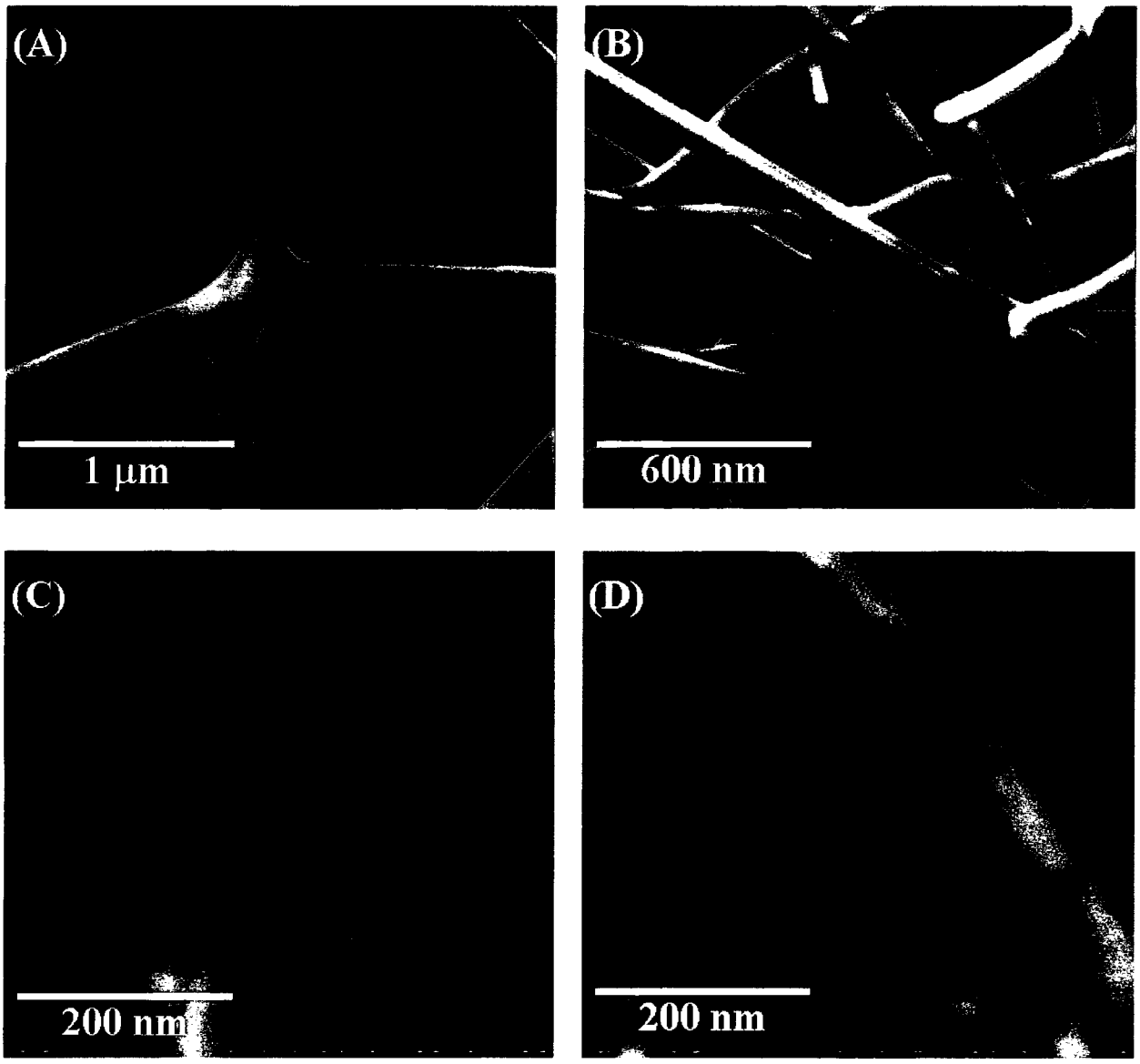

Figure 5.6 FESEM images of the nano fibers – Effect of calcination temperature
(A) TiO_2/PVAc composite (before calcination)
(B) TiO_2 calcined at 400°C
(C) TiO_2 calcined at 450°C
(D) TiO_2 calcined at 500°C

The diameters of the TiO_2 nanofibers generated in the present study were compared with the values of TiO_2 nanofibers reported in the literature sources. The diameters of TiO_2 nanofibers reported by Li and Xia (2003) was the closest to the TiO_2 nanofiber diameter reported in this study. The TiO_2 nanofiber diameter ranged from 30 – 80nm in the study reported by Li and Xia (2003); in comparison, TiO_2 nanofiber with diameters between 28 – 93nm was reported in this study. A comparative t-test was performed with the means reported by Li and Xia (2003) (53±8 nm) with that in the present study (54±11.5nm). The computed t-value (0.55) was smaller than the tabulated t-value (1.98) at 95% level of confidence (Montogomery, 1997). However, in the study of Li and Xia (2003) the TiO_2 nanofibers were in the form of a self supported mat. Madhugiri et al. (2004) reported immobilized TiO_2 nanofibers on aluminum support with diameter greater than 100nm. In another study, Doh et al. (2008) reported immobilized TiO_2 nanofibers on stainless support with a mean diameter of 168±45nm. Tekmen (2008) and Zhang et al. (2009) also reported immobilized TiO_2 nanofibers with diameter 54 - 78nm and 65 – 115 nm respectively. Hence, it is evident that the diameter of immobilized TiO_2 nanofibers fabricated in this study is significantly smaller than the diameter of immobilized TiO_2 nanofibers reported in the literature.

5.3.5. Stoichiometric composition of the TiO_2 nanofibers

The stoichiometric composition of the immobilized (on aluminium foil) nanofibers was established by an energy dispersive spectroscopic (EDS) analysis. Characteristic energy (K) lines (Figure 5.7) for titanium (Ti) and oxygen (O) were observed at 4.51 and 0.53 keV, respectively. Note, a small amount of carbon residue (0.28 keV) and background interference from the aluminum support (1.49 keV) were also identified in the EDS profile. The L-lines for Ti

were noted at 0.46 keV. The cumulative energy counts of the respective elements were translated into relative atomic percentages using GENESIS software. The Ti versus O ratio was computed from the relative atomic percentages. The computed [Ti]/[O] ratio of 0.47 were in agreement with the stoichiometric ratio for TiO_2 (Ti/O = 0.5).

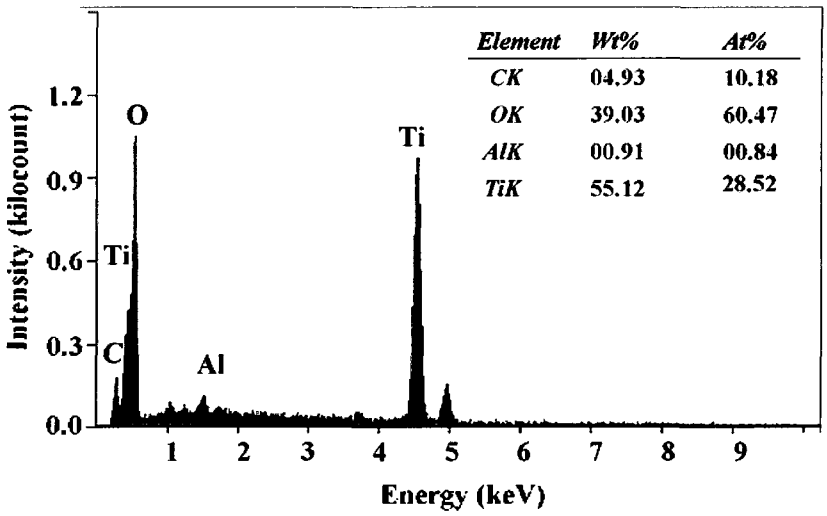

Figure 5.7 EDS profile of the TiO_2 nanofibers calcined at 400°C immobilized on aluminum support

5.3.6. Preparation of catalyst support material

A previous study by Peiró et al. (2002) had shown that Aluminum possesses good adhesion properties for the TiO_2 nanocatalyst. Moreover, it was also reported that surface roughness of the support surface improves the adhesion behavior of the TiO_2 nanocatalyst (Peiró et al., 2002). Hence, aluminum foil (McMaster-Carr, Robbinsville, NJ) with a density of 2.7 g/cm^3 and thickness of 76μm was used as catalyst support after surface treatment. The foil was washed with acetone, then rinsed with de-ionized water and later dried in air at 21°C. The clean aluminum foil was dipped for 30 minutes in an etching solution containing hydrogen peroxide (H_2O_2) and sulphuric acid (H_2SO_4) (Fischer Scientific, Ottawa, ON) at an optimized molar ratio of 0.7 – 0.8

mole H_2O_2 per mole H_2SO_4 (Lalman and Ray, 2009). Dipping the foil in the etching solution created a nano-porous aluminum surface with an anodized oxide layer. The treated foil was removed, washed thoroughly in de-ionized water and air dried at ambient temperature. The surface structure of the aluminum foil material before and after treatment is shown in Figure 5.8 (A and B). The treated aluminum foil with the porous surface and well marked surface roughness was used as support for the TiO_2 nanofibers (refer to Appendix C).

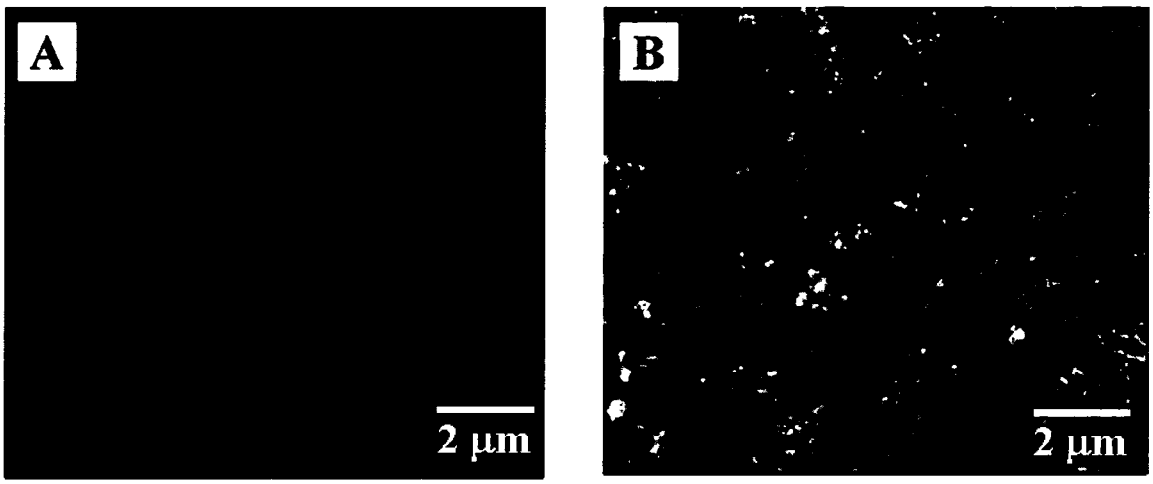

Figure 5.8 Images of aluminum support material, (A) before (B) after, surface treatment

5.3.7. Stability of the immobilized TiO_2 nanofiber catalyst

A study showed that the post-electrospinning treatment of nanofibers with THF improved the adhesion of the TiO_2 nanofibers onto an Aluminum support (Song et al., 2004). The study demonstrated that pre-treating TiO_2/PVAc nanofibers with THF vapors resulted in the formation of a thin film and interconnected bridge between the fibers. This procedure improved the adhesion characteristics of the TiO_2 nanofibers onto the substrate after calcination. However, Song et al. (2004) also reported that the treated fibers lost their fibrous structure. Recently, work by Ding et al. (2004) reported a strong interaction between TIP (sol-precursor for TiO_2) and

PVAc. According to Ding et al. (2004) the interaction between PVAc and TIP resulted in the formation of linking bridges which favored the adhesion of nanofibers onto the support surface. Further details describing the nature of the link had not been reported.

Based on the work reported by Song et al. (2004) and Ding et al. (2004), the surface-treated aluminum foil (decribed in section 5.3.6) was applied with a solution coating prior to electrospinning using a stainless steel doctor's blade which was set at a 45^{o} angle. The solution coating contained PVAc (45% (w/v) in a 3:2 DMF/THF mixture. Figure 5.6(A) showed the presence of interfiber connecting bridges in the electrospun PVAc/TiO_2 nanofibers. To investigate the adhesion property of the nanocatalyst onto the support surface, the tape test according to ASTM standards was performed (ASTM D3359-09-Test Method B, 2009). A moderate to good adherence (10 – 20% affected) of the immobilized electrospun TiO_2 nanofibers on surface-treated aluminum foil was observed (Classification 3B–2B). The immobilized nanocatalyst was also subjected to mechanical agitation in an aqueous medium to test the stability of the immobilized electrospun TiO_2 nanofibers. After stirring magnetically in water at 200-400 rotations per minute for 60 minutes, less than 5% loss in weight was observed for the immobilized nanofiber catalyst.

5.4. Conclusions

An immobilized TiO_2/PVAc nanofiber catalyst was produced by electrospinning a mixture of TIP with PVAc on a surface-treated aluminium foil. Subsequent heating and calcination of a TiO_2/PVAc nanofibers resulted in the formation of pure TiO_2 nanofibers. Thermal transitions of the composite (TiO_2/PVAc) nanofibers were determined by DSC and TGA (equipped with an

MS) studies. A vacuum drying followed by a stepwise calcination program was used to produce TiO_2 nanofibers from the nanocomposite fibers. A calcination temperature of 400°C was selected to produce pure anatase TiO_2 nanofibers. The pure anatase crystal structure of the TiO_2 nanofibers was confirmed by XRD. Aggregation and crystal growth was observed with an increasing calcination temperature. A higher potential gradient and lower infusion rate were observed as favourable for the formation of smaller diameter nanofibers. The diameters of immobilized nanofibers were compared with the literature values. The diameters of the immobilized TiO_2 nanofibers in this study were approximately 30 - 50% smaller than the diameters of the immobilized TiO_2 nanofibers reported in the literature. EDS was used to determine the [Ti]/[O] stoichiometric composition in the TiO_2 nanofibers. Finally, the stability of the immobilized TiO_2 nanofiber catalyst was evaluated. An adherence classification of 3B-2B (ASTM D 3359-09) with less than 5% loss in weight on the simulated catalytic application was observed. Improved adhesion characteristics of the TiO_2 nanofibers on the support material was accounted to the use of a chemically treated support surface.

5.5. References

1. Alves, A.K.; Berutti, F.A.; Clemens, F.J.; Graule, T.; Bergmann, C.P. (2009). Photocatalytic activity of titania fibers obtained by electrospinning. *Mater. Res. Bull.* 44, 312–317.
2. ASTM International (2009). Standard Test Methods for Measuring Adhesion by Tape Test. *D 3359-09*. Test Method B.
3. Ayres, J.; Simendinger, W. H.; Balik, C. M. (2007).Characterization of titanium alkoxide sol–gel systems designed for anti-icing coatings: I. Chemistry. *J. Coat. Technol. Res.*, 4, 463–471.
4. Bach, U.; Lupo, D.; Comte, P.; Moser, J. E.; Weissörtel, F.; Salbeck, J.; Spreitzer, H.; Grätzel, M. (1998). Solid-state dye-sensitized mesoporous TiO_2 solar cells with high photon-to-electron conversion efficiencies. *Nature*, 395, 583 – 585.

5. Baan, R.; Straif, K.; Grosse, Y.; Secretan, B.; El Ghissassi, F.; Cogliano, V. (2006). Carcinogenicity of carbon black, titanium dioxide, and talc. *The Lancet Oncol.*, 7, 295-296.

6. Barbe´, C.J.; Arendse, F.; Comte, P.; Jirousek, M.; Lenzmann, F.; Shklover, V.; Gra¨tzel, M. (1997). Nanocrystalline Titanium oxide electrodes for photovoltaic applications. *J. Am. Ceram. Soc.*, 80, 3157–71.

7. Bhatkhande, D.S.; Pangarkar, V.G.; Beenackers, A.A.C.M. (2001). Photocatalytic degradation for environmental applications - a review. *J. Chem. Technol. Biotechnol.*, 77, 102-116.

8. Blake, D.M. (1999). *Bibliography of work on the heterogeneous photocatalytic removal of hazardous compounds from water and air*. NREL/TP-570-26797. National Renewable Energy Laboratory, Golden, CO, Technical Report, 3, 1 – 7.

9. Carpio, E.; Zuniga, P.; Ponce, S.; Solis, J.; Rodriguez, J.; Estrada, W. (2005). Photocatalytic degradation of phenol using TiO_2 nanocrystals supported on activated carbon. *J. Mol. Catal. A – Chem.*, 228, 293–298.

10. Centi, G.; Perathoner, S. (2009). The Role of Nanostructure in Improving the Performance of electrodes for energy storage and conversion. *Eur. J. Inorg. Chem.* 2009, 3851–3878.

11. Chandrasekar, R.; Zhang, L.; Howe, J.Y.; Hedin, N.E.; Zhang, Y.; Fong, H. (2009). Fabrication and characterization of electrospun titania nanofibers. *J. Mater. Sci.*, 44, 1198–1205.

12. Chen, J-Y.; Chen, H-C.; Lin, J-N.; Kuo, C. (2008). Effects of polymer media on electrospun mesoporous titania nanofibers. *Mat. Chem. Phys.*, 107, 480 - 487.

13. Chien, A-T.; Lee, Y-H.; Lin K-F. (2008). Cross-linkable poly(vinyl acetate)/clay nanocomposite films cast from soap-free emulsion-polymerized lattices. *J. Appl. Polym. Sci.*, 109, 355–362.

14. Chronakis, I.S. (2005). Novel nanocomposites and nanoceramics based on polymer nanofibers using electrospinning process—A review. *J. Mat. Process. Technol.*, 167, 283–293.

15. Cui, X.M.; Nam, Y.S.; Lee, J.Y.; Park, W.H. (2008). Fabrication of zirconium carbide (ZrC) ultra-thin fibers by electrospinning. *Mat. Ltt.* 62, 1961 -1964.

16. Deitzel, J.M.; Kleinmeyer, J.; Harris, D.; BeckTan, N.C. (2001). The effect of processing variables on the morphology of electrospinning nanofibers and textiles, *Polymer,* 42, 261 - 272.

17. Dijkstra, M.F.J.; Michorius, A.; Buwalda, H.; Panneman, H.J.; Winkelman, J.G.M.; Beenackers, A.A.C.M. (2001). Comparison of the efficiency of immobilized and suspended systems in photocatalytic degradation. *Catal. Today*, 66, 487–494.

18. Ding, B.; Kim, J.; Kimura, E.; Shiratori, S.(2004). Layer-by-layer structured films of TiO_2 nanoparticles and poly(acrylic acid) on electrospun nanofibers. *Nanotechnology*, 15, 913–917.

19. Doh, S.J.; Kim, C.; Lee, S.G.; Lee, S.J.; Kim, H. (2008). Development of photocatalytic TiO_2 nanofibers by electrospinning and its application to degradation of dye pollutants. *J. Haz. Mat.*, 154, 118–127.

20. Doshi, J.; Renker, D.H. (1995). Electro spinning process and application of electrospun fibers. *J. Electrostat.*, 35, 151 - 160.

21. Formhals, A. (1934). Process and apparatus for preparing artificial threads; *US Patent* 1,975,504.

22. Frenot, A.; Chronakis, I. (2003). Polymer nanofibers assembled by electrospinning. *Curr. Opin. Colloid Interface Sci.*, 8, 64–75.

23. Fujihara, K.; Kumar, A.; Jose, R.; Ramakrishna, S.; Uchida, S. (2007). Spray deposition of electrospun TiO_2 nanorods for dye-sensitized solar cell. *Nanotechnology*, 18, 1 – 5.

24. Fujishima, A.; Honda, K. (1972). Electrochemical Photolysis of Water at a Semiconductor Electrode. *Nature*, 238, 37-38.

25. Guo, Y-G.; Hu, Y-S.; Sigle, W.; Maier, J. (2007). Superior electrode performance of nanostructured mesoporous TiO_2 (anatase) through efficient hierarchical mixed Conducting Networks. *Adv. Mater.*, 19, 2087–2091.

26. Hamid, M.A.; Rahman, I.A. (2003). Preparation of Titanium Dioxide (TiO_2) thin films by sol gel dip coating method. *Malay. J. Chem.*, 5, 1, 086 – 091.

27. He, J-H.; Xu, L.; Wu, Y.; Liu, Y. (2007). Review: Mathematical models for continuous electrospun nanofibers and electrospun nanoporous microspheres. *Polym. Int.*, 56, 1323–1329.

28. Holland, B.J.; Hay, J.N. (2002). The thermal degradation of poly (vinyl acetate) measured by thermal analysis – Fourier transform infrared spectroscopy. *Polymer*, 43, 2207 – 2211.

29. Houari, M.; Saidi, M.; Tabet, D.; Pichat, P.; Khalaf, H. (2005). The Removal of 4-chlorophenol and Dichloroacetic Acid in Water Using Ti-, Zr- and Ti/Zr-Pillared Bentonites as Photocatalyst. *Am. J. Appl. Sci.*, 2, 1136-1140.

30. Ibañez, P.F.; Malato, S.; Enea, O. (1999). Photoelectrochemical reactors for the solar decontamination of water. *Catal. Today*, 54, 329–339.

31. Jo, S.M.; Song, M.Y.; Ahn, Y.R.; Park, C.R.; Kim, D.Y. (2005). Nanofibril Formation of electrospun TiO_2 fibers and its application to dye-sensitized Solar cells. *J. Macromol. Sci., Pure Appl. Chem.*, 42, 1529–1540.

32. Jo, S.M.; Kim, D.K.; Jang, S.Y.; Park, N.G.; Yi, B.H. (2009). Dye-sensitized solar cell with metal oxide layer containing metal oxide nanoparticles produced by electrospinning and method for manufacturing same. *EU Patent* 2,031,613.

33. Johannes, S.; Krol Roel, V.D.; Sander T.H. (2007). Nanosized catalysts for the anode of a PEM fuel cell. *EU Patent* 1,808,920.

34. Kokubo, H.; Ding, B.; Naka, T.; Tsuchihira, H.; Shiratori, S. (2007). Multi-core cable-like TiO_2 nanofibrous membranes for dye-sensitized solar cells. *Nanotechnology*, 18, 1- 6.

35. Lalman, J.A.; Ray, S. (2009). Method of surface treatment of Aluminum foil and its alloy and method of producing immobilized nanocatalyst of transition metal oxides and their alloys, *US Patent 61/272,518* (Provisional).

36. Li, D.; Xia, Y. (2003). Fabrication of titania nanofibers by electrospinning. *Nano Lett.*, 3, 555 -560.

37. Madhugiri, S.; Sun, B.; Smirniotis, P.G.; Ferraris, J.P.; Balkus (Jr), K.J. (2004). Electrospun mesoporous titanium dioxide fibers. *Microporous Mesoporous Mater.*, 69, 77–83.

38. Matthews, R.W.; McEvoy, S.R. (1992). Photocatalytic degradation of phenol in the presence of near-UV illuminated titanium dioxide. *J. Photochem. Photobiol. A: Chem.*, 64, 231-246.

39. Montogomery, D.C. (1997). *Design and analysis of experiments*, fourth ed., John Wiley and Sons, New York, NY. pp. 660 (ISBN 0-471-15746-5).

40. Nuansing, W.; Ninmuanga, S.; Jarernboon, W.; Maensiri, S.; Seraphin, S. (2006). Structural characterization and morphology of electrospun TiO_2 nanofibers. *Mat. Sci. Eng. B.*, 131, 147 – 156.

41. Ollis, D. F.; Pelizzetti, E.; Serpone, N. (1991). Photocatalyzed destruction of water contaminants. *Environ. Sci.Technol.* 25, 1522-1529.

42. Peiró, A.M.; Brillas, E.; Peral, J.; Domènech, X.; Ayllón, J.A. (2002). Electrochemically assisted deposition of titanium dioxide on aluminium cathodes. *J. Mater. Chem.*, 12, 2769–2773.

43. Pozzo, R.L.; Baltanfis, M.A.; Cassano, A.E. (1997). Supported titanium oxide as photocatalyst in water decontamination: State of the art. *Catal. Today*, 39, 219-231.

44. Qiao, Y.; Bao, S-J.; Li, C.M.; Cui, X-Q.; Lu, Z-S.; Guo, J. (2008). Nanostructured polyaniline/titanium dioxide composite anode for microbial fuel cells. *Nano*, 2, 113–119

45. Ramaseshan, R.; Sundarrajan, S.; Jose, R.; Ramakrishna, S. (2007). Nanostructured ceramics by electrospinning. *J. App. Phys.*, 102, 1-17.

46. Ray, S.; Lalman, J.A.; Biswas, N. (2009). Using the Box-Benkhen technique to statistically model phenol photocatalytic degradation by titanium dioxide nanoparticles. *Chem. Eng. J.*, 150, 1, 15-24.

47. Reneker, D.H; Chun, I. (1996). Nanometre diameter fibres of polymer, produced by electrospinning. *Nanotechnology* 7, 216 – 223.

48. Reneker, D.; Chase, G.; Kataphinan, W.; Katta, P. (2008). Flexible ceramic fibers and process for making the same, *US Patent* 2008/0242178.

49. Sankapal, B.R. ; Sartale, S.D. ; Lux-Steiner, M.C. ; Ennaoui, A. (2006). Chemical and electrochemical synthesis of nanosized TiO_2 anatase for large-area photon conversion. *C. R. Chimie*, 9, 702–707.

50. Santana-Aranda, M.A.; Morán-Pineda, M.; Hernández, J.; Castillo, S. (2005). Physical properties of TiO_2 prepared by sol-gel under different pH conditions for photocatalysis. *Superficies y Vacío* 18, 46-49.

51. Sathyamoorthy, R.; Sudhagar, P.; Chandramohan, S.; Vijayakumar, K. P. (2007). Photoelectrical properties of crystalline titanium dioxide thin films after thermo-annealing. *Cryst. Res. Technol.*, 42, 498 – 503

52. Scotti, R.; D'Arienzo, M.; Morazzoni, F.; Bellobono, I.R. (2009). Immobilization of hydrothermally produced TiO_2 with different phase composition for photocatalytic degradation of phenol. *Appl. Catal. B – Environ.*, 88, 323-330.

53. Sheikh, F.A.; Barakat, N.A.M.; Kanjwal, M.A.; Chaudhuri, A. A.; Jung, I-H.; Lee, J. H.; Kim, H. Y. (2009). Electrospun antimicrobial polyurethane nanofibers containing silver nanoparticles for biotechnological applications. *Macromol. Res.*, 17, 688 – 696.

54. Sigmund, W.; Yuh, V.; Park, H.; Maneeratana, V.; Pyrgiotakis, G.; Daga, A.; Taylor, J.; Nino, J. C. (2006). Processing and structure relationships in electrospinning of Ceramic Fiber Systems. *J. Am. Ceram. Soc.*, 89, 395–407.

55. Song, M.Y.; Kim, D.K.; Ihn, K.J.; Jo, S.M.; Kim, D.Y. (2004). Electrospun TiO_2 electrodes for dye-sensitized solar cells. *Nanotechnology*, 15, 1861–1865.

56. Song, M.Y.; Kim, D.K.; Ihn, K.J.; Jo, S.M.; Kim, D.Y. (2005). New applications of electrospun TiO_2 electrode to solid-state dye-sensitized solar cells. *Syn. Met.*, 153, 77-80.

57. Subbiah, T.; Bhat, G.S.; Tock, R.W.; Parameswaran, S.; Ramkumar, S. S. (2005). Electrospinning of nanofibers. *J. Appl. Polym. Sci.*, 96, 557–569.

58. Tan, S-H.; Inai, R.; Kotaki, M.; Ramakrishna, S. (2005). Systematic parameter study for ultra-fine fiber fabrication via electrospinning process. *Polymer*, 46, 6128–6134

59. Tekmen, C.; Suslu, A.; Cocen, U. (2008).Titania nanofibers prepared by electrospinning. *Mat. Ltt.*, 62, 4470 - 4472

60. Viswanathamurthi, P.; Bhattarai, N.; Kim, C.K.; Kim, H.Y.; Lee, D.R. (2004). Ruthenium doped TiO_2 fibers by electrospinning. *Inorg. Chem. Commun.*, 7, 679 – 682.

61. Zhan, S.; Chen, D.; Jiao, X.; Tao, C. (2006). Long TiO_2 hollow fibers with mesoporous walls: sol-gel combined electrospun fabrication and photocatalytic properties. *J. Phys. Chem. B.*, 110, 11199-11204.

62. Zhang, X.; Xu, S.; Han, G. (2009). Fabrication and photocatalytic activity of TiO_2 nanofiber membrane, *Mat. Lett.*, 63, 1761–1763.

CHAPTER 6: DEVELOPING A STATISTICAL MODEL TO PREDICT THE DIAMETER OF ELECTROSPUN TITANIUM DIOXIDE NANOFIBERS USING BOX-BENKHEN DESIGN

6.1. Introduction

Upon illumination with light of specific wavelengths Titanium dioxide (TiO_2) generates highly reactive, free charge carriers (electron-hole pairs) (Linsebigler et al., 1995; Bhatkhande et al., 2001; Shah et al., 2002). The photo-generated charge carriers migrate to the TiO_2 surface and initiate oxidation-reduction reactions (Fujishima and Honda, 1972; Ollis et al., 1991; Barbe´ et al., 1997; Bach et al., 1998). In catalytic applications, the oxidation-reduction reactions are utilized to generate hydroxyl radicals ($^{\bullet}OH$) which mediate the oxidative degradation of organic contaminants (Matthews, 1992; Lee and Mills, 2004; Gogate and Pandit, 2004; Herrmann, 2005). Thus, generation of $^{\bullet}OH$ radicals in TiO_2 mediated photocatalysis is attributed to the semiconductor bandgap of TiO_2. The bandgap energy (E_g) of TiO_2 originates from the energy difference between the valance band (VB) and conduction band (CB) in its valance electron configuration. Other merits of TiO_2 include chemical inertness, lower biological toxicity, excellent photo-stability and high relative abundance (Rajeshwar, 1995; Bhatkhande et al., 2001; Carp et al., 2004; Herrmann, 2005).

Many studies have reported that the high catalytic surface area is a major reason for improved photocatalytic efficiency (Shah et al., 2002; Carp et al., 2004; Allen et al., 2004; Hurum et al., 2006). TiO_2 nanoparticles have large catalytic surface areas by virtue of their very small particle size. Hence, over the past few years several nanometer size TiO_2 formulations have been manufactured and tested for their photocatalytic potential (Bhatkhande et al., 2001;

Lee and Mills, 2004; Allen et al., 2004). In many of the reported photocatalytic applications TiO_2 nanoparticles have been used as slurry (Matthews and McEvoy, 1992; Blake, 2001; Bhatkhande et al., 2001; Lee and Mills, 2004). However, using nanoparticles in form of slurries are associated with severe practical constraints. The problems include poor settling tendency of nanoparticles, the need for solid/liquid separation to minimize catalyst loss, and human health hazards associated with fugitive emission of nanoparticles during slurry preparation (Ibañez et al., 1999; Houari et al., 2005; Baan et al., 2006). Immobilizing TiO_2 nanoparticles onto a support medium can potentially eliminate many problems associated with the use of nanoparticles in the form of slurries (Carp et al., 2004; Houari et al., 2005).

Dispersion of nanometre-sized particles on a high-surface-area support is a popular method of producing a high surface area supported catalyst system (Houari et al., 2005). However, a major bottleneck of this method is related to the loss of surface area caused by the sintering or aggregation of the nanoparticles onto the support surface during the thermal treatment (Ibañez et al., 1999). Particle sintering results in formation of a film or sheet on the support surface and the resultant supported catalyst system has a catalytic surface area smaller than that of discrete nanoparticles by a few orders of magnitude (Carp et al., 2004). Hence, developing an immobilized TiO_2 nanocatalyst system with surface area comparable to that of discrete nanoparticles is a research priority for enhanced catalytic performance.

The electrospinning process has been reportedly utilized to fabricate ultra thin fibers from a broad range of polymers (Subbiah et al., 2005). Recently, electrospinning has been extended to fabricate TiO_2 nanofibers through coupling with a sol-gel TiO_2 synthesis technique. The sol-gel technique involves the formation of TiO_2 from an organo-titanium salt precursor.. TiO_2 nanofibers are produced in a two step process. In the first stage, nanofibers are generated by

electrospinning a solution of a polymer mixed with the sol-gel precursor, and in the second stage, the composite nanofibers are subjected to a thermal treatment to obtain pure TiO_2 nanofibers (Li and Xia, 2003; Viswanathamurthi et al., 2004). The diameter, surface morphology and crystal structure of the electrospun TiO_2 nanofibers are affected by the characteristics of the spinning solution, electrospinning process variables, and conditions of thermal treatment (Chronakis, 2005; Watthanaarun et. al., 2005).

For a typical electrospinning process, the nanofiber diameters are strongly influenced by electrospinning process variables (Watthanaarun et. al., 2005; Sigmund et al., 2006). The effect of the electrostatic potential on diameters of polyvinylpyrrolidone-TiO_2 composite nanofibers was studied by Watthanaarun et al. (2005). The flow rates (infusion rates) of the electrospinning solution (Frenot and Chronakis, 2003) and separation distance between electrodes (Deitzel et. al., 2001a; Deitzel et. al., 2001b) have reportedly affected the fiber diameters for polyethylene oxide (PEO) nanofibers. The solution viscosity is also known to affect the nanofiber formation in electrospinning process. But to maintain the continuity of fiber formation the viscosity of the polymer solution is expected to be in the range of 130-160 centipoise (cps) (Cui et. al., 2008). The maximum post-electrospinning temperature is limited by the pyrolytic degradation of the carrier polymer and by the transformation of TiO_2 crystal from anatase to rutile form (Nuansing et. al., 2006). The growing interest in high surface area nanometric anatase TiO_2 for enhanced photocatalytic performance (Ding et al., 2004; Sigmund et al., 2006; Kumar et al., 2007) is a major reason for developing an approach which can simultaneously examine the impact of various electrospinning variables on the diameter of TiO_2 nanofibers.

The one-factor-at-a-time (OFAT) approach is a complex method to evaluate the effects of different variables on an experimental outcome. This approach assesses one factor at a time

instead of all the factors simultaneously. The OFAT approach is time-consuming, expensive and often leads to misinterpretation of results when interactions between different factors are significant (Myer and Montogomery, 2002; Ray, 2006). An alternative approach of accurately evaluating the impact of the variables on the process response (nanofiber diameter) is to vary all the factors simultaneously in a systematic manner using a statistical experimental design. Additionally, a polynomial model can be developed using the statistical experimental design procedure (Box et. al., 1978; Box and Draper, 1987).

Among the available experimental design methods, a full factorial design (FFD) is often considered impractical due to its requirement for a large number of experiments. Based upon the desirable feature of accurate prediction throughout the factor space, Central-Composite design (CCD) and Box-Benkhen design (BBD) are commonly selected experimental design procedures (Box and Draper, 1987; Myer and Montogomery, 2002; Bae and Shoda, 2005; Ray, 2006). However, for a quadratic model with three or more factors the BBD procedure is more advantageous than the CCD (Myer and Montogomery, 2002; Bae and Shoda, 2005).

The present study is focused on implementing the BBD procedure for the optimization of the electrospinning variables in order to fabricate TiO_2 nanofiber with smallest diameter possible. Three electrospinning process variables included in the study were the potential difference across electrodes, the infusion rate of the electrospinning solution, and the separation distance of the electrodes.

6.2. Materials and methods

6.2.1. Electrospinning apparatus

The electrospinning apparatus used in this study is shown in Figure 5.1 and a detailed desription of the instrument is presented in Chapter 5, Section 5.2.1. In short, the electrospinning apparatus consisted of a pumping system which was capable of delivering the viscous electrospinning solution at a specific flow rate and a variable high voltage power supply. The lowest flow capability of the delivery system was 0.03±0.001 µl/min. The delivery rate of the electrospinning solution was hereafter referred to as the infusion rate. The variable high voltage DC power supply was capable of producing a potential difference in the order of 0-50 kV. The positive (anode) terminal of a variable high voltage power supply was attached to the metallic needle of the solution delivery system, and the ground terminal (negative) was connected to the solid support material (cathode) for collecting the nanofibers. The distance of separation of the two electrodes (needle tip to the surface of the support) in the electrospinning apparatus was a variable and denoted as the separation distance. Based on the research presented in Chapter 5, Section 5.3.7 and 5.3.8, a chemically etched surface-treated aluminum foil (Lalman and Ray, 2009) was used as support material (collector plate) for the electrospun TiO_2 nanofibers.

Table 6.1: Factors and levels selected for the experimental study

Factors levels	Potential difference (kV)	Infusion rate (ml/h)	Separation distance (cm)
1	25	0.6	12.5
2	32.5	1.8	22.5
3	40	3.0	32.5

6.2.2. Experimental design and model development

A three factor three level BBD having three central points was used to examine the factor space, defined by the levels of the electrospinning variables, for minimum response output (TiO_2 nanofiber diameter (nm)). Three experimental factors (electrospinning variables) namely, potential difference across electrodes (denoted as potential difference), infusion rate of the electrospinning solution (denoted as infusion rate), and separation distance of the electrodes (denoted as separation distance) were evaluated at three levels: minimum or low level (denoted as 1), a central or medium level (denoted as 2), and a high or maximum level (denoted as 3) (Table 6.1).

Three levels of the potential difference were distributed between 25kV and 40 kV. The levels of the separation distance were chosen within a range of 12.5–32.5 cm. Below the lowest value of potential difference (< 25kV), fiber formation was not observed as the applied potential was lower than the opposing forces acting on the solution droplet at the needle tip. Similarly, above the highest separation distance (>32.5 cm), the electrical potential across electrodes was insufficient to draw a continuous strand of fluid jet across the electrodes, and the fiber formation was discontinuous. Beyond the highest value of potential difference (> 40kV) and lowest separation distance (12.5 cm), electrical arcs were observed between the electrodes as the static potential exceeded the resistance of the enclosed air inside the chamber. The infusion rate was adjusted between 0.6-3.0 $ml \cdot h^{-1}$. An infusion rate below 0.6 $ml \cdot h^{-1}$ resulted in the discontinuity of fiber formation because of insufficient fluid flow. The fiber formation above the infusion rate of 3.0$ml \cdot h^{-1}$ was transient as the infusion rate was too high for a solution drop to stay at the needle tip.

The factors and associated levels for the BBD are presented in Table 6.1. The design points of the BBD were chosen to evaluate a full quadratic model for the response function (nanofiber diameter (nm)). The experiments were conducted under factor-level conditions defined in Table 6.2. The effects of process factors other than the three, which were selected for the experimental design, were considered as an error for the experimental design under examination. The experimental error was assumed to be random and, therefore, the error can be considered estimable through replicate study at the design center. Three experiments were conducted at the design centre (Expt. 13, 14 and 15) to estimate the magnitude of error in the experimental analysis. The experiments were performed in a random manner in order to avoid any systematic bias in the outcomes.

Table 6.2: Design matrix for experimental factors and response at different factor levels.

	Experimental factors			**Response**		
				TiO_2 fiber diameter		
Expt. order	**Potential difference (kV)**	**Infusion rate ($ml \cdot h^{-1}$)**	**Separation distance (cm)**	**Rep 1 (nm)**	**Rep 2 (nm)**	**Rep 3 (nm)**
1	25	0.6	22.5	80.1	75.7	83.8
2	40	0.6	22.5	62.6	59.6	56.8
3	25	3	22.5	87	93.5	93.3
4	40	3	22.5	60.1	61.1	65.6
5	25	1.8	12.5	84.5	78.1	81.7
6	40	1.8	12.5	68.5	64.1	63.6
7	25	1.8	32.5	72.3	77.2	70.6
8	40	1.8	32.5	53.8	51.4	50.5
9	32.5	0.6	12.5	68.7	66.7	69.9
10	32.5	3	12.5	74.5	78.7	80.1
11	32.5	0.6	32.5	50.8	52.4	54.2
12	32.5	3	32.5	66.2	62.8	65.4
13	32.5	1.8	22.5	60.1	59	65.8
14	32.5	1.8	22.5	60.1	61.5	60.3
15	32.5	1.8	22.5	63.3	65.3	65.6

A multiple regression analysis (method of least square) was performed to compute the model terms from the experimental data (Box and Draper, 1987). The analysis of variance (ANOVA) was conducted with the experimental response to evaluate the full quadratic approximation of the BBD response surface model. The curvature of the response surface was determined from the order of the response surface model (Box et al., 1978).

An optimization analysis was performed to locate the optimal design points for the response surface model excluding the statistically insignificant terms from the full quadratic model. The design points for an accurate response prediction were identified using an optimality criterion. The optimality criterion provided a measure of fitting the data and it was used to evaluate the accuracy of the experimental design (Box and Draper, 1987). Computing the D-optimality value had been reported as a popular optimization method (Redhe et al., 2002). A numerical algorithm was used in the study to calculate the D-optimality value for all design points of the full quadratic model under evaluation. The D-optimality criterion minimized the variance among the regression coefficients of the fitted model and defined the optimal design points for an accurate prediction of the response within the factor-space under evaluation (Titterington, 1975). In the present study, an algorithm from the MINITAB statistical software (Version 15) (Minitab Inc., State College, PA) was used to identify the optimal design points for the response surface prediction. The final response surface model was further refined by deleting the terms which were associated with a level of significance greater than 5% ($p > 0.05$) from the quadratic model (Box and Draper, 1987).

The model was verified through the analysis of residuals. The residuals were defined as the difference between the model predicted value and the experimental outcome at identical factor levels within the design space under consideration (Myer and Montogomery, 2002; Box and

Draper, 1987). For a well predicted model, the residuals were expected to follow a normal distribution (occurrences are random) (Box and Draper, 1987). The Anderson-Darling (AD) test is a statistical tool that was used to quantify the deviation for a set of residuals from a normal distribution. The validity of the distribution of residuals in the AD test at a 5% level of significance confirmed the model accuracy (Stephens, 1974).

6.2.3. Electrospinning

Titanium tetraisopropoxide (TIP), an organo-titanium sol-gel precursor of TiO_2 (> 99.95% purity) and polyvinyl acetate (PVAc (average molecular weight (M_w) 50,000 Daltons)), a carrier for the TIP, were purchased from Alfa Aesar (Ward Hill, MA). Acetic acid (>99% purity), a stabilizer for sol-gel conversion of TIP, was procured from EMD (Gibbstown, NJ). Dimethylformamide (DMF) and tetrahydrofuran (THF), solvents were supplied by Fischer Scientific (Ottawa, ON).

TIP was stabilized with glacial acetic acid in a molar ratio of 1: 4 mole TIP per mole acetic acid under slow stirring conditions (Solution A). A 45% (weight per unit volume (w/v)) solution of PVAc was prepared by dissolving polymer beads in 3:2 volumetric mixtures of DMF and THF (Solution B). The electrospinning mixture (Solution C) was prepared by mixing the TIP solution (Solution A) with 45% PVAc (w/v) solution (Solution B).

Jo et al. (2005) observed that TIP/PVAc ratio or the Ti-content was the one most important electrospinning solution parameter which determined the morphology of the nanofibers. Hence, the Ti-content of the electrospinning solution was varied by mixing various proportions of the TIP solution (Solution A) with Solution B. Jo et al. (2005) also reported that roughened fiber morphology with a reduced diameter was associated with lower Ti-content. The lowest Ti-

content reported by Jo et al. (2005), which resulted in TiO_2 fibers with diameter of approximately 100nm, was 7.0% (weigh/weight (w/w)). In the present study, Ti-contents lower than 7.0% were examined. Ti-content was varied at three levels 1.3%, 2.6%, and 3.9%. Beyond the lowest Ti-content (1.3%) sol-gel conversion was very slow and the nanofibers disintegrated during electrospinning. Above the highest level of Ti-content (3.9%) the electrospinning was discontinuous at the lowest level of infusion rate (0.6 $ml \cdot h^{-1}$) due to rapid sol-gel conversion and solidification at the needle tip.

The syringe containing the electrospinning solution (Solution C) was placed in the syringe pump and the infusion rate of the pump was adjusted to a desired value (Table 6.2). The solution was delivered at a constant flow rate to the stainless steel needle connected to the positive terminal of the high voltage DC power supply. The ground terminal was attached to the surface-treated aluminum support and positioned at a specific level (separation distance = 12.5 to 32.5 cm) (Table 6.2). Upon applying a potential difference within 25-40 kV (level defined in Table 6.2) to the needle tip, a fluid jet ejected from the capillary tip. After an initial instability period of few seconds, a steady fluid jet headed for the grounded support. As the jet accelerated towards the support, the solvent evaporated and a charged TiO_2/PVAc composite fiber was deposited on the solid support.

The TiO_2/PVAc composite fiber was subjected to the vacuum drying (105°C under a vacuum of 600mm Hg for 2 hours) and later, slow heating and calcination in air to eliminate the polymer backbone from the nano-composite fiber. Eventually an immobilized TiO_2 nanofiber catalyst was obtained (Renekar *et al.*, 2008; Zhang *et al.*, 2009). The heating program confirmed in thermal characterization study presented in Chapter 5, Section 5.3.1, was followed to fabricate the immobilized TiO_2 nanofiber catalyst. The specimen was heated at the rate of 1.5°C/min in a

temperature programmable oven to 300°C, and thereafter, it was calcined in a muffle furnace set at 400 °C for an additional 2 hours. The immobilized nanofiber sample was then cooled to ambient temperature, cleaned with a gentle stream of clean dry air (to strip-off the loose particles attached on the surface of the catalyst), and rinsed in ultrapure water to remove any remaining polymer ash. The supported TiO_2 nanofibers were then dried at 105°C and examined for fiber diameter using microscopic imaging techniques.

6.2.4. Analytical measurements used to characterize the TiO_2 nanocatalyst

Images of the TiO_2 nanocatalyst were obtained using a field emission scanning electron microscope (FESEM) (Quanta 200, FEI Company, Hillsboro, OR). An additional detail of the instrument is presented in Chapter 5, Section 5.2.4. The specific surface area (m^2/g) of the immobilized TiO_2 nanofibers was determined using the Brunauer-Emmett-Teller (BET) gas adsorption technique according to the procedure desctribed in Chapter 3, Section 3.2.3.

6.3. Results and discussions

6.3.1. Effect of electrospinning process variables on nanofiber diameters

The effect of three experimental factors, potential difference, infusion rate and separation distance on the diameter of the electrospun TiO_2 nanofibers were evaluated at different experimental levels tabulated in Table 6.1. The ejection of fluid jet and formation of nanofibers was a process which involved a complex force balance. The applied electrical potential resulted in an electrical polarization stress which tends to elongate the fluid drop accumulated at the needle tip. The viscous drag resisted the electrical stretching force and surface tension opposes the electrostatic repulsive force. Beyond the point, where the electrostatic force overcame the

surface tension barrier, a charged fluid jet was ejected from the needle tip and accelerated towards the grounded cathode. During the flight, the charged fluid jet encountered bending instability due to columbic repulsion between the charged sections of the jet. The bending instability was responsible for the stretching of the solidifying strand (Reneker et. al., 2000; Yarin et. al., 2001; Shim et. al., 2001; Sigmund et al., 2006). Thus, an inverse relationship exists between the diameter of the nanofibers and the applied potential difference across electrodes (kV). In accordance with the theory, a decrease in the fiber diameter was observed with increasing potential difference (Figure 6.1(A)). When the applied electrostatic force (under lower applied potential) struggled to overcome the surface tension barrier a higher variability of the fiber diameters was observed due to non-uniformity in the ejected fluid jets.

Increase in the infusion rate ($ml \cdot h^{-1}$) directly translated into higher mass throughput at the needle tip. Thus, the fiber formation ceased below a certain mass throughput rate ($< 0.6\ ml \cdot h^{-1}$) under a specific applied electrostatic potential. Fiber formation at the highest level of infusion rate ($> 3.0\ ml \cdot h^{-1}$) was disturbed by gelation and solidification of accumulated sol solution at the needle tip. At the lower infusion rate of $0.6\ ml.h^{-1}$, restricted mass throughput and instability due to surface tension (Rayleigh instability) of the fluid resulted in a higher variation of the fiber diameter (Figure 6.1(B)). The most stable electrospinning of nanofibers were observed near the middle setting of the infusion rate ($1.8\ ml.h^{-1}$).

A higher separation distance between electrodes resulted in longer travelling time for the charged jet ejected from needle tip. Consequently, a larger separation distance caused the electrospun fibres to become more elongated. Also, a longer travel time of the fluid jet was favourable towards a greater loss of solvents and improved sol-gel conversion. Thus, an inverse

relationship between the separation distances and diameter of nanofibers was also observed. Smaller diameter nanofibers were produced as the separation distance increased (Figure 6.1(C)).

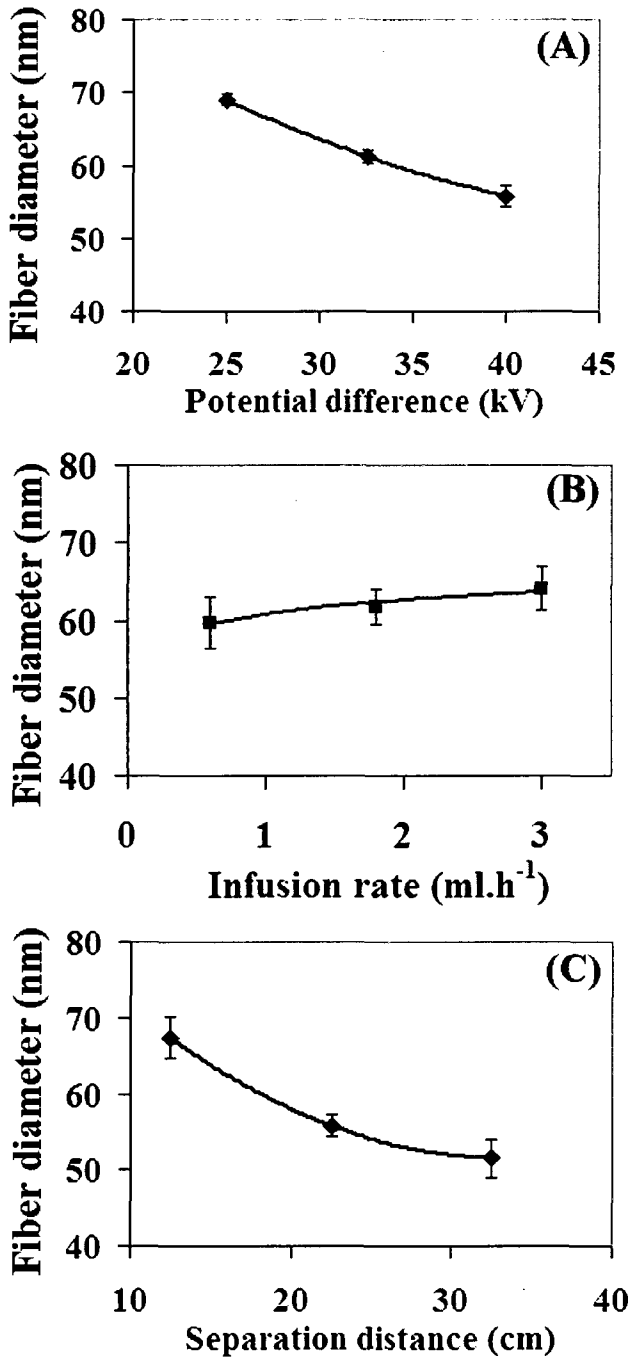

Figure 6.1 Main effect plot of electrospinning process variables on nanofiber diameter (A) Potential difference; (B) Infusion rate; (C) Separation distance [Average with standard deviation (SD) for triplicate samples are shown]

6.3.2. Response surface analysis

For the response surface analysis, the TiO_2 nanofibers were generated at each design point of the three factors (potential difference (kV), infusion rate ($ml.h^{-1}$) and separation distance (cm)) and three levels (high (3), medium (2) and low (1)) of the BBD (Table 6.2). Considering this design, three replicates sets (blocks) of 15 experiments were performed. The diameters of TiO_2 nanofibers from each experiment were measured. The diameter of the TiO_2 nanofiber was considered as the response variable, and the data was statistically treated to develop a response surface model (RSM). The experimental response for the design with the natural level of the experimental factors in form of a matrix is presented in Table 6.2. A quadratic model described by Equation 6.1 was used to express the factors as a function of the fiber diameter. In Equation (6.1), a_0 to a_9 are regression coefficients for the respective model terms. The potential difference across electrodes is denoted as "kV", infusion rate as "$ml{\cdot}h^{-1}$", and separation distance between the electrodes is expressed as "cm"

$$\begin{aligned} TiO_2 \text{ fiber diameter (nm)} = {} & a_0 + a_1 \times (kV) + a_2 \times \left(ml \cdot h^{-1} \right) + a_3 \times (cm) \\ & + a_4 \times (\text{kV})^2 + a_5 \times \left(ml \cdot h^{-1} \right)^2 + a_6 \times (cm)^2 \\ & + a_7 \times (kV) \times \left(ml \cdot h^{-1} \right) + a_8 \times (kV) \times (cm) + a_9 \times \left(ml \cdot h^{-1} \right) \times (cm) \end{aligned} \tag{6.1}$$

Three dimensional (3D) surface plots of the response variable (fiber diameter (nm)) for the experimental factors (two-factor-at-a-time) are represented in Figure 6.2 (A-C). The surfaces in the 3D plots were developed by connecting the points of equal response (equal fiber diameter). The 3D surface plot of the potential difference versus the infusion rate (Figure 6.2(A)) showed that highest potential difference (40 kV) with lowest value for the infusion rate (0.6 $ml{\cdot}h^{-1}$) was able to produce the smallest diameter nanofibers. The change in the infusion rate resulted in a

reduction of the fiber diameter. These observations were in contradiction with the results of the OFAT study, where the relation between the fiber diameter and the infusion rate was not apparent (Figure 6.1(B)). These further explained the significance of the comprehensive analysis of the experimental variables in a BBD presented in this paper. A non-linear relationship of the response (fiber diameter) with the variable (infusion rate) was predicted from the curvature of the response surface. Irrespective of the level of potential difference, an increase in the separation distance favoured the formation of smaller diameter fibers. However, a combination of the higher potential difference (40 kV) and longer separation distance (32.5 cm) was best suitable for the formation of smaller diameter fibers (Figure 6.2(B)). At higher potential differences, the variability among the ejected section of the fluid jet from needle tip was minimum (as surface tension barrier was subdued and time available for gelation at needle tip was insufficient), hence thinning of ejected jets were solely controlled by the time of flight of the jet between needle tip and the collector plate. Accordingly, longer separation distance (longer time of flight) at higher potential difference values produced finer nanofibers (smaller diameter). The response surface in Figure 6.2(C) showed that at lower separation distance, where the electrostatic gradient (kV per cm) was high, the effect of variation on the infusion rate was less marked. Larger time of flight of fluid jets at higher separation distance and lower infusion rate produced smaller diameter nanofibers. Note, at higher potential difference, electrospinning was less sensitive to variation in infusion rate and smooth ejection of fluid jets from needle tip was favoured. However, diameter reduction of the ejected jets (stretching of the jets) was essentially controlled by longer time of flight, *ie.* longer separation distance (between the tip and collector).

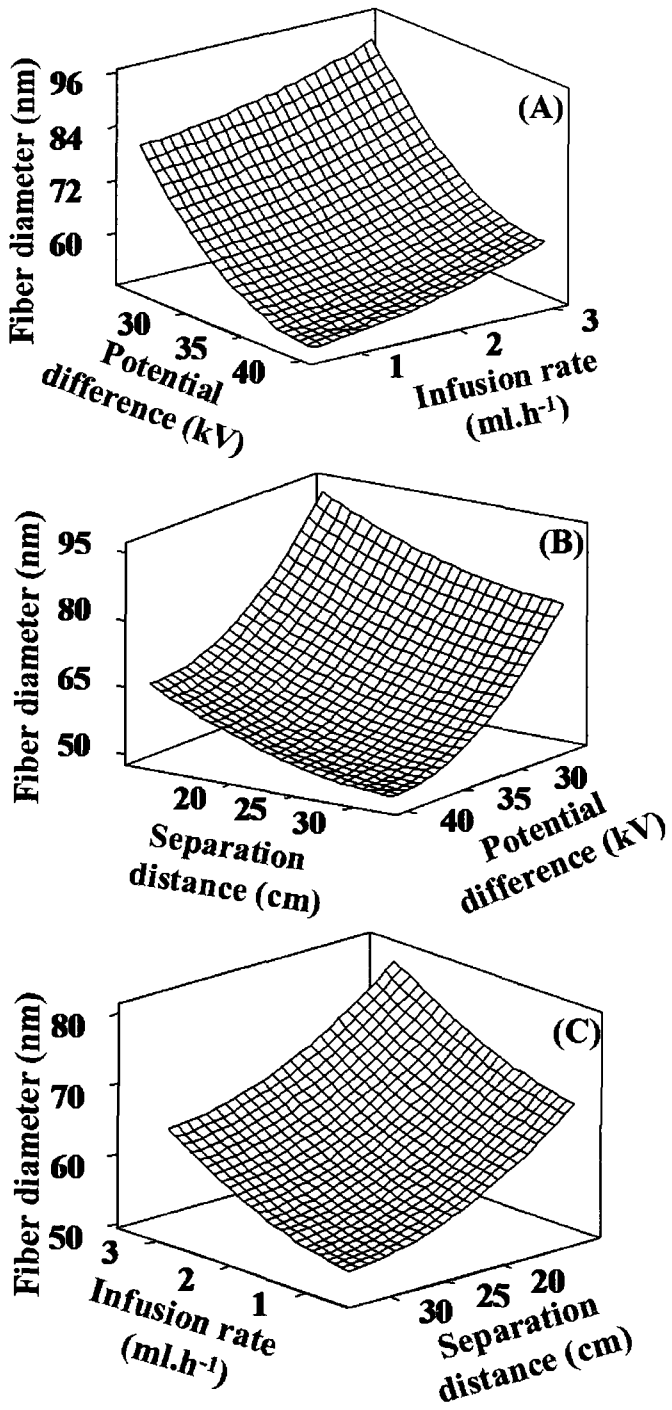

Figure 6.2 3D surface plots of the response variable (fiber diameter (nm)) for the experimental factors (two-factor-at-a-time)

(A) Potential difference and infusion rate

(B) Separation distance and Potential difference

(C) Infusion rate and separation distance

[Lines in the 3D surface plots connect the points of equal response]

6.3.3. Development of response surface model

An analysis of variance (ANOVA) was performed to evaluate the full quadratic response surface model presented (Equation 6.1). The ANOVA results (Table 6.3) of the experimental data revealed that the model was statistically significant (at 5% level of significance) with linear and quadratic terms. The interaction terms of the model were statistically insignificant ($p = 0.062$). Note the difference between replicates was statistically insignificant ($p = 0.907$). The error for the model was evaluated by computing the lack-of-fit. The p-value of 0.585, associated with the lack-of-fit suggested that the response surface model was statistically significant (and lack-of-fit was insignificant) at 5% level of significance. A backward elimination method was applied and statistically insignificant terms ($p > 0.05$) were deleted from the full quadratic model to obtain a refined response surface model. Further optimization analysis was performed to identify the optimal design points for the model excluding the statistically insignificant interaction terms. The numerical optimization based on the D-optimality criterion, was used to identify the design points for the optimal design.

The coefficients of the quadratic model were calculated using multiple regression analysis with the experimental data (fiber diameter (nm)) from the optimal design. The regression coefficients with their respective p-values are tabulated in Table 6.4. Note the terms that were statistically significant at 95% confidence level ($p \leq 0.05$) were included in the final response surface model (Equation 6.2). The quadratic response surface model (Equation 6.2) defined the diameter of TiO_2 nanofiber (response) as a function of the three electrospinning variables; potential difference (kV), infusion rate ($ml \cdot h^{-1}$), and separation distance (cm).

$$\text{TiO}_2 \text{ fiber diameter (nm)} = 295.61 - 10.72 \times (kV) + 0.17 \times \left(ml \cdot h^{-1}\right) - 2.17 \times (cm) + 0.13 \times (\text{kV})^2 + 1.27 \times \left(ml \cdot h^{-1}\right)^2 + 0.03 \times (cm)^2 \quad (6.2)$$

Table 6.3: ANOVA results of the experimental response at different factor levels.

Source	DF	Seq SS	Adj MS	F	P
Blocks	2	2.12	1.06	0.1	0.907
Regression					
Linear	3	4252.22	182.31	16.91	0.000 (*)
Square	3	672.66	224.22	20.8	0.000 (*)
Interaction	3	86.97	28.99	2.69	0.062
Residual Error					
Lack-of-Fit	27	31.48	10.49	2.3	0.585
Pure Error		2.00	9.14	4.57	
Total	44	5369.78			

Notes
1. DF = degrees of freedom
2. Seq SS = sequential sum of square
3. Adj MS = adjusted mean of square
4. (*) = values are statistically significant at 5% level of significance

Table 6.4: Regression coefficients of the response surface model for TiO_2 fiber diameter

Term	Coefficient	Regression Coefficient	P
Constant	a_0	295.61	0.000
kV	a_1	(-)10.72	0.000
ml·h^{-1}	a_2	0.17	0.042
cm	a_3	(-)2.17	0.016
kV × kV	a_4	0.13	0.001
ml·h^{-1} × ml·h^{-1}	a_5	1.27	0.031
cm× cm	a_6	0.03	0.050

6.3.4. Verification of the response surface model

A plot of the experimental data against values predicted by the model (Figure 6.3(A)) revealed a reasonable correlation for the experimental response (R-square = 0.914). The residuals (difference between the predicted and experimental fiber diameter) played an important role in judging the adequacy of the fit of the model to experimental data. A normal distribution of residuals ensure an adequate fit of the model to the experimental data. The AD statistic was used to confirm the normal distribution of the residuals (Figure 6.3(B)) (Stephens, 1974). The calculated AD statistic (0.285) was lower than the critical value of the AD statistic (0.752) for a sample size of 45 at 5% level of significance (Stephens, 1974). The value of AD statistic with associated p-value (p = 0.594 (greater than 0.05)) confirmed a normal distribution of residuals and suggested that the model prediction correlated reasonably well with the experimental results over the factor-space analyzed in the study. The results of a paired t-test confirmed that the difference between the experimental mean and model predicted mean of the response (TiO_2 fiber diameter) was statistically insignificant at a 95% level of confidence. For the two sets of data under consideration, the difference between the mean values was considered statistically insignificant when $t_{computed}$ (1.13) is less than $t_{tabulated}$ (2.14) (Box et al., 1978; Montogomery, 1997).

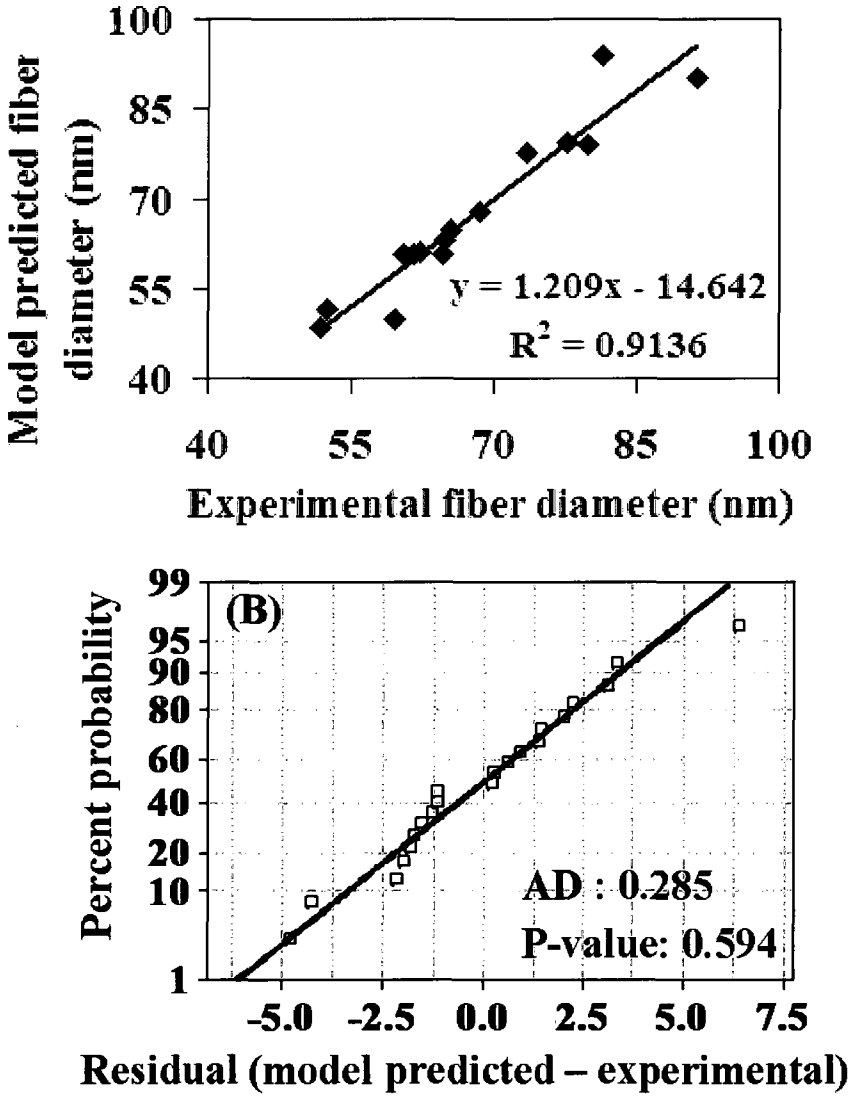

Figure 6.3 Assessment of the accuracy of the response surface model

(A) Plot of model predicted fiber diameter against experimental fiber diameter

(B) Anderson-Darling normality plot of residuals (model predicted hydrogen yield minus experimental hydrogen yield).

[AD: Anderson Darling statistic; P: level of confidence]

6.3.5. Validation of the response surface model

A separate validation study was performed for each of the three factors (potential difference, infusion rate and separation distance) under evaluation. Additional experiments were conducted to confirm the validity and accuracy of the response surface model for the design variables. The model predictions were compared with the experimentally observed results for potential difference values ranging from 25 to 40 kV (Figure 6.4(A)). With exception of the experimental observation at 25kV, the model predicted fiber diameter closely correlated with the experimentally observed values. The predicted fiber diameter for the lower setting of potential difference (25 kV) was slightly over-estimated compared to the experimental observation. Note the variability (standard deviation) in diameter values for fibers generated at 25kV (Expt. order. 1, 3, 5 and 7 (Table 6.2)) was higher than that at 32.5kV and 40kV. An increase in the fiber diameter correlated with an increase in the infusion rate (Figure 6.4(B)). Notice the experimental fiber diameter at lower infusion rate was higher than the model prediction. The inherent variability of the electrospinning process under the limiting mass throughput (at low infusion rate) can likely account for the difference between the model prediction and the experimental observation. The model predictions were in agreement with the experimental values for all the levels of separation distance (Figure 6.4(C)).

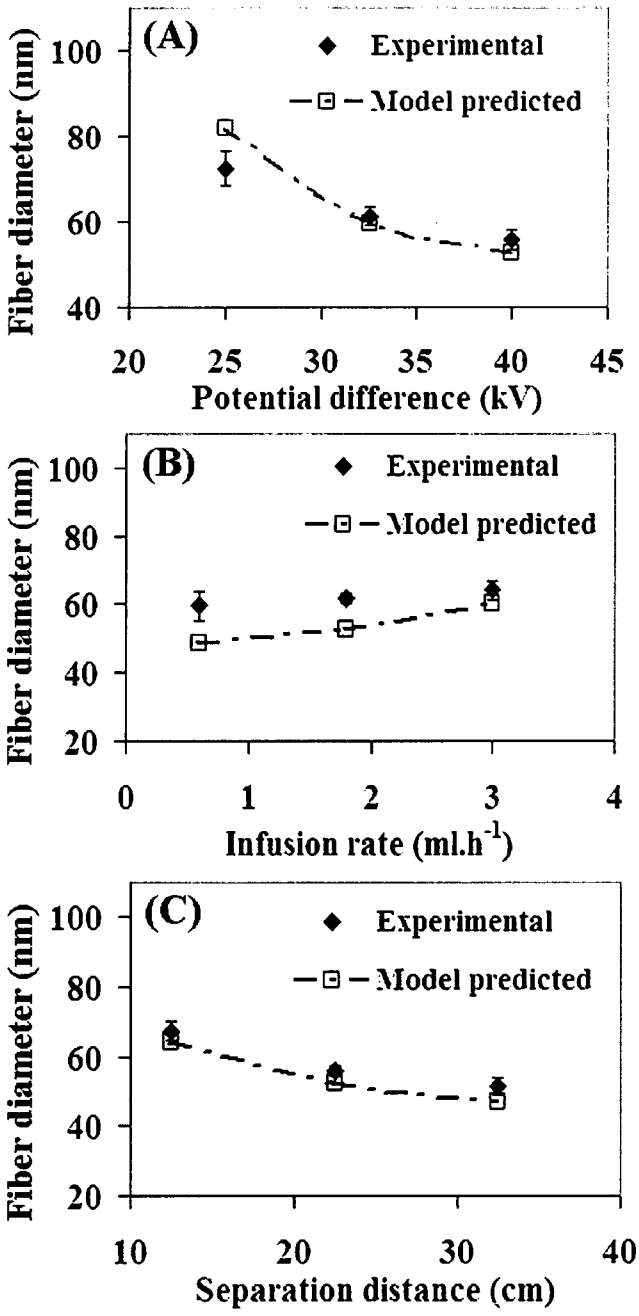

Figure 6.4 Validation of the model prediction against experimental values for the design factors under consideration.

(A) Fiber diameter versus potential difference
[Infusion rate: 1.8 $ml.h^{-1}$; Separation distance: 22.5 cm]

(B) Fiber diameter versus infusion rate
[Potential difference:. 40 kV; Separation distance: 22.5 cm]

(C) Fiber diameter versus separation distance
[Potential difference:. 40 kV; Infusion rate: 1.8 $ml.h^{-1}$]

[Average with standard deviation (SD) for triplicate samples are shown]

6.3.6. Optimization of the surface area of the TiO_2 nanofibers

The electrospinning condition for minimum response (TiO_2 fiber diameter) was located by overlaying the 3D surface plots. The response surface model was then used to predict the fiber diameter under identified electrospinning conditions which yielded a minimum fiber diameter. A minimum response value (TiO_2 nanofiber diameter) of 43.3nm was computed with the response surface model with a potential difference of 40kV, an infusion rate set at 0.6ml·h^{-1} and separation distance between electrodes of 32.5cm. Under the identical setting of electrospinning process variables, the experimentally obtained diameter of TiO_2 nanofiber (47.8 ± 8.7 nm) was 9.5% higher than the model prediction (43.3nm). Additional experiments were conducted at the computed optimal factor setting of 40 kV electrostatic potential, 0.6 ml·h^{-1} infusion rate, and 32.5 cm separation distance with electrospinning solutions of varying Ti-content. The Ti-content in the electrospinning solution varied from 1.3%, 2.6% to 3.9%. Increasing Ti-content in the electrospinning solution was observed to increase the diameter of the nanofibers (Figure 6.5).

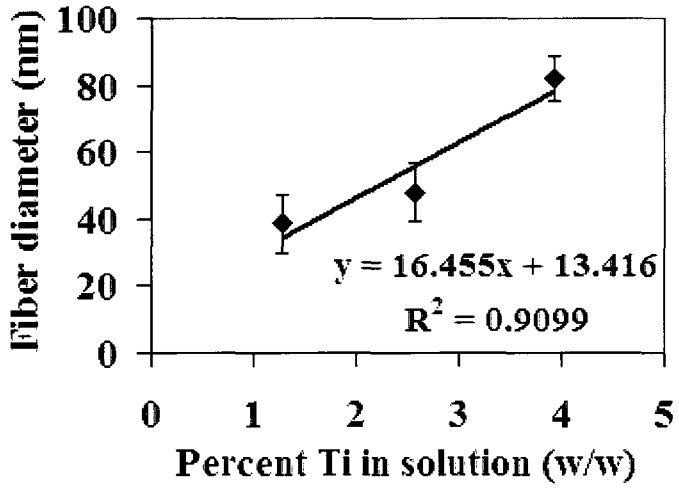

Figure 6.5 Plot of nanofiber diameter against Ti-content in the electrospinning solution [Average with standard deviation (SD) for triplicate samples are shown]

At a high Ti content (in the electrospinning solution), more TiO_2 formation per unit length of the charged strand deposited on the collector surface was observed. This resulted in TiO_2 nanofibers bearing a larger diameter (Figure 6.5). The response surface model (Equation 6.2) was further modified to include a term (Ti %) representing the Ti-content (in the electrospinning solution). The modified response surface model for predicting the diameter of TiO_2 nanofibers (nm) involving the electrospinning variables is presented in Equation 6.3. The model prediction (31.6 nm) was 19% lower than the diameter of experimentally obtained TiO_2 nanofibers (39.0 ± 6.6 nm).

$$\begin{aligned} TiO_2 \text{ fiber diameter (nm)} = 261.91 - 10.72 \times (kV) + 0.17 \times \left(ml \cdot h^{-1}\right) - 2.17 \times (cm) \\ + 0.13 \times (\text{kV})^2 + 1.27 \times \left(ml \cdot h^{-1}\right)^2 + 0.03 \times (cm)^2 + 16.27 \times (Ti\,\%) \end{aligned} \quad (6.3)$$

The specific surface area (SSA) of the TiO_2 nanofibers was determined from physisorption of nitrogen at – 196°C (77°K) between 0.0 to 0.3 relative pressure by BET analysis. The SSA of the TiO_2 nanofibers generated at optimal settings of the electrospinning variables was measured. The electrospun nanofibers obtained at the optimal setting of 40 kV potential difference, 0.6 $ml \cdot h^{-1}$ infusion rate, and 32.5 cm separation distance using an electrospinning solution containing 1.3% Ti had a fiber diameter of 39±6.6 nm. A SSA of 259 ± 23 $m^2 \cdot g^{-1}$ was recorded for TiO_2 nanofiber with a diameter of 39±6.6 nm. This recorded SSA of TiO_2 nanofibers is only 5.8% lower than that recorded by Ray et al. (2009) for 5 nm (275 ± 15 $m^2 \cdot g^{-1}$) TiO_2 nanoparticles (manufactured by Alfa Aesar, Wardhill, MA).

Table 6.5: Comparative TiO_2 fiber diameter of the present study against literature values.

Literature source	Diameter of TiO_2 nanofibers	Specific surface area (SSA)
Li and Xia (2003)	53 ± 8 nm	Not reported
Ding et al. (2004)	200 - 300 nm	Not reported
Lee et al. (2005)	53 - 109 nm	Not reported
Nuansing et al. (2006)	80 - 100 nm	Not reported
Kumar et al. (2007)	60 -150 nm.	Not reported
Doh et al. (2008)	168 ± 45	Not reported
Tekmen (2008)	54 - 78 nm	Not reported
Jo et al. (2009)	100 – 500 nm	3 – 100 $m^2 \cdot g^{-1}$
Zhang et al. (2009)	65 - 115 nm.	Not reported
Alves et al. (2009)	544 ± 270 nm	53.42 $m^2 \cdot g^{-1}$
Present study	**39 ± 6.5 nm**	**259 ± 23 $m^2 \cdot g^{-1}$**

The TiO_2 nanofiber diameters in the present study were compared with values reported in the literature sources (Table 6.5). From Table 6.5, it is evident that TiO_2 nanofibers produced during this study have the smallest diameter. The TiO_2 nanofiber diameter reported by Li and Xia (2003) is the next largest size when compared to the diameter reported in this study. A comparative t-test was performed with the means reported by Li and Xia (2003) (53 ± 8 nm) with that in the present study (39 ± 6.5 nm). The test concluded that the means are statistically different at 95% level of confidence ($t_{calculated}$ (11.5) > $t_{tabulated}$ (1.98)) (Montogomery, 1997). The SSA is seldom reported in the literature together with the fiber diameter. Other than the two recent reports (Jo et al., 2009; Alves et al., 2009), Kokubo et al. (2004) reported a SSA of 100 $m^2 \cdot g^{-1}$ for TiO_2 nanocatalyst measured after disintegrating the fibrous structure. SSA of the immobilized TiO_2 nanofibers observed in this study is much larger when compared to the SSA of

nanofibers reported in the literature (Table 6.5) and comparable with the SSA of discrete nanoparticles.

6.4. Conclusions

A response surface model based on the BBD technique was developed to predict the diameter of TiO_2 nanofibers produced by sol-gel electrospinning. The three experimental factors considered in this study included applied potential difference across the electrodes, infusion rate, and separation distance between the electrodes. Except at a lower setting of potential difference (25kV) and low infusion rate ($0.6ml{\cdot}h^{-1}$), the model prediction was consistent with experimentally observed fiber diameter. Due to increasing process instability, the variability associated with the low setting of the potential difference and infusion rate was large compared to the other experimental levels. A minimum fiber diameter was predicted when the potential difference was set at 40kV, infusion rate at $0.6ml{\cdot}h^{-1}$, and separation distance between the electrodes at 32.5cm. The experimentally obtained TiO_2 nanofibers diameter (47.8±8.7 nm) was 9.5% larger than the model predicted value of 43.3 nm. Other than the potential difference, infusion rate, and separation distance the Ti-content in the electrospinning solution significantly affected the nanofiber diameter. Hence, a modified model for the TiO_2 nanofiber diameter was developed by incorporating a term which accounted for the Ti-content. Under optimal settings (40 kV applied potential, 0.6 $ml{\cdot}h^{-1}$ infusion rate, and 32.5cm separation distance) the predicted nanofiber diameter of the refined model at 1.3% Ti-content (31.6 nm) was 19% lower than the experimental diameter of 39.0±6.6 nm. The diameter of the immobilized TiO_2 nanofiber in this study was significantly less than the values reported in the literature. The SSA of TiO_2

nanofibers (259 ± 23 $m^2 \cdot g^{-1}$) was approximately 6% less than the SSA of 5 nm TiO_2 nanoparticles.

6.5. References

1. Allen, N.S.; Edge, M.; Ortega, A.; Sandoval, G.; Liauw, C. M.; Verran, J.; Stratton, J.; McIntyre, R. B. (2004). Degradation and stabilisation of polymers and coatings: nano versus pigmentary titania particles. *Polym. Degrad. Stab., 85*, 927-946.
2. Alves, A.K.; Berutti, F.A.; Clemens, F.J.; Graule, T.; Bergmann, C.P. (2009). Photocatalytic activity of titania fibers obtained by electrospinning. *Mater. Res. Bull.* 44, 312–317.
3. Bach, U.; Lupo, D.; Comte, P.; Moser, J. E.; Weissörtel, F.; Salbeck, J.; Spreitzer, H.; Grätzel, M. (1998). Solid-state dye-sensitized mesoporous TiO_2 solar cells with high photon-to-electron conversion efficiencies. *Nature*, 395, 583 – 585.
4. Bae, S.; Shoda, M. (2005). Statistical optimization of culture conditions for bacterial cellulose production using Box-Behnken design, *Biotechnol. Bioeng.*, 90 (2005) 20-28.
5. Barbe′, C.J.; Arendse, F.; Comte, P.; Jirousek, M.; Lenzmann, F.; Shklover, V.; Gra¨tzel, M. (1997). Nanocrystalline Titanium oxide electrodes for photovoltaic applications. *J. Am. Ceram. Soc.*, 80, 3157–71.
6. Baan, R.; Straif, K.; Grosse, Y.; Secretan, B.; El Ghissassi, F.; Cogliano, V. (2006). Carcinogenicity of carbon black, titanium dioxide, and talc. *The Lancet Oncol.*, 7, 295-296.
7. Bhatkhande, D.S.; Pangarkar, V.G.; Beenackers, A.A.C.M. (2001). Photocatalytic degradation for environmental applications - a review, *J. Chem. Technol. Biotechnol.*, 77 102-116.
8. Blake, D.M. (2001). *Bibliography of work on the heterogeneous photocatalytic removal of hazardous compounds from water and air*. NREL/TP-510-3131. National Renewable Energy Laboratory, Golden, CO. Technical Report, 4, 3 – 16.
9. Box, G.E.P.; Hunter, W.G.; Hunter, W.S. (1978). *Statistics for Experimenters: An Introduction to Design, Data Analysis, and Model Building*, John Wiley and Sons, New York, NY, pp. 510 - 536. (ISBN 0-471-09315-7)
10. Box, G.E.P; Draper, N.R. (1987). *Empirical Model Building and Response Surfaces*, John Wiley & Sons, New York, NY, pp. 205 – 477 (ISBN 0-471-81033-9).
11. Carp, O.; Huisman, C.L.; Reller, A. (2004). Photoinduced reactivity of titanium dioxide. Prog. *Solid State Chem.* 32, 33-177.
12. Chronakis, I.S. (2005). Novel nanocomposites and nanoceramics based on polymer nanofibers using electrospinning process—A review, *J. Mat. Process. Technol.*, 167, 283–293
13. Cui, X.M.; Nam, Y.S.; Lee, J.Y.; Park, W.H. (2008). Fabrication of zirconium carbide (ZrC) ultra-thin fibers by electrospinning, *Mat. Lett.*, 62, 1961 -1964.

14. Deitzel, J.M.; Kleinmeyer, J.; Harris, D.; BeckTan, N.C. (2001b), The effect of processing variables on the morphology of electrospinning nanofibers and textiles, *Polymer,* 42, 261-272.

15. Deitzel, J.M.; Kleinmeyer, J.; Harris, D.; BeckTan, N.C. (2001a). Controlled deposition of electrospun poly(ethylene oxide) fibers, *Polymer,* 42, 8163–8170.

16. Ding, B.; Kim, C.K.; Kim, H.Y.; Seo, M.K.; Park, S.J. (2004). Titanium dioxide nanofibers prepared by using electrospinning method. *Fiber Polym.*, 5, 105 – 109.

17. Doh, S.J.; Kim, C.; Lee, S.G.; Lee, S.J.; Kim, H. (2008). Development of photocatalytic TiO_2 nanofibers by electrospinning and its application to degradation of dye pollutants. *J. Haz. Mat.*, 154, 118–127.

18. Frenot, A.; Chronakis, I. (2003). Polymer nanofibers assembled by electrospinning. *Curr. Opin. Colloid Interface Sci.*, 8, 64–75.

19. Fujishima, A.; Honda, K. (1972). Electrochemical Photolysis of Water at a Semiconductor Electrode. *Nature*, 238, 37-38.

20. Gogate, P.R.; Pandit, A.B. (2004). A review of imperative technologies for wastewater treatment I: oxidation technologies at ambient conditions. *Adv. Environ. Res.* 8, 501–551.

21. Herrmann, J.M. (2005). Heterogeneous photocatalysis: state of the art and present applications. *Top. Catal.* 34, 49-65.

22. Houari, M.; Saidi, M.; Tabet, D.; Pichat, P.; Khalaf, H. (2005). The removal of 4-chlorophenol and dichloroacetic acid in water using Ti-, Zr- and Ti/Zr-Pillared Bentonites as photocatalyst. *Am. J. Appl. Sci.,* 2, 1136-1140.

23. Hurum, D.C.; Agrios, A.G.; Crist, S.E.; Gray, K.A.; Rajh, T.; Thurnauer, M.C. (2006). Probing reaction mechanisms in mixed phase TiO_2 by EPR. *J. Electron. Spectrosc. Relat. Phenom., 150*, 155–163.

24. Ibañez, P.F.; Malato, S.; Enea, O. (1999). Photoelectrochemical reactors for the solar decontamination of water. *Catal. Today,* 54, 329–339.

25. Jo, S.M.; Song, M.Y.; Ahn, Y.R.; Park, C.R.; Kim, D.Y. (2005). Nanofibril Formation of electrospun TiO_2 fibers and its application to dye-sensitized Solar cells. J. *Macromol. Sci., Pure Appl. Chem.*, 42, 1529–1540.

26. Jo, S.M.; Kim, D.K.; Jang, S.Y.; Park, N.G.; Yi, B.H. (2009). Dye-sensitized solar cell with metal oxide layer containing metal oxide nanoparticles produced by electrospinning and method for manufacturing same. *EU Patent 2,031,613.*

27. Kumar, A.; Jose, R.; Fujihara, K.; Wang, J.; Ramakrishna, S. (2007). Structural and Optical Properties of Electrospun TiO_2 Nanofibers, *Chem. Mater.*, 19, 6536–6542.

28. Kokubo, H.; Ding, B.; Naka, T.; Tsuchihira, H.; Shiratori, S. (2007). Multi-core cable-like TiO_2 nanofibrous membranes for dye-sensitized solar cells. *Nanotechnology*, 18, 1- 6.

29. Lalman, J.A.; Ray, S. (2009). Method of surface treatment of Aluminum foil and its alloy and method of producing immobilized nanocatalyst of transition metal oxides and their alloys, *US Patent 61/272,518* (Provisional).

30. Lee, S.K.; Mills, A. (2004). Detoxification of water by semiconductor photocatalysis, *J. Ind. Eng. Chem., 10,* 173-187.

31. Lee, S-H; Tekmen, C.; Sigmund, W.M. (2005). Three-point bending of electrospun TiO_2 nanofibers. *Mat. Sci. Eng.,* 398, 77–81.

32. Li, D.; Xia, Y. (2003). Fabrication of titania nanofibers by electrospinning. *Nano Lett.,* 3, 555 -560.

33. Linsebigler, L.; Lu, G.; Yates Jr., J.T. (1995). Photocatalysis on TiO_2 surfaces: Principles, mechanisms and selected results. *Chem. Rev.*, 95, 735-758.

34. Matthews, R.W. (1992). Photocatalytic oxidation of organic contaminants in water: An aid to environmental preservation, *Pure Appl. Chem.* 64, 1285-1290.

35. Matthews, R.W.; McEvoy, S.R. (1992). A comparison of 254nm and 350 nm of TiO_2 in simple photocatalytic reactors. *J. Photochem. Photobiol. A., 66*, 355-366.

36. Montogomery, D.C. (1997). *Design and analysis of experiments*, fourth ed., John Wiley and Sons, New York, NY. pp. 536 - 660 (ISBN 0-471-15746-5).

37. Myer, R.H.; Montogomery, D.C. (2002). *Response surface methodology: Process and product optimization using designed experiment*, second ed., John Wiley and Sons, New York, NY. pp. 343-350 (ISBN 0-471-41255-4).

38. Nuansing, W.; Ninmuanga, S.; Jarernboon, W.; Maensiri, S.; Seraphin, S. (2006). Structural characterization and morphology of electrospun TiO_2 nanofibers. *Mat. Sci. Eng. B.,* 131, 147 – 156.

39. Ollis, D. F.; Pelizzetti, E.; Serpone, N. (1991). Photocatalyzed destruction of water contaminants. *Environ. Sci.Technol.* 25, 1522-1529.

40. Rajeshwar, K. (1995). Photoelectrochemistry and the environment. *J. Appl. Electrochem.* 25, 1067-1082.

41. Ray, S. (2006). RSM: A statistical tool for process optimization, *Ind. Tex. Jour.*, 117, (2006) 24-30.

42. Ray, S.; Lalman, J.A.; Biswas, N. (2009). Using the Box-Benkhen technique to statistically model phenol photocatalytic degradation by titanium dioxide nanoparticles, *Chem. Eng. J.,* 150, 15-24.

43. Redhe, M.; Forsberg, J.; Jansson, T.; Marklund, P-O.; Nilsson, L. (2002). Using the response surface methodology and the D-optimality criterion in crashworthiness related problems, *Struct. Multidisc. Optim.,* 24, 185-194.

44. Reneker, D.H.; Yarin, A.L.; Hao, F.; Koombhongse, S. (2000). Bending instability of electrically charged liquid jets of polymer solutions in electrospinning, *J. Appl. Phys.,* 87, 4531-4547.

45. Renekar, D.; Chase, G.; Kataphinan, W.; Katta, P. (2008). Flexible ceramic fibers and process for making the same, *US Patent 2008/0242178.*

46. Shah, S.I.; Li, W.; Huang, C.-P.; Jung, O.; Ni, C. (2002). Study of Nd^{3+}, Pd^{2+}, Pt^{4+} and Fe^{3+} dopant effect on photoreactivity of TiO_2 nanoparticles. *Proc. Natl. Acad. Sci. USA*, 99 (Suppl. 2): 6482 - 6486.

47. Shim, Y.M.; Hohman, M.M.; Brenner, M.P.; Rutledge, G.C. (2001). Experimental characterization of electro spinning: The electrically forced jet and in stabilities, *Polymer,* 42, 9955-9967.

48. Sigmund, W.; Yuh, J.; Park, H.; Maneeratana, V.; Pyrgiotakis, G.; Daga, A.; Taylor, J.; Nino, J. C. (2006). Processing and Structure Relationships in Electrospinning of Ceramic Fiber Systems, *J. Am. Ceram. Soc.,* 89, 395–407.

49. Stephens, M.A. (1974). EDF Statistics for Goodness of Fit and Some Comparisons. *J. Am. Stat. Soc.*, 69, 730-737.

50. Subbiah, T.; Bhat, G.S.; Tock, R.W.; Parameswaran, S.; Ramkumar, S. S. (2005). Electrospinning of nanofibers. *J. Appl. Polym. Sci.*, 96, 557–569.

51. Tekmen, C.; Suslu, A.; Cocen, U. (2008).Titania nanofibers prepared by electrospinning. *Mat. Ltt.,* 62, 4470 - 4472

52. Titterington, D.M. (1975). Optimal design: some geometrical aspects of D-optimality, *Biometrika*, 62, 313-320.

53. Viswanathamurthi, P.; Bhattarai, N.; Kim, C.K.; Kim, H.Y.; Lee, D.R. (2004). Ruthenium doped TiO_2 fibers by electrospinning. *Inorg. Chem. Commun.,* 7, 679 – 682.

54. Watthanaarun, J.; Pavarajarn, V.; Supaphol, P. (2005). Titanium (IV) oxide nanofibers by combined sol–gel and electrospinning techniques: preliminary report on effects of preparation conditions and secondary metal dopant, *Sci. Technol. Adv. Mat.,* 6, 240-245.

55. Yarin, A.L.; Koombhongse, S.; Reneker, D.H. (2001). Taylor Cone and Jetting from Liquid Droplets in Electrospinning of Nanofibers, *J. Appl. Phys.*, 90, 4836-4846.

56. Zhang, X.; Xu, S.; Han, G. (2009). Fabrication and photocatalytic activity of TiO_2 nanofiber membrane, *Mat. Lett.,* 63, 1761–1763.

CHAPTER 7: EVALUATION OF AN IMMOBILIZED TITANIUM DIOXIDE NANOCATALYST FOR PHOTOCATALYTIC PERFORMANCE

7.1. Introduction

In recent years, oxidative degradation of organic pollutants in an aqueous phase using a photo-illuminated heterogeneous catalyst has emerged as a potential technology for treating industrial effluents (Ollis et al., 1991). The process, generically identified as heterogeneous photocatalysis, relies on using hydroxyl ($^{\bullet}OH$) radicals to mediate oxidation of the organic contaminants into carbon dioxide (CO_2) and water using specific wavelengths of light (Bhatkhande et al., 2001; Lee and Mills, 2004). Heterogeneous photocatalysis offers a unique advantage over other alternative treatment methods as the technology can be classified as a 'green' treatment approach. Among the reported photocatalysts (ferric oxide (Fe_2O_3), cadmium sulfide (CdS), tungsten oxide (WO_3), zinc oxide (ZnO), titanium dioxide (TiO_2)) which have been used, TiO_2 has received the most attention due to its chemical inertness, lower biological toxicity, excellent photo-stability, high relative abundance, and above all, an oxidative potential for generating $^{\bullet}OH$ radicals (Rajeshwar, 1995; Bhatkhande et al., 2001; Carp et al., 2004; Herrmann, 2005).

The specific surface area (SSA) and crystal structure are two important parameters controlling the photocatalytic performance of TiO_2 (Rajeshwar, 1995; Gogate and Pandit, 2004; Carp et al., 2004; Hurum et al., 2006). For TiO_2 particles, SSA is a function of the particle size. TiO_2 within the micrometer range is largely utilized in paint manufacturing (Allen et al., 2004). The loss of charge carriers and inefficient light scattering are the main reasons for poor photocatalytic activity of the pigment grade micrometric TiO_2 particles (Shah et al., 2002; Allen

et al., 2004; Carp et al., 2004). The crystal structure dictates the bandgap energy and the oxidative potential of TiO_2. Rutile, anatase, brookite and monoclinic are four common TiO_2 crystal structures (Carp et al., 2004; Herrmann, 2005). Among the different crystal forms of TiO_2, anatase has the highest bandgap energy (E_g), and more photocatalytic activity than rutile and other crystal forms of TiO_2 (Bhatkhande et al., 2001). Rutile is the more stable form; however, for particle sizes less than 14nm in diameter, anatase is thermodynamically more stable (Zhang and Banfield, 1998). Thus, anatase TiO_2 nano-structures are desirable for photocatalytic applications.

Increasing innovations in manufacturing have permitted processes to produce particle sizes in the nanometer range. Several nanometer size TiO_2 formulations have been synthesized and evaluated for their photocatalytic potential (Blake, 1999; Bhatkhande et al., 2001; Sankapal et al., 2006). Various physical techniques (such as spluttering and vapor deposition) and chemical methods (for instance, hydrothermal and glyco-thermal crystallization) have been tested for synthesizing TiO_2 nanoparticles (Blake, 1999; Carp et al., 2004; Sankapal et al., 2006; Centi and Perathoner, 2009). However, the most successful method of synthsizing TiO_2 nanoparticles is the sol-gel based synthesis method (Sayilkan et al., 2005). In the sol-gel method, a titanium alkoxide (sol-precursor) is hydrolyzed to produce nano-sized high surface area TiO_2 particles. Homogeneity of the nanoparticles, well defined fine structure of TiO_2, high surface area, and ease of coupling with catalyst immobilization techniques are some of the advantages of the sol-gel technique over other synthesis methods (Sayilkan et al., 2005; Carp et al., 2004).

Sol-gel derived TiO_2 nanoparticles are used as an aqueous dispersion or slurry for photocatalytic studies (Dijkstra et al., 2001). However, the use of TiO_2 nanoparticles in the form of slurry is associated with several limitations related to the practical application of the catalyst

(Houari et al., 2005). Nanoparticles tend to aggregate when wet, resulting in loss of surface area (refer Appendix B), and therefore, nano-particle slurries require vigorous mechanical agitation in order to minimize particle aggregation during the photocatalytic reaction (Hurum et al., 2006). The photocatalytic efficiency of nanoparticle slurry is dependent upon the penetration depth of the incident radiation. Increasing TiO_2 nanoparticle concentration causes higher turbidity, and thereby severely impairs the depth of penetration of the incident radiation (Ling et al., 2004). Additionally, the nanoparticle slurry process requires a supplementary post-treatment solid/liquid separation process for catalyst recovery (Houari et al., 2005). Also, there are human health hazards associated with fugitive emissions of nanoparticles during slurry preparation (Baan et al., 2006). An approach to minimize these limitations is to immobilize the nano-particles onto a fixed or fluidized support.

A popular method for immobilizing TiO_2 for photocatalysis is the in-situ production of nanoparticles by the sol-gel technique and subsequent deposition onto a solid support via dip coating (Hamid and Rahman, 2003). However, a major drawback of this immobilized TiO_2 catalyst system is the lower photocatalytic rates compared to the discrete nanoparticle slurry (Dijkstra et al., 2001). The lower photocatalytic rate of the immobilized system is related to the loss of surface area caused by particle sintering or aggregation on the support surface during the thermal treatment (Carp et al., 2004; Houari et al., 2005). Sintering results in the formation of large particle aggregate or film on the support surface and the resultant supported catalyst therefore has a surface area smaller than that of discrete nanoparticles by a few orders of magnitude (Ibañez et al., 1999). An alternative approach of producing a catalyst with surface area comparable to that of the nanoparticles is to fabricate TiO_2 nano-structures and subsequently immobilize them onto a support.

A technique for fabricating immobilized nano-structures onto a fixed support is electrospinning. In the electrospinning process, a high static voltage is used to produce ultrafine fibers with diameters in the nanometric range (Reneker and Chun, 1996). The electrospinning technique has been successfully exploited to generate small diameter fibers and to fabricate large surface area membranes (Frenot and Chronakis, 2003; Subbiah *et al.*, 2005). Recently, electrospinning has also been applied to the production of nanofibers of metal oxides and ceramics (Chronakis, 2005; Sigmund et al., 2006).

Li and Xia (2003) demonstrated the coupling of the sol-gel technique of TiO_2 nanoparticle formation with electrospinning process and produced TiO_2 nanofibers in a two step process. Initially, the nanofibers are fabricated by electrospinning a sol-precursor of TiO_2 with a high molecular weight polymer. The purpose of the polymer is to impart rheological stability and act as a carrier for the titanium salt during nanofiber formation (Li and Xia, 2003). Later the composite nanofibers of the polymer and TiO_2 are subjected to calcination treatment to obtain pure TiO_2 fibers. To date, several attempts have been reported towards developing immobilized TiO_2 nanofiber catalysts for photocatalytic application (Madhugiri et al., 2004; Doh et al., 2008; Alves et al., 2009). However, none of the earlier reports have been very successful in developing a high surface area immobilized TiO_2 nanofibers catalyst for photocatalytic application. Poor stability of the immobilized catalyst system (Madhugiri et al., 2004; Doh et al., 2008) and inferior photocatalytic performance compared to nanoparticles (Madhugiri et al., 2004; Alves et al., 2009) are two limitations observed by the earlier researchers. Hence, the intent of the present study is to develop a photocatalyst system by immobilizing TiO_2 nanofibers onto a fixed solid support and compare the photocatalytic performance of immobilized TiO_2 nanofibers with that of

the nanoparticles slurry. The SSA, crystal structure, and bandgap energy of the immobilized TiO_2 nanofiber catalyst are also to be determined as part of the investigation.

7.2. Materials and methods

7.2.1. Materials

Titanium tetraisopropoxide (TIP), an organo-titanium sol-gel precursor to titanium dioxide (> 99.95% purity) and polyvinyl acetate (PVAc (average molecular weight (M_w) 50,000 Daltons)), a carrier for the TIP, were purchased from Alfa Aesar (Ward Hill, MA). Acetic acid (>99% purity), a stabilizer for sol-gel conversion of TIP, was procured from EMD (Gibbstown, NJ). Dimethylformamide (DMF) and tetrahydrofuran (THF), solvents were supplied by Fischer Scientific (Ottawa, ON). Titanium dioxide (>99.9% purity) nanoparticles (5nm and 10nm particle size) used in the experiment were procured from Alfa Aesar (Ward Hill, MA). X-ray diffraction was used to ensure the anatase type crystal structure of the nanoparticles. Phenol (Reagent grade, >99% purity) was procured from Sigma Aldrich (Oakville, ON). Ultrapure water (18M-ohm resistivity) used in this study was generated by a NANOpure Diamond water unit (Thermo Fisher Scientific, Waltham, MA).

7.2.2. Electrospinning apparatus

The electrospinning apparatus (Figure 5.1) consist of a pumping system capable of delivering a viscous solution at a constant flow rate to a metallic capillary. The metallic capillary was connected to a positive (anode) terminal of a variable high voltage DC power and the negative or ground terminal (cathode) was attached to a collector surface (conducting solid catalyst support material), where the charged nanofibers are deposited. A detail of the apparatus is described in

Chapter 5, Section 5.2.1. The two electrodes (needle tip to the surface of the solid support) were separated by a distance (32.5 cm), This distance was established as favorable for the formation of ultrafine nanofibers based on the optimization study reported in Chapter 6, Section 6.3.6.

7.2.3. Choice of catalyst support material

The type of support material used to immobilize TiO_2 nanoparticles can be classified as fixed and fluidized support. Glass plates (Hamid and Rahman, 2003; Ling et al., 2004), glass fibres (Pozzo et al., 1997), polymeric fibres (Ding et al., 2004) and textile materials (Bozzi et al., 2005) are some reported fixed catalyst support materials. Materials used for fluidized application include activated charcoal (Carpio et al., 2005) and bentonites (Houari et al., 2005). Fluidized materials are not suitable as (collector) solid support in electrospinning because these are unorganized small particles, and in some cases these are non-conducting. A fixed support materials such as glass, also presents a problem because it is non-conducting. In comparison aluminum support is capable of quickly dissipating static charges and hence, can be used as collector ground. Moreover, previous work reported that aluminum possesses good adhesion property for the TiO_2 nanocatalyst. The roughness of the support surface improved the adhesion behavior of immobilized TiO_2 nanocatalyst (Peiró et al., 2002). Hence, a newly developed surface-treated aluminum foil with nanoscale surface roughness (Lalman and Ray, 2009) was chosen for supporting the electrospun TiO_2 nanofibers (refer Appendix C). Based on the findings of other studies (Ding et al., 2004; Song et al., 2004), the surface-treated aluminum foil was used in TiO_2 nanofiber immobilization after an additional surface treatment. The detail of the catalyst support preparation procedure is described in Chapter 5, Section 5.3.6.

7.2.4. Preparation of the electrospinning solution

A sol-gel precursor for fabricating TiO_2 is TIP. TIP solution was prepared by stabilizing with glacial acetic acid in a molar ratio of 1: 4 mol TIP per mol acetic acid under slow stirring conditions (Solution A). Solution A was mixed with a polymer solution to maintain a viscosity within 130-160 centipoise (cps) (Cui et al., 2008). Polyvinyl acetate (PVAc) was reported to have better miscibility with TIP and maintain better homogeneity of the phases during electrospinning (Jo et al., 2005). Hence, PVAc was selected for the study. A PVAc solution was prepared by dissolving polymer beads in 3:2 volumetric mixtures of DMF and THF (Solution B). The viscosity of a 45% (weight per unit volume (w/v)) solution of PVAc (Mw 50,000 Dalton) in 3:2 (v/v) DMF/THF was measured using a cone and plate viscometer (Brookfield CAP 1000 viscometer, Brookfield, Middleboro, MA). The viscosity was 147.8±0.6cps at shear rate $\geq 10{,}000 s^{-1}$. The electrospinning solution (Solution C) was prepared by mixing the TIP solution (Solution A) with 45% PVAc (w/v) solution (Solution B). The Titanium (Ti) content (by weight) in the electrospinning solution was varied by mixing various proportions of the TIP solution (Solution A). The Ti-content (1.3%, 2.6% and 3.9% as Ti by weight) were selected based on the results of the optimum study presented in Chapter 6, Section 6.3.6.

7.2.5. Electrospinning and catalyst immobilization

A syringe containing the electrospinning solution (Solution C) was placed in the syringe pump and the infusion rate of the pump was adjusted to a desired value of 0.6 $ml \cdot h^{-1}$. The stainless steel needle of the syringe was connected to the positive terminal of the high voltage DC power supply. The ground terminal was attached to the surface-treated aluminum (foil) support (collector) and positioned at 32.5 cm from the needle tip. The observations presented in Chapter 5, Section 5.3.7 showed that interaction of PVAc with TIP resulted in the formation of

linking bridge, which favored the adhesion of nanofibers on to the support surface. Hence, in the present study the surface-treated aluminum foil was applied with a coating of PVAc (45% (w/v) in 3:2 DMF/THF) by means of a stainless steel doctor's blade (blade angle 45°) prior to electrospinning (as described in Chapter 5, Section 5.3.7), and used as the collecter for nanofibers.

Upon applying a potential difference of 40kV, a fluid jet was ejected from the capillary (needle) tip. After an initial instability period of few seconds, a steady fluid jet headed towards the grounded support. As the jet accelerated towards the cathode, the solvent evaporated and charged TiO_2/PVAc composite fibers were deposited on the solid support (treated aluminum foil). TiO_2/PVAc nanofibers were dried under a vacuum of 600mm Hg at 105°C for 2 hours to remove the residual solvent and allow for further stabilization of the structure (Madhugiri et al., 2004; Sheikh et al., 2009). The vacuum dried nanofibers were subjected to a step-wise heat treatment as described in Chapter 5, Section 5.3.1. The steps included a slow heating (at rate of 1.5°C/min) of TiO_2/PVAc nanofiber in a temperature programmable oven to 300°C, followed by calcination in a muffle furnace (Thermolyne 1300, Thermo Fisher Scientific Inc., Newington, NH) to a final calcination temperature (400° – 500°C) for an additional 2 hours. The immobilized nanofibers were then cooled to ambient temperature, cleaned with a gentle stream of clean dry air, rinsed in ultrapure water, and finally, dried at 105 °C.

The anatase is the most photocatalytically active crystal form of TiO_2 (Bhatkhande et al., 2001). Calcination temperatures between 400° to 500°C was examined by earlier researchers for the fabricating anatase TiO_2 photocatalyst (Chandrasekar et al., 2009; Alves et al., 2009; Zhang et al., 2009; Kumar et al., 2007). Teleki et al. (2008) reported that temperatures greater than 400°C can induce phase transformation of TiO_2 from anatase to rutile. The temperatures of

450°C (Doh et al., 2008) and 500°C (Alves et al., 2009) had also been reported for immobilizing TiO_2 nanofiber catalysts. Hence, in the present study three calcination temperatures (400°, 450° and 500°C) were examined for their effect on the morphology, band gap energy and (SSA) of the photocatalyst.

7.2.6. Nanocatalyst characterization

The crystalline structure of the immobilized TiO_2 nanofibers was quantified using a X-ray diffractometer (D8 Discover, Bruker Corporation, Milton, ON). The details of the instrument configuration are reported in Chapter 5, Section 5.2.4. The nanofibers were scraped from the support in order to determine the crystal structure. The crystalline phases were identified by comparing the interplanar spacing and the diffraction peaks against JCPDS cards (Joint Committee on Powder Diffraction Standards (JCPDS), powder diffraction file, Card No. 21-1272 (anatase) and 21-1276 (rutile), Swarthmore, PA). The mass fraction of rutile phase (X_R) was computed using Spurr equation, Equation 7.1 (Scotti et al., 2009). The term I_A and I_R (Eqn. 3) are the integrated intensities of the (101) anatase and (110) rutile crystal plane respectively.

$$\frac{1}{X_R} = 1 + 0.8\left(\frac{I_A}{I_R}\right) \tag{7.1}$$

Images of the nanofibers were obtained using a field emission scanning electron microscope (FESEM) (Quanta 200, FEI Company, Hillsboro, OR). An additional detail of the instrument is described in Chapter 5, Section 5.2.4. The diameters of the nanofibers were measured from the FESEM images using an image processing software (SCANDIUM, Olympus Soft Imaging Solutions Corp, Lakewood, CO). The surface details of the nanofibers were imaged using multimode scanning probe atomic force microscope (AFM) (Nanoscope IV, Veeco Instruments Inc., Plainview, NY) fitted with TESP probe in tapping mode. The minimum scanning area of

the AFM was 0.16 μm^2. The AFM images were analyzed using Nanoscope software, version 6.13 (Veeco Instruments Inc., Plainview, NY).

The TiO_2 nanocatalysts were optically characterized to determine the bandgap energy by measuring the transmittance of incident light with wavelengths between 200 to 400nm using a UV-visible spectrophotometer (Cary 50, Varian Inc, Palo Alto, CA). The SSA (m^2/g) of the TiO_2 nanocatalyst was determined from physisorption of nitrogen (N_2) gas (BOC, Windsor, ON) under relative pressure (P/P_o) of 0.0–0.3 at 77.34K in a surface area analyzer (NOVA 1200e, Quantachrome Instruments, Boynton Beach, FL) using the Brunauer-Emmett-Teller (BET) principle.

7.2.7. Photocatalytic experimental set-up

Photocatalytic experiments were performed in photocatalytic reaction tubes (25mm inner diameter (ID) x 250mm length) fabricated from GE-214 clear fused quartz silica (Technical Glass Products Inc., Painesvile, OH). A model pollutant (phenol) was dissolved in water and the supported TiO_2 nanofiber catalyst was dipped in the reaction liquid. In comparative with nanoparticles, a TiO_2 nanoparticle slurry was added instead of the supported catalyst. The headspace of each reaction tube was purged with oxygen for 10 minutes, and sealed with Teflon® lined 20mm silicone rubber septa (Cobert Associates, St Louis, MO) and aluminum crimp caps (Cobert Associates, St Louis, MO). The sealed reaction tubes were then placed in a modified Rayonet RPR-100 ultraviolet (UV) photocatalytic chamber (Southern New England Ultraviolet Co., Branford, CT). The custom built photocatalytic chamber was equipped with sixteen phosphor-coated low-pressure mercury lamps on the outer perimeter and a centrally located rotating inner carousel (Figure 7.1). Three or six quartz reaction tubes were placed on the inner rotating carousel and irradiated with 300nm monochromatic UV light at an average

irradiance of 9 mW/cm^2 (measured using a UV-X radiometer (UV Process Supply Inc., Chicago, IL). Over the duration of each photocatalytic experiment, a fixed amount of liquid solution was withdrawn from the reaction tubes at specific time intervals. The liquid samples were stored in screw capped culture tubes (13mm ID x 100mm length) (VWR International, Mississauga, ON) wrapped with aluminum foil for further quantitative analysis. The residual substrate concentration in the liquid samples were analyzed by high performance liquid chromatograph (HPLC).

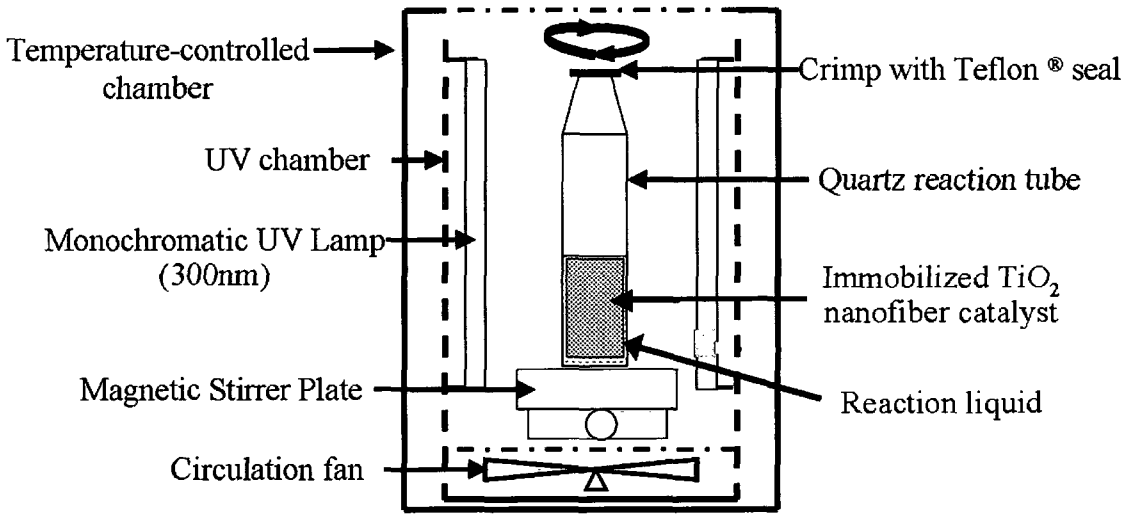

Figure 7.1 Schematic diagram of photocatalytic apparatus (and reaction set-up)

Phenol is a classified carcinogen, teratogen, mutagen and endocrine disruptor. Notice that phenol is a basic structural entity of many other ecotoxins and endocrine disrupting chemicals. Phenol and phenol derivatives has an annual global production of approximately 3 million tones, and are routinely used in the manufacture of resins, insulation panels, herbicides and pesticides paints and lubricants (Envirnmental Health Criteria (EHC) 161, 1994). Hence, phenol was selected as the model pollutant (substrate) for the photocatalytic experiments in this study.

7.2.8. Analysis

Degradation of the phenol (substrate) was monitored using a HPLC (Dionex Ultimate 3000, Sunnyvale, CA) equipped with a UV-visible photodiode array (PDA) detector set at 215 nm and configured with an Acclaim C18-3μm-2.1mm (ID) x 100mm (length) column (Dionex, Sunnyvale, CA). The analysis was conducted isothermally with the oven temperature set at 45°C and an eluent (acetonitrile-water mixture (1:4)) (Fisher Scientific, Ottawa, ON) flow rate set at 0.4 ml/min. The detection limit for phenol was 5μg/l.

7.3. Results and discussions

7.3.1. Effect of varying Ti content on the immobilized nanofibers

The diameter of TiO_2 nanofibers immobilized on the support surface was measured to determine the effect of varying the Ti-content. FESEM images of TiO_2 nanofibers fabricated from electrospinning solution with different Ti-content are presented in Figure 7.2 (A-C). Figure 7.2 (D-F) present histograms of TiO_2 nanofiber diameters for respective FESEM images. Smaller diameters were recorded for nanofibers generated using an electrospinning solution with lower Ti-content. Increasing Ti-content in electrospinning solution is associated with more TiO_2 formation and deposition as nanofibers on the support surface. Hence, Ti rich electrospinning solution results in nanofibers with larger diameters after thermal stabilization.

Higher variability in the nanofiber diameters was observed for increasing Ti-content. The smallest fiber diameter of 19 nm (with range of 19 – 49 nm) was measured for 1.3% Ti content (Table 7.1). Increasing the Ti content in the electrospinning solution caused faster gelation and solidification. Gelation of Ti containing sol-precursor changed the surface tension and the

viscosity property of the solution during electrospinning and this was the major reason for higher variability in the fiber formation (Tekmen et al., 2008).

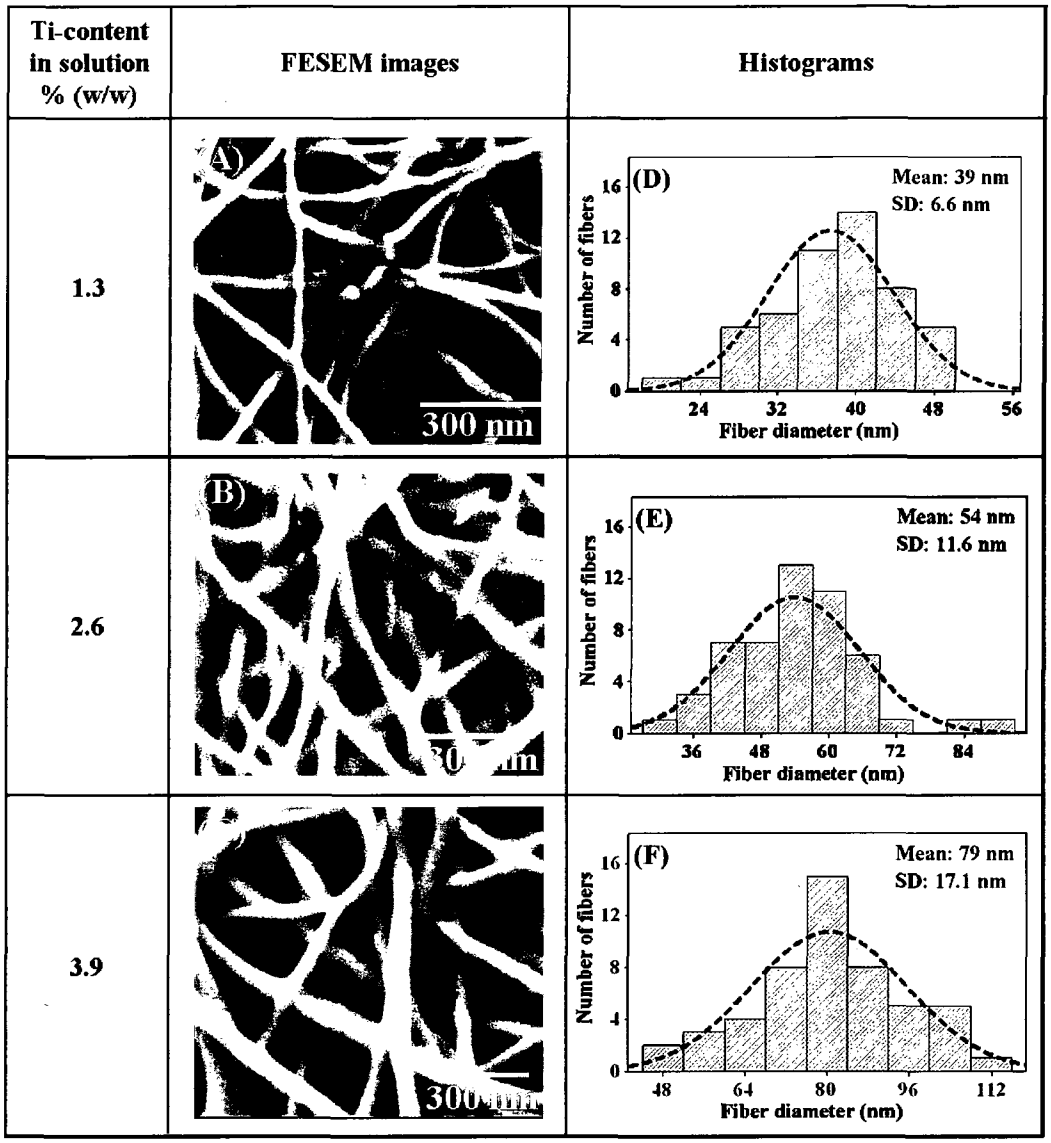

Figure 7.2 Effect of varied Ti-content of the electrospinning solution on nanofiber diameters.
(A) FESEM image of nanofibers, 1.3 % Ti-content
(B) FESEM image of nanofibers, 2.6% Ti-content
(C) FESEM image of nanofibers, 3.9% Ti-content
(D) Histogram of nanofiber diameter, 1.3 % Ti-content
(E) Histogram of nanofiber diameter, 2.6 % Ti-content
(F) Histogram of nanofiber diameter, 3.9 % Ti-content

The SSA associated with immobilized nanofibers generated from electrospinning solutions with different Ti-contents are tabulated in Table 7.1. Decreasing SSA with increasing Ti-content in the electrospinning solution is directly related to the loss of the surface area due to increased fiber diameter at higher Ti-content.

Table 7.1: Effect of Ti-content on the characteristics of immobilized TiO_2 nanofibers.

Ti-content in solution % (w/w)	**Fiber diameter (nm)**		**Specific surface area ($m^2.g^{-1}$)**
	Range	**Mean ± SD**	
1.3	19-49	39±6.5	259±23
2.6	28-93	54±11.6	108±23
3.9	45-109	79±17.1	90±11

7.3.2. Effect of calcination temperature on the immobilized nanofibers

According to Teleki et al. (2008), the phase transformation of TiO_2 from anatase to rutile occured at calcination temperature of approximately 400°C. Calcination temperatures of 450°C (Doh et al., 2008) and 500°C (Alves et al., 2009) have also been reported in literature for immobilization of TiO_2 nanofiber catalyst. Hence, in the present study the effects of three different calcination temperatures, 400°, 450° and 500°C, on the properties of TiO_2 nanofibers electrospun from solution containing 2.6% Ti were examined. The diameter of TiO_2 nanofibers, after calcination at 400°C, 450°C and 500°C were 54 ± 11.6 nm (designated as A), 50 ± 14.3 nm (designated as B) and 49 ± 15.1 nm (designated as C) respectively. The fiber diameters were statistically compared using the t-statistic to examine the effect of calcination temperature. The results of the t-test were 1.55 (t_{A-B}), 0.34 (t_{B-C}) and 1.88 (t_{A-C}) respectively. The calculated t-test values were less than the tabulated t-value of 2.08 at 95% confidence level (Montogomery,

1997). Thus, increasing calcination temperature from 400° to 500°C was concluded to have no significant effect on the diameter of TiO_2 nanofibers.

The SSA of the TiO_2 nanofibers calcined at 400°, 450° and 500°C are presented in Table 7.2. The SSA of the TiO_2 nanofibers was considerably reduced (from 108±23 to 54±9) as the calcination temperature increased from 400° to 450°C. The decrease in SSA on further increase in calcination temperature from 450°C to 500°C is much less (from 54±9 to 39±11). The examination of the TiO_2 nanofibers calcined at 400°, 450° and 500°C using AFM and FESEM, revealed the cause for the decrease in the SSA (Figure 7.3 (A- F)). Notice the decrease in surface roughness in AFM images and appearance of distinct cracks due to aggregations in FESEM images with increasing calcination temperatures. The sintering of the pores and loss of surface texture of the nanofiber with increasing temperatures resulted in a decrease in the SSA. Hence, a temperature of 400°C was left invariant (from studies presented in Chapter 5, Section 5.3.1 and 5.3.2) as the calcination temperature for fabricating TiO_2 nanofibers with high SSA.

Table 7.2: Effect of calcination temperature on the diameter and specific surface area

Calcination temperature (°C)	**Fiber diameter (nm)**	**Specific surface area ($m^2 \cdot g^{-1}$)**
400	54 ± 11.6	108 ± 23
450	50 ± 14.3	54 ± 9
500	49 ± 15.1	39 ± 11

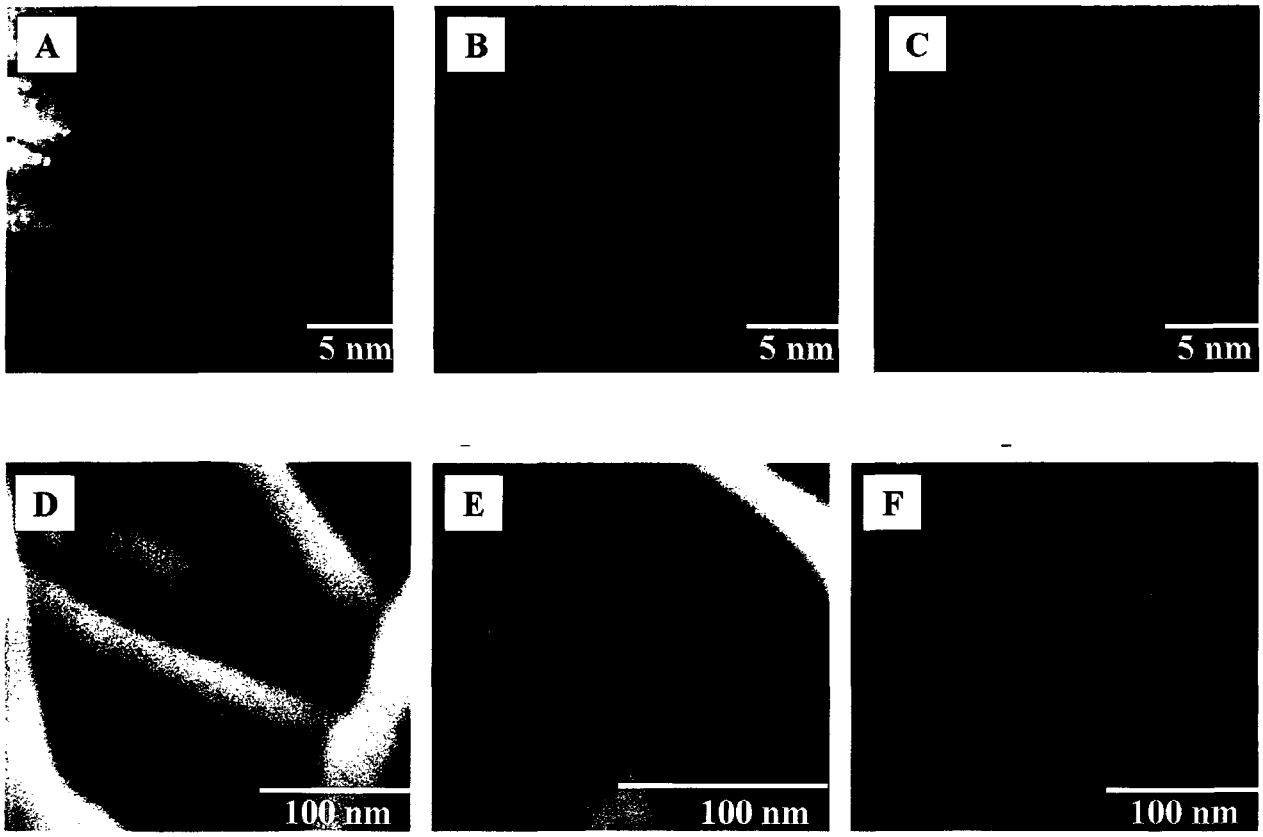

Figure 7.3 Effect calcination temperature on the surface texture of TiO_2 nanofibers (A) AFM image, 400°C; (B) AFM image, 450°C; (C) AFM image, 500°C (D) FESEM image, 400°C; (E) FESEM image, 450°C; (F) FESEM image, 500°C

7.3.3. Crystalline phase and the bandgap energy of the nanofibers

The TiO_2 nanofibers calcined at three different temperatures (400°, 450° and 500°C) were analyzed for the crystalline phase and the bandgap energy. X-ray diffraction (XRD) studies were conducted to determine the crystalline phase of the nanofibers. From the d-spacing and the 2θ x-ray diffraction angle the crystal planes were identified and compared with the reported d-spacing values of pure crystalline phases. Anatase is the only crystal phase identified in the TiO_2 nanofibers calcined at 400°C. X-ray diffraction peaks for both anatase and rutile TiO_2 crystal phases were observed in nanofibers calcined at 450°C and 500°C. The integrated intensities of

the (101) anatase crystal plane (101) at 3.51Å and rutile crystal plane (110) at 3.24Å ((JCPDS, PDF, Card No. 21-1272 (anatase) and 21-1276 (rutile)) were calculated. From the integrated intensities of anatase (I_A) and rutile (I_R) the mass fraction of rutile phase (X_R) was computed using Equation 7.1. The rutile mass fraction (%) are tabulated in Table 7.3. Increasing calcination temperature was observed to increase the rutile phase for the TiO_2 nanofibers.

Table 7.3: Effect of calcination temperature on crystal phase and bandgap energy

Calcination temperature (°C)	Mass fraction of crystal phase (%)		Bandgap energy (eV)
	Anatase	Rutile	
400	100	0	3.24
450	96	4	3.13
500	73	27	3.03

The bandgap energy (E_g) of the TiO_2 nanofibers was computed from the measured transmittance of ultra-violet radiation using Plank-Einstein equation, Equation 7.2.

$$E_g = hc/\lambda_{min} \quad (7.2)$$

where, λ_{min} is the wavelength of incident radiation with minimum transmittance, h is Plank's constant and c is the speed of light (constant). The computed E_g for the TiO_2 nanofibers calcined at 400°, 450° and 500°C were tabulated in Table 7.3. The highest E_g was recorded for the TiO_2 nanofibers calcined at 400°C. Notice decreasing E_g values are observed with increasing calcination temperature. An increase in calcination temperature from 400°C to 500°C resulted in an increase in the rutile mass fraction in the TiO_2 nanofibers. The E_g value for the rutile phase (3.0 eV) was lower than that of the anatase crystal phase (3.2 eV) (Bhatkhande et al., 2001). Decreasing E_g values for TiO_2 nanofibers with increasing calcination temperature from 400°C to 500°C was likely due to increase in the mass fraction of the rutile phase.

7.3.4. Effect of nanofiber loading on the specific surface area

Electrospinning and subsequent immobilization result in layer-by-layer deposition of TiO_2 nanofibers onto the support surface. The number of deposited layers of nanofibers in practice is synonymous to the mass of TiO_2 nanofibers deposited. The mass of TiO_2 deposited per unit area of the support was varied by repeating the electrospinning deposition process. Increased nanofiber loading resulted in decrease of SSA for the immobilized nanofiber catalyst (Figure 7.4(A)). A maximum SSA was recorded for TiO_2 nanofiber loading of 0.9 $g \cdot m^{-2}$. Notice the decrease in SSA tends to level (reach a plateau) beyond 1.4 $g \cdot m^{-2}$ of TiO_2 loading. The reason can be explained using the schematic presented in Figure 7.4(B). The surface to surface contacts of nanofibers during repeated deposition caused a loss of available surface area at points where the fibers were in contact with each other. Thus, increasing the deposition of TiO_2 nanofibers per unit area of support lessen the available surface area for monolayer adsorption of adsorbate gas molecules (nitrogen) and thereby resulted in lowered specific surface area (SSA) values. The limitation of the electrospinning apparatus in distributing the catalyst for uniform coverage of support surface was noticed at loading below 0.9 $g \cdot m^{-2}$. Hence, the nanofiber loading rate below 0.9 $g \cdot m^{-2}$ was not examined.

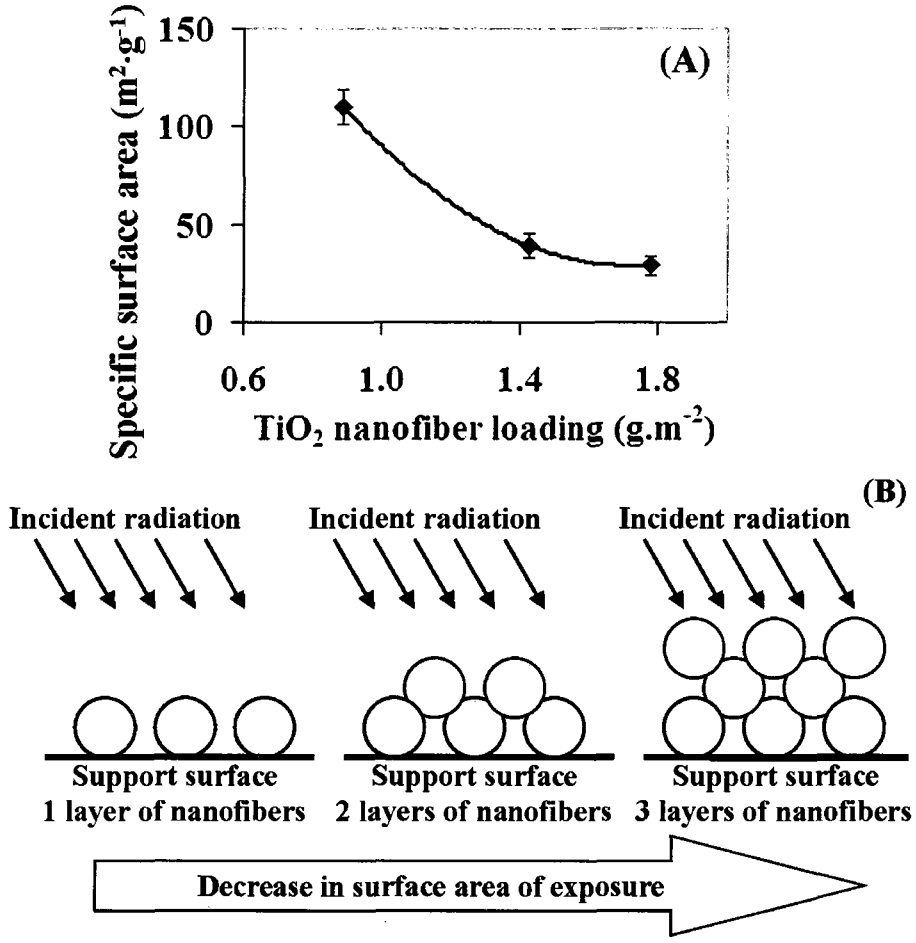

Figure 7.4 (A) Effect of TiO_2 nanofiber mass loading per unit area of support on specific surface area

(B) Schematic diagram relating layer-by-layer build-up of nanofibers with loss of surface area

7.3.5. Photocatalytic performance of immobilized TiO_2 nanofiber catalyst

The impingement of light on the TiO_2 surface with photon energy greater than the band gap (E_g) generates electron-hole pairs (Lee and Mills, 2004). The charge carriers (electrons in conduction band or hole in valence band) either recombine with the bulk of the material or migrate to the particle surface (Linsebigler et al., 1995). In aqueous medium, the electron–hole pairs initiate an oxidation–reduction reactions at the TiO_2 surface to produce $^{\bullet}OH$ radicals

(Herrmann, 2005). A factor determining the photocatalytic performance of TiO_2 is the band gap energy, which controls the photo-mediated charge carrier formations and subsequent degradation rate of organic pollutants (Bhatkhande et al., 2001). The SSA is another important factor which controls the number of free charge carriers on the TiO_2 surface (Carp et al., 2004). The selected immobilized TiO_2 nanofiber catalyst (denoted as NF) for photocatalytic experiments (electrospun from 1.3% Ti-containing solution and calcined at 400°C) had minimum fiber diameter of 39±6.6 nm, a maximum SSA of (259±23 $m^2 \cdot g^{-1}$) and the band gap energy of 3.24 eV. These were the optimum values (highest SSA and E_g) in comparison to fibers which were manufactured from 2.6% or 3.9% Ti containing solution and calcined at higher temperatures (450 °C or 500°C).

The experimental condition for phenol photocatalysis were adopted from the literature (Ray et al., 2009). The reaction conditions were as follows: phenol concentration = 40 $mg \cdot l^{-1}$, TiO_2 concentration = 0.5 $g \cdot l^{-1}$ and a reaction temperature of 37 ± 2°C. The dissolve oxygen (DO) level was maintained at 7.8 $mg \cdot l^{-1}$. The mass of TiO_2 was 25 mg (50 ml reaction volume containing 0.5 $g \cdot l^{-1}$ TiO_2) for the 39±6.6 nm diameter nanofibers supported on surface-treated aluminium foil (NF). Phenol degradation in the presence and absence of TiO_2 catalyst was assessed by monitoring the residual phenol concentration against reaction time (Figure 7.5(A)). Approximately 5% phenol degradation was observed in the absence of the TiO_2 catalyst (control). Within 60 minutes, 60 ± 1 % of phenol was degraded in photocatalytic reactions with NF (TiO_2 nanofiber) catalyst. Phenol degradation was observed to follow apparent first order kinetics according to equation (7.3).

$$-(dC/dt) = kC \qquad \text{or,} \qquad -\left[\ln\left(\frac{C}{C_O}\right)\right] = kt \tag{7.3}$$

where, k is the reaction rate constant, referred hereafter as apparent degradation rate constant (min^{-1}), C is the phenol concentration ($mg \cdot l^{-1}$) and $(-dC/dt)$ is the first order degradation rate. $-\ln(C/C_O)$ was plotted against the reaction time (t) to determine the apparent degradation rate constant (Figure 7.5(B)). The photocatalytic degradation rate with NF was recorded as 6.5 times faster than the control (photolytic rate).

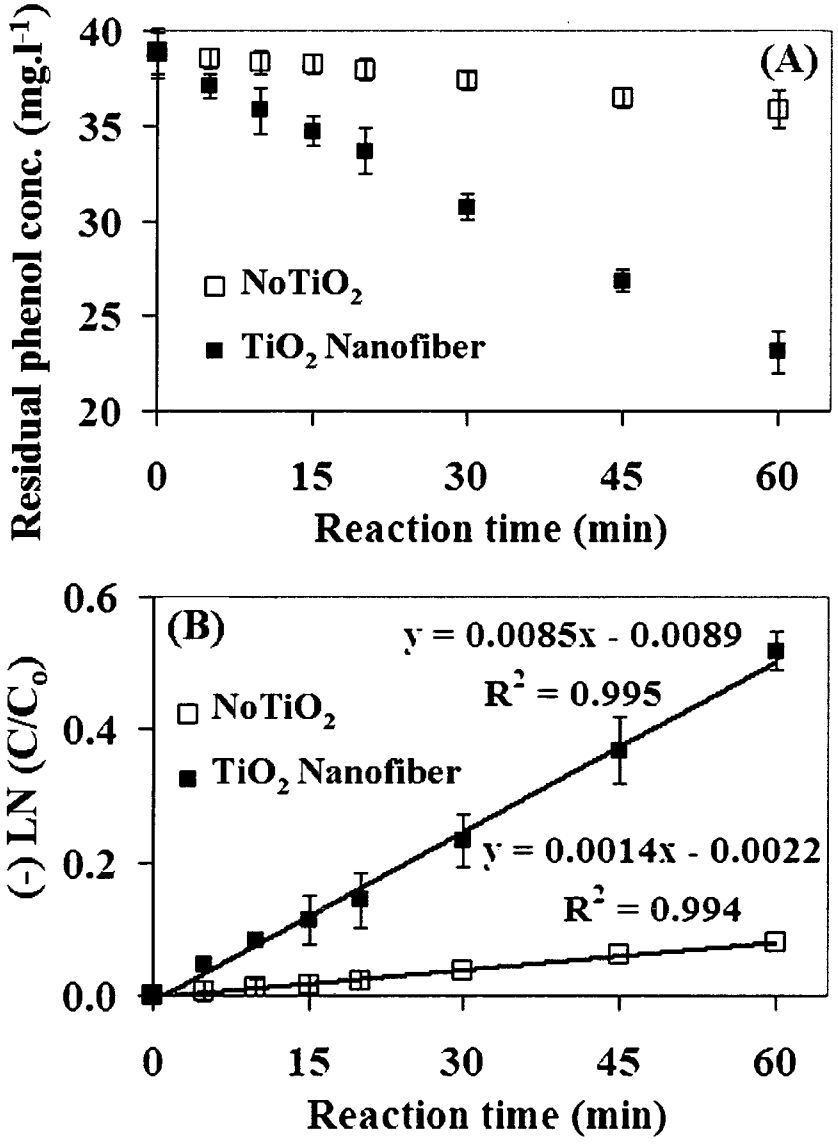

Figure 7.5 Degradation profiles for photocatalysis of phenol in presence and in absence of TiO_2 nanofiber catalyst

(A) Residual phenol concentration; (B) Apparent degradation rate

The apparent degradation rate of phenol with NF (TiO_2 nanofibers) was compared with TiO_2 nanoparticles of comparable specific surface area. TiO_2 nanoparticles with particle size of 5nm, specific surface area of 275±15 $m^2 \cdot g^{-1}$ and band gap energy of 3.23 eV (>99% anatase crystal phase) was compared with the NF catalyst. The photocatalytic rates for NF and 5nm nanoparticles were tabulated in Table 7.4. The quantum yield (ε) was determined using equation (7.4) (Lee and Mills, 2004).

$$\varepsilon = \frac{\text{(number of phenol molecules degraded per unit time)}}{\text{(number of incident photon per unit time)}} \qquad (7.4)$$

The quantum yield for control experiments (without TiO_2) was 10 times lower than the photocatalytic experiments with TiO_2 (nanofibers or nanoparticles). Higher degradation rate and quantum yield in photocatalytic experiments compared to the controls (photolysis) were attributed to the presence of TiO_2. Presence of TiO_2 facilitate higher conversion of incident photons to $^{\bullet}OH$ radicals, and thereby effect enhanced photocatalytic degradation rates (Bhatkhande et al., 2001; Herrmann, 2005).

Table 7.4: Comparative photocatalytic degradation rate for phenol with different catalyst

Type	Specific surface area ($m^2 \cdot g^{-1}$)	Nominal size of nanoparticles (nm)	Mean diameter of nanofibers (nm)	Apparent degradation rate (min^{-1})	Degradation rate ($\mu mol \cdot l^{-1} \cdot min^{-1}$)	Quantum yield
Nanoparticle	(275 ± 15)[a]	5		(0.0034 ± 0.0005)[a]	(3.5 ± 0.47)[a]	(0.19 ± 0.025)[a]
Nanofibers	(259 ± 23)[a]		(39 ± 6.6)[b]	(0.0085 ± 0.0001)[a]	(7.4 ± 0.35)[a]	(0.40 ± 0.019)[a]
Control (No TiO_2)				(0.0014 ± 0.0002)[a]	(1.2 ± 0.15)[a]	(0.03 ± 0.004)[a]

[a] Average and standard deviation for triplicate samples.
[b] Average and standard deviation for 50 fibers.

The quantum yield as well as photocatalytic degradation rate of NF was twice that observed for the 5 nm TiO_2 nanoparticles (of comparable SSA). The photocatalytic results clearly showed that, the immobilized NF has greater catalytic efficiency. Lower photocatalytic rates and quantum yield of the nanoparticles compared to NF could be accounted to the loss of SSA due to intrinsic aggregation tendency of nanoparticles in suspension (refer Appendix B).

The photocatalytic performance for the NF catalyst was compared with the results reported by Madhugiri et al. (2004). These authors studied the photocatalytic activity of electrospun TiO_2 nanofibers for phenol degradation and reported the SSA, approximate fiber diameter and photocatalytic degradation rate. Madhugiri et al. (2004) reported a photocatalytic degradation rate of 1.9 ± 0.16 $\mu mol \cdot l^{-1} \cdot min^{-1}$ for phenol with TiO_2 nanofibers, having diameter greater than 100nm and SSA of $32 m^2 \cdot g^{-1}$. In comparison, the photocatalytic rate observed for NF (TiO_2 nanofibers) in the present study was 3.9 times (7.4 ± 0.35 $\mu mol \cdot l^{-1} \cdot min^{-1}$) higher than the value reported by Madhugiri et al., (2004). The higher SSA (259 ± 23 $m^2 \cdot g^{-1}$) of NF (TiO_2 nanofibers) observed in this study had likely resulted in a better photocatalytic performance.

7.3.6. Performance of immobilized TiO_2 nanofiber catalyst after repeated use

A health hazard associated with the use of nanoparticle in suspension is release of remnant nanocatalyst particle into the environment via catalytic process effluent. Additionally, the loss of catalyst particles via process efflent is also uneconomical. Thus, reusability of the immobilized TiO_2 nanofiber catalyst is an important characteristic from the commercial standpoint. Hence, the NF catalyst was subjected to repeated photocatalytic experiments (cycle) to establish the reusability of the nanocatalyst.

The photocatalysis of phenol was monitored for 4 consecutive experimental cycles after thoroughly washing the NF photocatalyst in ultrapure de-ionized water after each experimental cycle. The photocatalytic degradation rate ($\mu mol \cdot l^{-1} \cdot min^{-1}$) and quantum yield was computed for each photocatalytic experimental cycle from the apparent degradation rate (Eqn. 7.3 and 7.4).

The observed phenol degradation rate and respective quantum yield values are tabulated in Table 7.5. The photocatalytic rates of 1st cycle and 4th cycle were compared using t-test at 95% level of confidence. The calculated t-value 1.85 ($p = 0.206$) was smaller than tabulated t-value 3.18 (Montogomery, 1997). Hence, it was concluded that no significant change was observed in the photocatalytic performance of the NF photocatalyst in 4 consecutive experiments. After the 4th cycle, the NF photocatalyst was heated at 199°C for 120 minutes and re-evaluated for photocatalytic performance. The photocatalytic rate of 5th cycle (6.77 ± 0.32 $\mu mol \cdot l^{-1} \cdot min^{-1}$) was in close agreement with that observed for the 4th cycle (6.44 ± 0.44 $\mu mol \cdot l^{-1} \cdot min^{-1}$). The results demonstrated the reusability of the NF (TiO_2 nanofibers) photocatalyst and confirmed that the photocatalyst retained its catalytic ability after repeated use (till 5 cycles examined).

Table 7.5: Photocatalytic degradation rate for phenol with nanofiber catalyst on mutiple use

Photocatalytic cycle	**Degradation rate ($\mu mol.l^{-1}.min^{-1}$)**	**Quantum yield**
1	(7.14 ± 0.16) [a]	(0.38 ± 0.01) [a]
2	(6.74 ± 0.32) [a]	(0.36 ± 0.02) [a]
3	(6.47 ± 0.22) [a]	(0.35 ± 0.01) [a]
4	(6.64 ± 0.44) [a]	(0.36 ± 0.02) [a]
--	Heated at 199°C for 120 minutes	
5	(6.77 ± 0.32) [a]	(0.36 ± 0.02) [a]

[a] Average and standard deviation for triplicate samples

7.4. Conclusions

TiO_2 nanofibers produced by sol-gel electrospinning were immobilized on a surface-treated aluminum foil through controlled thermal treatment. The effect of varying Ti-content in the electrospinning solution and final calcination temperature on the diameter and the SSA of the immobilized nanofiber catalyst were examined. The catalyst with smaller diameters, generated from electrospinning solution with lower Ti content, was associated with higher variability. Increasing the calcination temperature from 400°C to 500°C resulted in a considerable loss of SSA without significantly affecting the fiber diameter. Higher aggregation on fiber surface with increasing calcination temperature was accounted for the decrease in the SSA of the immobilized nanofiber catalyst. Decrease in the bandgap energy was observed at higher calcination temperature due to increased rutile content in the TiO_2 nanofibers. The mass of TiO_2 nanocatalyst immobilized per unit area of the aluminum support affected the SSA of the immobilized catalyst. Repeated deposition of the nanofibers on the support surface resulted in a decrease of the SSA. The immobilized nanofiber catalyst (NF) with SSA of 259±23 $m^2 \cdot g^{-1}$ and band gap energy of 3.24 eV was used for degrading phenol in the photocatalytic experiments. The photocatalytic degradation rate of the nanofiber catalyst (NF) was approximately 3.9 times higher than the value reported in the literature and 2 times higher than that observed with TiO_2 nanoparticle of a comparable specific surface area (275±15 $m^2 \cdot g^{-1}$). The immobilized nanofiber catalyst was subjected to repeated photocatalytic experiments and no significant change in performance was noted after 5 successive experimental cycles.

7.5. References

1. Alves, A.K.; Berutti, F.A.; Clemens, F.J.; Graule, T.; Bergmann, C.P. (2009). Photocatalytic activity of titania fibers obtained by electrospinning. *Mater. Res. Bull.* 44, 312–317.
2. Allen, N.S.; Edge, M.; Ortega, A.; Sandoval, G.; Liauw, C.M.; Verran, J.; Stratton, J.; McIntyre, R. B. (2004). Degradation and stabilisation of polymers and coatings: nano versus pigmentary titania particles. *Polym. Degrad. Stab., 85*, 927-946.
3. Baan, R.; Straif, K.; Grosse, Y.; Secretan, B.; El Ghissassi, F.; Cogliano, V. (2006). Carcinogenicity of carbon black, titanium dioxide, and talc. *The Lancet Oncol.,* 7, 295-296.
4. Bhatkhande, D.S.; Pangarkar, V.G.; Beenackers, A.A.C.M. (2001). Photocatalytic degradation for environmental applications - a review, *J. Chem. Technol. Biotechnol.* 77 102-116.
5. Blake, D.M. (1999). Bibliography of work on the heterogeneous photocatalytic removal of hazardous compounds from water and air. *NREL/TP-570-26797.* National Renewable Energy Laboratory, Golden, CO, Technical Report 3, 1 – 7.
6. Bozzi, A.; Yuranova, T.; Guasaquillo, I.; Laub, D.; Kiwi, J. (2005). Self-cleaning of modified cotton textiles by TiO_2 at low temperatures under daylight irradiation. *J. Photochem. Photobiol. A: Chem.*, 174, 156–164.
7. Carp, O.; Huisman, C.L.; Reller, A. (2004). Photoinduced reactivity of titanium dioxide. Prog. *Solid State Chem.* 32, 33-177.
8. Carpio, E.; Zuniga, P.; Ponce, S.; Solis, J.; Rodriguez, J.; Estrada, W. (2005). Photocatalytic degradation of phenol using TiO_2 nanocrystals supported on activated carbon. *J. Mol. Catal. A: Chem.* 228, 293–298.
9. Chandrasekar, R.; Zhang L.; Howe, J.Y.; Hedin, N.E.; Zhang, Y.; Fong, H. (2009). Fabrication and characterization of electrospun titania nanofibers. *J Mater Sci.,* 44, 1198–1205.
10. Chronakis, I.S. (2005). Novel nanocomposites and nanoceramics based on polymer nanofibers using electrospinning process—A review. *J. Mat. Process. Technol.*, 167, 283–293.
11. Centi, G.; Perathoner, S. (2009). The Role of Nanostructure in Improving the Performance of electrodes for energy storage and conversion. *Eur. J. Inorg. Chem.* 2009, 3851–3878.
12. Cui, X.M.; Nam, Y. S.; Lee, J.Y.; Park, W.H. (2008). Fabrication of zirconium carbide (ZrC) ultra-thin fibers by electrospinning. *Mat. Ltt.* 62, 1961 -1964.
13. Dijkstra, M.F.J.; Michorius, A.; Buwalda, H.; Panneman, H.J.; Winkelman, J.G.M.; Beenackers, A.A.C.M. (2001). Comparison of the efficiency of immobilized and suspended systems in photocatalytic degradation. *Catal. Today*, 66, 487–494.

14. Ding, B.; Kim, J.; Kimura, E.; Shiratori, S.(2004). Layer-by-layer structured films of TiO_2 nanoparticles and poly(acrylic acid) on electrospun nanofibers. *Nanotechnology*, 15, 913–917.

15. Doh, S.J.; Kim, C.; Lee, S.G.; Lee, S.J.; Kim, H. (2008). Development of photocatalytic TiO_2 nanofibers by electrospinning and its application to degradation of dye pollutants. *J. Haz. Mat.*, 154, 118–127.

16. Environmental Health Criteria (EHC) No. 161 (1994). *Phenol.* World Health Organization. Geneva, Switzerland. (ISBN 92-4-157161-6).

17. Frenot, A.; Chronakis, I. (2003). Polymer nanofibers assembled by electrospinning. *Curr. Opin. Colloid Interface Sci.*, 8, 64–75.

18. Gogate, P.R.; Pandit, A.B. (2004). A review of imperative technologies for wastewater treatment I: oxidation technologies at ambient conditions. *Adv. Environ. Res.*, 8, 501–551.

19. Hamid, M.A.; Rahman, I.A. (2003). Preparation of Titanium Dioxide (TiO_2) thin films by sol gel dip coating method. *Malay. J. Chem.*, 5, 1, 086 – 091.

20. Herrmann, J. M. (2005). Heterogeneous photocatalysis: state of the art and present applications, *Top. Catal.* 34, 49 – 65.

21. Houari, M.; Saidi, M.; Tabet, D.; Pichat, P.; Khalaf, H. (2005). The Removal of 4-chlorophenol and Dichloroacetic Acid in Water Using Ti-, Zr- and Ti/Zr-Pillared Bentonites as Photocatalyst. *Am. J. Appl. Sci.,* 2, 1136-1140.

22. Hurum, D.C.; Agrios, A.G.; Crist, S. E.; Gray, K.A.; Rajh, T.; Thurnauer, M.C. (2006). Probing reaction mechanisms in mixed phase TiO_2 by EPR. *J. Electron. Spectrosc. Relat. Phenom.* 150, 155–163.

23. Ibañez, P.F.; Malato, S.; Enea, O. (1999). Photoelectrochemical reactors for the solar decontamination of water. *Catal. Today*, 54, 329–339.

24. Jo, S.M.; Song, M.Y.; Ahn, Y.R.; Park, C.R.; Kim, D.Y. (2005). Nanofibril Formation of electrospun TiO_2 fibers and its application to dye-sensitized Solar cells. *J. Macromol. Sci., Pure Appl. Chem.*, 42, 1529–1540.

25. Kumar, A.; Jose, R.; Fujihara, K.; Wang, J.; Ramakrishna, S. (2007). Structural and optical properties of electrospun TiO_2 nanofibers. *Chem. Mater.*, 19, 6536–6542.

26. Lalman, J.A., and Ray, S.; (2009). Method of surface treatment of Aluminum foil and its alloy and method of producing immobilized nanocatalyst of transition metal oxides and their alloys. *US Patent* 61/272,518 (Provisional).

27. Lee, S. K.; Mills, A. (2004). Detoxification of water by semiconductor photocatalysis, J. *Ind. Eng. Chem.,* 10, 173-187.

28. Li, D.; Xia, Y. (2003). Fabrication of titania nanofibers by electrospinning. *Nano Lett.,* 3, 555 -560.

29. Ling, C.M.; Mohamed, A.R.; Bhatia, S. (2004). Performance of photocatalytic reactors using immobilized TiO_2 film for the degradation of phenol and methylene blue dye present in water stream. *Chemosphere*, 57, 547–554.

30. Linsebigler, L.; Lu, G.; Yates Jr., J.T. (1995). Photocatalysis on TiO_2 surfaces: Principles, mechanisms and selected results. *Chem. Rev.*, 95, 735-758.

31. Madhugiri, S.; Sun, B.; Smirniotis, P. G.; Ferraris, J. P.; Balkus (Jr), K. J. (2004). Electrospun mesoporous titanium dioxide fibers. *Microporous Mesoporous Mater.*, 69, 77–83.

32. Montogomery, D.C. (1997). *Design and analysis of experiments*, fourth ed., John Wiley and Sons, New York, NY. pp. 660 (ISBN 0-471-15746-5).

33. Ollis, D.F.; Pelezzetti, E.; Serpone, N. (1991). Photocatalyzed destruction of water contaminants, *Environ. Sci. Technol.* 25, 1522-1529.

34. Peiró, A.M.; Brillas, E.; Peral, J.; Domènech, X.; Ayllón, J.A. (2002). Electrochemically assisted deposition of titanium dioxide on aluminium cathodes. *J. Mater. Chem.*, 12, 2769–2773.

35. Pozzo, R.L.; Baltanfis, M.A.; Cassano, A.E. (1997). Supported titanium oxide as photocatalyst in water decontamination: State of the art. *Catal. Today*, 39, 219-231.

36. Rajeshwar, K. (1995). Photoelectrochemistry and the environment. *J. Appl. Electrochem.* 25, 1067-1082.

37. Ray, S.; Lalman, J.A.; Biswas, N. (2009). Using the Box-Benkhen technique to statistically model phenol photocatalytic degradation by titanium dioxide nanoparticles. *Chem. Eng. J.*, 150, 1, 15-24.

38. Reneker, D.H.; Chun, I. (1996). Nanometer diameter fibers of polymer, produced by electrospinning. *Nanotechnology*, 7, 216 – 223.

39. Sankapal, B.R. ; Sartale, S.D. ; Lux-Steiner, M.C. ; Ennaoui, A. (2006). Chemical and electrochemical synthesis of nanosized TiO_2 anatase for large-area photon conversion. *C. R. Chimie*, 9, 702–707.

40. Sayilkan, F.; AsiltTurk, M.; Sayilkan, H; Onal, Y.; Akarsu, M.; Arpae, E (2005). Characterization of TiO_2 Synthesized in alcohol by a Sol-Gel Process: The effects of annealing temperature and acid catalyst. *Turk. J. Chem.*, 29, 697 - 706.

41. Scotti, R.; D'Arienzo, M.; Morazzoni, F.; Bellobono, I.R. (2009). Immobilization of hydrothermally produced TiO_2 with different phase composition for photocatalytic degradation of phenol. *Appl. Catal. B – Environ.*, 88, 323-330.

42. Shah, S.I.; Li, W.; Huang, C.-P.; Jung, O.; Ni, C. (2002). Study of Nd^{3+}, Pd^{2+}, Pt^{4+} and Fe^{3+} dopant effect on photoreactivity of TiO_2 nanoparticles. *Proc. Natl. Acad. Sci. USA*, 99 (Suppl. 2): 6482 - 6486.

43. Sheikh, F.A.; Barakat, N.A.M.; Kanjwal, M.A.; Chaudhuri, A.A.; Jung, I-H.; Lee, J.H.; Kim, H.Y. (2009). Electrospun antimicrobial polyurethane nanofibers containing silver nanoparticles for biotechnological applications. *Macromol. Res.*, 17, 688 – 696.

44. Sigmund, W.; Yuh, V.; Park, H.; Maneeratana, V.; Pyrgiotakis, G.; Daga, A.; Taylor, J.; Nino, J. C. (2006). Processing and structure relationships in electrospinning of Ceramic Fiber Systems. *J. Am. Ceram. Soc.*, 89, 395–407.

45. Song, M.Y.; Kim, D.K.; Ihn, K. J.; Jo, S.M.; Kim, D.Y. (2004). Electrospun TiO_2 electrodes for dye-sensitized solar cells. *Nanotechnology*, 15, 1861–1865.

46. Subbiah, T.; Bhat, G.S.; Tock, R.W.; Parameswaran, S.; Ramkumar, S. (2005). Electrospinning of Nanofibers. *J. Appl. Polym. Sci.*, 96, 557–569.

47. Tekmen, C.; Suslu, A.; Cocen, U. (2008).Titania nanofibers prepared by electrospinning. *Mat. Ltt.*, 62, 4470 – 4472

48. Teleki, A.; Wengeler, R.; Wengeler, L.; Nirschl, H.; Pratsinis, S.E. (2008). Distinguishing between aggregates and agglomerates of flame-made TiO_2 by high-pressure dispersion. *Powder Technol.*, 181, 292–300.

49. Zhang, H.; Banfield, J.F. (1998). Thermodynamic analysis of phase stability of nanocrystalline titania. *J. Mat. Chem.* 8, 2073 – 2076.

50. Zhang, X. ; Xu, S. ; Han,G. (2009). Fabrication and photocatalytic activity of TiO_2 nanofiber membrane, *Mat. Lett.* 63, 1761–1763.

CHAPTER 8: CONCLUSIONS AND RECOMMENDATIONS

The work outlined in this dissertation described several important aspects of using Titanium dioxide (TiO_2) as a photocatalyst. The outcomes from the initial two phases of research, detailed in Chapter 3 to Chapter 4, presented several key findings on the photocatalytic degradation of phenol and phenol derivatives using TiO_2 nanoparticles. Later chapters of this dissertation (Chapter 5 to Chapter 7) focused on fabrication and characterization of an immobilized TiO_2 nanocatalyst with improved catalytic properties.

Photocatalysis is a surface phenomenon and therefore, the photocatalytic degradation process is affected by the surface area of the photocatalyst. Many of the earlier studies have used commercially available nanoparticles as a photocatalyst and reported that smaller nanoparticles were associated with higher photocatalytic activity by virtue of their higher surface area. In Chapter 3 (Phase 1) of this dissertation, the effects of four variables on the photocatalytic process were critically assessed with phenol as the model pollutant. Along with TiO_2 concentration (loading), dissolved oxygen (DO) level and substrate concentration, the size of TiO_2 nanoparticles were also evaluated for their effects on the photocatalytic rate. The results of a statistical analysis showed that increasing surface area due to diminished nanoparticle size does not necessarily enhance the photocatalytic rate. There exists an optimum particle size below which quantum size effect restricted the enhancement in the photocatalytic rate. A numerical algorithm based optimization study showed that approximately 10nm diameter of TiO_2 nanoparticle was optimum for photocatalytic performance. This result was validated with experimental data. The Chapter 3 also described the development of a model which consolidated the different factors affecting the photocatalytic degradation rate of phenol.

Chapter 4 (Phase 2) was an extension of the research presented in Chapter 3. The model developed for photocatalytic degradation of phenol (phenol model) was validated using data for the degradation of a phenol derivative, *p*-cresol. *p*-Cresol was selected as model pollutant due to its widespread industrial application and continued commercial use. The phenol model was observed to be valid for predicting the degradation rate of *p*-cresol. The photocatalytic behavior of *p*-cresol was examined in the context of computed activation energy and quantum yield. In the presence of TiO_2 nanoparticles, *p*-Cresol degraded faster than phenol.

Chapter 5 (Phase 3) was focused on the fabrication of an immobilized TiO_2 nanofiber catalyst with improved stability. The composite nanofibers of TiO_2 and a polymer (PVAc) were generated by electrospinning. The composite nanofibers were characterized by DSC, TGA, FTIR, and XRD. FTIR studies confirmed the removal of the constituent polymer (PVAc) from the composite nanofibers when the sample was heated at 400°C for 2 hours. The XRD studies showed that the nanofibers calcined at 400°C comprised of TiO_2 with anatase crystal structure. Anatase is the photocatalytically most active crystal form of TiO_2. The effect of increasing calcination temperature on the fiber morphology was studied. The FESEM images showed increased sintering of nanofibers on the support surface at calcination temperatures higher than 400°C. The stoichiometric composition of the nanofibers was confirmed by energy dispersive spectroscopy (EDS). A [Ti]/[O] atomic ratio of 0.47 was recorded for the nanofibers. Earlier studies reported that a lack of stability of immobilized catalyst was due to the poor adhesion between the support and the TiO_2 nanofibers. A two step approach was developed to resolve the problem. In the first step, the catalyst support surface was chemically treated; in the second step, nanofibers were bridged by external means to the support surface. A surface-treated aluminum foil was selected as the catalyst support. Bridging between the nanofibers was achieved by

applying a polyvinyl acetate (PVAc) polymer coating. The immobilized TiO_2 nanofiber catalyst demonstrated good adhesion (3B-2B as per ASTM D 3359-09) to the support. The weight loss of the immobilized catalyst due to mechanical agitation in water for 1 hour was negligible (< 5%).

Chapter 6 described statistical optimization of the electrospinning process variables using the Box-Benkhen design (BBD) procedure for minimizing the TiO_2 nanofiber diameter. A three factor three level BBD was used to examine the effect of the experimental variables on the diameter of TiO_2 nanofibers. Potential difference across electrodes, infusion rate of electrospinning solution, and separation distance between electrodes were the three experimental factors evaluated. Higher potential difference (40kV), lower infusion rate (0.6 $ml \cdot h^{-1}$) and higher separation distance (32.5cm) were reported to yield TiO_2 nanofibers with a minimum diameter. The Ti-content of the electrospinning solution was observed to affect the nanofiber diameter. The lowest fiber diameter was generated using a 1.3% Ti-containing solution. Electrospinning a solution containing 1.3% Ti at an optimum setting of 40kV potential difference across electrodes separated by 32.5cm at infusion rate of 0.6 $ml \cdot h^{-1}$ produced nanofibers with average diameter of 39.5 ± 6.6 nm. The diameter of the nanofibers reported in the study was significantly lower than the values reported by other researchers.

In Chapter 7, the photocatalytic performance of the TiO_2 nanofibers was examined. Higher calcination temperature promoted sintering of pores resulting in a loss of SSA. Increasing the Ti-content of electrospinning solution also caused loss of surface area. An increase in the catalyst loading beyond $0.9 g \cdot m^{-2}$ had a negative impact on the SSA of the nanofiber catalyst. A decrease in the bandgap energy was observed with increasing calcination temperature beyond 400°C. Higher anatase-to-rutile crystal transformation at temperatures higher than 400°C was accounted for reduced bandgap values. The immobilized nanocatalyst with maximum SSA and highest

band gap energy was evaluated in photocatalytic experiments with phenol as a model pollutant. The observed photocatalytic rate with the nanofiber catalyst was twice that observed with TiO_2 nanoparticle of comparable SSA. The immobilized nanofiber catalyst was subjected to repeated photocatalytic experiments; no significant change in the photocatalytic performance was observed after 5 experiments. A literature search revealed that the photocatalytic rates observed with the immobilized nanofiber catalyst developed in this study was approximately 4 times higher than the rates obtained with immobilized catalyst which were used in past studies.

The study presented in this dissertation reported a novel TiO_2 nanofiber catalyst with enhanced photocatalytic performance and improved stability. This research achievement can be considered significant from an engineering standpoint because it could lead to the use of an immobilized nanocatalyst in bench-scale photocatalytic reactors. However, a few obstacles are required to be resolved before the nanocatalyst can be made commercially available. The transformation from batch production to a continuous production process based on batch studies will entail redesigning the existing process. A uniform distribution of the catalyst on the support surface on continuous basis is another requirement (Martin et al., 1999). The present electrospinning apparatus needs significant restructure and additional optimization before this immobilization technique can be commercialized. Several multi-nozzle solution delivery systems are reported in the literature (Kim et al., 2006; Yoon et al., 2008; Yang et al., 2008). Adoption of similar design with reciprocating traverse of the nozzle and the collector can be considered for uniform deposition of the catalyst on the support surface.

Another important consideration that deserves attention is the energy dependence of the immobilization process. Thermal treatment of the catalyst is highly energy dependent. Recently, a process for generating TiO_2 nanowire has been reported. The study reported producing

nanowires without the use of polymer backbone. However, the researchers did not provided any information regarding immobilizing the nanowire catalyst (Xie and Shang, 2007; Sui et al., 2008). A polymer free immobilization process can significantly reduce the energy requirement of this catalyst fabrication process. A study on the polymer free nanocatalyst immobilization is recommended for future work.

References

1. Martin, C.A.; Camera-Rhoda, G.; Santarelli, F. (1999). Effective design of photocatalytic reactors: influence of radiative transfers on their properties. *Catal. Today*, 48, 307 - 313.
2. Kim, G.H.; Cho, Y.S.; Kim, W.D. (2006) Stability analy-sis for multi-jets electrospinning process modified with a cylindrical electrode. *Euro. Polym. J.*, 42, 2031-2038.
3. Yoon, H.; Kim, G.H.; Kim, W.D. (2008) Electrohydro-dynamic process supplemented by multiple-nozzle and auxiliary electrodes for fabricating PCL nanofibers, *Polymer*, 32, 334-339.
4. Yang, Y.; Jia, Z.; Li, Q; Hou, L; Guan, Z. (2008). Electrospinning uniform fibers with a special regular hexagonal distributed multi-needle system. *J. Phys.: Conf. Series*, 142, 012027.
5. Xie, R-C; Shang, J.K. (2007). Morphological control in solvothermal synthesis of titanium dioxide. *J. Mat. Sci.* 42, 6583 – 6589.
6. Sui, R.; Thangadurai, V.; Berlinguette, C.P. (2008). Simple protocaol for generating TiO_2 nanofibers in organic media. *Chem. Mater.* 20, 7022 – 7023.

CHAPTER 9: ENGINEERING SIGNIFICANCE

Increasing toxicological health impacts coupled with widespread usage and environmental discharge in large quantities are some important factors driving the research towards developing an effective treatment strategy for removal of the phenolic contaminants. The treatment of phenolic contaminants is a challenge to existing treatment technologies. Heterogeneous photocatalysis can be classified as a 'green' remedial solution for phenolic contaminants. The general goal of this dissertation is to evaluate titanium dioxide (TiO_2) as a potential heterogeneous photocatalyst for degrading phenolic compounds from aqueous phase.

The factors affecting TiO_2 mediated photocatalytic degradation of phenolic contaminants are critically analyzed for a batch set-up in Chapter 3 and Chapter 4. The studies presented in these chapters demonstrated the use of Box-Benkhen experimental design (BBD) for screening and consolidating the process variables into a statistical model. The model had accurately predicted the photocatalytic degradation rate constant for phenol (Chapter 3) and *p*-cresol (Chapter 4) at various process conditions; over a range of TiO_2 size, TiO_2 concentration, dissolve oxygen (DO) concentration and substrate (phenol or *p*-cresol) concentration. The model for the photocatalytic degradation rate constant could be used as an effective tool for predicting the residual level of phenol or *p*-cresol in the process effluent under a specific setting of process parameter. The model can also be used to determine the level of the process variables (factors) for achieving a target photocatalytic degradation rate or can be used for comparison between more than one process condition. Another significant outcome from phase 1 (Chapter 3) and phase 2 (Chapter 4) is identification and validation of the optimum nanoparticle size for maximum photocatalytic activity. The implication can be helpful in selections of TiO_2 nanoparticle catalyst and thereby, has the potential to improve the efficiency of the existing photocatalytic treatment systems.

The use of TiO_2 nanoparticle as slurry for photocatalytic application is associated with several practical limitations. Immobilization of TiO_2 on solid support is a better approach; however, the existing immobilized TiO_2 nanocatalyst also has serious bottlenecks. Chapter 5 to Chapter 7 focused on improving the shortcomings of the TiO_2 immobilized nanocatalyst. Chapter 5 reported an immobilized TiO_2 nanofiber catalyst with improved stability. Improved stability together with nanometric dimensions can have a useful consequence on the application of the immobilized TiO_2 catalytic systems. TiO_2 nanofibers were fabricated using electrospinning technique. The electrospinning process was statistically evaluated in Chapter 6 for fabricating TiO_2 nanofibers with smaller diameters. The effect of potential difference across electrodes, infusion rate and separation distance between electrodes on nanofiber diameter was analyzed through BBD. A model was developed for predicting the diameter of the nanofiber knowing the electrospinning process conditions. The existence of a similar model for predicting the TiO_2 nanofiber diameter from sol-gel electrospinning was not reported in the literature. A relationship between nanofiber diameter and specific surface area of the immobilized catalyst was reported in Chapter 7. In combination the knowledge delivered in Chapter 5 to Chapter 7 can be very useful in fabricating customized TiO_2 catalyst with desired attributes. The optimization study of the sol-gel electrospinning of TiO_2 nanofibers presented in Chapter 6 revealed the levels of the electrospinning variables associated with lowest fiber diameter and helped to fabricate TiO_2 nanofibers with smallest reported diameter. The results from Chapter 7 showed that the immobilized TiO_2 nanofiber catalyst with smallest fiber diameter had comparable specific surface area (SSA) and higher photocatalytic activity than that of discrete nanoparticles. In summary, the outcomes of these sections (Chapter 5 – 7) of the dissertation present an advancement in the structure-property relationship of the TiO_2 photocatalyst.

The overall engineering significance of the research presented in this dissertation lies in its accomplishment towards adding more insightful understanding to the photocatalytic process in terms of process variable interactions and development of an immobilized TiO_2 photocatalyst with lesser practical limitation and improved catalytic activity.

APPENDIX A: CALIBRATION CURVES

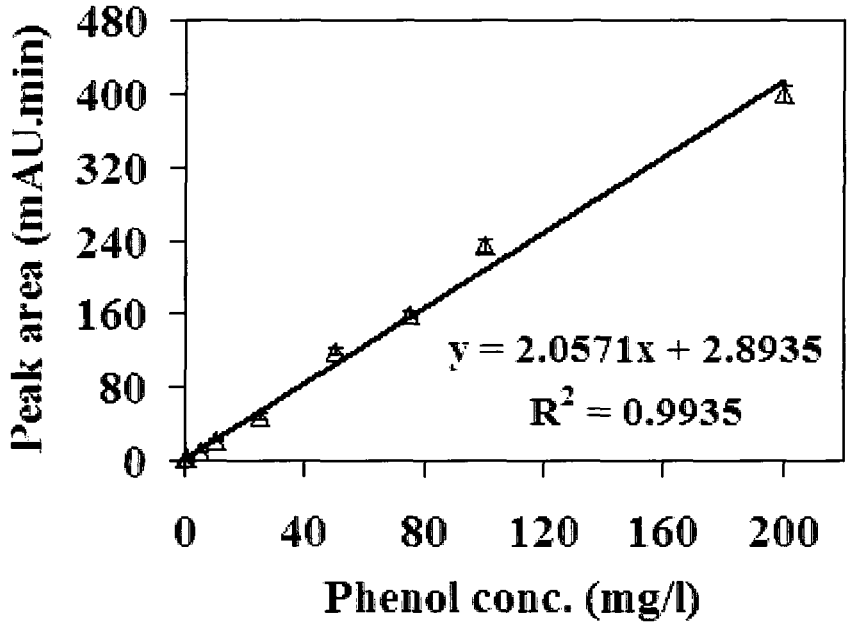

Figure A1 Phenol Calibration Curve in HPLC

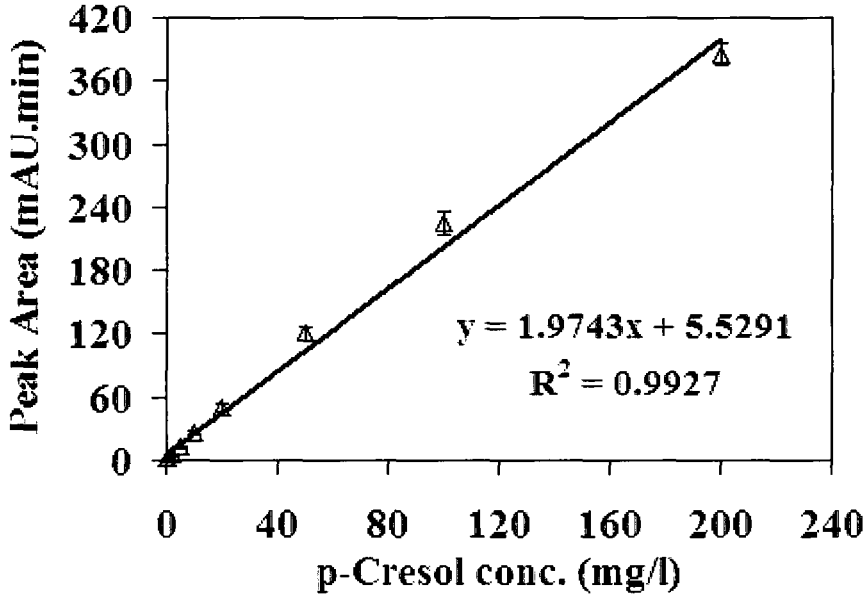

Figure A2 *p*-Cresol Calibration Curve in HPLC

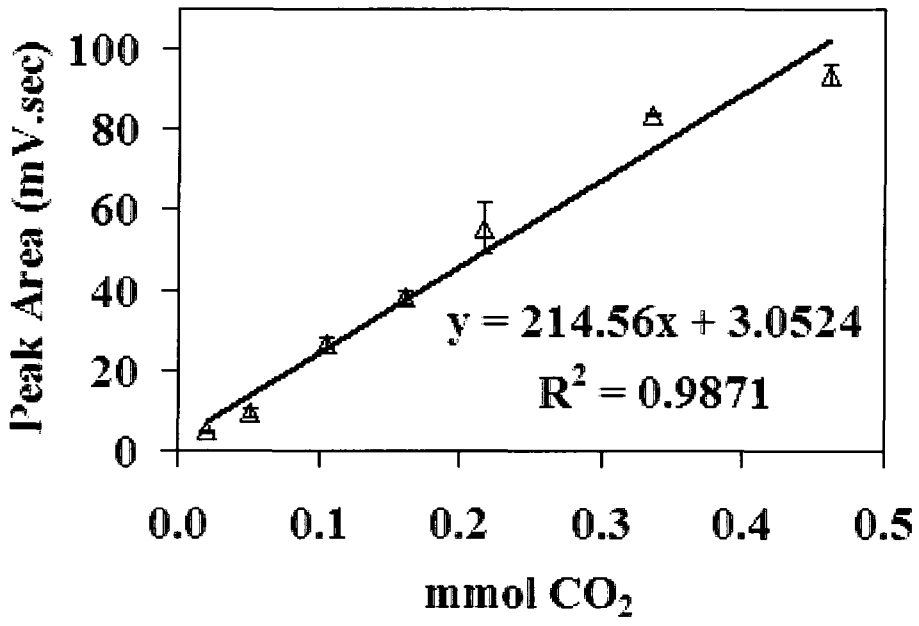

Figure A3 CO_2 Calibration Curve in GC

APPENDIX B: STUDY ON WET AGGEGATION OF TIO_2 NANOPARTICLES IN SLURRY

Table 1. Specific surface area and wet aggregate size for TiO_2 nanoparticles

Nominal size of dry nanoparticles (nm)	Diameter of wet aggregates of nanoparticles (nm)	Specific surface area (SSA) - dry ($m^2 \cdot g^{-1}$)
5	$(167 \pm 37)^a$	$(275 \pm 15)^a$
10	$(99 \pm 26)^a$	$(131 \pm 12)^a$
32	$(80 \pm 20)^a$	$(47 \pm 2)^a$

[a] Average and standard deviation for triplicate samples.

APPENDIX C: IMAGES OF CATALYST SUPPORT

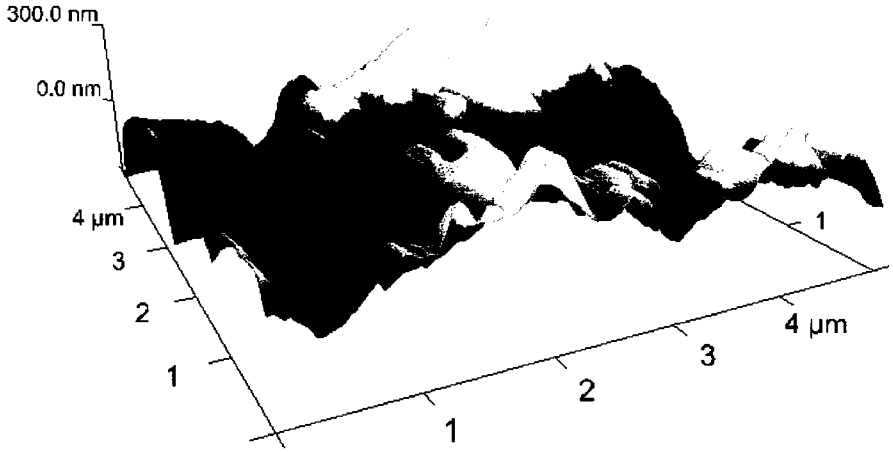

Figure C1 AFM image of the surface of the treated aluminum foil used as support for TiO_2 nanofiber immobilization

Figure C2 FESEM image of the cross-section of the treated aluminum foil used as support for TiO_2 nanofiber immobilization

APPENDIX D: ELECTROSPINNING CONTROL STUDY WITH POLYVINYL ACETATE

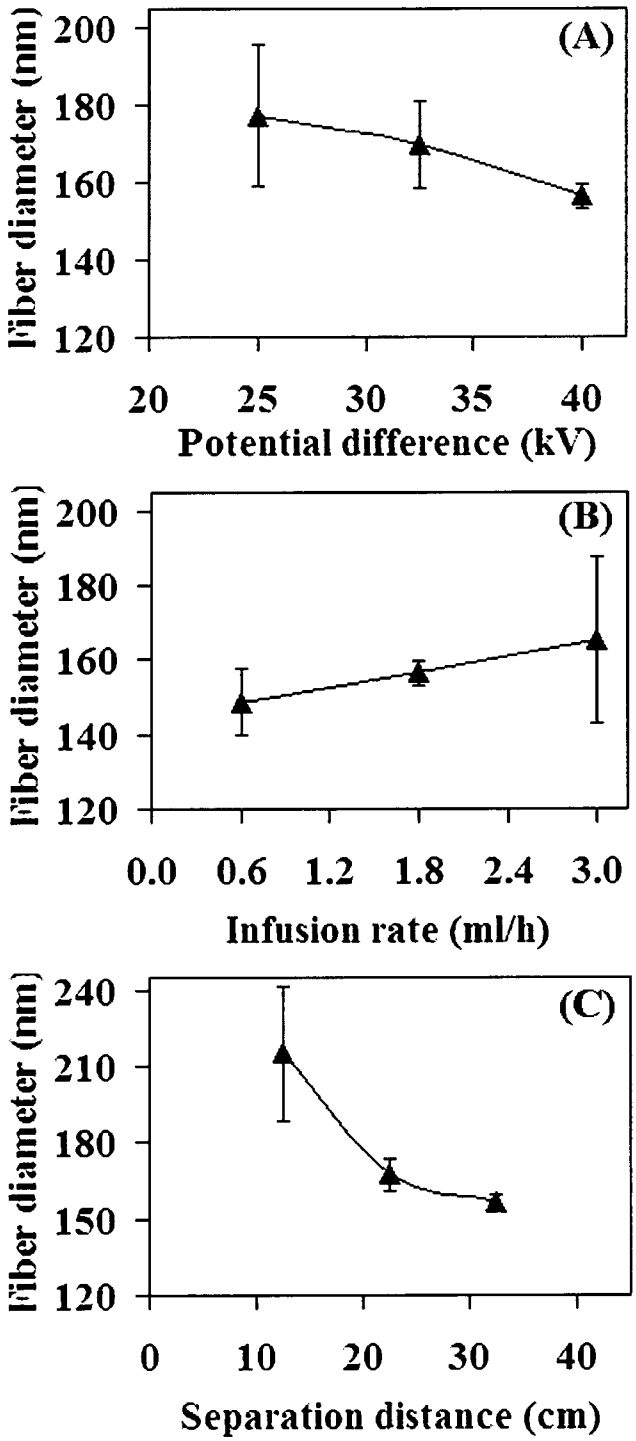

Figure D Effect of electrospinning variables on the diameter of polyvinyl acetate (PVAc) nanofibers

(A) Potential difference; (B) Infusion rate; (C) Separation distance

APPENDIX E: CALCULATION OF QUANTUM YIELD

Quantum yield (ε)

$$\varepsilon = \frac{\text{(number of phenol molecules degraded per unit time)}}{\text{(number of incident photon per unit time)}} \quad \text{(E1)}$$

Degradation rate (mole degraded per unit time)

$$-(dC/dt) = kC \quad \text{(E2)}$$

where, C is molar concentration (mol/l) and k is the apparent degradation rate constant ($time^{-1}$).

For reaction volume, V (l), moles of phenol degrading per unit time = V × C × k (E3)

1 mole is known to contain 6.023×10^{23} molecules, Avogadro number (A)

Number of phenol molecules degraded per unit time

$$= A \times V \times C \times k \quad \text{(E4)}$$

Energy per photon (E),

$$E = hc/\lambda \quad \text{(E5)}$$

where, h is Planck's constant, c is speed of light

Incident energy per unit time = Intensity of incident radiation (I) × Area (S) (E6)

$$\text{Number of incident photon per unit time} = \frac{I \times S}{E} \quad \text{(E7)}$$

Substituting E4 and E7 in E1,

$$\varepsilon = \frac{A \times V \times C \times k}{\frac{I \times S}{E}} \quad \text{(E8)}$$

E.g.,

for V = 0.05 l, C = 0.001 mol/l, k = 5.67×10^{-5} s^{-1}, I = 89.8 W/m^2, S = 0.0074 m^2, λ = 3×10^{-7} m

ε is computed by plugging the values in E8.

Resultant quantum yield, ε = 0.17

APPENDIX F: PROTOCOL FOR EVALUATION OF MODEL ACCURACY AND RESPONSE OPTIMIZATION

F-1. EVALUATION OF MODEL ACCURACY

A model that does not accurately predict the response cannot provide good answers to the underlying engineering or scientific questions under investigation. Hence, assessment of the accuracy in prediction is an important step in model building sequence (Box *et al.*, 1978). The analysis of residuals is a statistical technique for estimation of model accuracy and fit. The residual is the difference between the model predicted value and the experimental outcome at identical factor levels within the design space under consideration (Myer and Montogomery, 2002). For a well predicted model, the residuals are expected to follow a normal distribution and their occurrences are random (Box and Draper, 1987; Myer and Montogomery, 2002). Graphical analyses of residual techniques, such as, scatter plot of residuals and histogram of residuals, are good indicator of model accuracy (Montogomery, 2005). However, more conclusive method is to compute the Anderson-Darling (AD) statistic. AD statistic quantifies the deviation for a set of residuals and assesses the normal distribution of residuals by comparing the computed AD statistics against reference value (Stephens, 1974). The validity of the distribution of residuals usually tested at a 5% level of significance to confirm the model accuracy.

F-2. RESPONSE OPTIMIZATION

The identification of optimum process conditions favorable for a targeted (maximum or minimum) response is of great significance in engineering processes. The evaluation of a factor space involving combination of the process factors and their levels through experimental design procedure is a primary step for the response optimization (Box and Draper, 1987). Next is to

develop a statistical model for accurate prediction of response surface. The contour of the response surface is determined using the model. A graphical method of response optimization is overlaying contour plot (Box and Draper, 1987; Myer and Montogomery, 2002). However, a precise method of locating the optimum condition is to use optimality criterion. The optimality criterion provides a measure of fitting the data to a model (Box and Draper, 1987). Computing the D-optimality value is a popular optimization method. The D-optimality criterion minimizes the variance among the model coefficients and defines the factor level combination for optimum response (Redhe *et al.*, 2002). The numerical algorithm used for computing the D-optimality values for different factor levels within the design space. Several factor level combinations are evaluated for selecting the optimum solution.

References

1. Box, G.E.P.; Hunter, W.G.; Hunter, W.S. (1978). *Statistics for Experimenters: An Introduction to Design, Data Analysis, and Model Building*, John Wiley and Sons, New York, NY, pp. 510 - 536. (ISBN 0-471-09315-7)

2. Box, G.E.P; Draper, N.R. (1987). *Empirical Model Building and Response Surfaces*, John Wiley & Sons, New York, NY, pp. 205 – 477 (ISBN 0-471-81033-9).

3. Myer, R.H.; Montogomery, D.C. (2002). *Response surface methodology: Process and product optimization using designed experiment*, second ed., John Wiley and Sons, New York, NY. pp. 343-350 (ISBN 0-471-41255-4).

4. Montogomery, D.C. (2005). *Design and analysis of experiments*, sixth ed., John Wiley and Sons, New York, NY. pp. 373-606 (ISBN 0-471-66159-7)

5. Redhe, M.; Forsberg, J.; Jansson, T.; Marklund, P-O.; Nilsson, L. (2002). Using the response surface methodology and the D-optimality criterion in crashworthiness related problems, *Struct. Multidisc. Optim.*, 24, 185-194.

6. Stephens, M. A. (1974). EDF Statistics for Goodness of Fit and Some Comparisons. *J. Am. Stat. Soc.*, 69, 730-737.

VITA AUCTORIS

NAME:	Srimanta Ray
PLACE OF BIRTH:	Kolkata, West Bengal, India
YEAR OF BIRTH:	1975
EDUCATION:	University of Calcutta, Kolkata, India Bachelors of Chemistry 1993 – 1996
	University of Calcutta, Kolkata, India Bachelors of Fiber Technology 1997 – 2001
	Indian Institute of Technology, Delhi, India Masters of Fiber Science and Technology 2001 – 2002
	University of Windsor, Windsor, Ontario Doctorate in Environmental Engineering 2006 – 2010